NONCOVALENT FUNCTIONALIZATION OF GRAPHENE

A Dissertation

Presented to the Faculty of the Graduate School

of Cornell University

In Partial Fulfillment of the Requirements for the Degree of

Doctor of Philosophy

by

Jason Adam Mann

August 2013

NONCOVAlENT FUNCTIONALIZATION OF GRAPHENE

Jason Adam Mann, Ph. D.

Cornell University 2013

Graphene is a newly available conductive material ideally suited for forming well-defined interfaces with electroactive compounds. Aromatic moieties typically interact with the graphene surface to maximize Van der Waals interactions, predisposing most compounds to lie flat on its basal plane. A tripodal motif binds multivalently to graphene through three pyrene moieties and projects easily varied functionality away from the surface. The thermodynamic and kinetic binding parameters of a tripod bearing a redox-active Co(II) *bis*-terpyridyl complex were investigated electrochemically. The complex binds strongly to graphene and forms monolayers with a molecular footprint of 2.3 nm^2 and a $\Delta G_{ads} = -38.8 \pm 0.2$ kJ mol^{-1}. Its monolayers are stable in fresh electrolyte for more than 12 h and desorb from graphene 1000 times more slowly than model compounds bearing a single aromatic binding group. Tripods with naphthalene or phenanthrene moieties also desorb more rapidly than those with pyrene, but reach greater monolayer densities. Noncovalent functionalization also allows assembled functionality to behave dynamically on the surface, afeature not observed in conventional self assembled monolayers. In addition, while biomacromolecuels adsorbed on bare graphene can lose their function, tripods bearing N-hydroxy succinimidyl ester groups immobilize both antibodies and Concanavalin A without loss of function. This result represents an important step forward in the design of flexible biosensors and provides a modular method for engineering the surface chemistry of graphene for biological applications.

BIOGRAPHICAL SKETCH

Jason Adam Mann was born in Easton, Maryland, and began his schooling there at age five at home with his elder brother Joseph under the tutelage of their mother Cynthia Mann and their grandmother Dolores Albright. At age seven, Jason and his family moved to Farmville, Virginia where Jason's interests expanded into animal husbandry and eventually veterinary medicine. Inspired by his time on the farm Jason, now age sixteen, matriculated to Longwood University, majoring in biology on the pre-veterinary medicine track of study. It was in the course of studying biology at Longwood that Jason first experimented with chemistry, as college students often do with habit forming substances, becoming nearly instantly addicted. In his sophomore year, Jason took on chemistry as a second major, still with the intent of pursuing veterinary medicine. However, as graduation loomed near, Jason questioned whether he could give up chemistry for medicine, and finding the answer a resounding "NO!" decided to pursue graduate studies in chemistry. Following graduation *summa cum laude* from Longwood in 2008, Jason moved to Ithaca, New York to pursue his passion for chemistry at Cornell University. In August of 2008, Jason joined the newly founded group of William Dichtel, first as a summer research assistant and later as one of Will's first graduate students. As such, Jason had the pleasure of working on a myriad of projects in the Dichtel Group, the main body if which were focused on the noncovalent functionalization of graphene. Jason graduated as the first Ph.D. from the Dichtel Group in May 2013 and will continue his professional development as a postdoctoral fellow with Professor James Tour at Rice University in Houston, Texas.

Dedicated to the three women who made me who I am:

My loving wife,

My patient mother,

and

My proud grandmother

ACKNOWLEDGMENTS

I would like to thank Professor William Dichtel for all of his support, patience, and instruction and for the opportunity to work in a world class lab with world class people. I must also thank Professor Héctor Abruña for serving on my special committee, and for welcoming me into his molecular electronics subgroup, where I learned more than any organic chemist should know about electrochemistry. I must also thank Professor Geoffrey Coates for serving on my special committee and for the advice and support he has provided throughout my time at Cornell.

I would be remiss if I did not thank Dave Wise, who worked with me on the design of the Dichtel Group's Schlenk lines as well as several iterations of microscale electrochemical cells, and then deftly sculpted them into the works of art that enabled many of our group's feats of science. Not to mention all of the broken glassware that he rebuilt, better, faster, and stronger than before. I would also like to thank Ivan Keresztes for all of his help with NMR through the years. Dave Neish and Larry Stull also deserve thanks for keeping Baker Lab from falling down around us as we work.

I must also thank my many collaborators, especially Professor Joaquín Rodríguez-López, who furthered my electrochemical enlightenment and made Chapter 4 of this dissertation possible. Dr. Thomas Alava deserves special thanks for his role in bringing the tripods into the world of nanobiotechnology. In addition, both Joaquín and Thomas deserve thanks for being awesome people, with whom it was an absolute pleasure to work. Nicole Ritzert was key as a source of scientific and random discussion both of which I enjoyed immensely.

My groupmates also deserve my thanks for all of the support, discussion, suggestions, and fun that they have provided. Dr. Eric Spitler deserves my thanks for mentoring me during my first year. David Bunck deserves special thanks for acting as my coffee dealer, helping to

deepen my addiction, and for officiating my wedding. Abraham Saldivar deserves my thanks for many useful discussions and for being an incredible friend, even if he did eat things like Chickenanas™. Our courtyard training sword sessions and coffee breaks are sorely missed. Catherine DeBlase deserves my thanks for frequent coffee fueled scientific discussions, dealing with my nosiness, and for being a sport when my meddling entered her social life as I set her up with Michael Mulzer. Hasan Arslan deserves special thanks for being my best friend in the group. Hasan is the only person in the group with whom I can joke with and confide in as I would my brother, and that is a priceless thing in the stressful years of graduate school.

My family deserves my thanks for all of their love and support not only during graduate school, but in the 20 years that led me to my current path. The sacrifices that my mother made over the years to ensure my education and the development of my character have made me the man I am now. The early education that my Mother provided, shaped by walks through the woods and trips to museums, zoos, and aquaria certainly created the inquisitive nature that I now enjoy. The constant competition and encouragement from my brother, Joseph, has taught me to always strive to become better.

I must also acknowledge Professor Peter Wolczanski, not for advice but for teaching Chem 6050 and making it an exceptionally demanding course. The difficulty that I had in Prof. Wolczanski's course led me to the greatest blessing in my life, Crisita Carmen Hojilla Atienza. If Chem 6050 had not been so challenging, I never would have sought her help and we may never have become such close friends, and if we had not become friends, we would not be married today. Lastly, I must thank my beautiful, loving wife, Crisita. Not only is she my closest friend, and my supportive partner, she has also been a source of motivation and inspiration without which I would have been incapable of completing my Ph.D.

TABLE OF CONTENTS

LIST OF FIGURES

CHAPTER ONE

CHAPTER TWO

APPENDIX ONE

CHAPTER THREE

APPENDIX TWO

CHAPTER FOUR

APPENDIX THREE

CHAPTER FIVE

APPENDIX FOUR

CHAPTER SIX

APPENDIX FIVE

LIST OF TABLES

CHAPTER ONE

NONCOVALENT FUNCTIONALIZATION OF GRAPHENE BY MOLECULAR AND POLYMERIC ADSORBATES

1.1 Abstract

The desirable properties and increased availability of single and few-layer graphene have motivated interest in interfacing functional molecules and materials to its high surface-area basal plane. The surface of pristine graphene lacks chemical functionality to allow for covalent modification without interrupting its continuous π-orbital system. In contrast, noncovalent functionalization does not suffer from these drawbacks and offers a means to tune graphene properties and incorporate molecular recognition or other active elements. In this Chapter, we describe emerging strategies to interface molecular compounds and polymers to graphene as well as the enhanced properties and new functions that they impart.

1.2 Introduction

Graphene refers to a single layer or a few layers of the two-dimensional, honeycomb lattice of graphitic carbon. It has attracted intense interest since the isolation of single layer graphene (SLG) by mechanical exfoliation and subsequent demonstration of its desirable properties.[1] A broad range of attractive features of graphene have emerged, including its exceptional charge carrier mobility, high strength and flexibility, transparency, and impermeability to molecular and atomic species, a combination of properties not found in other materials.[2] At first, the availability of pristine graphene samples was limited by the low throughput of the exfoliation method. Higher throughput approaches have since emerged, each with its own strengths and drawbacks, which together provide access to either bulk

quantities or large-area, substrate-supported samples. The two-step oxidation/exfoliation of graphite to graphene oxide, followed by reduction back to graphene, is highly scalable, but the resulting chemically converted graphene invariably retains oxidized defects.[3] Thermal decomposition of SiC provides access to wafer scale epitaxial graphene grown directly on insulating substrates.[4-6] This method produces graphene of excellent quality, but is limited by the high cost of SiC substrates and the extreme temperatures (*ca.* 1400 °C) required. Finally, in chemical vapor deposition (CVD) methods, a gaseous carbon source is decomposed over a thin film of a transition metal catalyst (usually Cu, Ni, or Ru).[7-8] This method can access large area samples, as demonstrated by a roll-to-roll process for 30 inch-wide SLG described in 2010.[9] The relative ease of removing the metal catalyst after growth has led to the development of polymer-mediated transfer processes that enable SLG to be supported on most substrates.[10-11] Other developments in CVD production of graphene include accessing multilayer samples,[12] dramatically increasing the graphene grain size,[13-14] and integrating SLG with hexagonal boron nitride.[15] These rapid developments ensure graphene's availability and relevance for both bulk and nanometer-scale device applications.

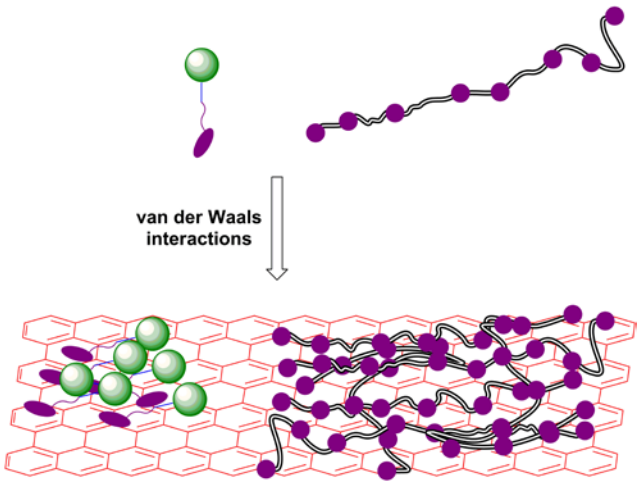

Figure 1.1. Schematic of noncovalent functionalization of graphene using polymers and small molecule adsorbates.

As these applications emerge, it has become increasingly desirable to interface functional molecules or polymers to graphene (Figure 1.1). Unlike conventional electrode materials, such as silicon, transition metals, or indium tin oxide (ITO), graphene lacks reactive functionality or established self-assembled monolayer chemistries to mediate functionalization. Furthermore, because of its single or few-layer thickness, covalent modification of the basal plane degrades many of graphene's desirable properties. Noncovalent functionalization strategies do not suffer from these drawbacks, as they do not affect the transparency, or conductivity (except through doping) of the material.[16] In this chapter, we highlight noncovalent functionalization strategies for graphene that are based on molecular and polymeric adsorbates and their roles in imparting added function or improved graphene properties. Although early work in this area successfully utilized commercially available compounds, some of the most intriguing examples of noncovalent graphene fucntionalization have emerged from designed or iteratively improved systems. Therefore, collaborative efforts among graphene experimentalists, theorists, and synthetic chemists will greatly benefit further progress in this area.

1.3 Noncovalent Functionalization Utilizing Molecular Species

Assembling molecules on the graphene basal plane through Van der Waals interactions represents an operationally simple method to introduce arbitrary functionality to the graphene surface and to influence its charge carrier density. SLG's atomically precise structure makes it suitable for crystallizing molecules in two-dimensions and has inspired our efforts to control molecular orientation through multivalent binding interactions. Several considerations are important for evaluating molecular assembly on graphene. Differences in molecular size and coverage, which can range from fractions of monolayers to multilayers, strongly influence the

accessibility of the graphene basal plane and its electronic properties. It is also important to match the stability of the adsorbed monolayers or multilayers to the desired application. For example, applications that involve exposure to solvent or heat require more robust molecule-SLG interactions than molecular layers formed and utilized under ultrahigh vacuum (UHV) conditions. In other cases, weakly adsorbed but highly ordered adlayers might be desirable, such as for transporting charge within organic electronic devices. Thus far, relatively few compounds have been used to functionalize SLG noncovalently (Figure 1.2), although structure-property relationships derived from the extensive studies of molecular crystallization on highly ordered pyrolytic graphite[17-24] and the noncovalent functionalization of carbon nanotubes[25-28] are also informative.

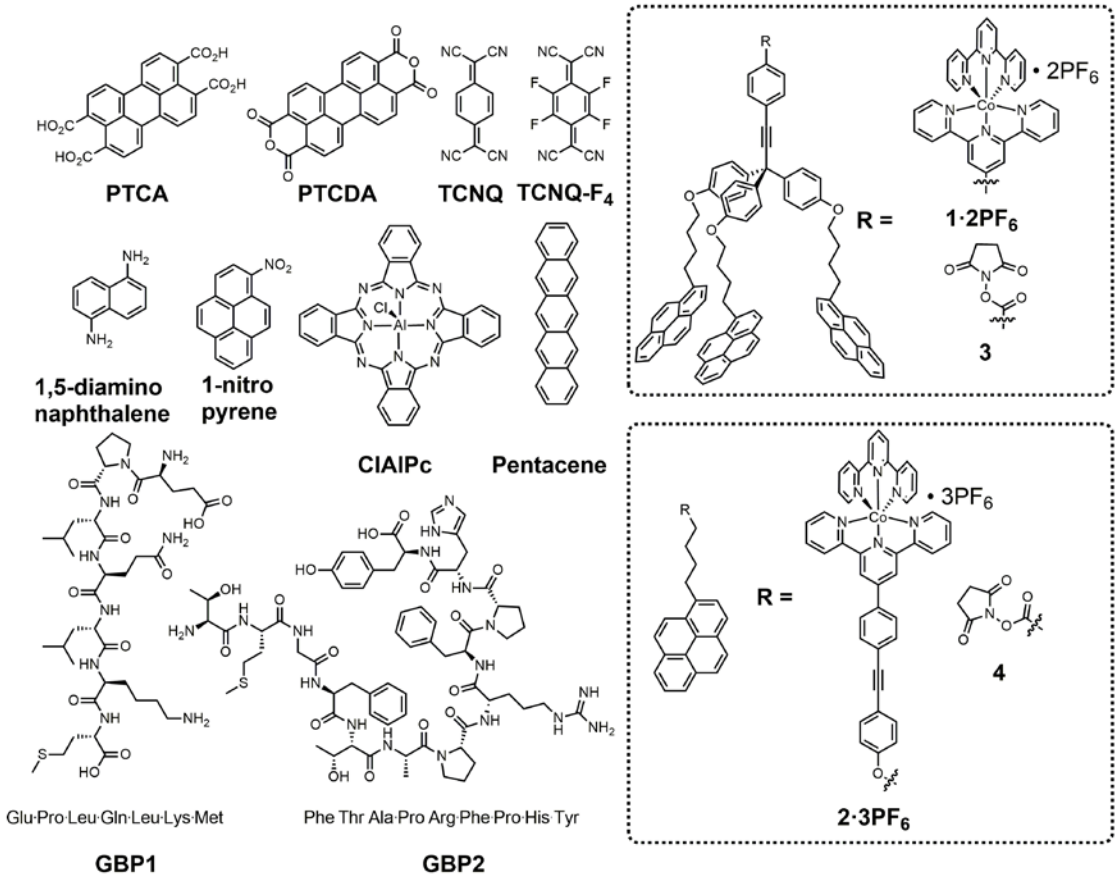

Figure 1.2. Molecular adsorbates discussed in this chapter.

Early examples of functionalizing substrate-supported SLG were motivated by the need to deposit uniform gate dielectrics to fabricate graphene-based field effect transistors (GFETs). Dai and coworkers observed that atomic layer deposition (ALD) of Al_2O_3 onto the graphene basal plane provided poor coverage, as the oxide formed almost exclusively at edges and defect sites (Figure 1.3).[29] These locations presumably contain oxidized carbon functionality that seed Al_2O_3 growth. In contrast, continuous Al_2O_3 films grow on SLG functionalized with a monolayer of perylene tetracarboxylic acid (PTCA), whose four carboxylic acid groups serve as Al_2O_3 nucleation sites. These monolayers mediated the growth of conformal coatings as thin as 3 nm. Hersam and co-workers subsequently deposited the corresponding anhydride (perylene tetracarboxylic dianhydride, PTCDA) onto epitaxial graphene under UHV conditions.[30] Careful control of the molecular deposition parameters associated with this approach yielded 2D crystalline PTCDA monolayers, despite the presence of defects and step-edges on the SLG (Figure 1.4). The PTCDA monolayers also mediated the formation of continuous ALD films of both Al_2O_3 and HfO_2, a technologically relevant high-dielectric constant material.[31] Metal evaporated onto the oxide films provided capacitors with low leakage currents ($\sim 10^{-9}$ A cm^{-2}) and one of the highest capacitances (700 nF cm^{-2}) reported for top-gated GFETs, suggesting that the seeded monolayers were free of pinhole defects.

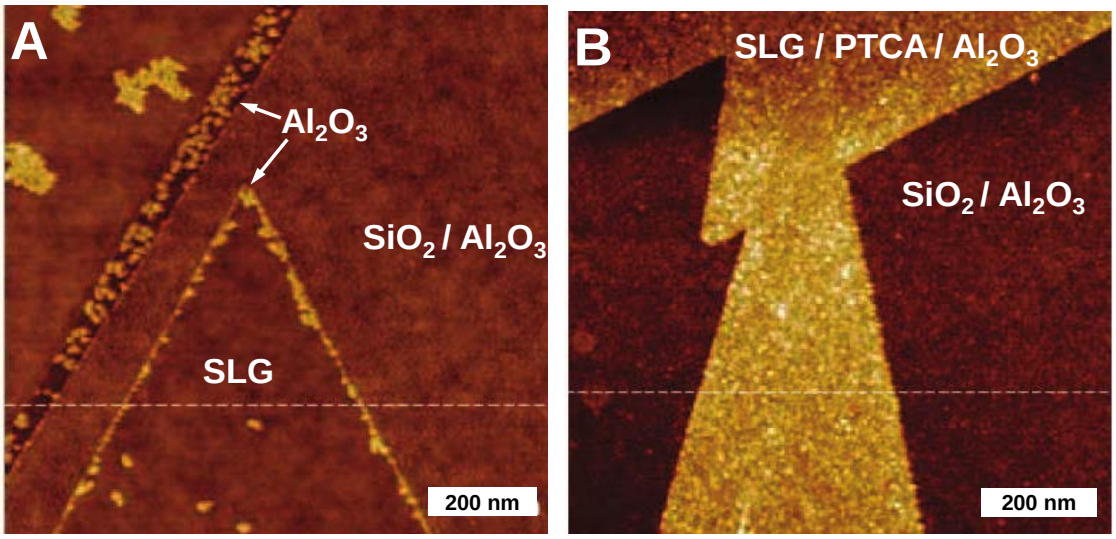

Figure 1.3. AFM images of Al_2O_3 grown using ALD on (A) pristine SLG and (B) SLG functionalized with a monolayer of PTCA. Al_2O_3 growth is localized to edge and defect sites on pristine SLG but forms uniform coatings on the PTCA monolayers (Adapted with permission from ref. 29 Copyright 2008 American Chemical Society).

Adsorbing molecules onto SLG provides a mild, modular, patternable, and potentially reversible means to tune graphene's charge carrier density. Feng and co-workers calculated the shift of the charge-neutrality point of few-layer epitaxial graphene (FLG) induced by the adsorption of the small molecule *p*-type dopant tetracyanoquinodimethane (TCNQ) and its perfluorinated derivative (F_4-TCNQ).[32] The computational results were confirmed experimentally by 0.6 eV and 1.4 eV shifts in the FLG work function for TCNQ and F_4-TCNQ, respectively, at deposition thicknesses under 3 nm. Coletti and co-workers subsequently demonstrated that deposition of a 0.8 nm thick coating of F_4-TCNQ fully compensated for the inherent *n*-type doping of bilayer epitaxial graphene on SiC.[33] Such tuning provides a means to replicate the superior electronic performance of suspended, exfoliated SLG samples, which are difficult to fabricate, using easily accessible substrate-supported SLG. In the case of bilayer graphene, the adsorbed layer increases its bandgap to as

high as 0.3 eV. Similar, albeit less controlled effects were observed when the F_4-TCNQ was introduced from solution. Complementary, spatially resolved doping was demonstrated by Y. T. Chen and co-workers using a PDMS-based flow cell.[34] The authors deposited 1,4-diaminonaphthalene (a *n*-type dopant) and 1-nitropyrene (a *p*-type dopant) onto different regions of an SLG device. Removing the flow cell provided heterojunctions composed of differently doped graphene, which showed two charge neutrality points in FET measurements delineating *p*+-*p*, *p*-*n*, and *n*-*n*+ regimes under various gate biases.

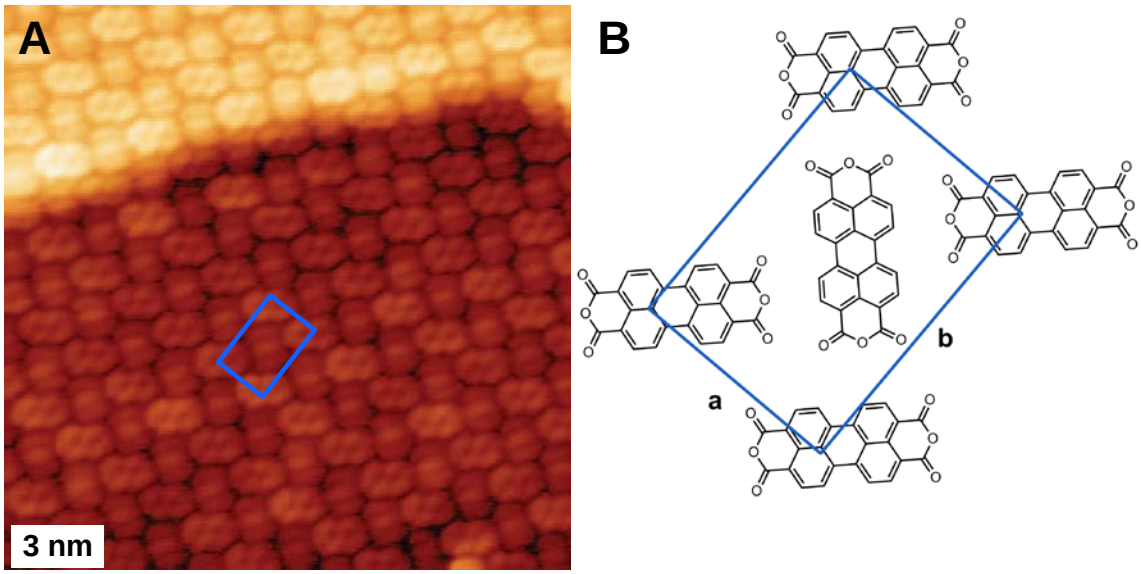

Figure 1.4. (A) High resolution STM image of a self assembled monolayer of PTCDA deposited on epitaxial graphene under UHV conditions showing the highly ordered, long range packing of the PTCDA molecules. (B) Line-angle structures showing the unit cell structure and parameters a and b. (Adapted with permission from ref. 30 Copyright 2009 Nature Publishing Group)

Many compounds, especially those with extended π-electron systems, adsorb onto graphene with different orientations than those observed on other device-relevant substrates. These differences in molecular orientation strongly impact organic electronic device performance. For example, W. Chen and co-workers deposited chloroaluminum

phthalocyanine (ClAlPc) onto an SLG-coated ITO substrate under UHV conditions and noted that the Al-Cl bond was oriented normal to the surface.[35] This orientation maximizes the Van der Waals interactions between the ClAlPc and SLG. In contrast, the ClAlPc sat 45^{o} off normal when deposited onto bare ITO. Cho and co-workers demonstrated the effect of this phenomenon on performance of FETs comprised of pentacene. Much like ClAlPc, pentacene lies flat on the graphene surface but adopts an upright configuration on SiO_2 gate dielectrics. The upright configuration is desirable for organic FETs (OFETs), as it orients the pentacene π-electron systems to transport charge between the source and drain electrodes. Indeed, pentacene OFETs based on pristine SLG exhibit higher charge transfer resistance and lower charge carrier mobilities than when polymer residues, which orient the pentacene molecules laterally, remain on the SLG surface.[36] In contrast, photovoltaic devices, in which charge transport occurs vertically, might benefit from the vertically stacked molecular orientation directed by SLG.

Likewise, the aromatic heterocycles of nucleic acids adsorb to graphene,[16] much as they do to carbon nanotubes[28] Loh and coworkers anodized epitaxial graphene to introduce oxygenated defects, while leaving pristine graphene regions, thus providing a means to compare the utility of noncovalent assembly and covalent tethering of single-stranded probe DNA (ssDNA) within the same device platform.[37] An electrochemical assay that detected complementary or single-base mismatched ssDNA demonstrated comparable detection limits for both immobilization methods, but covalently immobilized ssDNA exhibited a larger dynamic range. Li and coworkers evaluated DNA hybridization on CVD graphene within a transistor device platform,[38] in which ssDNA strands adsorbed to a graphene conductance channel detect complementary ssDNA in solution. The hybridization process induces partial

desorption of the probe strand, which affects the doping level of the graphene. This strategy achieved detection limits of 0.01 nM and differentiated between complementary and single-base mismatched ssDNA targets. The authors also immobilized the probe strands on Au nanoparticles (NPs) on the graphene surface, which achieved improved upper detection limits, likely attributable to a higher density of immobilized strands.

A phage-display strategy was utilized by McAlpine and co-workers to identify two oligopeptides that absorb to the graphene basal plane.[39] The phage-display approach begins with a population of bacteriophages bearing various oligopeptides, which are exposed to graphite flakes. Bacteriophages from this population that bind to graphite are washed from the flakes, and then amplified. Five iterations of this process with increasingly stringent washes prior to amplification provided a heptapeptide (graphene binding peptide 1, GBP1) and dodecapeptide (GBP2) that bind strongly and preferentially to graphitic surfaces. For example, Au nanoparticles functionalized with GBP1 selectively assembled onto graphene patterned on Si wafers. Furthermore, GFETs functionalized with a bifunctional peptide consisting of GBP1 conjugated to a tetrapeptide that binds trinitrotoluene (TNT) exhibited resistance changes in response to trace vapors of the explosive.

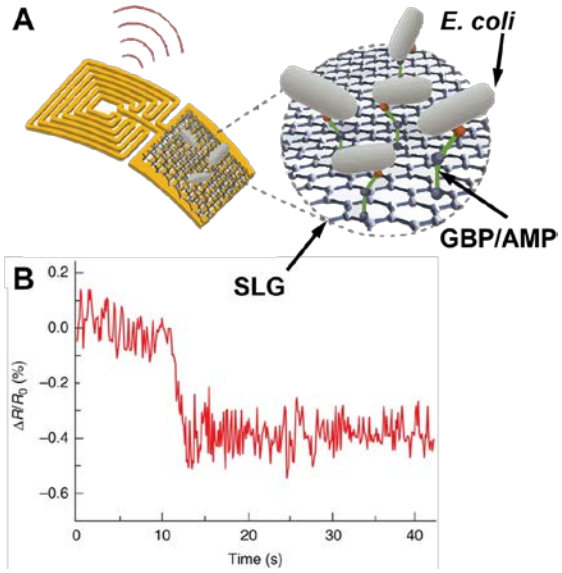

Figure 1.5. (A) Schematic of a flexible graphene biosensor with inductor coil for wireless readout using GBP to noncovalently functionalize graphene with an AMP for use as a bacteria sensor. (B) Resistance change associated with detection of a single *E. coli* cell observed using the GBP/AMP/SLG conjugate.

Subsequent biosensors based on bifunctional peptides incorporating GBPs illustrate several attractive features of graphene.[40] GBP2 conjugated to an antimicrobial peptide (AMP) was assembled onto graphene-on-silk devices, which were adsorbed to biological surfaces such as tooth enamel and muscle tissue. Capacitance measurements at the GBP/AMP modified graphene surface were used to detect individual binding events of *E. coli* cells from saliva (Figure 1.5). Binding events were detected wirelessly using an interdigitated electrode array interfaced to an inductive coil. These examples demonstrate the importance of graphene's flexibility and conductivity for next generation biosensors and shows that GBPs are a promising platform for further study of noncovalent graphene functionalization.

electrode array interfaced to an inductive coil. These examples demonstrate that GBPs are a promising platform for further study of noncovalent graphene functionalization.

Although many of the above compounds are useful for modifying the graphene surface, their monolayers are often unstable in effective solvents for the binding groups. Dichtel and co-workers designed a multivalent tripod-shaped compound capable of binding SLG through three pyrene "feet", which we describe in detail in Chapter Two of this dissertation.[41] The compound features a tetrahedral core that directs the binding groups toward the graphene while displaying the arbitrary functionality away from the surface. Self-assembly of a $Co(tpy)_2$ tripod **1·2PF$_6$** was first compared to monovalent **2·3PF$_6$** using cyclic voltammetry. Both compounds form monolayers on the SLG surface from micromolar concentration solutions of the binding group, with the larger **1·2PF$_6$** achieving a higher than expected fractional coverage (81% vs 33% expected) relative to **2·3PF$_6$** (Figure 1.6A). This finding, combined with an analysis of the electron transfer kinetics of the two compounds, suggests that the tripods adopt an upright configuration on the SLG surface. In addition, the monovalent complex **2·3PF$_6$** desorbs from graphene 1000 times more rapidly, disappearing in under 10 min, than **1·2PF$_6$**, which retains 86% of its saturation coverage after 12 h. A subsequent scanning electrochemical microscopy study of microspots of **1·2PF$_6$** on SLG demonstrated that the tripods are mobile on the graphene surface, in which the outward diffusion of the tripods from the microspots was fit to a 2D diffusion model, discussed in detail in Chapter Four of this dissertation.[42] These findings highlight an as-yet unrealized opportunity of noncovalent functionalization strategies: dynamic or stimuli responsive functions derived from molecular motion on the SLG surface. Dynamic and stimuli responsive systems may include enzymes that operate in tandem, light harvesting arrays that rearrange upon adsorption, photochemical or electrochemical switches, or even living cells attached to the graphene surface.

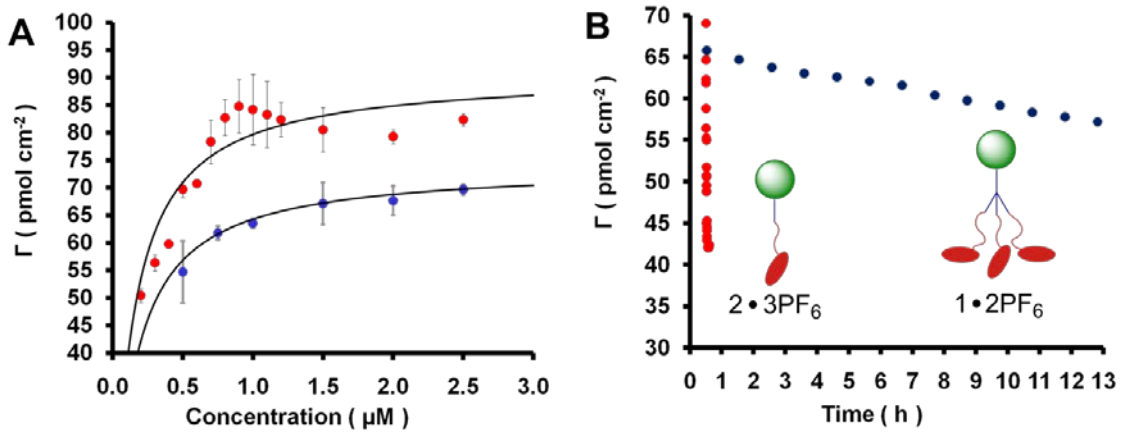

Figure 1.6. (A) Langmuir binding isotherms of **1·2PF$_6$** (blue) and **2·3PF$_6$** (red) on SLG. (B) Plots of coverage (Γ) vs time for monolayers of **1·2PF$_6$** (blue) and **2·3PF$_6$** (red) that were formed on SLG electrodes and then transferred to fresh THF / NH_4PF_6 electrolyte solution at t = 0 (Adapted with permission from ref. 41 Copyright 2011 American Chemical Society).

The kinetic stability of the tripod monolayers was also leveraged to anchor proteins relevant to biosensors on SLG. An anti-*E.coli* antibody is readily captured by bare SLG, as well as by SLG bearing monolayers of tripod **3** or pyrene butyrate **4**, which both feature N-hydroxysuccinimidyl(NHS) esters for bioconjugation reactions. However, only the antibody-functionalized tripod monolayers bind *E. coli* cells at above background levels (Figure 1.7), while antibodies adsorbed to SLG or attached to **4** show similar levels of *E.coli* recognition as a monolayer of a mistmatched (anti-bovine serum albumin) antibody supported on **3**.[43] These findings are discussed in detail in Chapter 5 of this dissertation.

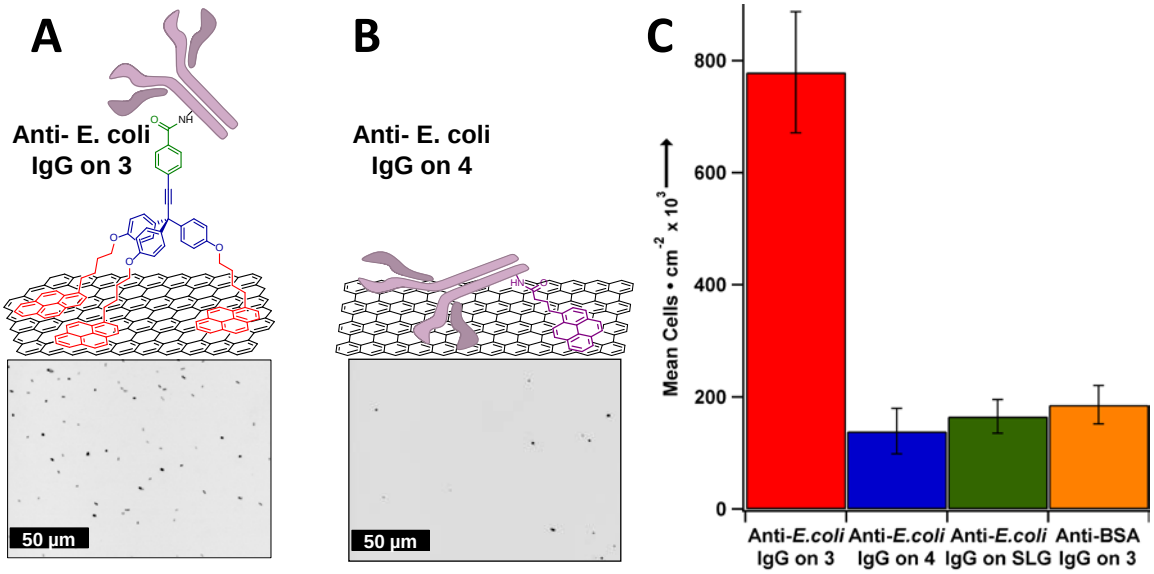

Figure 1.7. Fluorescence micrographs of captured *E. coli* cells stained with propidium iodide and schematic illustrations for (A) tripod immobilization of anti-*E. coli* antibody and (B) monopod immobilization of anti-*E. coli* antibody. (C) Bar graph showing average number of cells captured using different methods of immobilization of anti-*E. coli* antibody (Adapted with permission from ref. 43 Copyright 2013 Wiley Publishing Group).

Similar findings were observed for the lectin protein Concanavalin A (ConA). Tripod bound ConA retained its ability to recognize both dissolved oligosaccharides and those found on *Bacillus subtilis* cell walls, whereas the protein showed no evidence of these functions when adsorbed directly to the SLG.[44] Our study involving ConA is discussed in detail in Chapter 6 of this dissertation. These findings demonstrate the value of robust noncovalent binding groups for preserving the function of proteins on SLG, which are otherwise prone to deleterious denaturation.

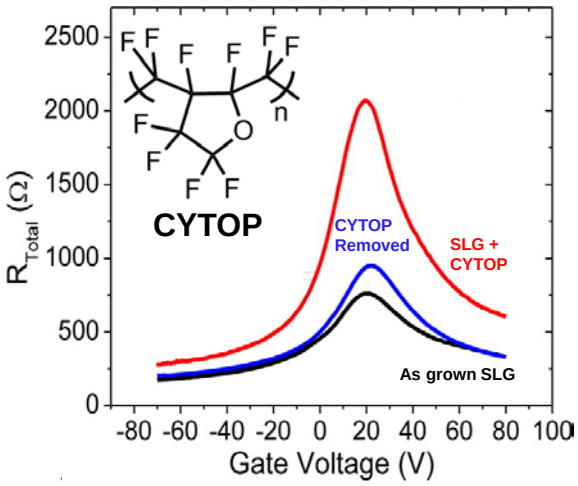

Figure 1.8. Resistance vs gate voltage plot showing GFET characteristics of as grown SLG (black), SLG doped using CYTOP fluoropoylmer (red), and SLG after removal of CYTOP using solvent (blue). Inset: structure of a monomer unit of CYTOP (Adapted with permission from ref. 46 Copyright 2013 American Chemical Society).

1.4 Polymeric Adsorbates

Interfacing polymeric thin films to SLG can confer many desirable features, including mechanical strength and/or flexibility,[45] tunable changes in doping,[46-48] and a large number of reactive functional groups.[49] In contrast to monomeric adsorbates, polymers form less ordered, thicker layers that enable them to serve as environmental barriers and supporting or active layers. Polymers are also straightforward to introduce, usually via solution deposition, and may be patterned through a variety of lithographic techniques. SLG derived from CVD processes is prepared on metal foils and transferred to substrates of interest using a sacrificial polymer layer, typically poly(methyl methacrylate) (PMMA). Ruoff and coworkers developed an approach to dope the SLG during the transfer process by employing the fluoropoylmer poly(perfluoroalkenylvinyl ether) (CYTOP) in place of PMMA.[47] Hypsochromic shifts of the graphene G and 2D Raman bands, as well as changes in the Dirac point, were observed after annealing the CYTOP polymer layer, which presumably induces the alignment of local dipole

moments along the polymer chain with respect to the SLG. Dodabalapur and coworkers subsequently demonstrated improved FET device performance, including increased on:off current ratios and a Dirac point observable within the device's working potential range (Figure 1.8), by performing the graphene transfer using PMMA and introducing CYTOP during device fabrication. Together these findings indicate that fluoropolymers are effective and convenient *p*-type dopants for SLG.[46]

More exotic polymer films have also been used to impart improved performance or added function to graphene based transistors. Ahn and co-workers utilized a block copolymer/ionic liquid gel gate electrode witin GFETs constructed on flexible, transparent polymer substrates.[50] The high dielectric constant of the polymer/ionic liquid gate provided a large current modulation of 2.4 mA over a 3V bias range, as compared to 0.4 mA over a 40 V range for similar GFETs with Si/SiO_2 gates. Chien and coworkers demonstrated a ternary logic device based on a GFET functionalized with a photoactive azobenzene-containing polymer.[48] Azobenzene isomerization is associated with a change in dipole moment that alters the carrier density of the underlying graphene. The alignment of these dipoles was further controlled by applying an external electric field during the photoisomerization. In this way, irradiation under oppositely polarized fields and no applied field provide three device states that were nonvolatile for at least 50 s. Finally, Szopek and co-workers utilized a poly(ethylene imine) (PEI) layer to transform a GFET into a CO_2 sensor.[51] The amines of the PEI layer reversibly bind CO_2, which induces a change in the SLG conductance (Figure 1.9). Unfunctionalized GFETs showed no measurable CO_2 response. These representative examples suggest that a vast array of functional polymers and molecular recognition strategies might prove useful in GFET devices.

It has also proven possible to perform spatially controlled polymerizations on the graphene surface. For example, Zhou and co-workers used a soft lithographic approach to print 2 μm wide strips of methacrylic macroinitiators bearing both pyrene (for graphene binding) and bromostyrene (polymer initiator) side chains.[49] Polymerization under atom transfer radical polymerization conditions provided 100-300 nm thick polymer brushes in the patterned regions. The method was shown to be general to several monomer classes and graphene types (CVD, reduced graphene oxide, and graphene oxide).

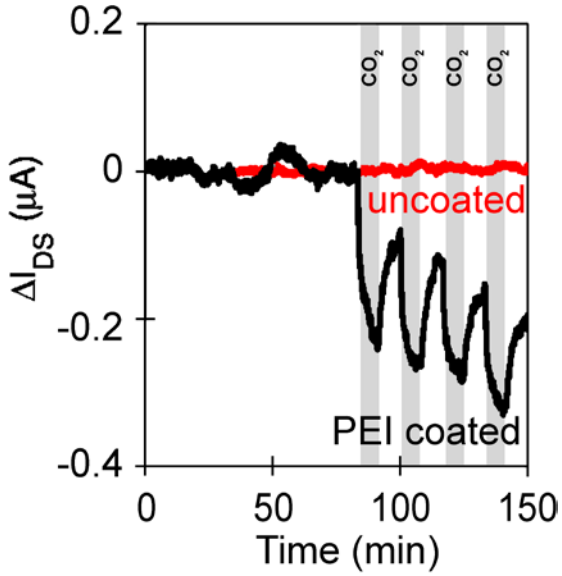

Figure 1.9. Change in conductivity of GFETs prepared using (red) uncoated graphene and (black) polyethylene imine coated graphene upon the successive introduction of 4 mbar of CO_2 (Adapted with permission from ref. 51 Copyright 2012 American Institute of Physics).

Dichtel and coworkers recently used SLG to crystallize oriented thin films of a class of two-dimensional polymers known as covalent organic frameworks (COFs, Figure 1.10),[52-55] which had been previously isolated as insoluble polycrystalline powders. Despite interest in these materials for optoelectronic devices, processing, achieving electrical contact, and performing advanced spectroscopy are all difficult on the polycrystalline powder form. Two-dimensional COF thin films ranging in thickness from 30-400 nm crystallize on the SLG

surface under solvothermal growth conditions, in which an SLG-coated substrate is included in the reaction mixture. The resulting films are highly crystalline and oriented with the stacking direction normal to the graphene surface, as determined by grazing incidence x-ray diffraction.

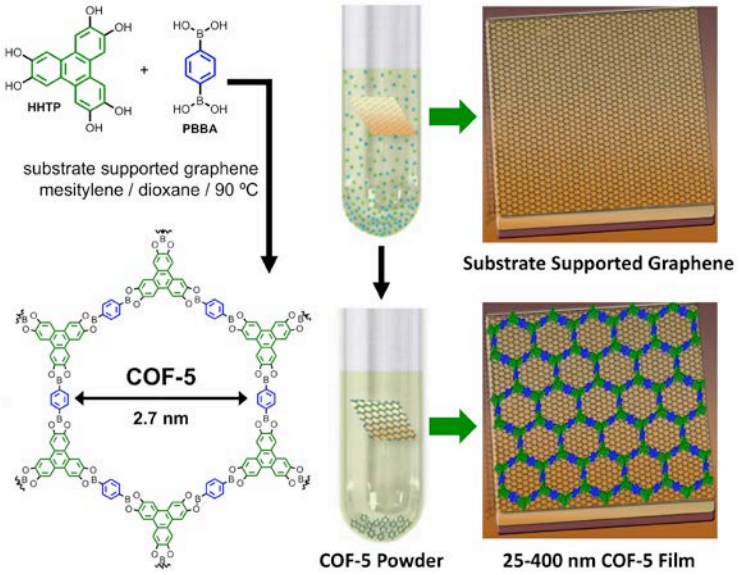

Figure 1.10. Schematic representation of the solvothermal polymerization of hexahydroxytriphenylene and benzene-1,4-*bis*-boronic acid to form COF-5 on single layer graphene (Reproduced with permission from ref. 53 Copyright 2011 American Association for the Advancement of Science).

These films point a way forward for many new applications for 2D polymer films, including organic photovoltaics, energy storage devices, and other applications that will leverage their structural precision and predictable synthesis.

1.5 Conclusions and Outlook

Graphene's single-atom thickness, desirable electronic properties, and mechanical stability have already attracted interest for transparent electrodes and FETs and are likely to be leveraged within other device platforms. In their current form, GFETs are of particular

interest for sensing devices, although practical strategies to induce a sufficiently large bandgap, combined with effective complementary doping methods, might expand their relevance to integrated logic circuits. Graphene's atomically precise structure also makes it an intriguing platform for mediating molecular and polymer assembly. Molecular functionalization provides ultrathin layers or well-defined monolayers that have served as dopants and as nucleation sites to ensure conformal oxide coatings through atomic layer deposition. Graphene-binding peptides and more elaborate multivalent binding groups form monolayers with useful stability on the graphene surface, even in solution under infinite dilution conditions, and have anchored oligopeptides and proteins, respectively, on the surface while maintaining their function. Similarly, commercially available polymers have been used to mechanically stabilize SLG during its transfer to arbitrary substrates and to tune its charge carrier density. More elaborate polymer architectures and macromolecules with active functionality have provided devices with improved performance and advanced functions, but the possibilities of these polymer/graphene hybrid devices are only now emerging. Graphene has shown great promise as a growth substrate for thin films of covalent organic frameworks and represents a natural interface for other classes of 2D polymers as new methods for their synthesis become available. Based on recent advances, functionalized graphene might be incorporated into sensor arrays, serve as a flexible and transparent electrode in organic electronic devices, or act as a transparent barrier materials for *in situ* optical and electron microscopy. The enhanced properties of the binding groups described above warrant further study and will benefit from close collaborations between device scientists and engineers, synthetic chemists, and theorists to maximize their utility.

1.6 Acknowledgements

We acknowledge financial support from Cornell University, a Sloan Research Fellowship, the Research Corporation for Science Advancement, and the Camille and Henry Dreyfus Foundation. We also acknowledge NSF support through use of the Cornell Nanofabrication Facility/NNIN and the Cornell Center for Materials Research facilities. J.A.M. gratefully acknowledges the Integrative Graduate Education and Research Traineeship (IGERT) Program in the Nanoscale Control of Surfaces and Interfaces which is supported under NSF Award DGE-0654193, the Cornell Center for Materials Research, and Cornell University.

REFERENCES

(1) Novoselov, K. S.; Geim, A. K.; Morozov, S. V.; Jiang, D.; Zhang, Y.; Dubonos, S. V.; Grigorieva, I. V.; Firsov, A. A. Electric Field Effect in Atomically Thin Carbon Films. *Science* **2004,** *306*, 666-669.

(2) Allen, M. J.; Tung, V. C.; Kaner, R. B. Honeycomb Carbon: A Review of Graphene. *Chem. Rev.* **2009,** *110*, 132-145.

(3) Dreyer, D. R.; Park, S.; Bielawski, C. W.; Ruoff, R. S. The chemistry of graphene oxide. *Chem. Soc. Rev.* **2010,** *39*, 228-240.

(4) Emtsev, K. V.; Bostwick, A.; Horn, K.; Jobst, J.; Kellogg, G. L.; Ley, L.; McChesney, J. L.; Ohta, T.; Reshanov, S. A.; Rohrl, J.; Rotenberg, E.; Schmid, A. K.; Waldmann, D.; Weber, H. B.; Seyller, T. Towards wafer-size graphene layers by atmospheric pressure graphitization of silicon carbide. *Nature Mater.* **2009,** *8*, 203-207.

(5) Huang, H.; Wong, S. L.; Tin, C.-C.; Luo, Z. Q.; Shen, Z. X.; Chen, W.; Wee, A. T. S. Epitaxial growth and characterization of graphene on free-standing polycrystalline 3C-SiC. *J. Appl. Phys.* **2011,** *110*, 014308/1-014308/5.

(6) Strupinski, W.; Grodecki, K.; Wysmolek, A.; Stepniewski, R.; Szkopek, T.; Gaskell, P. E.; Gruneis, A.; Haberer, D.; Bozek, R.; Krupka, J.; Baranowski, J. M. Graphene Epitaxy by Chemical Vapor Deposition on SiC. *Nano Lett.* **2011,** *11*, 1786-1791.

(7) Reina, A.; Jia, X.; Ho, J.; Nezich, D.; Son, H.; Bulovic, V.; Dresselhaus, M. S.; Kong, J. Large Area, Few-Layer Graphene Films on Arbitrary Substrates by Chemical Vapor Deposition. *Nano Lett.* **2008,** *9*, 30-35.

(8) Mattevi, C.; Kim, H.; Chhowalla, M. A review of chemical vapour deposition of graphene on copper. *J. Mater. Chem.* **2011,** *21*, 3324-3334.

(9) Bae, S.; Kim, H.; Lee, Y.; Xu, X.; Park, J.-S.; Zheng, Y.; Balakrishnan, J.; Lei, T.; Ri Kim, H.; Song, Y. I.; Kim, Y.-J.; Kim, K. S.; Ozyilmaz, B.; Ahn, J.-H.; Hong, B. H.; Iijima, S. Roll-to-roll production of 30-inch graphene films for transparent electrodes. *Nature Nanotech.* **2010,** *5*, 574-578.

(10) Lee, Y.; Bae, S.; Jang, H.; Jang, S.; Zhu, S.-E.; Sim, S. H.; Song, Y. I.; Hong, B. H.; Ahn, J.-H. Wafer-Scale Synthesis and Transfer of Graphene Films. *Nano Lett.* **2010,** *10*, 490-493.

(11) Regan, W.; Alem, N.; Aleman, B.; Geng, B. S.; Girit, C.; Maserati, L.; Wang, F.; Crommie, M.; Zettl, A. A direct transfer of layer-area graphene. *Appl. Phys. Lett.* **2010,** *96* (11), 1131021-1131023.

(12) Chen, S.; Cai, W.; Piner, R. D.; Suk, J. W.; Wu, Y.; Ren, Y.; Kang, J.; Ruoff, R. S. Synthesis and Characterization of Large-Area Graphene and Graphite Films on Commercial Cu–Ni Alloy Foils. *Nano Lett.* **2011,** *11*, 3519-3525.

(13) Li, X.; Magnuson, C. W.; Venugopal, A.; Tromp, R. M.; Hannon, J. B.; Vogel, E. M.; Colombo, L.; Ruoff, R. S. Large-Area Graphene Single Crystals Grown by Low-Pressure Chemical Vapor Deposition of Methane on Copper. *J. Am. Chem. Soc.* **2011,** *133*, 2816-2819.

(14) Yan, Z.; Lin, J.; Peng, Z.; Sun, Z.; Zhu, Y.; Li, L.; Xiang, C.; Samuel, E. L.; Kittrell, C.; Tour, J. M. Toward the Synthesis of Wafer-Scale Single-Crystal Graphene on Copper Foils. *ACS Nano* **2012,** *6*, 9110-9117.

(15) Levendorf, M. P.; Kim, C.-J.; Brown, L.; Huang, P. Y.; Havener, R. W.; Muller, D. A.; Park, J. Graphene and boron nitride lateral heterostructures for atomically thin circuitry. *Nature* **2012,** *488*, 627-632.

(16) Georgakilas, V.; Otyepka, M.; Bourlinos, A. B.; Chandra, V.; Kim, N.; Kemp, K. C.; Hobza, P.; Zboril, R.; Kim, K. S. Functionalization of Graphene: Covalent and Non-Covalent Approaches, Derivatives and Applications. *Chem. Rev.* **2012,** *112*, 6156-6214.

(17) Chiang, S. Scanning Tunneling Microscopy Imaging of Small Adsorbed Molecules on Metal Surfaces in an Ultrahigh Vacuum Environment. *Chem. Rev.* **1997,** *97*, 1083-1096.

(18) Nyffenegger, R. M.; Penner, R. M. Nanometer-Scale Surface Modification Using the Scanning Probe Microscope: Progress since 1991. *Chem. Rev.* **1997,** *97*, 1195-1230.

(19) Ward, M. D. Bulk Crystals to Surfaces: Combining X-ray Diffraction and Atomic Force Microscopy to Probe the Structure and Formation of Crystal Interfaces. *Chem. Rev.* **2001,** *101*, 1697-1726.

(20) Mali, K. S.; Adisoejoso, J.; Ghijsens, E.; De Cat, I.; De Feyter, S. Exploring the Complexity of Supramolecular Interactions for Patterning at the Liquid–Solid Interface. *Acc. Chem. Res.* **2012,** *45*, 1309-1320.

(21) Kamat, P. V. Graphene-Based Nanoassemblies for Energy Conversion. *J. Phys. Chem. Lett.* **2011,** *2*, 242-251.

(22) Shin, H.-J.; Choi, W. M.; Choi, D.; Han, G. H.; Yoon, S.-M.; Park, H.-K.; Kim, S.-W.; Jin, Y. W.; Lee, S. Y.; Kim, J. M.; Choi, J.-Y.; Lee, Y. H. Control of Electronic Structure of Graphene by Various Dopants and Their Effects on a Nanogenerator. *J. Am. Chem. Soc.* **2010,** *132*, 15603-15609.

(23) Chen, Z.; Berciaud, S.; Nuckolls, C.; Heinz, T. F.; Brus, L. E. Energy Transfer from Individual Semiconductor Nanocrystals to Graphene. *ACS Nano* **2010,** *4*, 2964-2968.

(24) Yin, P.; Kim, T.-H.; Choi, J.-W.; Lee, K. Prospects for graphene-nanoparticle-based hybrid sensors. *Phys. Chem. Chem. Phys.* **2013**, DOI: 10.1039/C3CP51901E.

(25) Huang, L.; Wu, B.; Yu, G.; Liu, Y. Graphene: learning from carbon nanotubes. *J. Mater. Chem.* **2011,** *21*, 919-929.

(26) Backes, C.; Hauke, F.; Hirsch, A. Carbon Functionalization: The Potential of Perylene Bisimide Derivatives for the Solubilization of Carbon Nanotubes and Graphene. *Adv. Mater.* **2011,** *23*, 2534.

(27) Yang, W.; Ratinac, K. R.; Ringer, S. P.; Thordarson, P.; Gooding, J. J.; Braet, F. Carbon Nanomaterials in Biosensors: Should You Use Nanotubes or Graphene? *Angew. Chem., Int. Ed.* **2010,** *49*, 2114-2138.

(28) Tasis, D.; Tagmatarchis, N.; Bianco, A.; Prato, M. Chemistry of Carbon Nanotubes. *Chem. Rev.* **2006,** *106*, 1105-1136.

(29) Wang, X.; Tabakman, S. M.; Dai, H. Atomic Layer Deposition of Metal Oxides on Pristine and Functionalized Graphene. *J. Am. Chem. Soc.* **2008,** *130*, 8152-8153.

(30) Wang, Q. H.; Hersam, M. C. Room-temperature molecular-resolution characterization of self-assembled organic monolayers on epitaxial graphene. *Nature Chem.* **2009,** *1*, 206-211.

(31) Alaboson, J. M. P.; Wang, Q. H.; Emery, J. D.; Lipson, A. L.; Bedzyk, M. J.; Elam, J. W.; Pellin, M. J.; Hersam, M. C. Seeding Atomic Layer Deposition of High-k Dielectrics on Epitaxial Graphene with Organic Self-Assembled Monolayers. *ACS Nano* **2011,** *5*, 5223-5232.

(32) Sun, J. T.; Lu, Y. H.; Chen, W.; Feng, Y. P.; Wee, A. T. S. Linear tuning of charge carriers in graphene by organic molecules and charge-transfer complexes. *Phys. Rev. B* **2010,** *81*, 155403.

(33) Coletti, C.; Riedl, C.; Lee, D. S.; Krauss, B.; Patthey, L.; von Klitzing, K.; Smet, J. H.; Starke, U. Charge neutrality and band-gap tuning of epitaxial graphene on SiC by molecular doping. *Phys. Rev. B* **2010,** *81*, 235401.

(34) Cheng, H.-C.; Shiue, R.-J.; Tsai, C.-C.; Wang, W.-H.; Chen, Y.-T. High-quality graphene p-n junctions via resist-free fabrication and solution-based noncovalent functionalization. *ACS Nano* **2011,** *5*, 2051-2059.

(35) Mao, H. Y.; Wang, R.; Wang, Y.; Niu, T. C.; Zhong, J. Q.; Huang, M. Y.; Qi, D. C.; Loh, K. P.; Wee, A. T. S.; Chen, W. Chemical vapor deposition graphene as structural template to control interfacial molecular orientation of chloroaluminium phthalocyanine. *Appl. Phys. Lett.* **2011,** *99* (9), 093301-3.

(36) Lee, W. H.; Park, J.; Sim, S. H.; Lim, S.; Kim, K. S.; Hong, B. H.; Cho, K. Surface-Directed Molecular Assembly of Pentacene on Monolayer Graphene for High-Performance Organic Transistors. *J. Am. Chem. Soc.* **2011,** *133*, 4447-4454.

(37) Dubuisson, E.; Yang, Z.; Loh, K. P. Optimizing Label-Free DNA Electrical Detection on Graphene Platform. *Anal. Chem.* **2011,** *83*, 2452-2460.

(38) Dong, X.; Shi, Y.; Huang, W.; Chen, P.; Li, L.-J. Electrical detection of DNA hybridization with single-base specificity using transistors based on CVD-grown graphene sheets. *Adv. Mater.* **2010,** *22*, 1649-1653.

(39) Cui, Y.; Kim, S. N.; Jones, S. E.; Wissler, L. L.; Naik, R. R.; McAlpine, M. C. Chemical Functionalization of Graphene Enabled by Phage Displayed Peptides. *Nano Lett.* **2010,** *10*, 4559-4565.

(40) Mannoor, M. S.; Tao, H.; Clayton, J. D.; Sengupta, A.; Kaplan, D. L.; Naik, R. R.; Verma, N.; Omenetto, F. G.; McAlpine, M. C. Graphene-based wireless bacteria detection on tooth enamel. *Nat. Commun.* **2012,** *3*, 763.

(41) Mann, J. A.; Rodríguez-López, J.; Abruña, H. D.; Dichtel, W. R. Multivalent Binding Motifs for the Noncovalent Functionalization of Graphene. *J. Am. Chem. Soc.* **2011,** *133*, 17614-17617.

(42) Rodríguez-López, J.; Ritzert, N. L.; Mann, J. A.; Tan, C.; Dichtel, W. R.; Abruña, H. D. Quantification of the Surface Diffusion of Tripodal Binding Motifs on Graphene Using Scanning Electrochemical Microscopy. *J. Am. Chem. Soc.* **2012,** *134*, 6224-6236.

(43) Mann, J. A.; Alava, T.; Craighead, H. G.; Dichtel, W. R. Preservation of Antibody Selectivity on Graphene by Conjugation to a Tripod Monolayer. *Angew. Chem. Int. Ed.* **2013,** *52*, 3177-3180.

(44) Alava, T.; Mann, J. A.; Théodore, C.; Benitez, J. J.; Dichtel, W. R.; Parpia, J. M.; Craighead, H. G. Control of the Graphene–Protein Interface Is Required To Preserve Adsorbed Protein Function. *Anal. Chem.* **2013,** *85*, 2754-2759.

(45) Yan, C.; Kim, K. S.; Lee, S. K.; Bae, S. H.; Hong, B. H.; Kim, J. H.; Lee, H. J.; Ahn, J. H. Mechanical and Environmental Stability of Polymer Thin-Film-Coated Graphene. *ACS Nano* **2012,** *6*, 2096-2103.

(46) Ha, T. J.; Lee, J.; Chowdhury, S. F.; Akinwande, D.; Rossky, P. J.; Dodabalapur, A. Transformation of the Electrical Characteristics of Graphene Field-Effect Transistors with Fluoropolymer. *ACS Appl. Mater. Interfaces* **2013,** *5*, 16-20.

(47) Lee, W. H.; Suk, J. W.; Lee, J.; Hao, Y. F.; Park, J.; Yang, J. W.; Ha, H. W.; Murali, S.; Chou, H.; Akinwande, D.; Kim, K. S.; Ruoff, R. S. Simultaneous Transfer and Doping of CVD-Grown Graphene by Fluoropolymer for Transparent Conductive Films on Plastic. *ACS Nano* **2012,** *6*, 1284-1290.

(48) Lin, C. Y.; Chang, C. S.; Lin, J. H.; Hsu, C. C.; Chien, F. S. S. Optical controlled graphene-based nonvolatile ternary-logic transistor with azobenzene copolymer. *Appl. Phys. Lett.* **2013,** *102* (1), 0135051-0135055.

(49) Gao, T. T.; Wang, X. L.; Yu, B.; Wei, Q. B.; Xia, Y. Q.; Zhou, F. Noncovalent Microcontact Printing for Grafting Patterned Polymer Brushes on Graphene Films. *Langmuir* **2013,** *29*, 1054-1060.

(50) Kim, B. J.; Jang, H.; Lee, S. K.; Hong, B. H.; Ahn, J. H.; Cho, J. H. High-Performance Flexible Graphene Field Effect Transistors with Ion Gel Gate Dielectrics. *Nano Lett.* **2010,** *10* (9), 3464-3466.

(51) Sabri, S. S.; Guillemette, J.; Guermoune, A.; Siaj, M.; Szkopek, T. Enhancing gas induced charge doping in graphene field effect transistors by non-covalent functionalization with polyethyleneimine. *Appl. Phys. Lett.* **2012,** *100* (11), 1131061-1131064.

(52) Spitler, E. L.; Koo, B. T.; Novotney, J. L.; Colson, J. W.; Uribe-Romo, F. J.; Gutierrez, G. D.; Clancy, P.; Dichtel, W. R. A 2D Covalent Organic Framework with 4.7-nm Pores and Insight into Its Interlayer Stacking. *J. Am. Chem. Soc.* **2011,** *133*, 19416-19421.

(53) Colson, J. W.; Woll, A. R.; Mukherjee, A.; Levendorf, M. P.; Spitler, E. L.; Shields, V. B.; Spencer, M. G.; Park, J.; Dichtel, W. R. Oriented 2D Covalent Organic Framework Thin Films on Single-Layer Graphene. *Science* **2011,** *332*, 228-231.

(54) Feng, X.; Ding, X.; Jiang, D. Covalent organic frameworks. *Chem. Soc. Rev.* **2012,** *41*, 6010-6022.

(55) Colson, J. W.; Dichtel, W. R. Rationally synthesized two-dimensional polymers. *Nature Chem.* **2013,** *5*, 453–465.

CHAPTER TWO

MULTIVALENT BINDING MOTIFS FOR FUNCTIONALIZING GRAPHENE NONCOVALENTLY

2.1 Abstract

Single-layer graphene is a newly available conductive material ideally suited for forming well-defined interfaces with electroactive compounds. Aromatic moieties typically interact with the graphene surface to maximize Van der Waals interactions, predisposing most compounds to lie flat on its basal plane. Here we describe a tripodal motif that binds multivalently to graphene through three pyrene moieties and projects the modular functionality away from the surface. The thermodynamic and kinetic binding parameters of a tripod bearing a redox-active Co(II) *bis*-terpyridyl complex were investigated electrochemically. The complex binds strongly to graphene and forms monolayers with a molecular footprint of 2.3 nm^2 and a $\Delta G_{ads} = -38.8 \pm 0.2$ kJ mol^{-1}. Its monolayers are stable in fresh electrolyte solution for more than 12 h and desorb from graphene 1000 times more slowly than model compounds bearing a single aromatic binding group. Differences in the heterogeneous rate constants of electron transfer between the two compounds suggest that the tripod projects its redox couple away from the graphene surface. The work described in this chapter was performed in collaboration with Dr. Joaquín Rodrígues López., under the direction of Prof. H. D. Abruña and Prof. W. R. Dichtel and was published in the *Journal of the American Chemical Society* (Mann, J. A.; Rodríguez-López, J.; Abruña, H. D.; Dichtel, W. R. *J. Am. Chem. Soc.* **2011**, *133*, 17614.)

2.2 Introduction

Graphene's desirable electronic, optical, and mechanical properties have attracted considerable interest.[1] Advances in its growth via metal-catalyzed chemical vapor deposition (CVD),[2] the thermal decomposition of SiC,[3] and chemical reduction of graphene oxide (GO)[4] now provide convenient access to large-area samples, including films on flexible substrates.[5] As a result, graphene shows promise for inexpensive transparent electrodes,[6] transistors,[7] strain sensors,[8] ultrathin corrosion barriers,[9] and many other applications. Graphene's single-atom thickness and atomically precise structure also make it an attractive platform for molecular assembly and interfacing functional π-electron systems to bulk electrodes,[10] as well as a unique imaging platform for confined chemical transformations.[11] Modular and broadly applicable methods for functionalizing graphene's basal plane offer a means to manipulate its structure and/or electronic properties and will impact many of the above applications. Covalent attachment approaches disrupt the conjugation and thus, the electronic structure of the graphene sheet and take place preferentially at carbon atoms near defects and grain boundaries.[12]

Noncovalent functionalization strategies do not suffer from such drawbacks. These approaches have often focused on dispersing chemically converted graphene (CCG) in various solvents following the reduction of GO. Compounds designed for this purpose interact with CCG either at graphitic sites or residual carboxylate defects.[13] The basal planes of exfoliated, epitaxial, or CVD graphene samples have been functionalized less frequently. Alkane thiols assembled on exfoliated graphene were used to detect Hg^{2+} ions at ppm levels.[14] Polycyclic aromatic compounds assemble into stable, ordered structures on epitaxial graphene[15] and can shift its Fermi level[16] or serve as nucleation sites for atomic layer

deposition.[17] Xu *et al*. used pyrene butyrate to exfoliate graphite and disperse the resulting graphene layers in H_2O.[18] However, the strength of the pyrene – graphene interaction has not been reported, and individual pyrene rings lack the ability to precisely control both the distance and orientation of pendant functionality relative to the surface. Compounds capable of binding graphene with well-defined, multivalent interactions can provide robust monolayers that display active functionality away from the graphene surface, enabling these moieties to interact predictably with other species in solution.

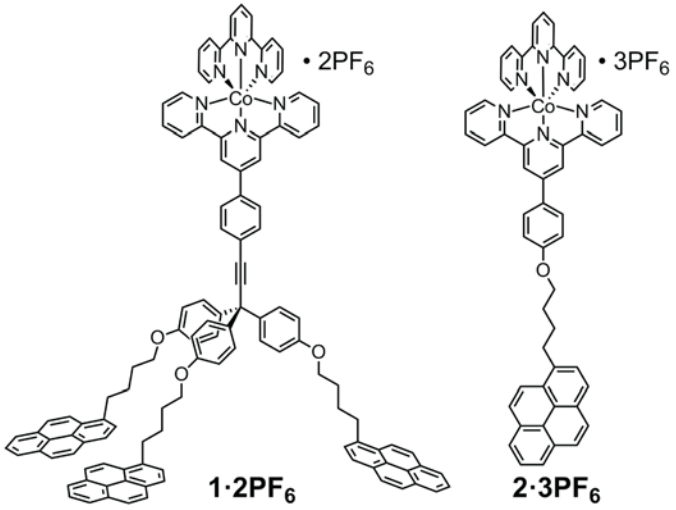

Figure 2.1 Structures of a tripodal graphene binder **1·2PF$_6$** and monovalent model compound **2·3PF$_6$**, each bearing a redox-active Co(tpy) complex for electrochemical characterization of their binding properties.

Here we describe a tripodal binding motif (Figure 2.1), which presents three pyrene "feet" that interact with graphene substrates. Tripodal architectures have been used to functionalize silicon,[19] gold,[20] and TiO_2[21] surfaces, where they have consistently demonstrated enhanced stability and orientational control relative to monopodal groups.[22] A Co^{+2} *bis*-terpyridyl complex ($[Co(tpy)_2]^{2+}$) was incorporated into the graphene-binding tripod **1·2PF$_6$** to measure the binding constant and surface coverage through electrochemical observation of the $Co^{2+/3+}$ redox couple. The characteristics of the monopodal $[Co(tpy)_2]^{3+}$ complex **2·3PF$_6$**

were also determined electrochemically to elucidate the effect of multivalency on the coverage and stability of the monolayers. Working electrodes based on single-layer graphene were first reported only recently,[23] and the following experiments are the first to characterize molecular self-assembly on the graphene basal plane using electrochemistry.

2.3 Design and Synthesis of the Tripodal Motif

The synthesis (Figure 2.2) of the tripodal binding motif is modular, allowing future variation of both the aromatic binding groups and the functionality of interest. Pyrene was selected as the binding group because it has been used extensively to functionalize carbon nanotubes.[24] The tetrahedral core **4** was established through the nucleophilic substitution of ethynyl magnesium bromide to tris(*p*-methoxyphenyl) methyl chloride. The terminal alkyne moiety of **4** was elaborated to a terpyridyl ligand through a Sonogashira cross-coupling, after which the three methoxy groups were demethylated with BBr_3.

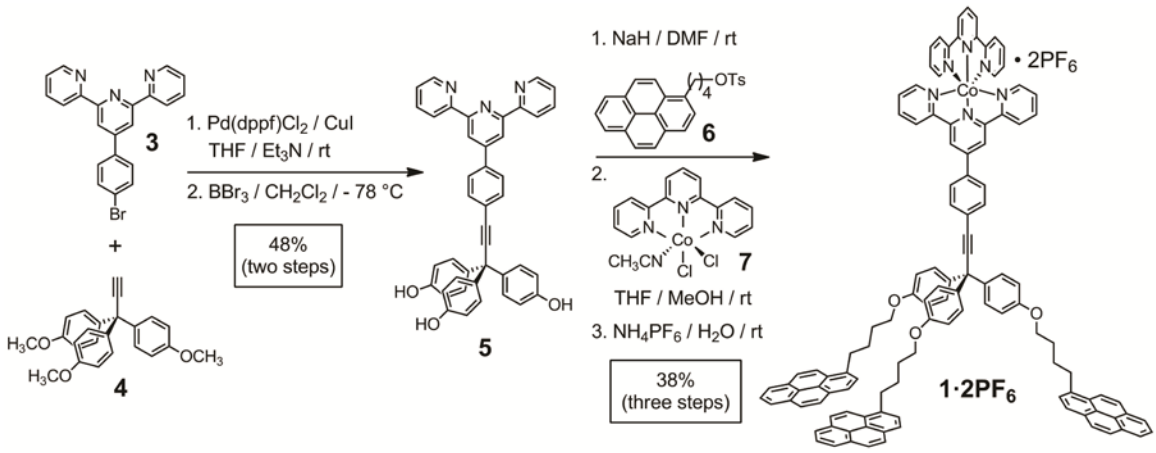

Figure 2.2 Synthesis of tripodal graphene binder **1·2PF6**.

The resulting triphenol **5** was alkylated under Williamson etherification conditions by the pyrene tosylate **6**. The resulting tripodal ligand was metallated via ligand exchange using excess $Co(tpy)Cl_2MeCN$ **7** to provide **1·2PF$_6$**. The Co^{+2} complex in **1·2PF$_6$** is paramagnetic,

complicating assignment of its NMR resonances. Nevertheless, its spectrum was consistent with the presence of a single Co^{+2} species. Electrospray ionization (ESI) and matrix assisted laser desorption ionization (MALDI) mass spectrometry each indicated the formation of **1·2PF$_6$** and did not show peaks corresponding to other $Co(tpy)_2$ complexes. We also oxidized **1·2PF$_6$** to the corresponding diamagnetic Co^{+3} species **1·3PF$_6$** using $AgPF_6$. The ^1H NMR spectrum of this complex indicated its structure and purity. We also synthesized the monopodal compound of similar structure **2·2PF$_6$**, though thin layer chromatography and ^1H NMR spectroscopy indicated that its terpyridyl ligands were substitutionally labile. $[Co(tpy)_2]^{+3}$ species are less prone to ligand exchange, and so we also oxidized **2·2PF$_6$** to the Co^{3+} species **2·3PF$_6$**, again using $AgPF_6$, to facilitate its characterization and storage.

2.4 Electrochemical Characterization of Monolayer Formation

Monolayer formation of the two compounds was characterized by cyclic voltammetry (CV) using a working electrode composed of CVD graphene transferred onto a silicon wafer (0.07 cm^2 active area, see section 2.A for fabrication details). Pt counter and pseudo-reference electrodes were used with analyte **1·2PF$_6$** or **2·3PF$_6$** in THF / NH_4PF_6 (0.1 M) supporting electrolyte. These experiments confirm adsorption of both complexes to the electrode surface. They also show chemically reversible but electrochemically quasi-reversible charge transfer kinetics for the $Co^{+2/+3}$ couple (*ca.* –0.2 V vs. Fc/Fc^+), as indicated by their voltammetric wave-shape and changes in oxidative and reductive peak potentials (ΔE_p) as a function of sweep rate (Figure 2.3A). The linear dependences of the peak current (see Appendix Figure A1.24) on the potential sweep rate indicates that the redox couple is confined to the electrode surface.[25]

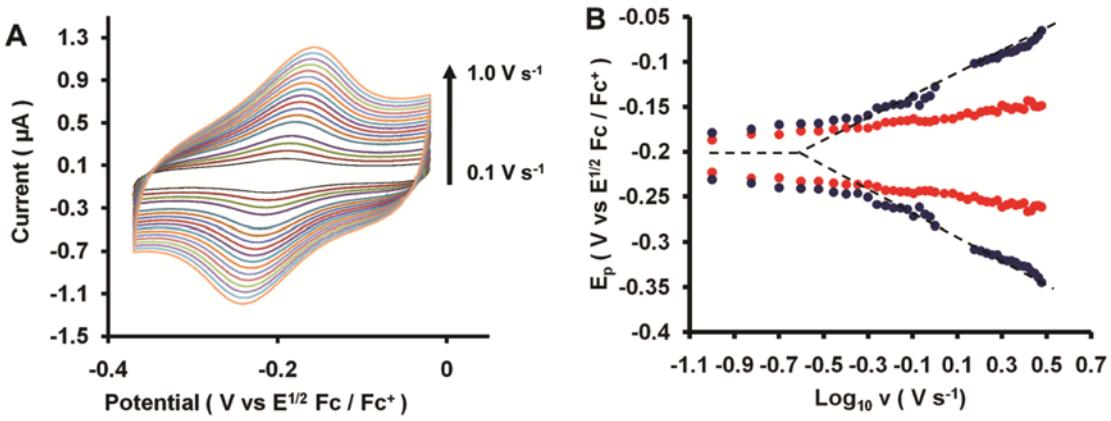

Figure 2.3 A: Cyclic voltammograms of **1·2PF$_6$** (1 μM) obtained at various scan rates on an SLG working electrode in THF / NH_4PF_6 (0.1 M). B: Laviron plots of **1·2PF$_6$** (blue) and **2·3PF$_6$** (red); peak potentials at different scan rates (0.1 V s^{-1} to 3.0 V s^{-1}) on SLG.

1·2PF$_6$ was designed to project its $Co(tpy)_2$ redox probe away from the SLG surface, a degree of orientational control not found in monopodal binding groups. We performed Laviron analyses (Figure 2.3 B) of the surface voltammetry[26] of both **1·2PF$_6$** and **2·3PF$_6$** to probe differences in electron transfer rates for the two binding motifs. For **1·2PF$_6$**, the peak potentials (E_p) of the anodic and cathodic scans converge to the value of the formal potential $E^{0'}$ at low scan rates (v), whereas larger peak separations are observed at higher scan rates. The symmetry and similar slope observed in the linear part of this plot for the anodic and cathodic branches suggest a transfer coefficient $\alpha \sim 0.5$ and analysis of the scan rate dependence (see Appendix) yields a heterogeneous charge transfer rate constant $k^0 = 13.5\ s^{-1}$. Additionally, analysis of the shape of the CVs (see Appendix) suggests no lateral interactions between the $Co^{+2/+3}$ redox centers, such that monolayer formation may be described by the Langmuir model (see below).

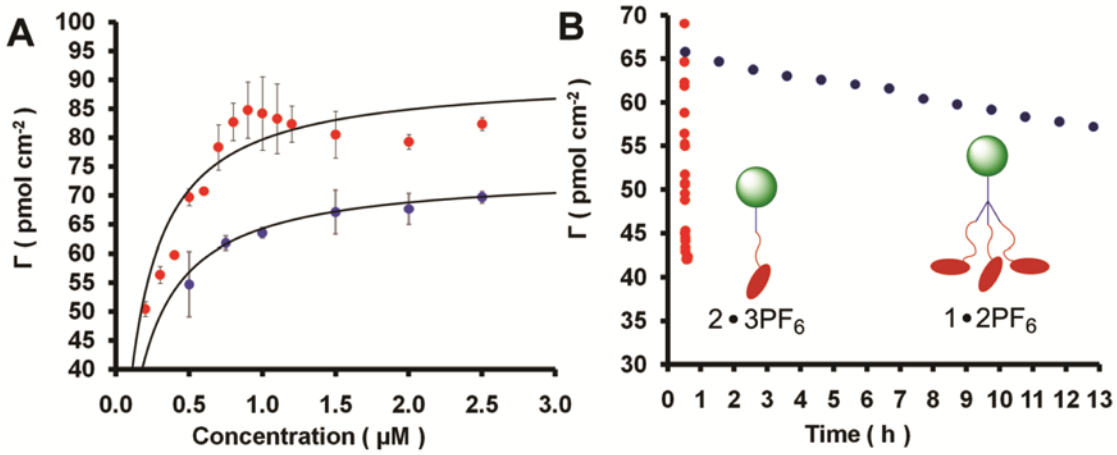

Figure 2.4 A: Langmuir binding isotherms of **1·2PF$_6$** (blue) and **2·3PF$_6$** (red) on SLG derived from surface coverages measured at various concentrations (0.1 μM-3 μM). B: Plots of coverage (Γ) vs time for monolayers of **1·2PF$_6$** (blue) and **2·3PF$_6$** (red) monolayers that were formed on SLG electrodes, and then transferred to fresh THF / NH_4PF_6 (0.1 M) electrolyte solution at t = 0.

The Laviron plot for **2·3PF$_6$** shows smaller peak separations than **1·2PF$_6$** at equivalent scan rates, which indicates faster electron transfer kinetics with a rate constant $k^0 \sim 18\ s^{-1}$ (see Appendix). The slower rate of electron transfer observed for **1·2PF$_6$** is consistent with the hypothesis that the tripod positions the redox center further away from the electrode than the monopodal model compound. Atomic force microscopy of the graphene electrodes before and after functionalization with the tripod showed no evidence for aggregation on the surface (see Appendix).

We integrated the peak currents in the CVs of **1·2PF$_6$** and **2·3PF$_6$** to obtain the total charge transferred (Q), from which the surface coverage (Γ) was calculated according to the relation $Q = nFA\Gamma$. Using the above method, we measured the surface coverage as a function of [**1·2PF$_6$**] or [**2·3PF$_6$**], respectively. These data were fit to the Langmuir isotherm model described by the equation $\Gamma = \Gamma_s Kc(Kc+1)^{-1}$ (where K is the equilibrium constant of binding and c is the concentration of adsorbate in solution) to determine the thermodynamic binding parameters for the monopodal and tripodal motifs. The isotherm of **1·2PF$_6$** (Figure 2.4A)

corresponds to a ΔG_{ads} of –38.8 ± 0.2 kJ mol^{-1} while the isotherm of **2·3PF$_6$** shows that it binds with a ΔG_{ads} of –38.3 ± 0.5 kJ mol^{-1}. Interestingly, the binding energies of the tripodal and monopodal compounds are similar, despite significant differences in the kinetic stability of the monolayers of the tripods (see below). It is possible that noncovalent interactions among the pyrene rings in the unbound form of **1·2PF$_6$** are disrupted upon binding to graphene, an energetic cost reflected in its ΔG_{ads}. We will revisit this consideration when designing future tripodal binding motifs.

The saturation coverage (Γ_s) of **1·2PF$_6$** is 73.9 ± 0.2 pmol cm^{-2}, which corresponds to a 2.3 nm^2 molecular footprint. The Γ_s of **2·3PF$_6$** is 90.7 ± 0.6 pmol cm^{-2}, a 1.7 nm^2 molecular footprint. The coverage of the monovalent binding compound is not significantly higher than that of the tripod, despite the tripod's larger size. This finding is consistent with our hypothesis that the Co(tpy)$_2$ complex of **2·3PF$_6$** weakly interacts with the graphene surface[27] and occupies a larger area on the surface than a single pyrene moiety. Thus, the tripodal design allows for improved orientational control of its functionality while maintaining comparable coverage.

Robust noncovalent functionalization requires that monolayers remain kinetically stable in the absence of excess adsorbate in solution. We evaluated the kinetic stability of monolayers of **1·2PF$_6$** and **2·3PF$_6$** by transferring functionalized graphene electrodes into blank electrolyte. The coverage of monovalent **2·3PF$_6$** rapidly diminished by 50% in just under 8 min, with a first-order rate constant k_d = 1.4 x 10^{-3} s^{-1} (Figure 2.4B). In contrast, **1·2PF$_6$** desorbed 1000 times more slowly, decreasing only about 14% over 12 h, with a first-order rate constant k_d = 3.5 x 10^{-6} s^{-1} (Figure 2.4B). Thus, though compounds bearing a single pyrene bind to graphene, their monolayers rapidly desorb in organic solvents. Monolayers

based on the tripodal binding motif are stable for hours under similar conditions, which should render them compatible with solution processing techniques, such as spin-coating or drop-casting, often employed during device fabrication. For example, we anticipate that appropriately functionalized tripod monolayers will serve as anchors for interfacing polymers or extended materials to the graphene surface, and that the kinetic stability of the tripod/graphene interaction will facilitate studies of molecular diffusion in two dimensions.

2.5 Conclusions

In conclusion, we have designed and synthesized a tripodal binding motif that adsorbs strongly on the basal plane of single-layer graphene. We also have measured, through electrochemistry, the kinetic and thermodynamic binding parameters of aromatic systems on graphene for the first time. The tripod directs the variable functionality, here a $Co(tpy)_2$ redox probe, away from the graphene surface, as suggested by differences in rates of electron transfer between tripodal and monovalent binding units. Our kinetic experiments demonstrate that individual pyrene units readily desorb from graphene in organic solvents. In contrast, tripodal binding motifs form stable monolayers that withstand infinite dilution conditions for hours. Future studies will focus on characterizing the structure and dynamics of this tripodal binding motif on the graphene surface using complementary spectroscopic and probe microscopy techniques. Graphene is both a new platform for molecular assembly and a technologically relevant electrode material, and specific non-covalent functionalization methods are needed to reliably control its interface to organic materials. Methods for preparing graphene with minimal defects and large grain size are advancing rapidly,[28] making functionalization of the pristine basal plane increasingly important. The orientational control

and kinetic stability of monolayers of tripodal systems will enable their use as anchors in a wide variety of contexts, including for integrating molecular compounds, extended materials, and biomolecules for optoelectronic, catalysis, and biosensing applications.

2.6 Acknowledgements

This research was supported by startup funds provided by Cornell University and the NSF-funded CCI-I Center for Molecular Interfacing (CHE-0847926). We also acknowledge NSF support through use of the Cornell Nanofabrication Facility/NNIN and the Cornell Center for Materials Research facilities. J.A.M. gratefully acknowledges the Integrative Graduate Education and Research Traineeship (IGERT) Program in the Nanoscale Control of Surfaces and Interfaces which is supported under NSF Award DGE-0654193, the Cornell Center for Materials Research, and Cornell University. We thank G. Gutierrez for preparation of intermediates, C. Tan for useful discussions, and S. Burkhardt for providing the TOC illustration.

REFERENCES

(1) (a) Allen, M. J.; Tung, V. C.; Kaner, R. B. *Chem. Rev.* **2009**, *110*, 132; (b) Geim, A. K. *Science* **2009**, *324*, 1530.

(2) (a) Levendorf, M. P.; Ruiz-Vargas, C. S.; Garg, S.; Park, J. *Nano Lett.* **2009**, *9*, 4479; (b) Li, X.; Cai, W.; An, J.; Kim, S.; Nah, J.; Yang, D.; Piner, R.; Velamakanni, A.; Jung, I.; Tutuc, E.; Banerjee, S. K.; Colombo, L.; Ruoff, R. S. *Science* **2009**, *324*, 1312; (c) Kim, K. S.; Zhao, Y.; Jang, H.; Lee, S. Y.; Kim, J. M.; Kim, K. S.; Ahn, J.-H.; Kim, P.; Choi, J.-Y.; Hong, B. H. *Nature* **2009**, *457*, 706; (d) Reina, A.; Jia, X.; Ho, J.; Nezich, D.; Son, H.; Bulovic, V.; Dresselhaus, M. S.; Kong, J. *Nano Lett.* **2008**, *9*, 30.

(3) Emtsev, K. V.; Bostwick, A.; Horn, K.; Jobst, J.; Kellogg, G. L.; Ley, L.; McChesney, J. L.; Ohta, T.; Reshanov, S. A.; Rohrl, J.; Rotenberg, E.; Schmid, A. K.; Waldmann, D.; Weber, H. B.; Seyller, T. *Nature Mater.* **2009**, *8*, 203.

(4) (a) Zhu, Y.; Murali, S.; Cai, W.; Li, X.; Suk, J. W.; Potts, J. R.; Ruoff, R. S. *Adv. Mater.* **2010**, *22*, 3906; (b) Green, A. A.; Hersam, M. C. *J. Phys. Chem. Lett.* **2009**, *1*, 544.

(5) Choi, D.; Choi, M.-Y.; Choi, W. M.; Shin, H.-J.; Park, H.-K.; Seo, J.-S.; Park, J.; Yoon, S.-M.; Chae, S. J.; Lee, Y. H.; Kim, S.-W.; Choi, J.-Y.; Lee, S. Y.; Kim, J. M. *Adv. Mater.* **2010**, *22*, 2187.

(6) (a) Kumar, A.; Zhou, C. *ACS Nano* **2010**, *4*, 11; (b) Li, X.; Zhu, Y.; Cai, W.; Borysiak, M.; Han, B.; Chen, D.; Piner, R. D.; Colombo, L.; Ruoff, R. S. *Nano Lett.* **2009**, *9*, 4359.

(7) (a) Lee, W. H.; Park, J.; Sim, S. H.; Lim, S.; Kim, K. S.; Hong, B. H.; Cho, K. *J. Am. Chem. Soc.* **2011**, *133*, 4447; (b) Liu, W.; Jackson, B. L.; Zhu, J.; Miao, C.-Q.; Chung, C.-H.; Park, Y. J.; Sun, K.; Woo, J.; Xie, Y.-H. *ACS Nano* **2010**, *4*, 3927.

(8) Wang, Y.; Yang, R.; Shi, Z.; Zhang, L.; Shi, D.; Wang, E.; Zhang, G. *ACS Nano* **2011**, ASAP DOI: 10.1021/nn103523t.

(9) Chen, S.; Brown, L.; Levendorf, M.; Cai, W.; Ju, S.-Y.; Edgeworth, J.; Li, X.; Magnuson, C. W.; Velamakanni, A.; Piner, R. D.; Kang, J.; Park, J.; Ruoff, R. S. *ACS Nano* **2011**, *5*, 1321.

(10) Colson, J. W.; Woll, A. R.; Mukherjee, A.; Levendorf, M. P.; Spitler, E. L.; Shields, V. B.; Spencer, M. G.; Park, J.; Dichtel, W. R. *Science* **2011**, *332*, 228.

(11) Yuk, J. M.; Kim, K.; Alemán, B. n.; Regan, W.; Ryu, J. H.; Park, J.; Ercius, P.; Lee, H. M.; Alivisatos, A. P.; Crommie, M. F.; Lee, J. Y.; Zettl, A. *Nano Lett.* **2011**, *11*, 3290.

(12) (a) Sun, Z.; Kohama, S.-i.; Zhang, Z.; Lomeda, J.; Tour, J. *Nano Res.* **2010**, *3*, 117; (b) Lim, H.; Lee, J. S.; Shin, H.-J.; Shin, H. S.; Choi, H. C. *Langmuir* **2010**, *26*, 12278.

(13) Dreyer, D. R.; Park, S.; Bielawski, C. W.; Ruoff, R. S. *Chem. Soc. Rev.* **2010**, *39*, 228.

(14) Zhang, T.; Cheng, Z.; Wang, Y.; Li, Z.; Wang, C.; Li, Y.; Fang, Y. *Nano Lett.* **2010**, *10*, 4738.

(15) (a) Khokhar, F. S.; van Gastel, R.; Poelsema, B. *Phys. Rev. B* **2010**, *82*, 205409; (b) Wang, Q. H.; Hersam, M. C. *Nature Chem.* **2009**, *1*, 206.

(16) (a) Cheng, H.-C.; Shiue, R.-J.; Tsai, C.-C.; Wang, W.-H.; Chen, Y.-T. *ACS Nano* **2011**, *5*, 2051; (b) Sun, J. T.; Lu, Y. H.; Chen, W.; Feng, Y. P.; Wee, A. T. S. *Phys. Rev. B* **2010**, *81*, 155403; (c) Coletti, C.; Riedl, C.; Lee, D. S.; Krauss, B.; Patthey, L.; von Klitzing, K.; Smet, J. H.; Starke, U. *Phys. Rev. B* **2010**, *81*, 235401; (d) Yong-Hui, Z.; Zhou, K.-G.; Xie, K.-F.; Zeng, J.; Zhang, H.-L.; Peng, Y. *Nanotechnology* **2010**, *21*, 065201.

(17) Wang, X.; Tabakman, S. M.; Dai, H. *J. Am. Chem. Soc.* **2008**, *130*, 8152.

(18) Xu, Y.; Bai, H.; Lu, G.; Li, C.; Shi, G. *J. Am. Chem. Soc.* **2008**, *130*, 5856.

(19) (a) Padmaja, K.; Wei, L.; Lindsey, J. S.; Bocian, D. F. *J. Org. Chem.* **2005**, *70*, 7972; (b) Yam, C. M.; Cho, J.; Cai, C. *Langmuir* **2004**, *20*, 1228.

(20) (a) Drew, M. E.; Chworos, A.; Oroudjev, E.; Hansma, H.; Yamakoshi, Y. *Langmuir* **2009**, *26*, 7117; (b) Sakata, T.; Maruyama, S.; Ueda, A.; Otsuka, H.; Miyahara, Y. *Langmuir* **2007**, *23*, 2269; (c) Nikitin, K.; Lestini, E.; Lazzari, M.; Altobello, S.; Fitzmaurice, D. *Langmuir* **2007**, *23*, 12147; (d) Kitagawa, T.; Idomoto, Y.; Matsubara, H.; Hobara, D.; Kakiuchi, T.; Okazaki, T.; Komatsu, K. *J. Org. Chem.* **2006**, *71*, 1362; (e) Whitesell, J. K.; Chang, H. K. *Science* **1993**, *261*, 73.

(21) (a) Clark, C. C.; Meyer, G. J.; Wei, Q.; Galoppini, E. *J. Phys. Chem. B* **2006**, *110*, 11044; (b) Galoppini, E. *Coord. Chem. Rev.* **2004**, *248*, 1283; (c) Long, B.; Nikitin, K.; Fitzmaurice, D. *J. Am. Chem. Soc.* **2003**, *125*, 15490; (d) Galoppini, E.; Guo, W.; Qu, P.; Meyer, G. J. *J. Am. Chem. Soc.* **2001**, *123*, 4342.

(22) Otsuki, J.; Shimizu, S.; Fumino, M. *Langmuir* **2006**, *22*, 6056.

(23) Li, W.; Tan, C.; Lowe, M. A.; Abruna, H. D.; Ralph, D. C. *ACS Nano* **2011**, *5*, 2264.

(24) (a) Tasis, D.; Tagmatarchis, N.; Bianco, A.; Prato, M. *Chem. Rev.* **2006**, *106*, 1105; (b) Chen, R. J.; Zhang, Y.; Wang, D.; Dai, H. *J. Am. Chem. Soc.* **2001**, *123*, 3838.

(25) Wopschall, R. H.; Shain, I. *Anal. Chem.* **1967**, *39*, 1514.

(26) Laviron, E. *J. Electroanal. Chem.* **1979**, *101*, 19.

(27) McQueen, E. W.; Goldsmith, J. I. *J. Am. Chem. Soc.* **2009**, *131*, 17554.

(28) (a) Iwasaki, T.; Park, H. J.; Konuma, M.; Lee, D. S.; Smet, J. H.; Starke, U. *Nano Lett.* **2011**, *11*, 79; (b) Yu, Q.*et al. Nature Mater.* **2011**, *10*, 443; (c) Li, X.; Magnuson, C. W.; Venugopal, A.; Tromp, R. M.; Hannon, J. B.; Vogel, E. M.; Colombo, L.; Ruoff, R. S. *J. Am. Chem. Soc.* **2011**, *133*, 2816; (d) Ajayan, P. M.; Yakobson, B. I. *Nature Mater.* **2011**, *10*, 415.

APPENDIX ONE

Table of Contents

A. Materials. Unless otherwise noted, reagents were purchased from commercial suppliers and used without further purification. 4'-(4-bromophenyl)-2,2':6',2"-terpyridine **4** and 4,4',4"-(prop-2-yne-1,1,1-triyl)tris(methoxybenzene) **3** were prepared using a literature procedure.[1] EtOAc, hexanes, and EtOH (absolute) were purchased from commercial sources and used without further purification. THF, CH_2Cl_2, DMF, and PhMe were purchased from commercial sources and purified using a custom-built activated alumina-based solvent purification system. Graphene electrodes were fabricated by transferring graphene derived from a chemical vapor deposition (CVD) procedure onto SiO_2/Si wafers.[2] Contacts were formed to the graphene electrodes by pressing a silver wire into a small amount of indium metal which had been pressed onto the graphene surface. Pt wire (20 Gauge - 99.9 % pure) was cleaned in a propane flame before each use. Glassware for electrochemistry was cleaned in a Nochromix™ / H_2SO_4 bath for 12 h, washed with H_2O (HPLC grade), dried in an oven at 150 ^oC for 3 h, and finally cooled in a dessicated chamber under dynamic vacuum.

Instrumentation. Infrared spectra of solid samples were recorded using a Thermo Nicolet iS10 FT-IR spectrometer with a diamond ATR attachment and are uncorrected.

Mass spectra were obtained on a Waters MALDI micro MX MALDI-TOF mass spectrometer using positive ionization in reflectron mode. A saturated solution of dithranol in CH_2Cl_2 was used as the matrix.

NMR spectra were recorded on a Varian INOVA 400 MHz spectrometer using a ^1H/X Z-PFG probe, a Bruker ARX 300 MHz spectrometer using a BBO probe, a Varian INOVA 500MHz spectrometer using a standard $^1H\{^{13}C, ^{15}N\}$ Z-PFG probe, or a Varian INOVA 600 MHz spectrometer using a standard $^1H\{^{13}C, ^{15}N\}$ XYZ-PFG probe with a 20 Hz sample spin rate.

Atomic force microscopy (AFM) analysis was performed on a Veeco DI 3100 AFM using silicon cantilevers in non-contact mode.

Electrochemistry experiments were performed on a Princeton Applied Research VersaSTAT 3 potentiostat using a standard three electrode configuration with graphene as the working-sense electrode, a Pt wire as the counter and a Pt wire pseudoreference. The analyses were performed in a custom made Teflon cell (Figure A1.1) that allowed exposure of a

controlled area of the graphene electrode (Figure A1.2) (total area *ca.* 2 cm^2, exposed area *ca.* 0.07 cm^2).

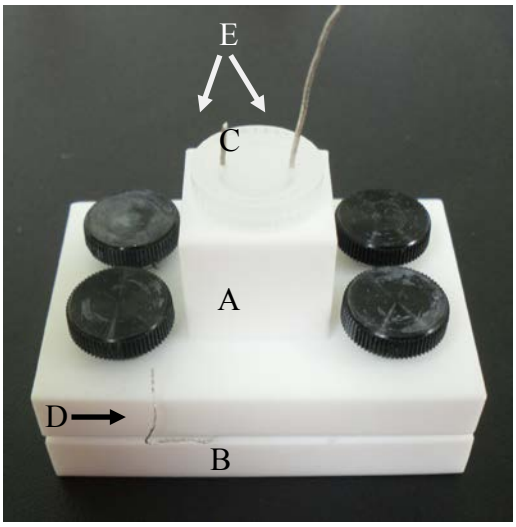

Figure A1.1. Electrode cell with (A) Teflon body with solution holder and electrode window, base (B) to secure the working electrode, and maintain a seal between the graphene surface and a Teflon o-ring. Evaporation is prevented using a polypropylene cap (C). (D) A Pt lead is attached to the graphene surface through and In pellet. (E) Pt counter and pseudo reference electrodes.

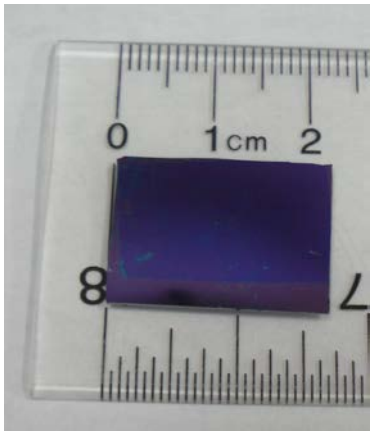

Figure A1.2. Representative image of CVD graphene after transfer to Si/SiO_2 that served as the working electrode.

B. Synthetic Procedures.

Scheme A1.1. Overall synthesis of a terpyridyl-functionalized graphene binding motif **S2**.

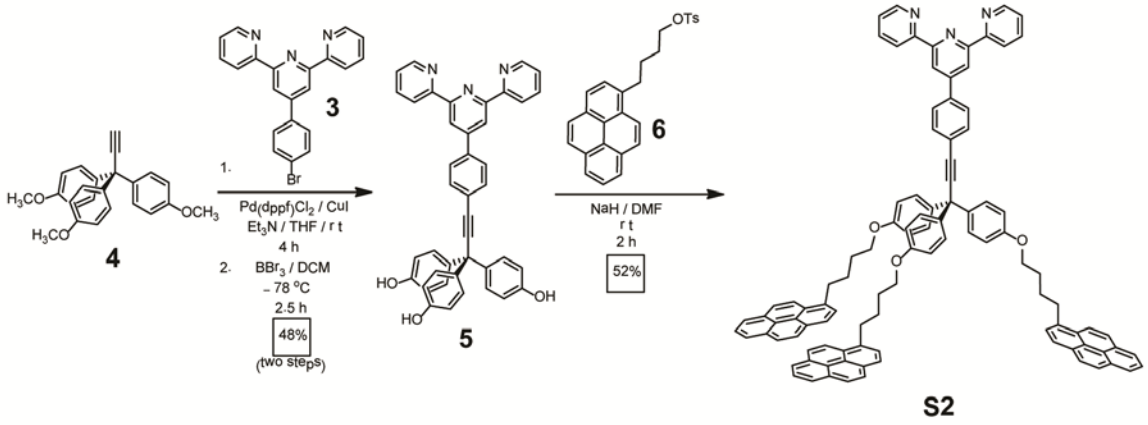

Scheme A1.2. Synthesis of **S1**.

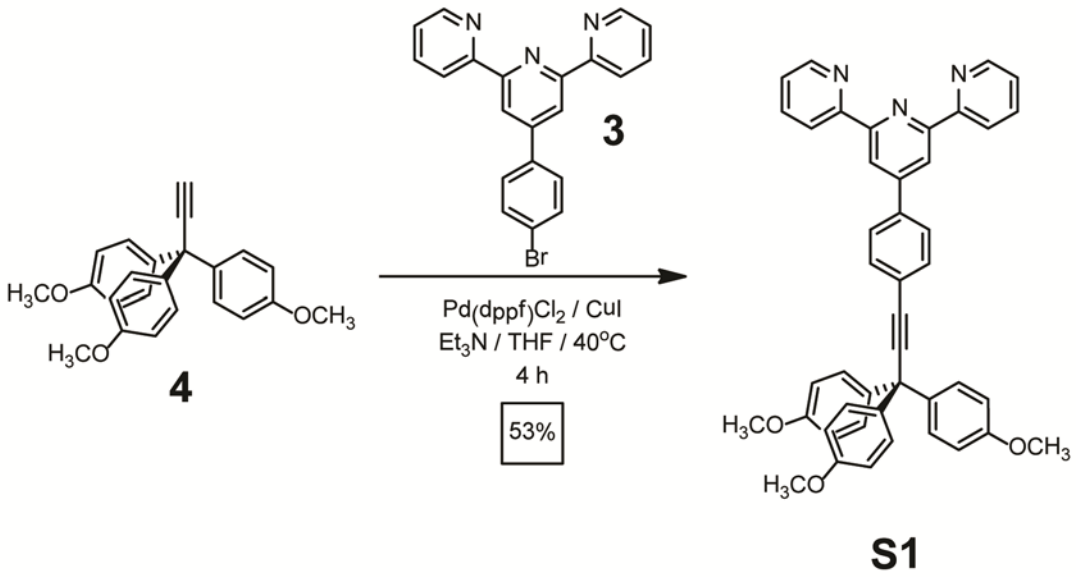

Preparation of trityl-functionalized terpyridyl S1. A 50 mL round bottom flask containing a stir bar was charged with **4** (1.007 g, 2.594 mmol), **3** (1.078 g, 3.008 mmol), CuI (60 mg, 0.315 mmol), and $Pd(dppf)Cl_2$ (170 mg, 0.147 mmol). These solids were placed under a N_2 atmosphere through three evacuation and backfilling cycles. Anhydrous THF (12 mL) and freshly distilled Et_3N (4.0 mL) were added to the reaction flask. The reaction mixture was heated to 40 ^oC for 4 hrs, after which the reaction was judged to have proceeded to completion by TLC (Al_2O_3, 10% EtOAc / hexanes, product R_f = 0.4). The reaction mixture was concentrated under vacuum, redissolved in CH_2Cl_2 (50 mL), and washed with H_2O (3 x

50 mL). The organic layer was dried ($MgSO_4$) and the solvent was removed under vacuum. The resulting crude solid was filtered through a pad of Al_2O_3 (DCM), reisolated, and then recrystallized from MeCN to provide **S1** (1.1g, 59% yield) as a white solid. **S1**: ^{1}H NMR (300 MHz, $CDCl_3$, 298K) δ 8.76 (s, *3',5'- pyridyl*, 2H), 8.75 (d, *J* = 5 Hz, *6,6″-pyridyl*, 2H), 8.70 (d, *J* = 8 Hz, *3,3″-pyridyl*, 2H), 7.87-7.97 (m, *3-aryl and 5,5″-pyridyl*, 4H), 7.63 (d, *J* = 8 Hz, *2-aryl*, 2H), 7.39 (ddd, *J* = 7 Hz, 5 Hz, 1 Hz, *4,4″-pyriyl*, 2H), 7.25 (d, 7 Hz, *trityl 3-aryl*, 6H), 6.86 (d, 7 Hz, *trityl 2-aryl*, 6H), 3.82 (s, *4-OCH$_3$* , 9H). ^{13}C NMR (75 MHz, $CDCl_3$, 298K) δ 158.7, 156.1, 150.1, 149.1, 138.4, 138.0, 137.9, 132.6, 130.6, 130.5, 127.6, 125.1, 124.47, 122.1, 119.4, 113.7, 98.3, 84.6, 55.7, 54.6. IR (solid, ATR) 2952 2930, 2907, 2834, 2161, 1583, 1504, 1246, 1175, 1032, 825, 790 cm^{-1}. MALDI-TOF-MS m/z Calcd. m/z 666.27 $[M+H]^+$. Found m/z 666.22 $[M+H]^+$.

Scheme A1.3. Demthylation of **S1** to tris(phenol) **5**.

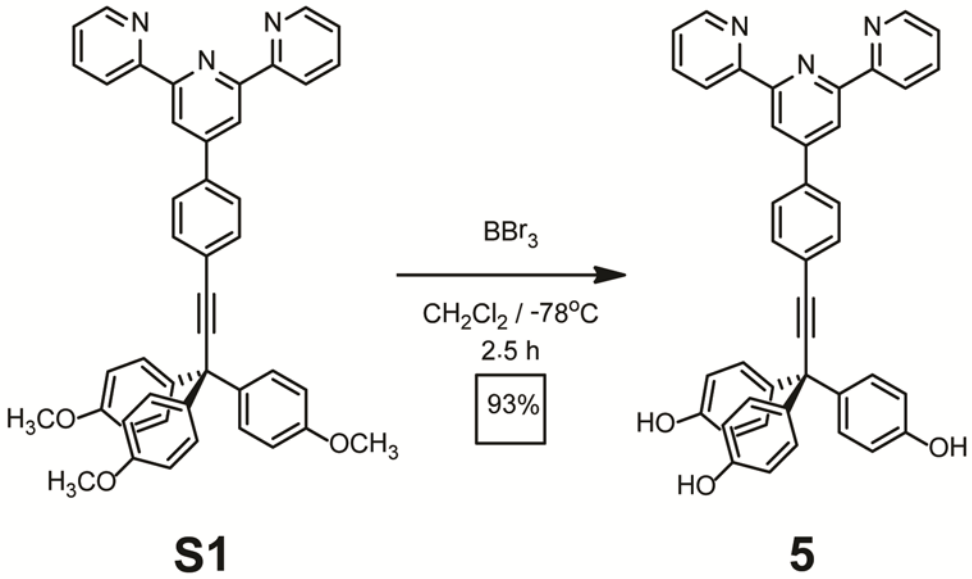

Preparation of tris(phenol) 5: A flame-dried 250 mL round bottom flask was charged with **S1** (670 mg, 1.006 mmol) and placed under a N_2 atmosphere. Anhydrous CH_2Cl_2 (50 mL) $CH_2Cl_2$was added, and the solution was cooled to -78 ^{o}C. A solution of BBr_3 in CH_2Cl_2 (1.0M, 50 mL, 50 mmol) was added using a gastight syringe, and the reaction mixture was warmed to 0 ^{o}C submerging the flask in a bath of ice water. The reaction was determined to be complete after 2 h by monitoring the MALDI-TOF-MS of an aliquot of the reaction mixture. The reaction mixture was poured into ice water (100 mL), and the resulting solid was isolated by filtration and redissolved in an aqueous KOH solution (~1.0 M , 45 mL). This aqueous solution was washed with EtOAc (3 x 25 mL). The combined organic layers were dried ($MgSO_4$), and the solvent was evaporated to provide **5** (0.620 g, 93% yield) as an off-white solid. **5**: ^{1}H NMR (300 MHz, DMSO-*d6*, 298K) δ 9.50 (s, *OH*, 3H), 8.73 (d, J = 4 Hz, *3,3″-pyridyl*, 2H), 8.66 (s, *3',5'-pyridyl,* 2H), 8.62 (d, J = 8 Hz, *6,6″-pyridyl,* 2H), 7.98 (td, J = 7 Hz, 1 Hz, *4,4″-pyridyl*, 2H), 7.90 (d, J = 8 Hz *2-aryl,* 2H), 7.66 (d, J = 8 Hz, *3-aryl,* 2H), 7.52 – 7.43 (td, 7 Hz, 1 Hz, *5,5″-pyridyl*, 2H), 7.05 (d, J = 8 Hz, *trityl 2-aryl,* 6H), 6.76 (d, J = 8 Hz, *trityl 2-aryl,* 6H). ^{13}C NMR (75 MHz, DMSO-*d*-6) δ 156.1, 155.8, 154.9, 149.4, 148.5,

137.5, 137.0, 135.9, 132.3, 129.7, 127.1, 124.6, 124.1, 121.0, 117.7, 114.8, 98.5, 83.6, 53.7, 30.8. IR (solid, ATR) 3051, 2930, 1702, 1588, 1505, 1172, 833, 827, 787 cm^{-1}. MALDI-TOF-MS: m/z 624.5 $[M+H]^+$. Anal. Calcd for $C_{42}H_{29}N_3O_3$: C, 80.88; H, 4.69; N, 6.74. Found: C, 80.65; H, 4.60; N, 6.72.

Scheme A1.4. Synthesis of pyrene-containing tosylate **6**.

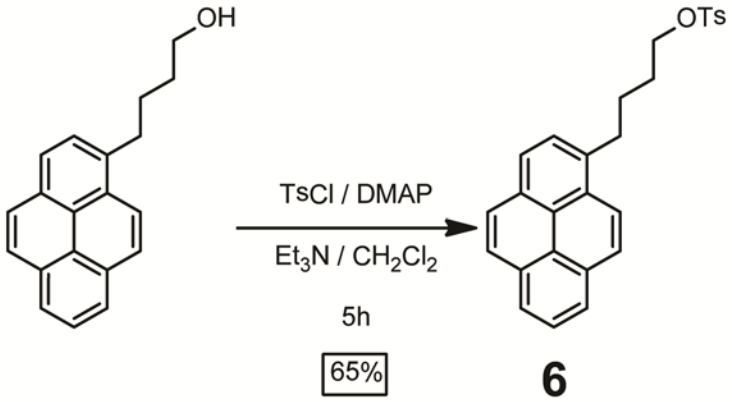

Preparation of pyrene-containing tosylate 6. A flame-dried 250 mL round bottom flask was charged with pyrene butanol (0.5131 g, 187 mmol) and a catalytic amount (5 mg, 0.04 mmol)of DMAP and placed under a N_2 atmosphere. Anhydrous CH_2Cl_2 (90 mL) and freshly distilled Et_3N (20 mL) were added to the reaction flask, and the solution was cooled to -10°C using a dry ice ethylene glycol bath, and a solution of *p*-toluenesulfonyl chloride in anhydrous CH_2Cl_2 (0.1 M, 10 mL, 3.88 mmol) was added drop-wise. The reaction was determined to be complete after 5 h by TLC (SiO_2, 20% EtOAc / 80% hexanes, product R_f=0.25).The reaction mixture was poured into water, and the organic layer washed with H_2O (3 x 20 mL). The organic layer was then dried ($MgSO_4$) and the solvent removed under vacuum. The resulting crude oil was purified by column chromatography (SiO_2, 20% EtOAc / 80% hexanes, product R_f=0.25) to provide **6** (0.527 g, 65% yield) as an off-white solid. **6:** ^{1}H NMR (400 MHz, $CDCl_3$, 298 K) δ 8.21 – 7.75 (m, *pyrene*, 9H), 7.73 (d, *J* = 8 Hz, *tosyl 2-aryl*, 2H), 7.23 (d, *J* = 8 Hz, *tosyl 3-aryl* 2H), 4.08 (t, *J* = 6 Hz, *1-butyl* CH_2, 2H), 3.31 (t, *J* = 7 Hz, *4-butyl* CH_2, 2H), 2.35 (s, *tosyl* CH_3, 3H), 1.96 – 1.74 (m, *2,3-butyl* CH_2, 4H). ^{13}C NMR (100 MHz, $CDCl_3$, 298 K) δ 144.6, 135.8, 131.4, 130.8, 129.9, 129.7, 129.7, 128.5, 127.8, 127.4, 127.3, 127.1, 126.7, 125.8, 124.9, 124.7, 123.1, 70.3, 32.7, 28.7, , 21.5. IR (solid, ATR) 3041, 2934, 1599, 1586, 1505, 1464, 1455, 1354, 1187, 1173, 841, 815, 661 cm^{-1}. MALDI-TOF-MS Calcd. m/z 429.152. Found m/z 429.232 $[M+H]^+$.

Scheme A1.5. Synthesis of pyrene-containing tripodal terpyridine **S2**.

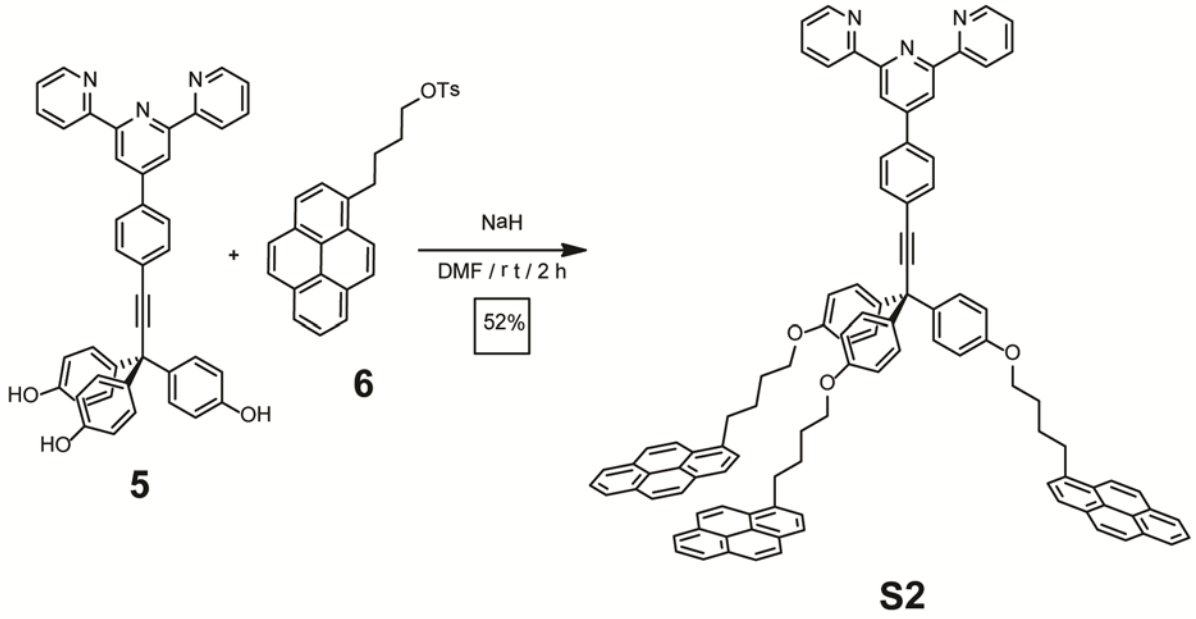

Preparation of pyrene-containing tripodal terpyridine S2. A 25 mL flame-dried round bottom flask was charged with **5** (51 mg, 0.080 mmol) and placed under a N_2 atmosphere. Anhydrous DMF (6 mL) was added to the reaction flask followed by excess NaH (60% suspension in mineral oil) changing the reaction mixture from yellow to green. After 20 min, a solution of **6** in anhydrous DMF (0.16 M, 2 mL, 0.323 mmol) was added. The reaction was determined to be complete after 2 h by TLC (NH_2-SiO_2 , PhMe product R_f = 0.33). The reaction mixture was poured into water (20 mL), filtered through celite and the celite washed with CH_2Cl_2. The resulting biphasic mixture was transferred to a separatory funnel and the CH_2Cl_2 layer removed and washed with H_2O (3 x 10 mL), dried ($MgSO_4$) and the solvent removed under vacuum. The crude oil was purified by flash chromatography (amine capped SiO_2, 50% hexanes / 50% PhMe-PhMe) to provide **S2** (40 mg, 35% yield) as a white foam. **S2:** ^{1}H NMR (400 MHz, $CDCl_3$, 298 K) δ 8.82 (s, *3′,5′- pyridyl,* 2H) 8.76 (d, *J* = 4 Hz, *J* = 1 Hz, *6,6″-pyridyl*, 2H), 8.26 (d, *J* = 9 Hz, 6.0, 3H), 8.18 – 7.81 (m, *pyrene, 2-aryl, 3,5,3″,5″-pyridyl,* 31H), 7.61 (d, *J* = 8.0, *3-aryl,* 2H), 7.67 – 7.58 (td, *J* = 6 Hz, 1 Hz, *4,4″-pyridyl*, 2H), 7.23 (d, *J* = 9 Hz, *trityl 2-aryl,* 6H), 6.85 (d, *trityl 3-aryl,* 6H), 4.02 (t, *J* = 6 Hz, *1-butyl ,* 6H), 3.41 (t, *J* = 7 Hz, *4-butyl*, 6H), 2.14 – 1.86 (m, *2,3-butyl*, 12H). ^{13}C NMR (101 MHz, $CDCl_3$, 298 K) δ 157.9, 156.2, 156.0, 149.5, 149.2, 138.0, 137.0, 136.6, 132.3, 131.5, 131.0, 130.2, 129.9, 128.7, 127.6, 127.3, 127.2, 126.7, 125.9, 125.2, 125.1, 124.9, 124.88, 124.8, 123.9, 123.5, 121.5, 118.7, 113.9, 67.7, 33.2, 29.8, 29.3, 28.3. IR (solid, ATR) 2974, 2922, 2863 cm^{-1}. MALDI-TOF-MS Calcd. m/z 1393.607. Found m/z 1393.529 $[M+H]^+$ Anal. Calcd for $C_{102}H_{77}N_3O_3$: C, 87.96; H, 5.57; N, 3.02. Found: C, 87.89; H, 5.84; N, 2.84.

Scheme A1.6. Synthesis of Co(tpy)Cl_2 ·MeCN **7**.

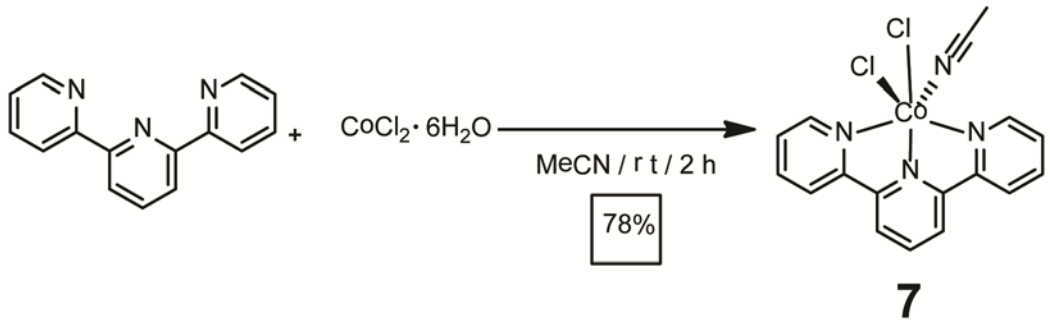

Preparation of Co(tpy)Cl_2 ·MeCN 7. A 50 mL round bottom flask was charged with 2,2':6',2''-terpyridine (203.1 mg, 0.87 mmol) and MeCN (25 mL). $CoCl_2.6H_2O$ (275.5 mg, 1.15 mmol) was added as a solid to the reaction mixture. The resulting red mixture was stirred for 2 h during which the mixture turned light green and a precipitate formed. The green solid was collected by filtration and washed with acetonitrile and diethyl ether to provide **7** (0.491 g, 78% yield). **7:** ^{1}H NMR (400 MHz, D_2O, 298 K) δ 189.5, 106.6, 83.7, 51.2, 34.1, 15.7, 1.9. ^{13}C resonances were not observed due to the paramagnetic nature of this compound. MALDI-TOF-MS Calcd 402.99 $[M]^+$. Found 402.6 $[M]^+$, 368.7 $[M\text{-}Cl]^+$, 327.7 $[M\text{-}Cl\text{-}MeCN]^+$. IR (solid, ATR) 3035, 2163, 1595, 1471, 1449, 769 cm^{-1}. Anal. Calcd. for $C_{15}H_{11}Cl_2CoN_3$: C, 49.62; H, 3.05; N, 11.57. Found: C, 49.31; H, 3.01; N, 11.59.

Scheme A1.7. Synthesis of (Terpyridine)(Tripod) Cobalt (II) $(PF_6)_2$ **1·2PF$_6$**.

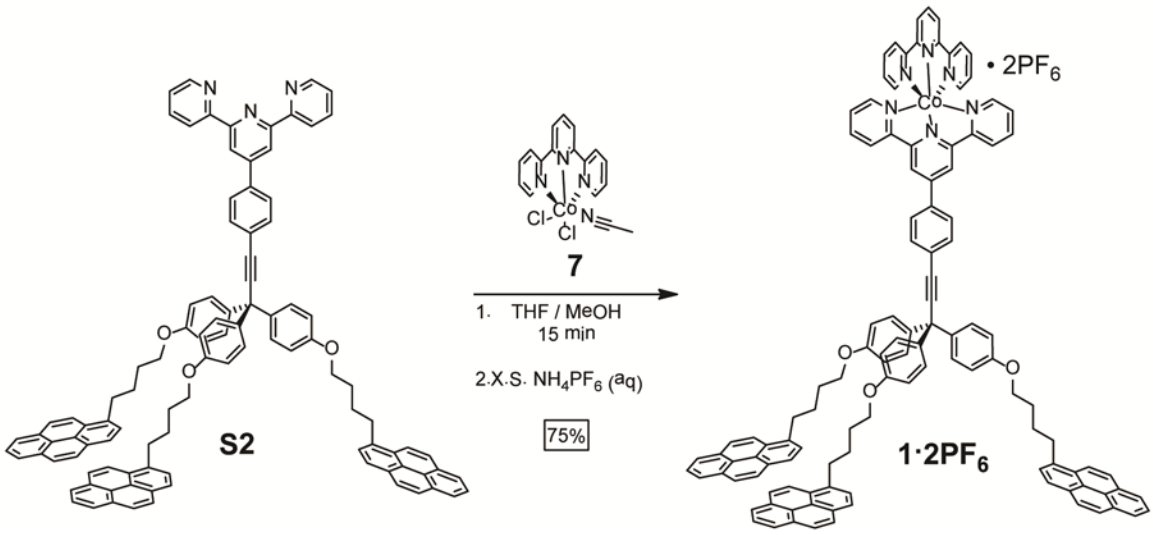

Preparation of (Terpyridine)(Tripod)Co$(PF_6)_2$ 1·2PF$_6$. A 20 mL scintillation vial was charged with **7** (0.029 g, 0.072 mmol) and methanol (3.6 mL). The mixture was stirred to give a suspension to which **S2** (50 mg, 0.036 mmol) was added slowly as a solution in THF (1.8 mL). After 15min of stirring, saturated aqueous NH_4PF_6 was added to precipitate the product which was collected by filtration, and washed with H_2O (3 x 2 mL) to provide **1·2PF$_6^-$** (0.045 g, 75% yield) as an orange powder. **1·2PF$_6^-$** : ^{1}H NMR (400 MHz, $CDCl_3$, 298 K) δ 96.03,

78.87, 70.70, 56.30, 45.99, 33.40, 23.49, 17.55, 14.18, 12.21, 9.21, 8.71, -11.47 (Knight shifted diagnostic peaks) . ^{13}C resonances were not observed due to the paramagnetic nature of this compound. ESI-MS calculated for $[C_{117}H_{88}CoN_6O_3]^{2+}$ $[M]^{2+}$ m/z 841.81 found m/z 841.78. MALDI-TOF-MS Calcd. m/z 1683.624. Found m/z 1683.535 $[M+H]^+$. IR (solid, ATR) 2922, 2853, 839 cm^{-1}.

Scheme A1.8. Synthesis of (Terpyridine)(Tripod) Cobalt (III) $(PF_6)_3$ **S3·3PF$_6$**.

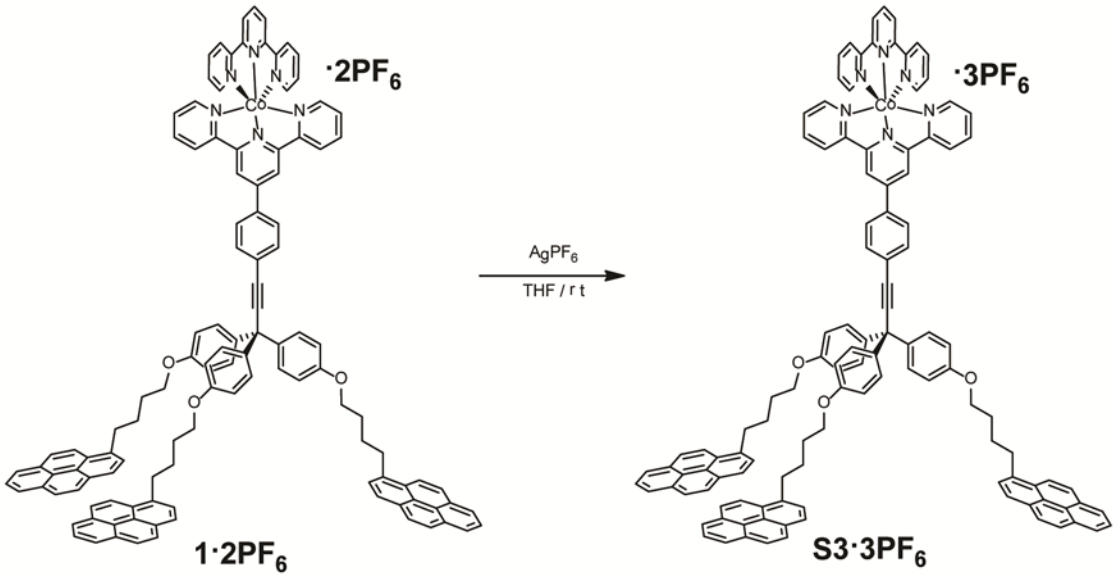

Preparation of (Terpyridine)(Tripod)Co(PF$_6$)$_3$ S3·3PF$_6$. A 1 dram vial was charged with **1·2PF$_6$** (0.010 g, 0.005 mmol), a stir bar, and THF (1 mL). Excess $AgPF_6$ was then added as a solid to the stirring mixture. After 15 min the resulting yellow mixture was filtered through celite, and the solvent removed to provide **S3·3PF$_6$** (0.010 g, quantitative) as a yellow solid. **S3·3PF$_6$:** ^{1}H NMR (600 MHz, CD_2Cl_2, 298 K) δ 8.86 (s, *3′,5′- pyridyl* 2H), 8.35 (d, *J* = 7.8 Hz, *6,6″-pyridyl*, 2H), 8.24 (d, *J* = 9.0 Hz, *2-aryl*, 2H), 8.16 – 7.9 (m, 33H), 7.83 (d, *J* = 7.6 Hz, *2-pyrenyl*, 3H) 7.42 (t, *J* = 6.3 Hz, *5,5″-pyridyl*, 2H), 7.31 (d, *J* = 5.4 Hz, *4,4″-pyridyl*, 2H), 7.24 (d, *J* = 8.7 Hz, *trityl 2-aryl*, 6H), 6.82 (d, *J* = 8.7 Hz, *trityl 3-aryl*,6H), 3.96 (t, *J* = 6.0 Hz, *4-butyl*, 6H), 3.35 (t, *J* = 7.7 Hz, *1-butyl*, 6H), 2.01 – 1.93 (m, *3-butyl*, 6H), 1.93 – 1.85 (m, *2-butyl*, 6H). ^{13}C NMR (125 MHz, CD_2Cl_2, 298 K) δ 158.1, 158.0, 157.9, 155.5, 155.4, 143.0, 137.3, 136.8, 133.8, 132.9, 131.8, 131.7, 131.6, 131.3, 130.8, 130.1, 130.0, 129.9, 129.6, 128.5, 128.4, 127.7, 127.6, 127.6, 127.5, 127.5, 127.4, 127.2, 127.06, 127.0, 127.0, 126.9, 126.4, 125.7, 125.1, 125.1, 125.1, 124.8, 124.8, 124.7, 124.6, 124.56, 124.5, 124.4, 124.3, 124.2, 124.1, 123.4, 123.3, 123.2, 113.9, 113.8, 67.7, 33.0, 30.6, 29.2, 28.2.

Scheme A1.9. Overall synthesis of a terpyridyl-functionalized monopodal graphene binding motif **S6**.

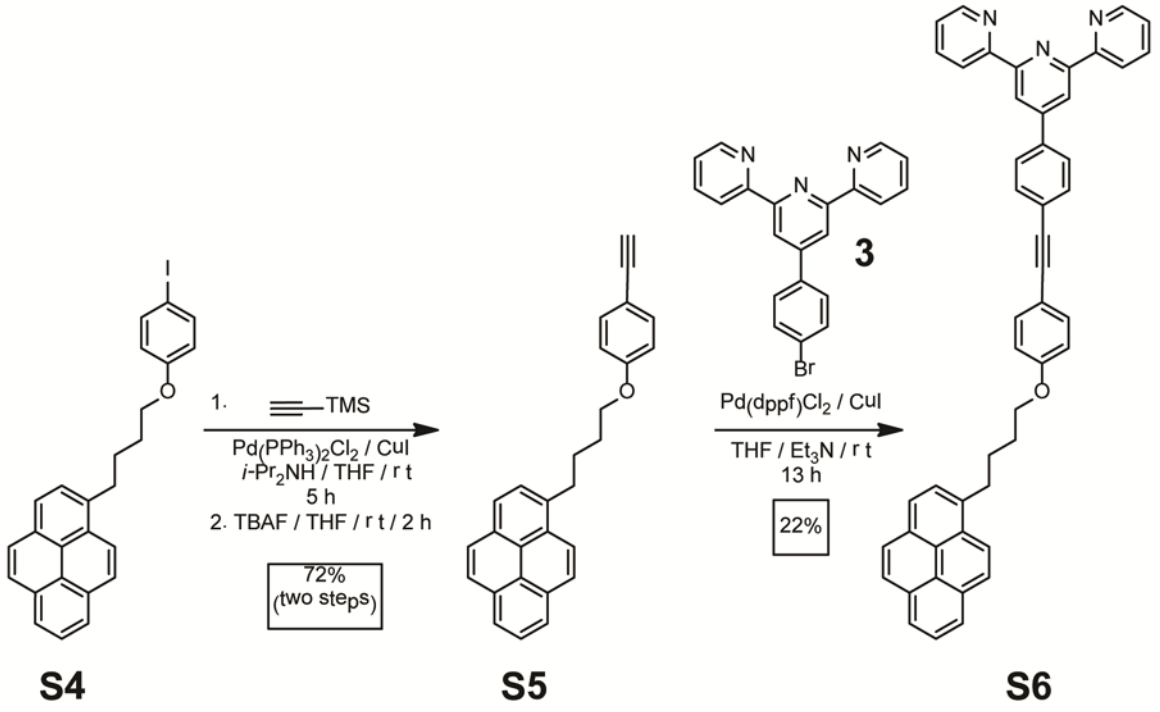

Scheme A1.10. Synthesis of 1-(4-(4-iodophenoxy)butyl)pyrene **S4.**

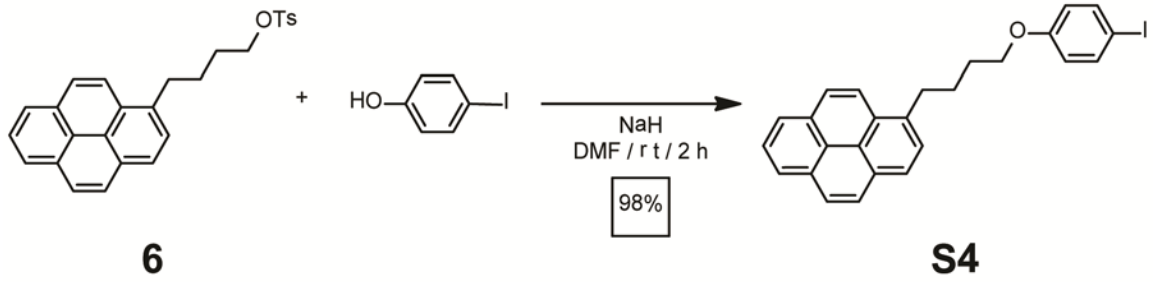

Preparation of 1-(4-(4-iodophenoxy)butyl)pyrene S4. A 250 mL round-bottom flask was charged with a 4-iodophenol (0.30 g, 1.36 mmol), **6** (0.70 g, 1.64 mmol), anhydrous DMF (14 mL), and NaH (0.3 g, 16 mmol) and placed under a N_2 atmosphere. The reaction was determined to be complete after 2 h by TLC (SiO_2 , 20% EtOAc / 80% hexanes, product R_f = 0.41). The reaction mixture was poured into H_2O (50 mL) and the resulting solid was isolated by filtration to provide **S4** (0.637 g, 98% yield) as a white powder. **S4:** ^{1}H NMR (400 MHz, $CDCl_3$, 298 K) δ 8.26 (d, *J* = 9 Hz, *3-pyrenyl*, 1H), 8.18 – 7.95 (m, *4,5,6,7,8,9,10-pyrenyl*, 7H), 7.86 (d, *J* = 8 Hz, *2-pyrenyl*, 1H), 7.51 (d, *J* = 7 Hz, *2-aryl*, 2H), 6.64 (d, *J* = 7Hz, *3-aryl*, 2H), 3.95 (t, *J* = 6 Hz, *1-butyl*, 2H), 3.40 (t, *J* = 8 Hz, *4-butyl*, 2H), 2.11 – 1.86 (m, *2,3-butyl*, 4H). ^{13}C NMR (75 MHz, $CDCl_3$, 298 K) δ 159.0, 138.3, 136.5, 131.6, 131.0, 130.0, 128.7, 127.6, 127.6, 127.4, 126.7, 125.9, 125.2, 125.0, 124.9, 124.8, 123.4, 117.0, 82.6, 67.9, 33.2, 29.2, 28.3. FT-IR (ATR) 3038, 2937, 2927, 2866, 1486, 1244, 841 cm^{-1}. MALDI-TOF-MS Calcd. m/z 476.06 $[M]^+$. Found m/z 476.12 $[M]^+$ Anal. Calcd. for $C_{26}H_{21}IO$: C, 65.56; H, 4.44. Found: C, 65.28; H, 4.51.

Scheme A1.11. Synthesis of 1-(4-(4-ethynylphenoxy)butyl)pyrene **S5.**

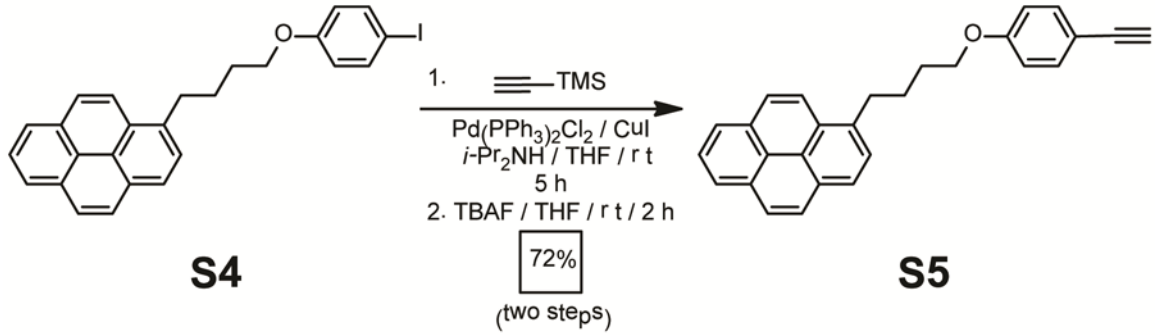

Preparation of 1-(4-(4-Ethynylphenoxy)butyl)pyrene S5. A flame-dried 5 mL round-bottom flask was charged with **S4** (0.50 g, 1.05 mmol) followed by CuI (0.02 g , 0.105 mmol) and $Pd(PPh_3)_2Cl_2$ (0.037 g , 0.052 mmol). These solids were placed under a N_2 atmosphere through three evacuation and backfilling cycles. Anhydrous THF (5.2 mL) and freshly distilled *i*-Pr_2NH (2.5 mL) were added to the flask, followed by TMS acetylene (0.29 mL, 2.09 mmol). The reaction was determined to be complete after 5 h by TLC (10% Et_2O / 90% hexanes, product R_f = 0.3). The reaction mixture was filtered through celite and the solvent was removed under vacuum. The crude oil was redissolved in THF (10 mL) and TBAF 75 wt% in H_2O (0.66 mL, 1.89 mmol) was added. The deprotection was determined to be complete after 2 h by IR, using the Si-C (831 cm^{-1}) stretch and alkyne C-H (3284 cm^{-1})stretch. The reaction mixture was diluted with CH_2Cl_2 (5 mL) and washed with H_2O (3 x 10 mL), dried ($MgSO_4$), and the solvent removed under vacuum. The resulting crude oil was purified by column chromatography (SiO_2, 10% EtOAc / 90% hexanes) to provide **S5** (0.239 g, 72%) as a white powder. **S5:** ^{1}H NMR (400 MHz, $CDCl_3$, 298 K) δ 8.28 (d, *J* = 9 Hz, *3-pyrenyl*, 1H), 8.20 – 7.96 (m, *4,5,6,7,8,9,10-pyrenyl*, 7H), 7.88 (d, *J* = 7 Hz, *2-pyrenyl*, 1H), 7.41 (d, 8 Hz, *2-aryl*, 2H), 6.83 (d, 8 Hz, *3-aryl,* 2H), 4.01 (t, *J* = 6 Hz, *1-butyl*, 2H), 3.42 (t, 6 Hz, *4-butyl*, 2H), 3.00 (s, *alkyne-CH*, 1H), 2.22 – 1.77 (m, *2,3-butyl*, 4H). ^{13}C NMR (100 MHz, $CDCl_3$, 298 K) δ 169.3, 159.6, 136.6, 133.7, 131.6, 130.0, 128.8, 127.7, 127.4, 127.4, 126.8, 126.0, 125.1, 125.0, 124.9, 123.5, 114.6, 114.1, 83.9, 75.9, 67.9, 33.3, 29.3, 28.4. IR (solid, ATR) 3284, 3039, 2940, 2869, 2104, 1604, 1505 cm^{-1}. MALDI-TOF-MS Calcd. m/z 374.17 $[M]^+$. Found m/z 374.47 $[M]^+$ Anal. Calcd. for $C_{28}H_{22}O$: C, 89.81; H, 5.92. Found: C, 89.72; H, 5.96.

Scheme A1.12. Synthesis of the pyrene-containing terpyridine **S6.**

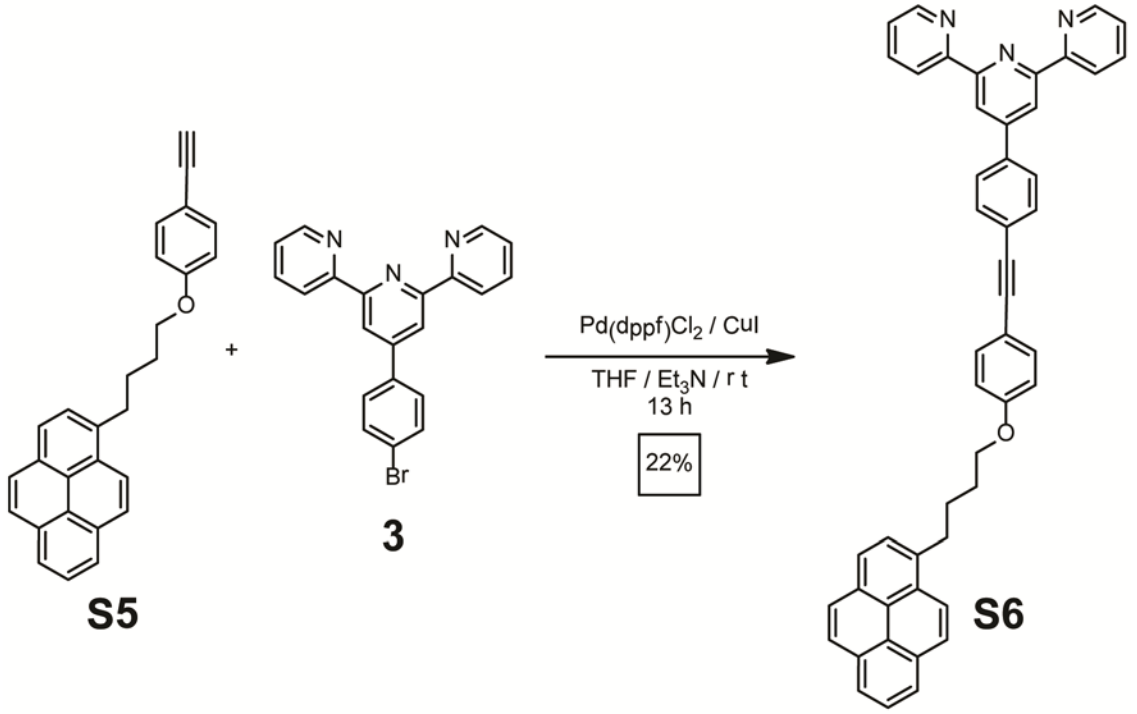

Preparation of the pyrene-containing terpyridine ligand S6. A flame-dried, 5 mL round-bottom flask was charged with 1-(4-(4-ethynylphenoxy)butyl)pyrene (0.127 g, 0.433 mmol), **S5** (0.110 g , 0.361 mmol), CuI (0.014 g , 0.072 mmol), and Pd(dppf)Cl_2 (0.042 g , 0.036 mmol). These solids were placed under a N_2 atmosphere through three evacuation and backfilling cycles. Freshly distilled triethylamine (1 mL) and anhydrous THF (2 mL) were then added to the flask. The reaction was determined to be complete after 13 h by MALDI-MS through disappearance of X. The reaction mixture was filtered through celite, the solvent removed under vacuum, the resulting oil re-dissolved in CH_2Cl_2 and the substance adsorbed onto celite. The resulting powder was purified by flash chromatography (amine SiO_2 10% EtOAc / 90% hexanes) to provide **S6** (0.055 g, 22% yield) as a yellow solid. **S6:** ^{1}H NMR (400 MHz, $CDCl_3$, 298 K) δ 8.78 (s, *3′,5′- pyridyl*, 2H), 8.75 (dd, *J* = 5 Hz, 1 Hz, *6,6″-pyridyl*, 2H), 8.70 (d, *J* = 8 Hz, *3,3″-pyridyl*, 2H), 8.29 (d, *J* = 9 Hz, *3-pyrenyl,* 1H), 8.20 – 7.87 (m, *pyrene, terpy 2-aryl, 4,4″-pyridyl,* 13H), 7.65 (d, *J* = 8 Hz, *terpy 3-aryl,* 2H), 7.48 (d, *J* = 9 Hz, *2-aryl,* 2H), 7.39 (ddd, *J* = 7 Hz, 5 Hz, 1 Hz, *5,5″-pyridyl* 2H), 6.89 (d, *J* = 9 Hz, *3-aryl,* 2H), 4.05 (t, *J* = 6 Hz, *1-butyl ,* 2H), 3.44 (t, *J* = 8 Hz, *4-butyl*, 2H), 2.27 – 1.77 (m, *2,3-butyl*, 4H). ^{13}C NMR (125 MHz, $CDCl_3$, 298 K) δ 137.7, 136.4, 134.0, 133.1, 132.0, 131.4, 130.9, 129.8, 128.6, 127.5, 127.3, 127.2, 126.6, 125.8, 125.1, 125.0, 124.9, 124.8, 124.7, 124.0, 123.3, 121.6, 118.8, 115.0, 114.7, 114.7, 114.5, 110.1, 110.0, 109.9, 109.7, 105.2, 67.7, 33.1, 29.1, 28.2. IR (solid, ATR) 3042, 2922, 2851, 2212, 1583 cm $^{-1}$. MALDI-TOF-MS Calcd. m/z 682.286. Found m/z 682.303 $[M+H]^+$.

Scheme A1.13. Synthesis of the pyrene containing monopodalterpyridine cobalt (III) complex **2·3PF$_6$.**

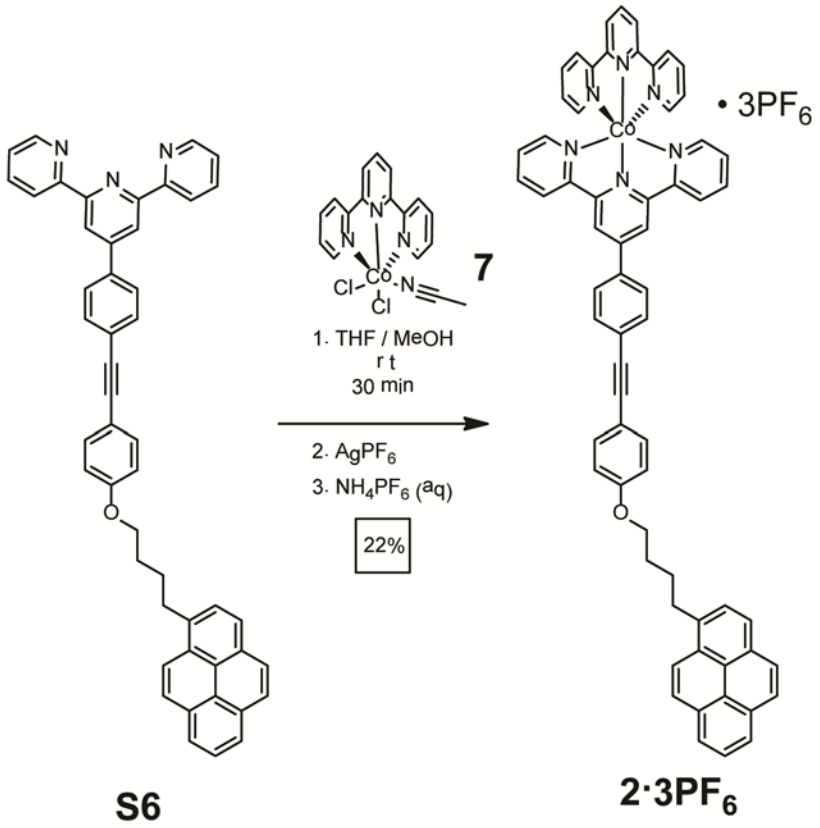

Preparation of the pyrene-containing monopodal Co(III) complex 2·3PF$_6$. A 25 mL round-bottom flask was charged with **7** (43.1 mg , 0.172 mmol) and the solid suspended in MeOH (3.6 mL) by stirring S**6** (29 mg, 0.043 mmol) was added slowly as a solution in THF (4.3 mL). The resulting red mixture was stirred for 30 min and excess $AgPF_6$ was added. The resulting yellow solution was allowed to stir for 20 min until TLC (SiO_2, 80% MeCN / 10% H_2O / 10% sat'd $NaNO_3$ (aq)) showed only Co^{+3} (yellow) species. The products were then precipitated by addition of excess saturated aqueous NH_4PF_6. The solids were collected by filtration and purified by column chromatography (SiO_2, 80% MeCN / 10% H_2O / 10% saturated aqueous $NaNO_3$ (aq)). The pure heteroleptic complex was precipitated from the column fractions by addition of excess saturated aqueous NH_4PF_6 followed by removal of the organic volatiles. The solids were collected by filtration, washed with water, and dried under vacuum to give **2·3PF$_6$** (0.019 g, 22% yield) as an orange powder. **2·3PF$_6$:** ^{1}H NMR (600 MHz, $(CD_3)_2CO$, 298 K) δ 9.82 (s, *3′,5′- pyridyl*, 2H), 9.42 (d, *J* =8.10 Hz, *3′,5′- pyridyl cap*, 2H), 9.33 (t, *J* =8.10 Hz, *4′- pyridyl cap*, 1H), 9.19 (dd, *J* = 7.92 Hz, 1.50 Hz, *3,3″-pyridyl*, 2H), 8.98 (dd, *J* = 7.94 Hz, 1.55 Hz, *6,6″-pyridyl*, 2H), 8.48 (d, *J* = 8.47 Hz, *2-phenyl*, 2H), 8.45-8.40 (m, *5,5″-pyridyl and cap*, *3-pyrenyl*, 5H), 8.26 (m, *J* = 7.55 Hz, *6-pyrenyl*, 1H), 8.25 (d, *J* = 7.55 Hz, *8-pyrenyl*, 1H), 8.23 (d, *J* = 7.67, *4-pyrenyl*, 1H), 8.20 (d, 9.33 Hz, *2-pyrenyl*, 1H), 8.13 (d, 8.90 Hz, *9-pyrenyl*, 1H), 8.11 (d, 8.90 Hz, *10-pyrenyl*, 1H), 8.04 (t, 7.55 Hz, *7-pyrenyl*, 1H), 8.03-7.98 (m, *5-pyrenyl*, *4′- pyridyl*, 2H), 7.92 (d, *J* = 8.47 Hz, 3-*phenyl*, 2H), 7.85 (dd, *J* = 5.97 Hz, 1.25 Hz, *6,6″-pyridyl cap*, 2H), 7.60-7.58 (m, *4,4″-pyridyls*, 4H), 7.55

(d, *J* = 8.69 Hz, 2′-*phenyl*, 2H), 7.05 (d, *J* = 8.69 Hz, 3′-*phenyl*, 2H), 4.19 (t, *J* = 6.36 Hz, 1-*butyl*, 2H), 3.49 (t, *J* = 7.39 Hz, 4-*butyl*, 2H), 2.02 (m, 2,3-*butyl*, 4H). ^{13}C NMR (125 MHz, $(CD_3)_2CO$, 298 K) δ 166.22, 163.02, 160.10, 157.48, 156.93, 156.85, 156.82, 156.75, 156.69, 154.52, 152.78, 152.76, 152.63, 148.49, 143.34, 143.23, 136.94, 135.44, 133.28, 132.78, 132.45, 131.51, 131.09, 131.05, 131.01, 129.93, 128.65, 128.62, 128.03, 127.54, 127.50, 127.42, 127.37, 127.25, 126.59, 126.02, 125.09, 124.96, 124.94, 124.85, 124.77, 123.53, 114.93, 114.92, 109.99, 67.82, 32.72. IR (solid, ATR) 2922, 2853, 839 cm^{-1}. MALDI-TOF-MS Expected: m/z 973.3065 $[M]^+$ Observed: m/z 973.255 $[M]^+$. ESI-MS Expected: 486.653 $[M\text{-}3PF_6]^{2+}$ Observed: 486.632 m/z $[M\text{-}3PF_6]^{2+}$.

C. NMR Spectra

Figure A1.3. ^{1}H NMR of terpyridine **S1** (300 MHz, $CDCl_3$, 298K).

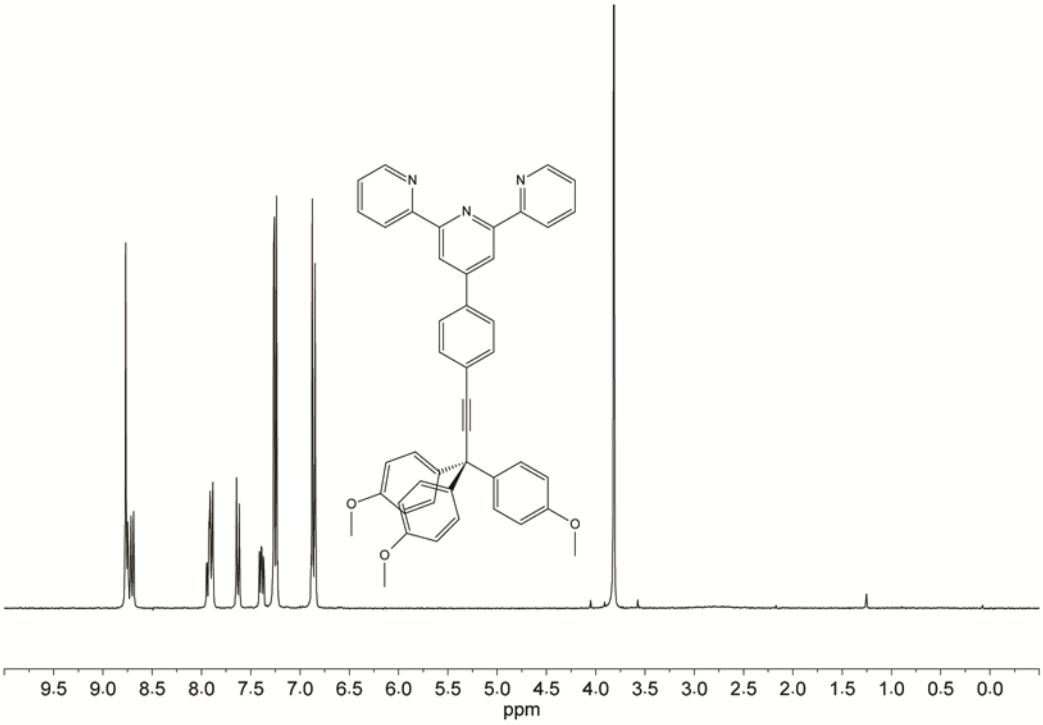

Figure A1.4. ^{13}C NMR of terpyridine **S1**(75 MHz, $CDCl_3$, 298K).

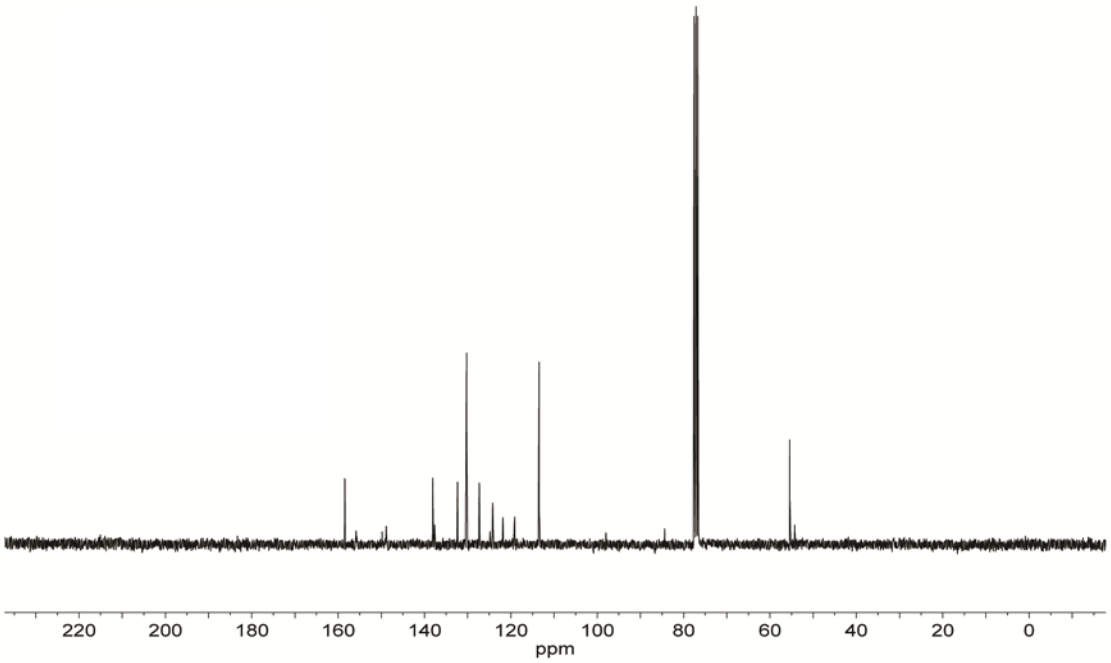

Figure A1.5. ^{1}H NMR of terpyridine **5** (300 MHz, $(CD_3)SO$, 298K).

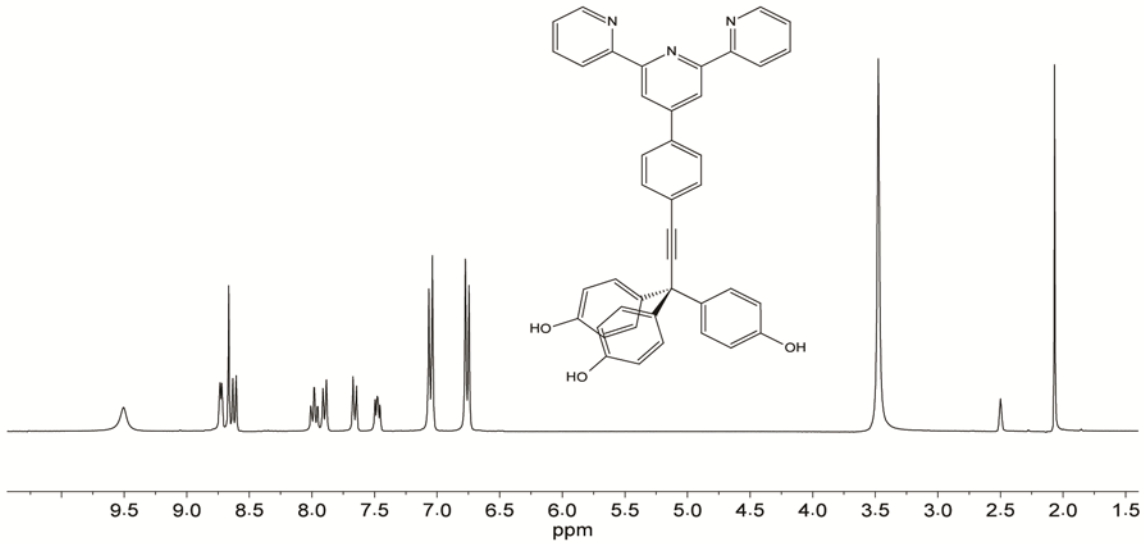

Figure A1.6. ^{13}C NMR of terpyridine **5** (75 MHz, $(CD_3)SO$, 298K).

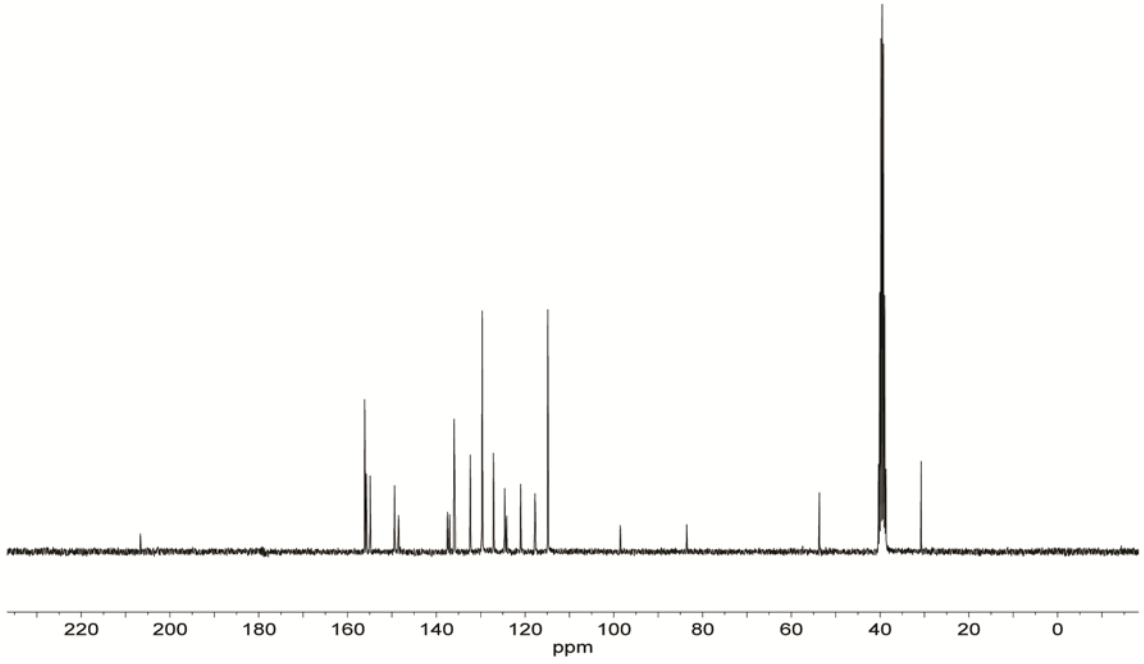

Figure A1.7. ^{1}H NMR of pyrene butanol tosylate **6** (400 MHz, $CDCl_3$, 298K).

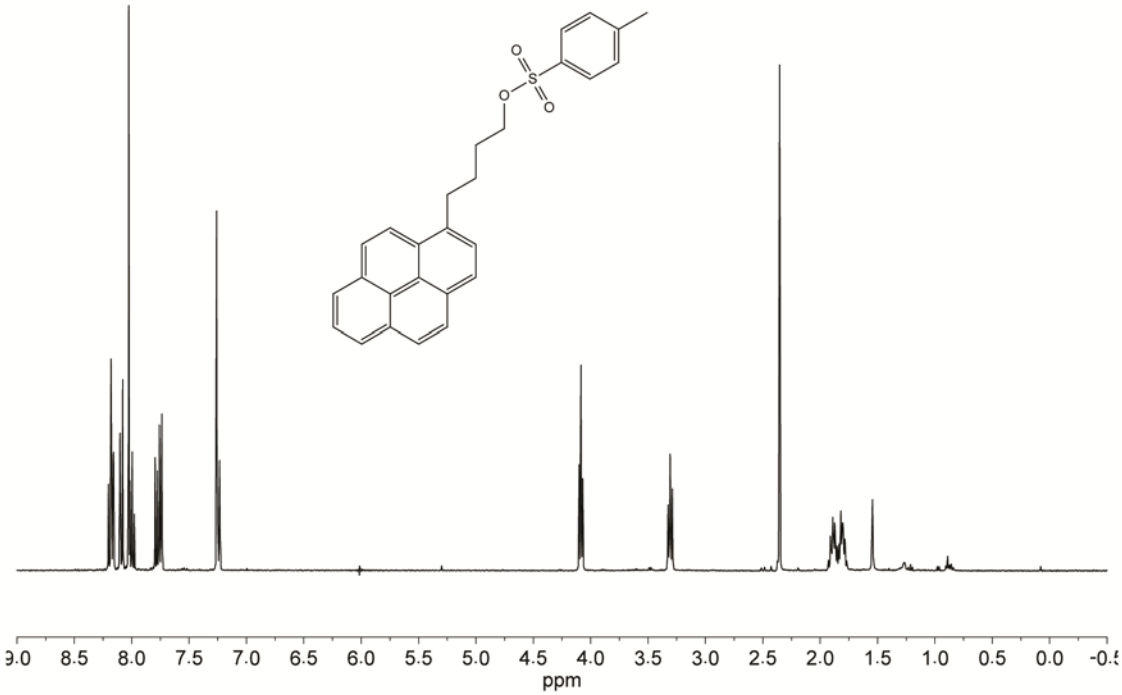

Figure A1.8. ^{13}C NMR of pyrene butanol tosylate **6** (100 MHz, $CDCl_3$, 298K).

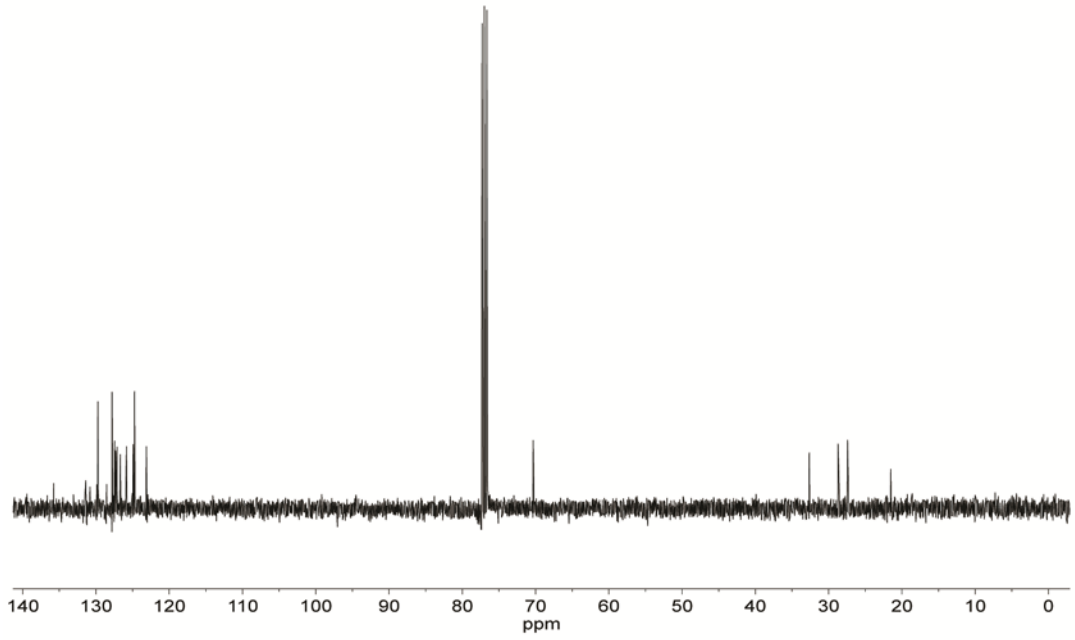

Figure A1.9. ^{1}H NMR of pyrene anchored tripod **S2** (400 MHz, $CDCl_3$, 298K).

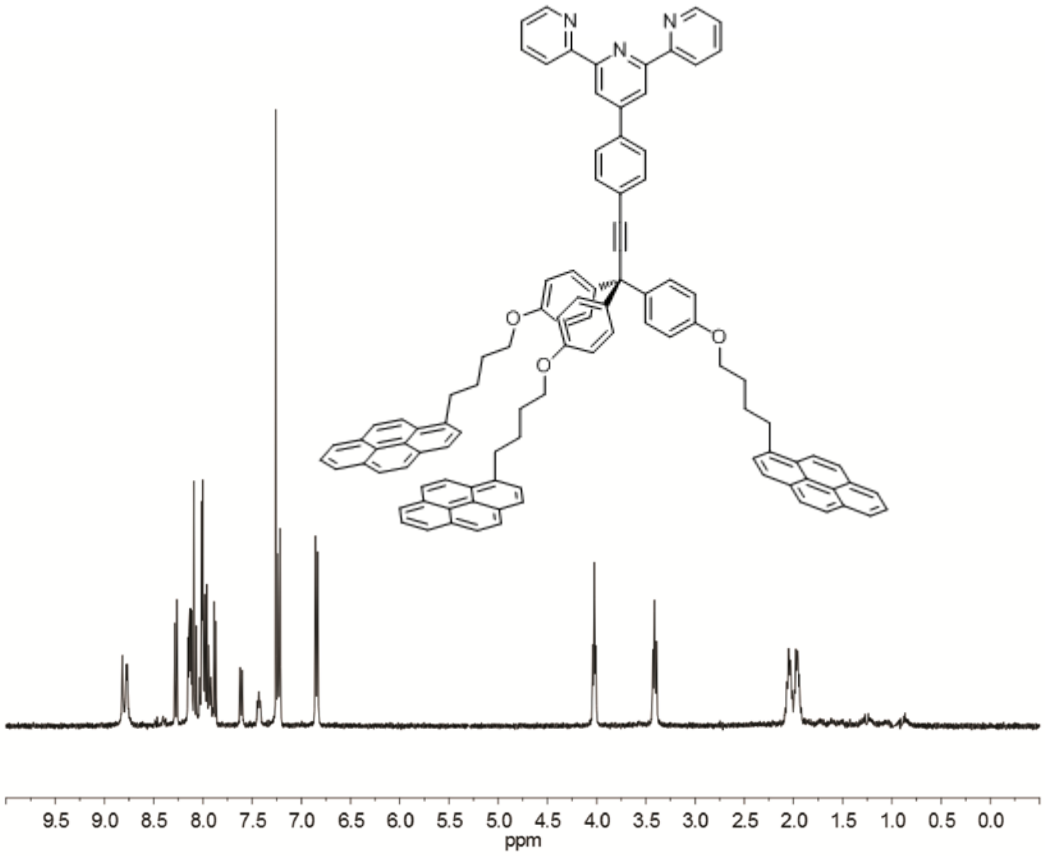

Figure A1.10. ^{13}C NMR of pyrene anchored tripod **S2** (100 MHz, $CDCl_3$, 298K).

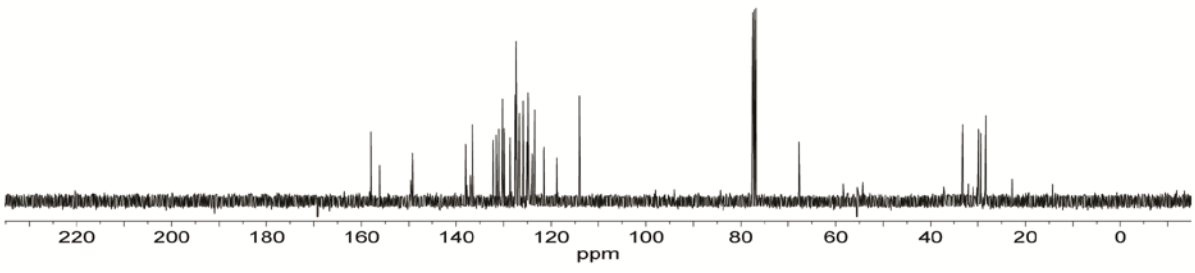

Figure A1.11. ^{1}H NMR of (tpy)$CoCl_2$MeCN **7** (400 MHz,D_2O, 298K).

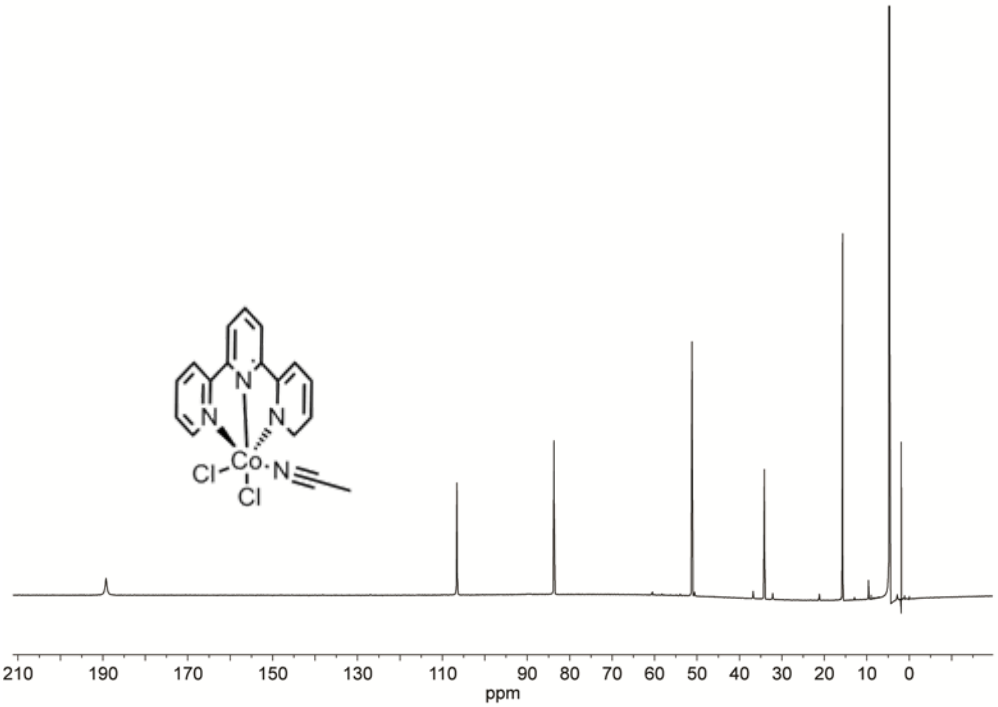

Figure A1.12. ^{1}H NMR of Co complex **1·2PF$_6$** (400 MHz, $CDCl_3$, 298K).

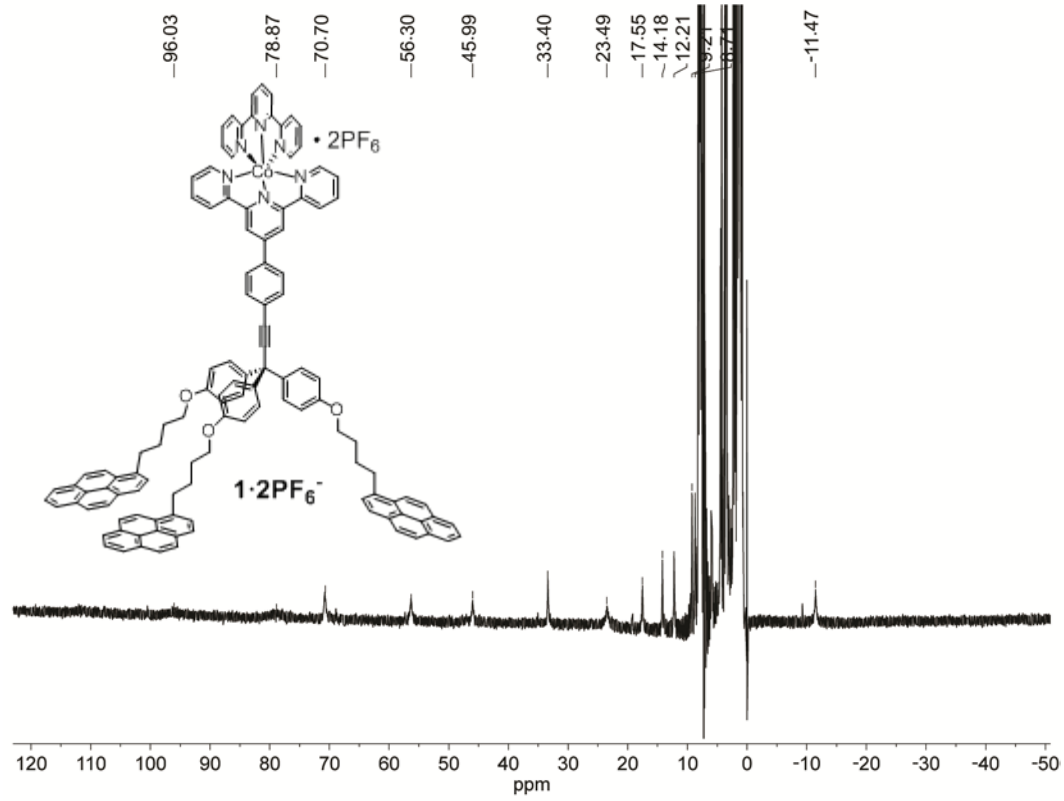

Figure A1.13. ^{1}H NMR of Co complex **S3·3PF$_6$** (600 MHz, CD_2Cl_2, 298K).

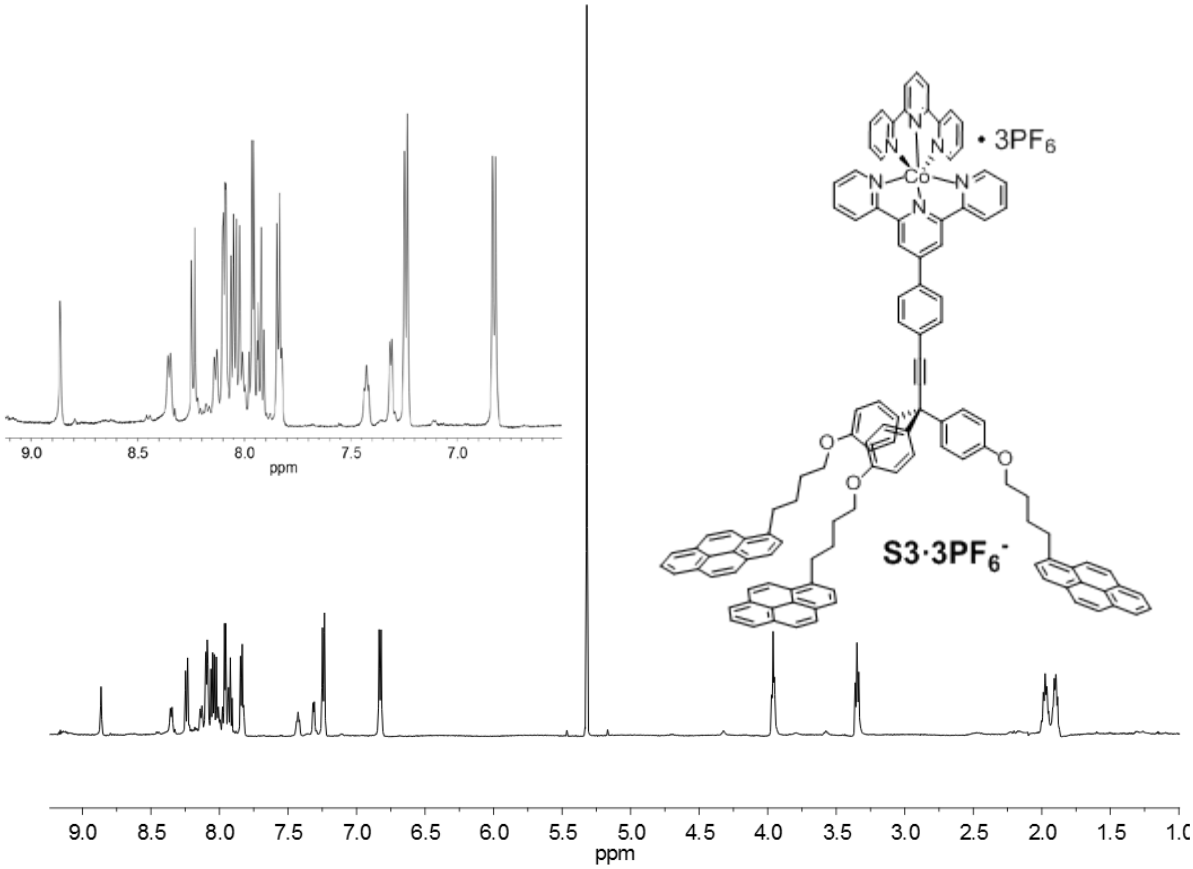

Figure A1.14. ^{13}C NMR of Co complex **S3·3PF$_6$** (125 MHz, CD_2Cl_2, 298K).

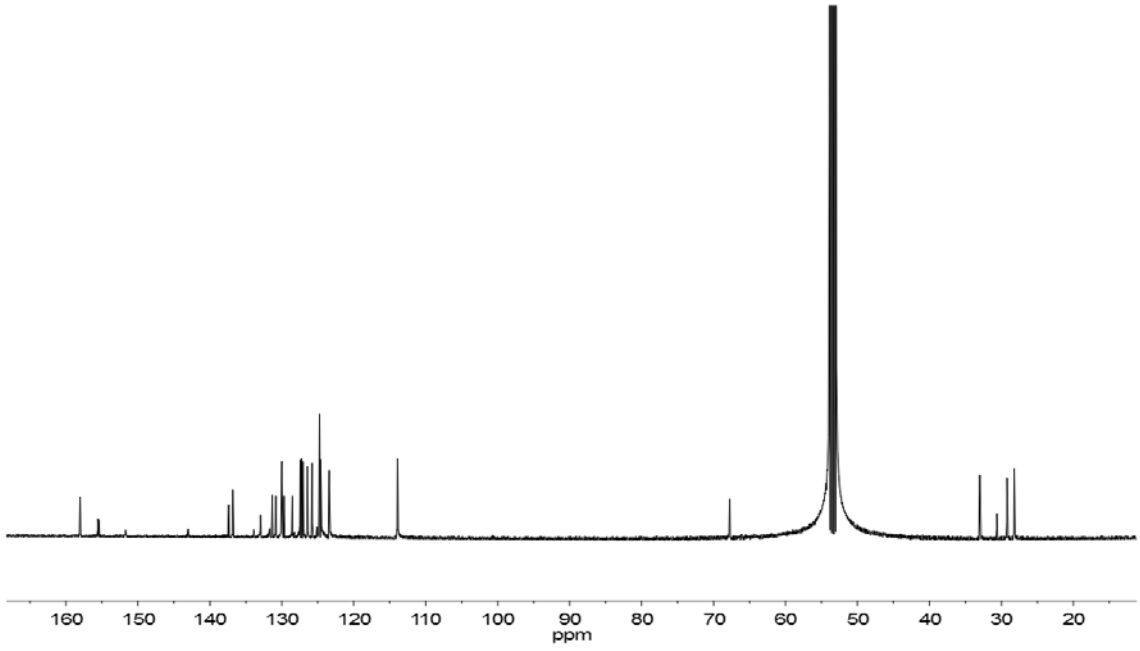

Figure A1.15. ^{1}H NMR of pyrene monopod precursor **S4** (400 MHz, $CDCl_3$, 298K).

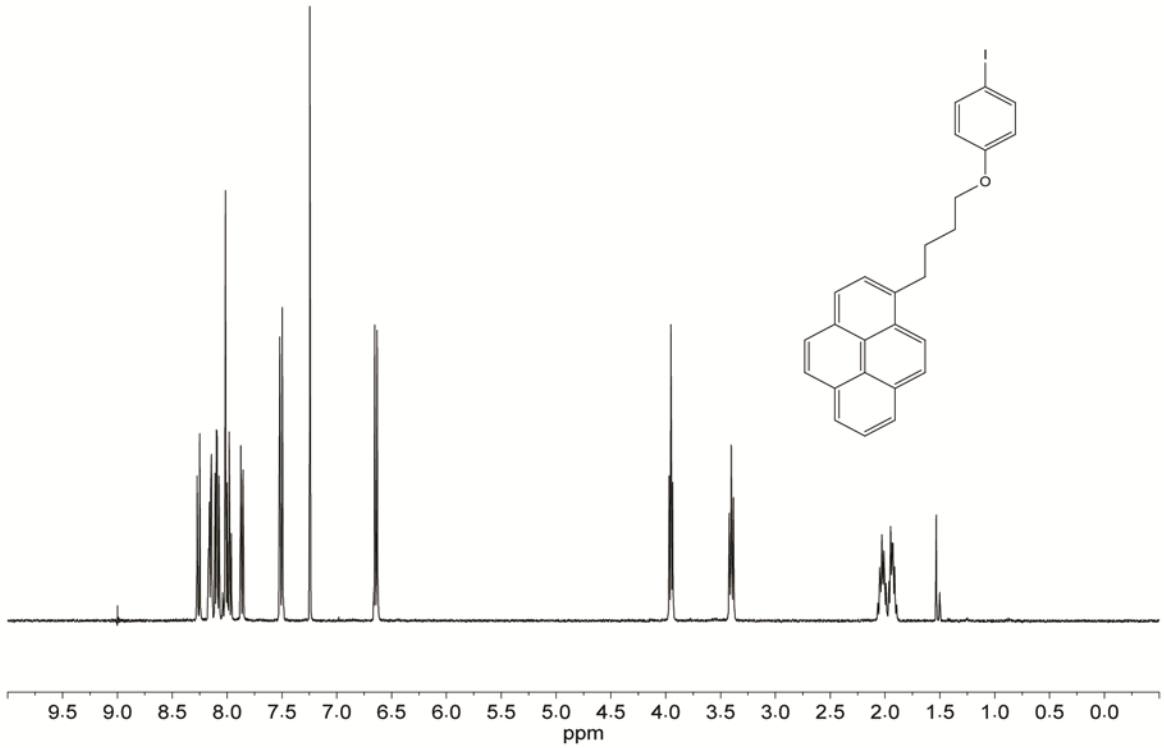

Figure A1.16. ^{13}C NMR of pyrene monopod precursor **S4** (100 MHz, $CDCl_3$, 298K).

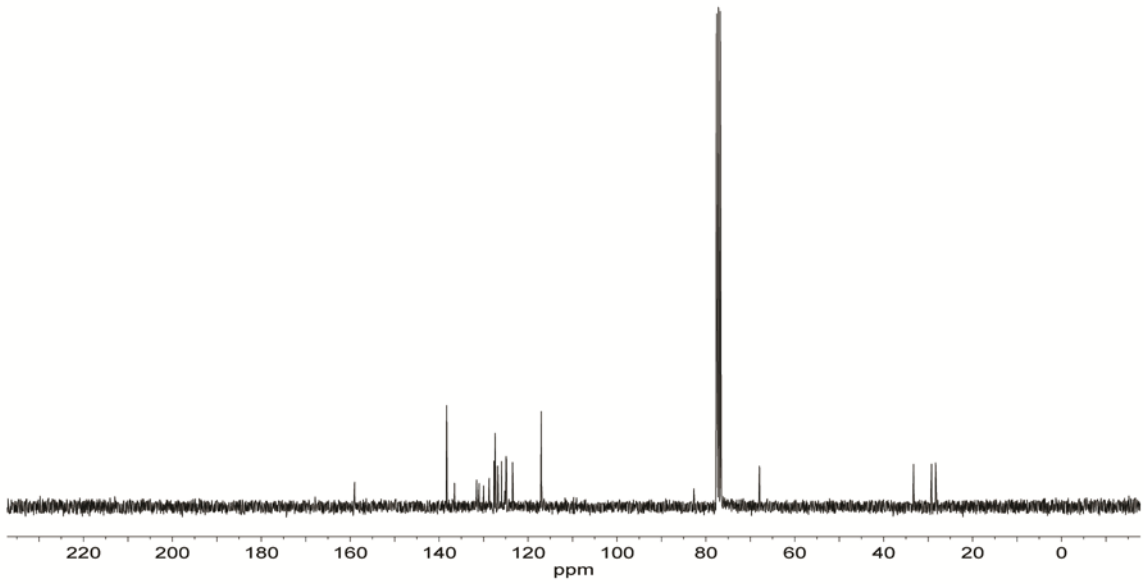

Figure A1.17. ^{1}H NMR of pyrene monopod precursor **S5** (400 MHz, $CDCl_3$, 298K).

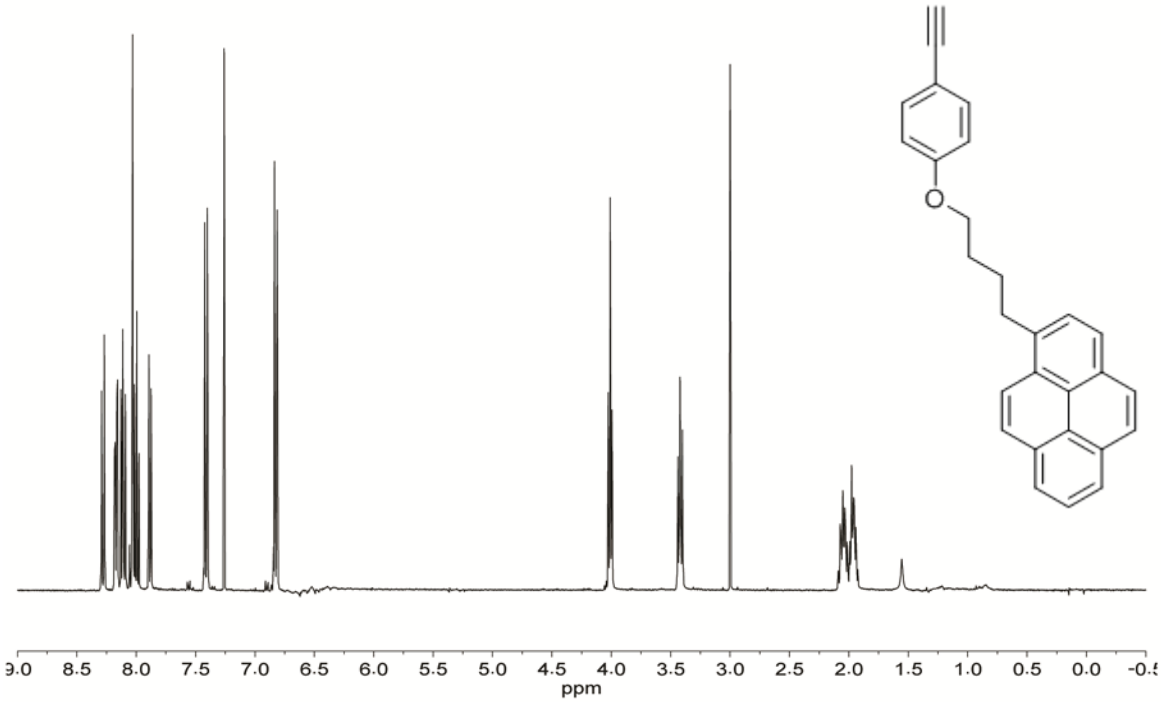

Figure A1.18. ^{13}C NMR of pyrene monopod precursor **S5** (100 MHz, $CDCl_3$, 298K).

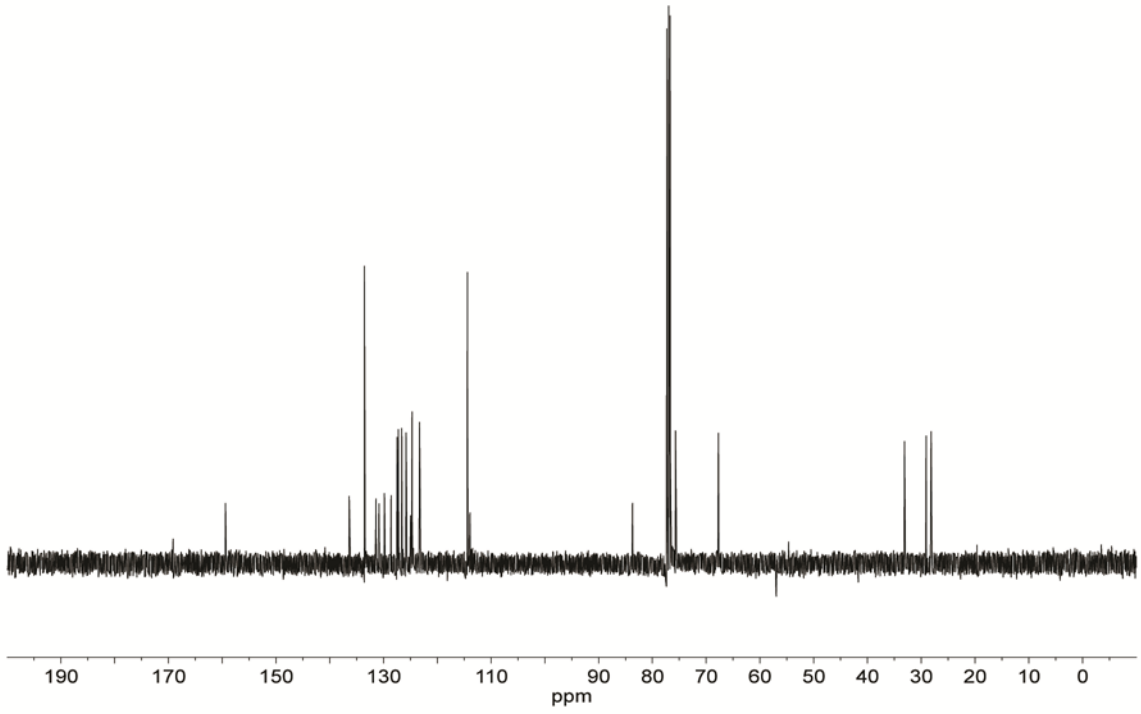

Figure A1.19. ^{1}H NMR of monopod ligand **S6** (400 MHz, $CDCl_3$, 298K).

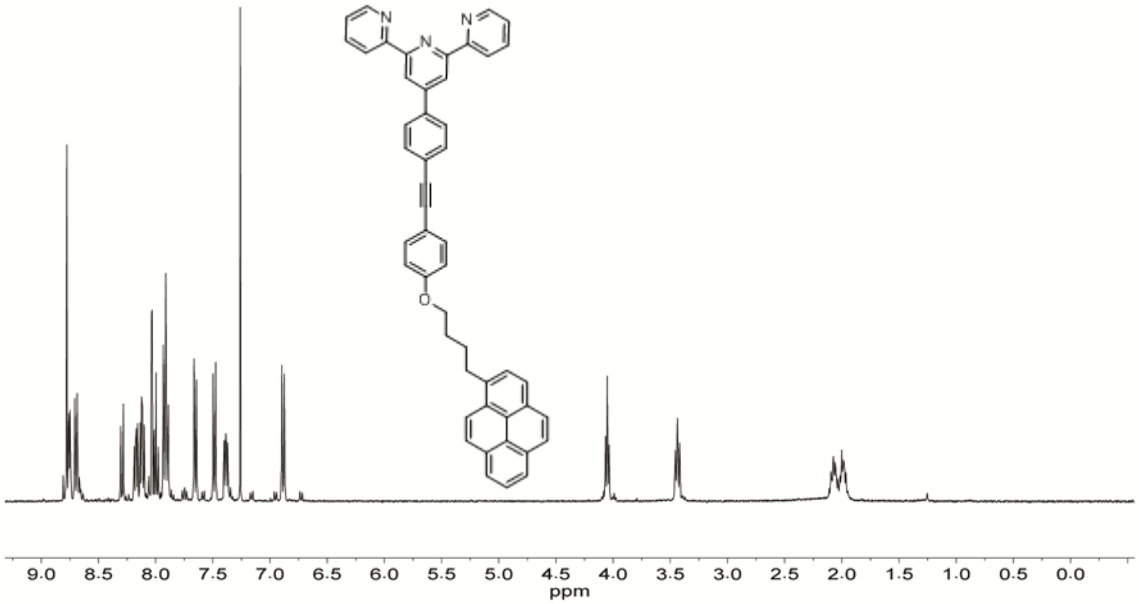

Figure A1.20. ^{13}C NMR of monopod ligand **S6** (100 MHz, $CDCl_3$, 298K).

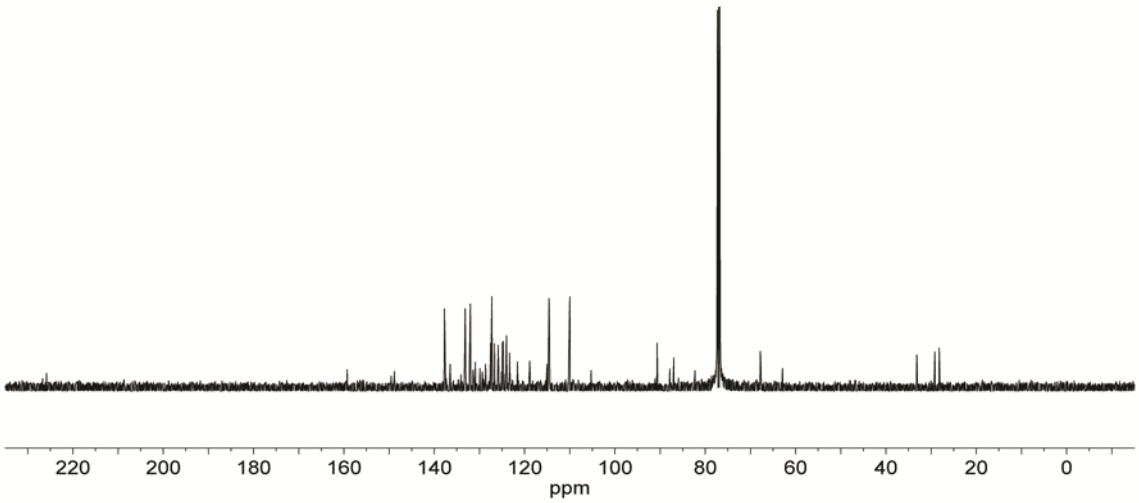

Figure A1.21. ^{1}H NMR of monopod Co complex **2·3PF$_6$** (600 MHz, $(CD_3)_2CO$, 298K).

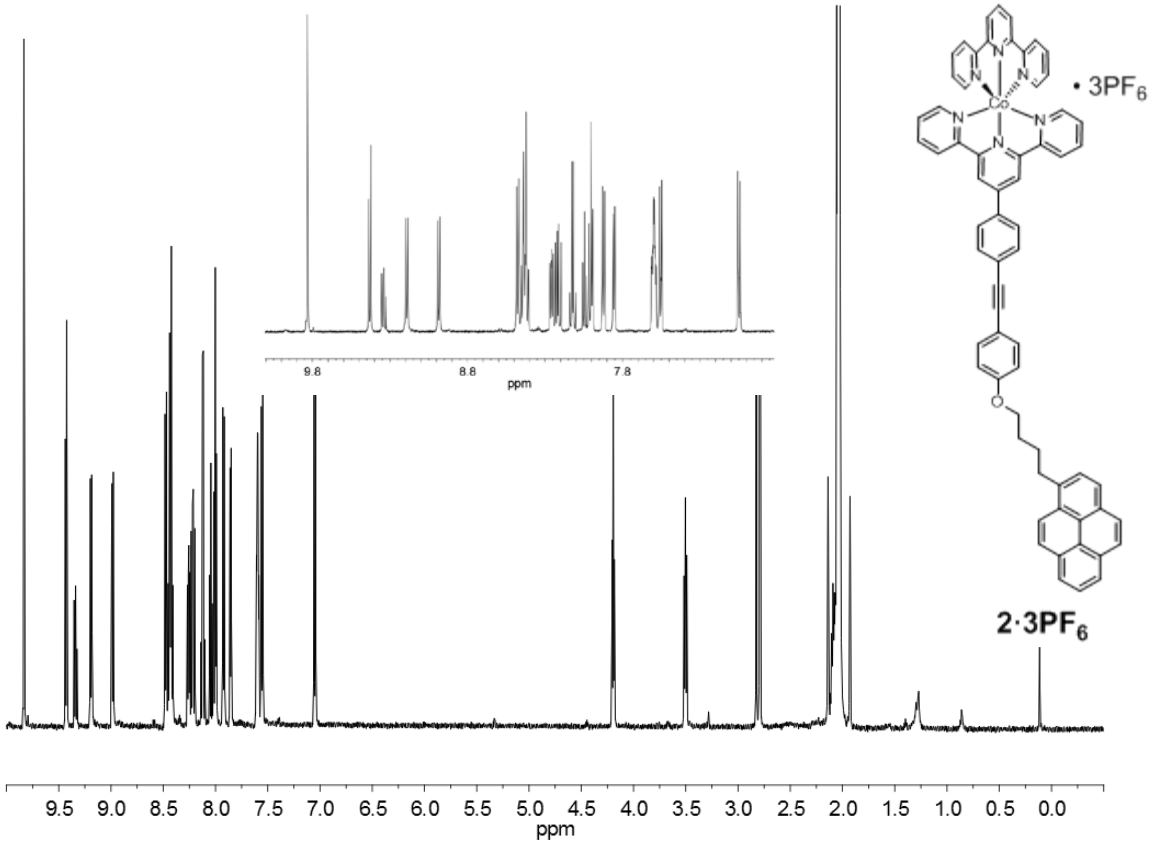

Figure A1.22. ^{13}C NMR of monopod Co complex **2·3PF$_6$** (125 MHz, $(CD_3)_2CO$, 298K).

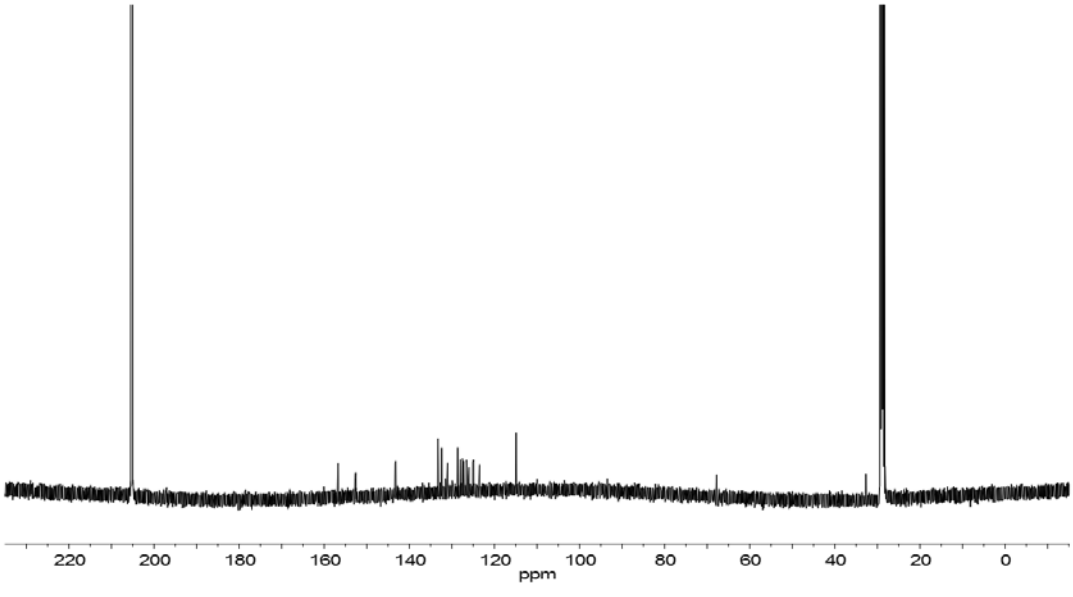

D. Electrochemical Characterization

Electrochemistry on graphene. All electrochemical experiments were carried out in 0.1M NH_4PF_6 in THF as supporting electrolyte under ambient conditions (i.e. oxygen and trace water). Graphene electrodes were prepared by transferring single-layer graphene grown on Cu foil by chemical vapor deposition onto Si/SiO_2 wafers.[2] Electrical contact was made to the graphene by pressing a Pt wire into a bead of In metal placed on the graphene surface outside of the electroactive region. All measurements used 1 mL of analyte solution. The electrochemical cell consisted of a custom made Teflon cell with a single compartment. Pt counter and pseudoreference electrodes were used. Cyclic voltammagrams were recorded in analyte solution in every case, except desorption experiments, which used supporting electrolyte only.

Figure A1.23. Cyclic voltammagrams at varying scan rates of monopod complex **2·3PF$_6$** adsorbed on a graphene (0.1M NH_4PF_6 in THF, 0.5 μM analyte, 0.1 V s^{-1} to 0.5 V s^{-1}).

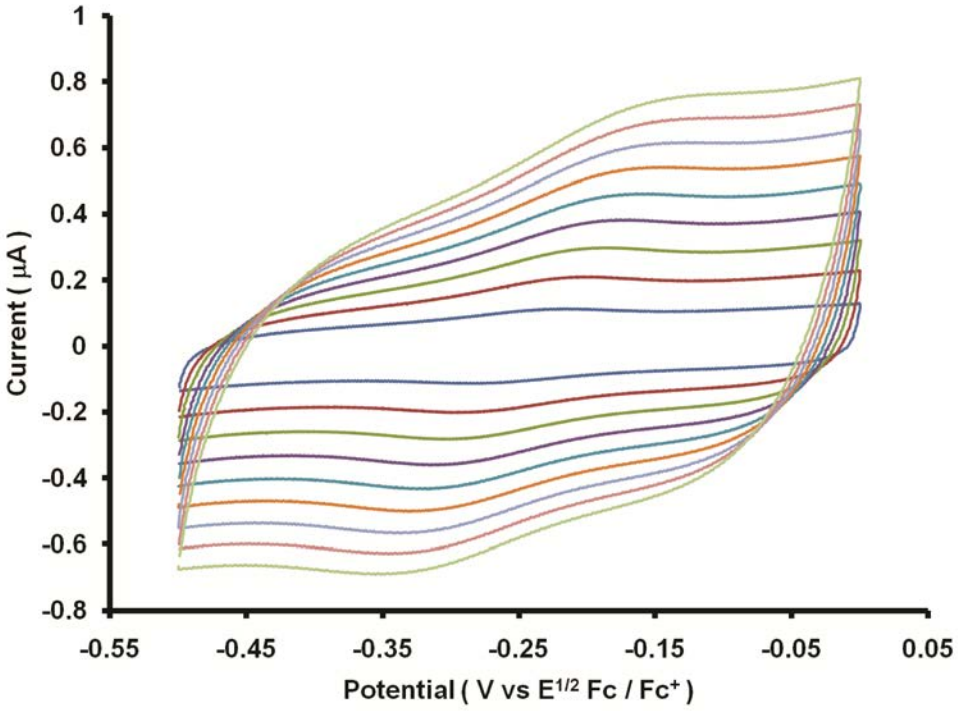

Figure A1.24. Plot of potential sweep rate vs. peak current for 0.5 μM **2·3PF$_6$** on graphene.

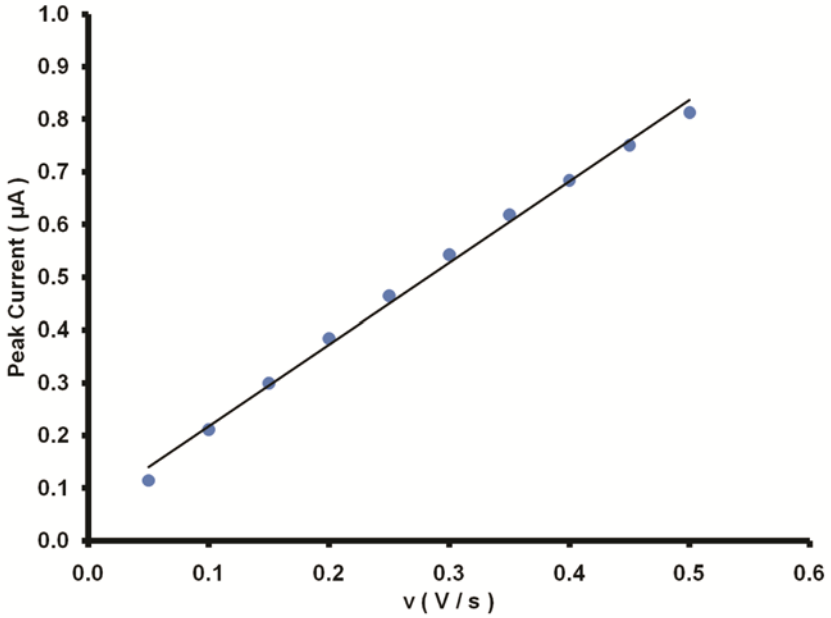

Figure A1.25. Langmuir binding isotherms for **2·3PF$_6$** (red) and **1·2PF$_6$** (blue) on graphene. The increase in coverage above 2.5 μM for **1·2PF$_6$** corresponds to multilayer coverage. Coverages in excess of a monolayer are not kinetically stable and drop to monolayer coverage upon rinsing the graphene surface with small amounts of blank electrolyte solution.

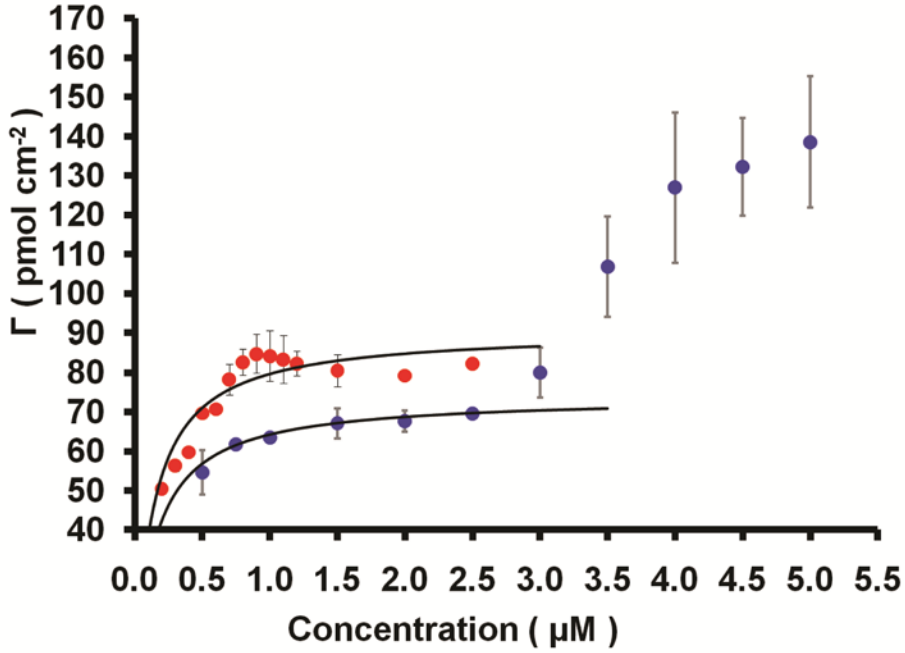

Figure A1.26. Plot of potential sweep rate vs. peak current for 1.0 μM **1·2PF$_6$** on graphene (constructed using the CV in Figure 2A).

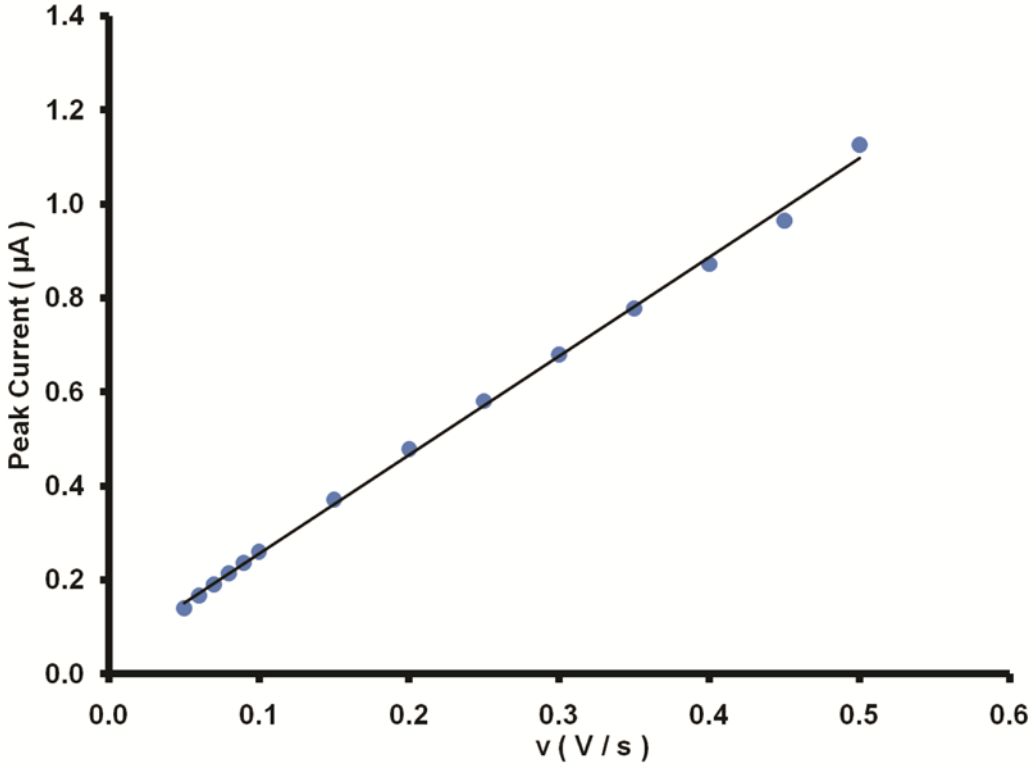

Kinetic analysis of cyclic voltammograms for 1·2PF$_6$ and 2·3PF$_6$. We evaluated the interfacial electron transfer kinetics between the $Co(tpy)_2$ redox couple and the graphene electrode using the criteria defined by Laviron.[3] Plots of E_p vs. $\log_{10}$ (ν) for **1·2PF$_6$** and **2·3PF$_6$** illustrate the difference in their kinetics qualitatively (Figure 2B). We calculated k^o for each compound by fitting the plot of the difference in peak current potentials of the anodic and cathodic scans (ΔE_p) against m^{-1} ($m = RTk^o(nF\nu)^{-1}$, where R is the universal gas constant, T is the temperature and *F* is Faraday's constant) to Laviron's master curve. For **1·2PF$_6$** (Figure S25), the fit is good and corresponds to $k^o = 13.5\ s^{-1}$ and $\alpha = 0.5$. However, the fit for **2·3PF$_6$** is not ideal. This non-ideal fit complicates the calculation of k^o, but we estimate $k^o \approx 18\ s^{-1}$ by assuming $\alpha = 0.5$ (Figure S26). It is possible that discrepancies in the rates of electron transfer between redox centers bearing tripodal and monopodal motifs arise from varying rates of electron tunneling induced by different distances between the redox center and the graphene electrode, or because of slight differences in their structure. Furthermore, discrepancies in fitting of **2·3PF$_6$** to Laviron's model might arise from phenomena outside of its scope. For example, the relatively fast desorption rate of **2·3PF$_6$** may give rise to dynamic processes (e.g. rotation in the vicinity of the electrode), and estimates of k^0 will reflect the distribution of distances of the redox center to the electrode.

Figure A1.27. Plot of the peak to peak separation of the anodic and cathodic peaks in the CV shown in Figure 2.2A versus the inverse of the kinetic parameter *m*. The fit to the Laviron master curve (black) for **1·2PF$_6$** used k^0= 13.5 s^{-1} as parameter to adjust the horizontal axis.

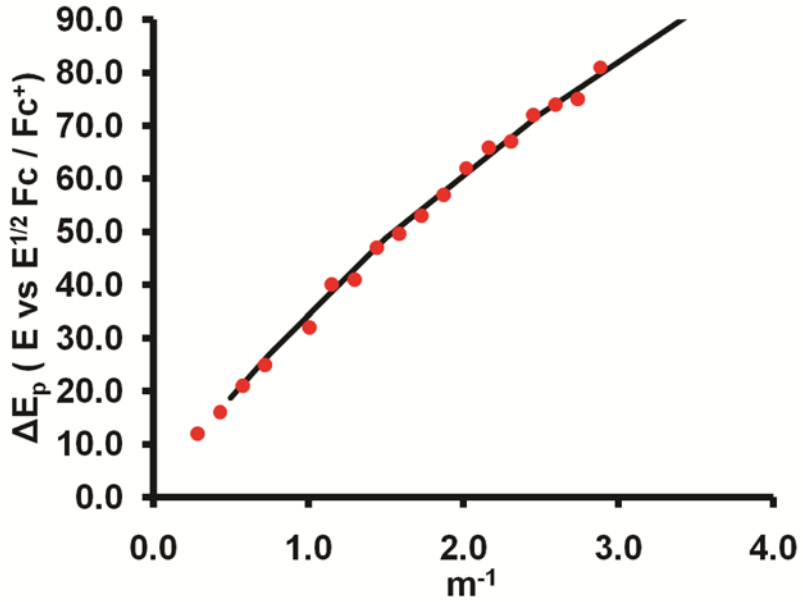

Figure A1.28. Plot of the peak to peak separation for the anodic and cathodic peaks in the CV shown in Figure A1.21 versus the inverse of the kinetic parameter *m*. The fit to the Laviron master curve (black) for **2·3PF$_6$** used k^0= 18 s^{-1} as parameter to adjust the horizontal axis.

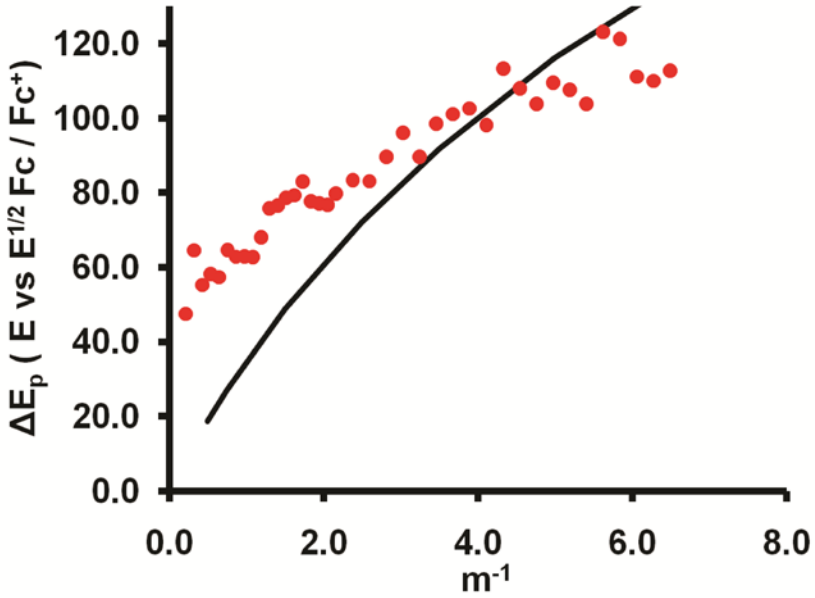

CV Simulations. We compared the experimental curves shown in Figure 2A to simulations to further evaluate the voltammetric behavior of **1·2PF$_6$**. We compared the experimental CVs to simulated *I-E* curves for Langmuirian conditions as a function of α, *m* and the overpotential η. Figures A2.27 and A2.28 show the experimental and simulated CVs for the lowest and highest scan rates shown in Figure 2.2A in the main text, ν = 0.1 V/s and 1 V/s, respectively. A constant capacitive contribution was added to match the experimental background current adequately, and we assumed that α = 0.5. The simulations, using the value of k^0 found in Figure A1.27B, reproduce the peak-to-peak separation at both scan rates and demonstrate that the shapes of the surface waves for both the oxidation and reduction of **1·2PF$_6$** conform to a Langmuir model. The presence of lateral interactions in the adsorbed species would distort the bell-shaped CV wave, but such distortions are nearly absent from the experimental data.

Figure A1.29. Experimental (red) and simulated (blue) CV for **1·2PF$_6$** at 0.1 V s^{-1}.

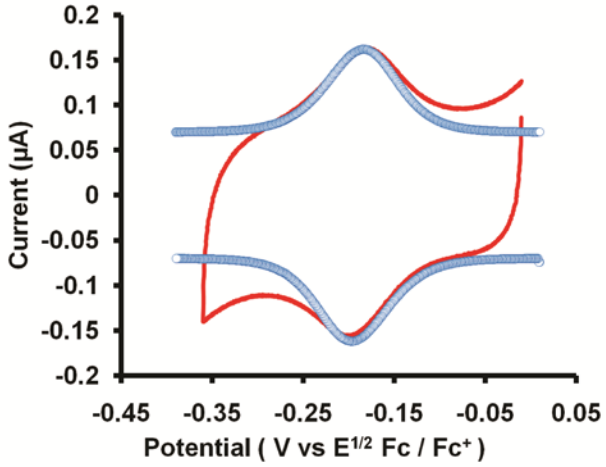

Figure A1.30. Experimental (red) and simulated (blue) CV for **1·2PF$_6$** at 1.0 V s^{-1}.

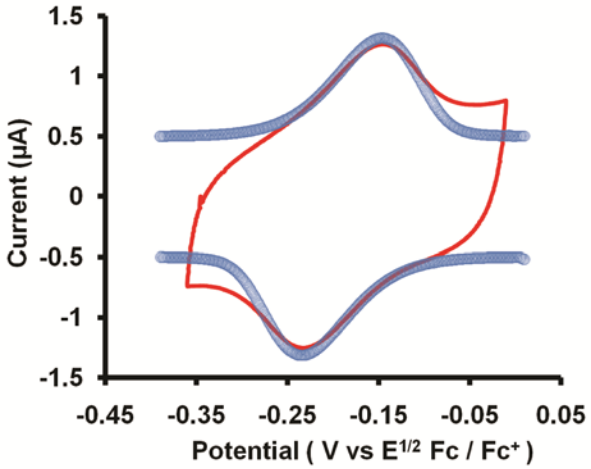

E. Atomic Force Microscopy

Figure A1.31. AFM of as transferred single layer graphene on silicon.

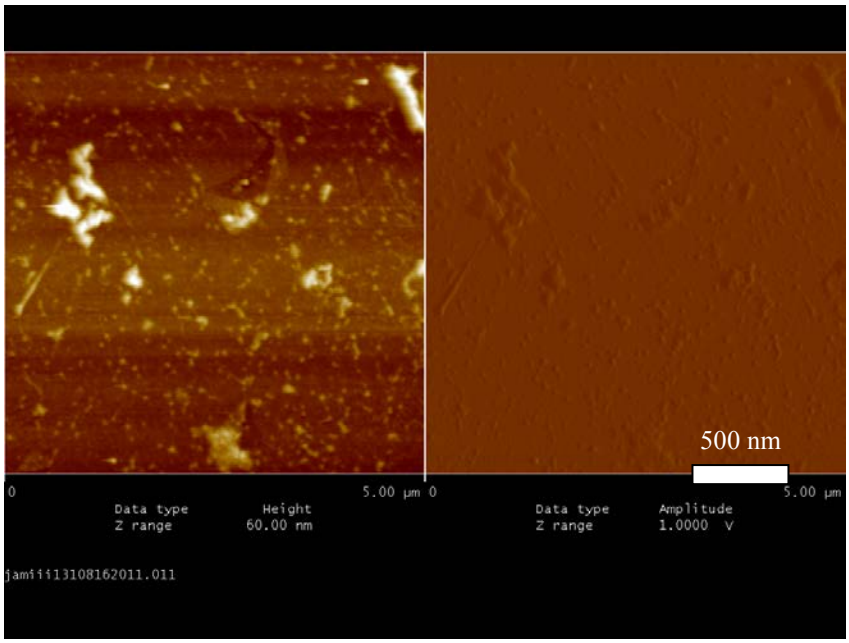

Figure A1.32. AFM of graphene functionalized with 2.5 µM **1**·**2PF$_6$**.

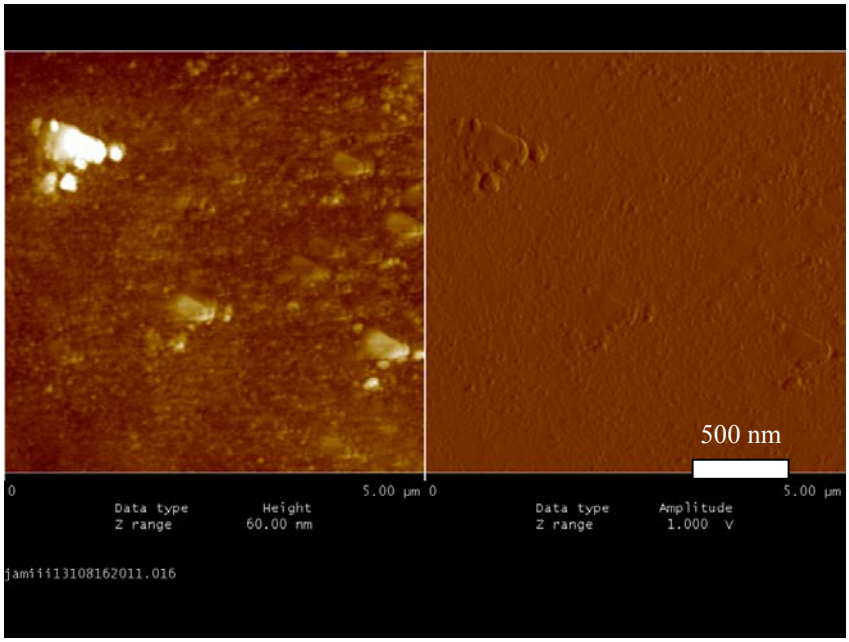

F. References

(1) (a) Wang, J.; Hanan, G. S. *Synlett* **2005**, *2005*, 1251; (b) Glass, T. E. *J. Am. Chem. Soc.* **2000**, *122*, 4522.
(2) Levendorf, M. P.; Ruiz-Vargas, C. S.; Garg, S.; Park, J. *Nano Lett.* **2009**, *9*, 4479.
(3) Laviron, E. *J. Electroanal. Chem.* **1979**, *101*, 19.

G. Complete references from chapter body

(28b) Yu, Q.; Jauregui, L. A.; Wu, W.; Colby, R.; Tian, J.; Su, Z.; Cao, H.; Liu, Z.; Pandey, D.; Wei, D.; Chung, T. F.; Peng, P.; Guisinger, N. P.; Stach, E. A.; Bao, J.; Pei, S.-S.; Chen, Y. P. *Nature Mater.* **2011**, *10*, 443.

CHAPTER THREE

IMPROVING THE BINDING CHARACTERISTICS OF TRIPODAL COMPOUNDS ON SINGLE LAYER GRAPHENE

3.1 Abstract

Graphene is an atomically thin, transparent, and conductive material of interest as an electrode in sensors, and energy conversion and storage devices, among others. Fully realizing its potential will require robust and general methods to anchor active functionality onto its pristine basal plane. Such strategies should not involve covalent bonding, which disrupts the graphene's π-electron system, from which most of its desirable properties arise. Polycyclic aromatic hydrocarbons interact with graphene through Van der Waals interactions, and we recently introduced a tripodal binding motif that forms robust monolayers that prevent protein denaturation on the graphene surface. Here we establish structure-property relationships for tripod binding groups across a series of tripods with different sized anchors. All members of the series adsorb strongly (ΔG_{ads} *ca.* -39 kJ mol^{-1}) to graphene's basal plane, but show kinetic stabilities that vary over two orders of magnitude and monolayer densities that vary by a factor of two. This study identifies phenanthrene anchors as superior to pyrene anchors on the basis of its increased monolayer density and similar kinetic stability. We also demonstrate that varying the length of the methylene linkers between the feet and tripodal core does not affect binding substantially. These results represent the first demonstration of structure-property relationships in the assembly of molecular adsorbates on graphene and provide a general framework for designing and evaluating future binding motifs.

3.2 Introduction

Graphene offeres a combination of useful properties found in no other single material, which has attracted intense research interest since the isolation of single-layer samples by mechanical exfoliation in 2004.[1] Single and few-layer graphene exhibit exceptional conductivity,[2] high strength and flexibility,[3] optical transparency,[4] and impermeability to atomic and molecular species.[5] Recent advances in graphene production, most notably using chemical vapor deposition (CVD) techniques, provide high quality,[6] large-area[7] samples that are readily transferred to arbitrary substrates.[8] SLG's increased availability and exceptional properties have inspired the development of general methods to interface molecular[9] and polymeric[10] species to its basal plane. These strategies are in their infancy relative to the established self-assembled monolayer chemistries available for metallic (such as gold, silver, and platinum),[11] metal oxide (e.g. indium-doped tin oxide),[12] and silicon electrodes.[13] Such covalent functionalization of graphene has been achieved using diazonium reagents,[14] but these reactions occur preferentially at edges and defect sites,[15] and degrade graphene's desirable properties at high functionalization densities.[16] Noncovalent functionalization avoids these undesirable features, which has motivated our efforts to design compounds that form predictable and robust self assembled monolayers on SLG.

In Chapter 2, we introduced a tripodal graphene binding motif that presents three pyrene "feet" to bind multivalently to the SLG surface.[17] Monolayers of these tripods form on SLG from dilute (μM) solutions and are 10^3 times more kinetically stable than those of comparable monovalent binding groups. Because they are interfaced to SLG noncovalently, the tripods are free to diffuse over the graphene basal plane, which was characterized using scanning electrochemical microscopy, as described in Chapter 4 of this dissertation.[18] In

addition, tripod monolayers capable of protein bioconjugation serve as effective anchors that preserve the function of attached antibodies[19] and lectin proteins (for additional details see Chapters 5 and 6).[20] In contrast, these proteins denature and lose their molecular recognition functions when adsorbed onto bare SLG or SLG functionalized with a monolayer of a monovalent pyrene anchors. The above findings have now led us to improve the tripod binding characteristics by exploring the influence of different binding groups on their molecular packing density and monolayer stability.

Here we show that tripods bearing phenanthrene and naphthalene "feet" form monolayers with higher molecular density than the pyrene tripod, consistent with their smaller binding groups. However, their monolayers show attenuated resistance to desorption under infinite dilution conditions. For example, naphthalene tripods form monolayers with 1.54 times higher density than pyrene tripods, but desorb 2.5 orders of magnitude more rapidly. This trade-off suggests that naphthalene feet are too small to be of practical use for many applications, although their packing density and stability are both superior to those of single pyrene moieties. In contrast, phenanthrene tripods offer increased molecular density (1.43 times that of pyrene tripods) but desorb only three times as quickly. As such, phenanthrene tripods are likely to be superior binding groups for many applications. Comparisons of the monolayer coverage and stability across the tripod series and for the monovalent pyrene anchor are also consistent with the hypothesis that the tripods adopt an upright conformation on the SLG surface. We also study the effect of shortening the four-carbon linker between the feet and tetrahedral core to a single methylene group. This change might be expected to weaken the tripod-SLG interaction by restricting the ability of all three feet to interact with the surface. However, we observe almost no change in density or monolayer stability between

the two compounds, suggesting that the choice of linker can be selected based on synthetic convenience. This work represents a significant step forward in our understanding of molecular assembly on the graphene basal plane and for the availability of general binding motifs for the noncovalent functionalization of SLG.

3.3 Results and Discussion

In Chapter 2, we discussed the coverage and kinetic stability of the $Co(tpy)_2$-functionalized tripod with pyrene feet **1a•2PF$_6$** and corresponding monovalent complex **2•3PF$_6$**. The phenanthrene and naphthalene tripods **1b•2PF$_6$** and **1c•2PF$_6$**, respectively, derive from a common alkyne precursor **3** (Scheme 3.1). Sonogshira cross-coupling between **3** and terpyridine **4**, followed by demethylation using BBr_3, provides tris(phenol) **5**. Williamson etherification of **5** with the appropriate polycyclic aromatic hydrocarbon (PAH) electrophile followed by formation of the heteroleptic $Co(tpy)_2$ complex, provides the series of tripods **1a-c•2PF$_6$**. The Co^{2+} complexs are paramagnetic, complicating their characterization using NMR spectroscopy, but oxidation to the corresponding Co^{3+} state using $AgPF_6$ provides readily characterized diamagnetic species. We also prepared two ferrocene-containing pyrene tripods with a variable number of methylene spacers (1 or 4) between the PAH feet and the tetrahedral core. Ferrocene was selected as an alternate redox couple because of its rapid electron transfer kinetics, ease of synthesis, and chemical stability. It was incorporated into tripods via intermediate **6**, which serves as a universal tripod precursor to which various feet and active head groups may be attached.

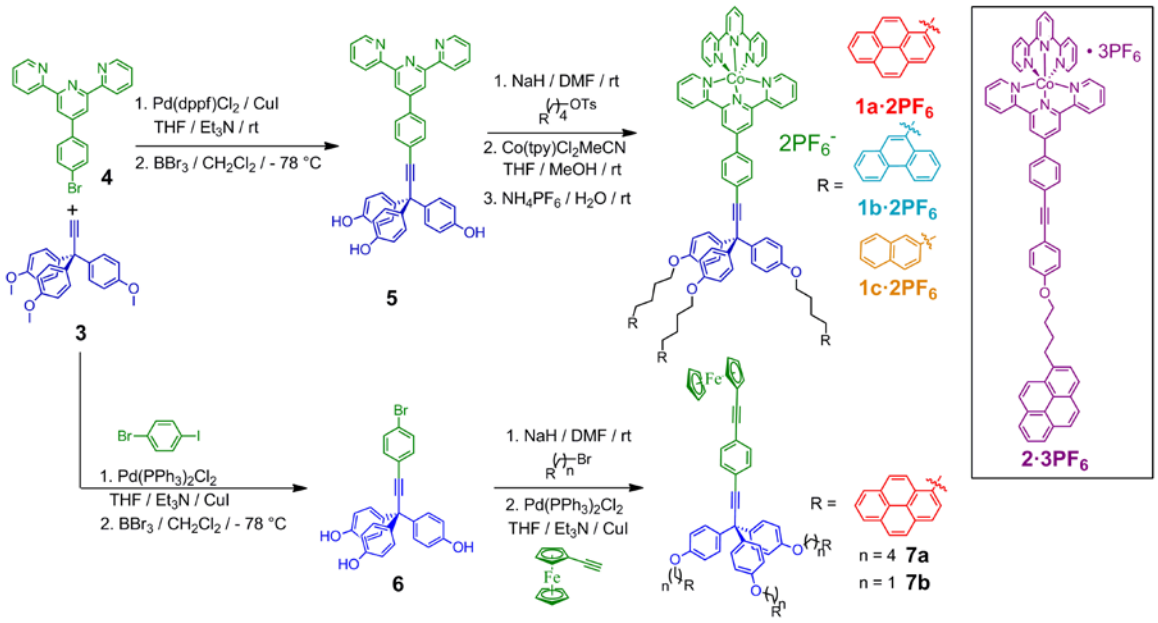

Scheme 3.1. The synthesis of **1a-c·2PF$_6$** and **7a-b**.

Cyclic voltammetry (CV) at SLG working electrodes (0.07 cm^2 active area, see Appendix for fabrication details; THF / 0.1M *n*-Bu$_4$NClO$_4$ supporting electrolyte) of each of the above compounds (**1a-c•PF$_6$**, Appendix Figure A2.35-36; **7a-b**, Figure A2.37-38) showed behavior consistent with electrode-bound redox couples. Compounds **1a-c•PF$_6$** showed quasireversible electron transfer kinetics, with peak separations of their oxidative and reductive waves (ΔE_p) *ca.* 100mV at potential sweep rates of 0.1V s^{-1}. Ferrocene compounds **7a-b** showed electrochemical reversibility, over the full range of scan rates examined (up to 0.5 V s^{-1}), as indicated by their ΔE_p of 0-60 mV (we attribute the variation of ΔE_p to variations in graphene electrode conductivity).[21] All five complexes showed complete chemical reversibility as indicated by consistent peak shape and height over many voltammetric cycles. The charge passed during oxidation and reduction is directly proportional to the monolayer density through the equation $\Gamma = Q(nFA)^{-1}$, in which Γ is the coverage, n is the number of electrons transferred, Q is the charge passed, F is the Faraday constant, and A is the

electroactive area of the working electrode. We used CV to construct adsorption isotherms by determining the surface coverage as a function of the solution concentration of compounds **1a-c·2PF$_6$**. The isotherms were fit to the Langmuir model using the equation $\Gamma = \Gamma_s K_c(K_c + 1)^{-1}$, allowing extraction of the monolayer saturation coverage (Γ_s) and energy of adsorption (ΔG_{ads}, Figure 3.1A). Each of the binding groups exhibits a favorable ΔG_{ads} of *ca.* -39 kJ mol^{-1} (see Appendix Table A3.1), which is relatively strong for noncovalently bound species.

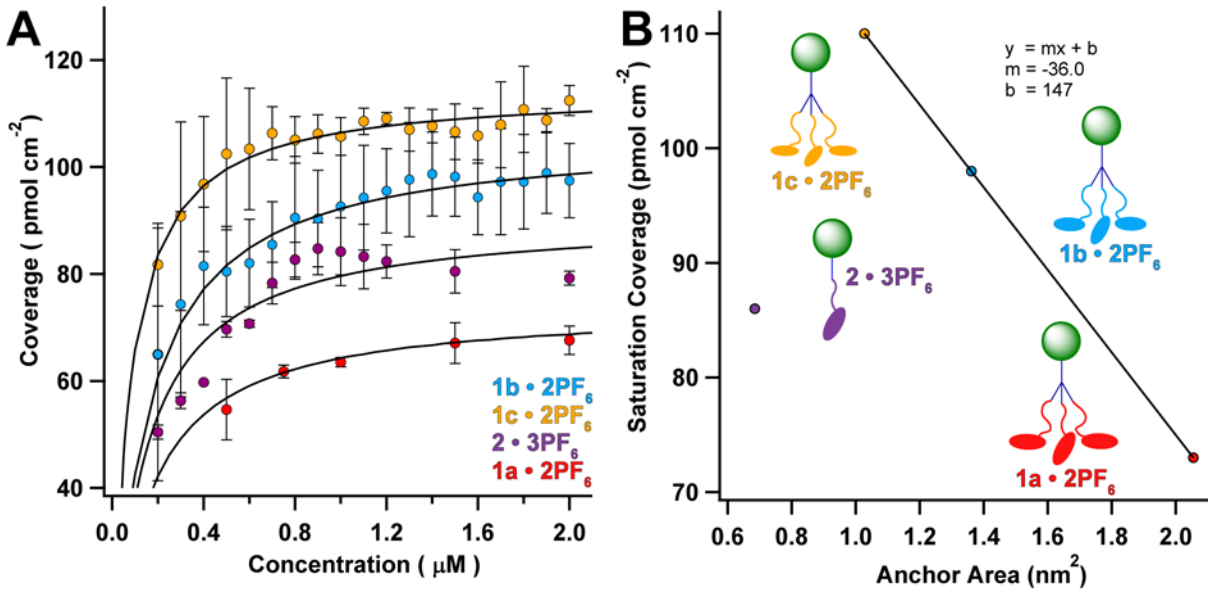

Figure 3.1. (A) Binding isotherms calculated from CV measurements of the coverage of **1a-c·2PF$_6$** at varying solution concentrations. (B) Plot of saturation coverage vs total anchor area, showing significant deviation from the expected value of a dense monolayer for **2•3PF$_6$**.

The pyrene tripod reaches saturation at Γ_s = 74 pmol cm^{-2}, corresponding to a footprint of 2.3 nm^2 (Figure 3.1A). Decreasing the anchor size by one aromatic ring to phenanthrene results in a substantially higher saturation coverage for **1b•2PF$_6$** of Γ_s = 106 ± 6 pmol cm^{-2}, corresponding to a molecular footprint of 1.6 nm^2. The naphthalene anchored tripod **1c•2PF$_6$** follows the same trend with Γ_s = 114 ± 3 pmol cm^{-2}, corresponding to a molecular footprint of 1.5 nm^2. The pyrene monopod **2•3PF$_6$** reaches lower coverage than either **1b•2PF$_6$** or **1c•2PF$_6$**

($\Gamma_s = 90.7 \pm 0.6$ pmol cm^{-2}), corresponding to a molecular footprint of 1.7 nm^2. The saturation coverages of the three tripod complexes scale linearly with the combined Connolly surface areas of their three feet, while the monolayers of **2•3PF$_6$** show lower than expected coverage based on the size of a single pyrene moiety (≈ 0.7 nm^2). This observation is consistent with our hypothesis that tripods adopt upright configurations, whereas molecules bearing a single pyrene are likely to lie flat to maximize their Van der Waals contact to the surface. This conclusion is further supported by our previous comparison of electron transfer rate constants between SLG and **1a•2PF$_6$** and **2•3PF$_6$**, respectively.[17] Although the pyrene monopod achieves moderately higher coverage than the pyrene tripod, its coverage is lower than the tripods anchored by smaller PAHs, which show saturation coverages consistent with dense monolayers (Figure 3.1B). These findings demonstrate that the multivalent tripod design is more effective than monovalent binding groups for organizing dense functionality on the SLG surface.

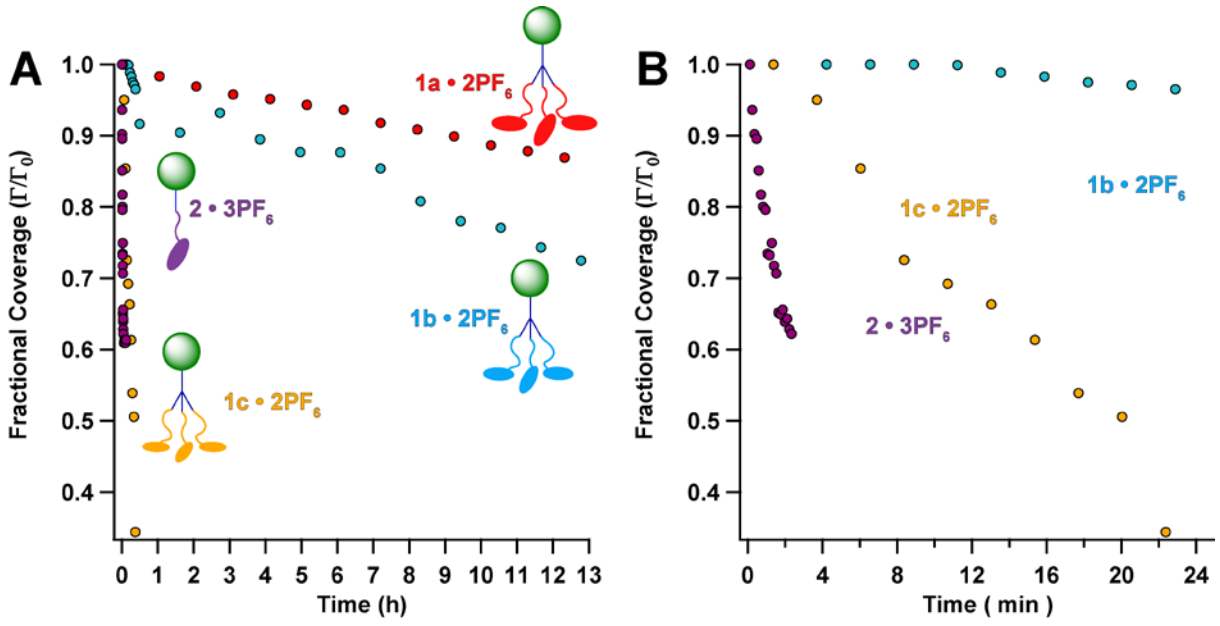

Figure 3.2. (A) Plot of fractional coverage vs time at for monolayers of **1a-c·2PF$_6$** and **2•3PF$_6$** after transfer to blank electrolyte. (B) Expanded view of the first 25 miuntes of desorption.

The stability of the monolayers of each complex shows a strong dependence on the nature of their binding groups. Differences in desorption rates were assessed by functionalizing SLG working electrodes with a monolayer of each complex, which was removed from the adsorbate solution and rinsed with fresh solvent to remove weakly bound molecules. Upon refilling the electrochemical cell with blank electrolyte solution, molecular desorption was quantified by performing periodic CVs for up to twelve hours (Figure 3.2).

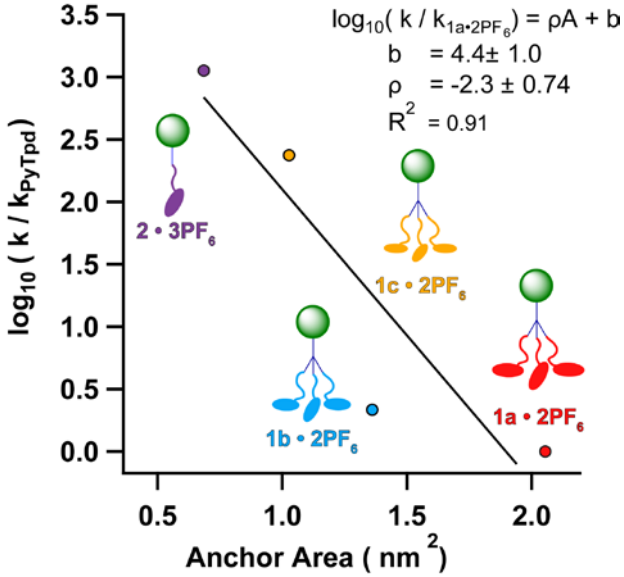

Figure 3.3. Plot of desorption rate ratio vs total anchor area for **1a-c·2PF$_6$** and **2•3PF$_6$**, showing linear free energy relationship consistent with Van der Waals adsorption.

Figure 3.2A and 3.2B show the resulting desorption curves for **1a-c·2PF$_6$** and the monopodal model compound **2·3PF$_6$** over the full time range and the first 25 min, respectively. The pyrene tripod **1a•2PF$_6$** is exceptionally stable, as it retains 86% of its initial coverage after 12 h, corresponding with desorption rate constant k = 3.5 x 10^{-6} s^{-1}. The phenanthrene tripod **1b•2PF$_6$** desorbs approximately twice as fast (k = 7.0 x 10^{-6} s^{-1}), the naphthalene tripod **1c•2PF$_6$** desorbs approximately 200 times more rapidly (k = 6.2 x10^{-4} s^{-1}), and the monovalent compound **2•3PF$_6$** desorbs 1000 times faster (k = 1.4 x 10^{-3} s^{-1}). The

differences in desorption rates exhibit a linear free energy relationship with the surface area of the binding group (Figure 3.3), suggesting that the stability of future PAH-based binding motifs can be predicted from their Van der Waals surface areas. In this way, the tripod design offers a means to achieve high surface-area contacts needed for stable monolayers without the resorting to giant PAHs, which generally show poor solubility and can be difficult to prepare. Finally, it should be noted that these desorption rates correspond to infinite dilution conditions in good solvents for the binding groups. We anticipate that desorption will be slower in poor solvents for the tripod, possibly mitigating the trade-off between monolayer density and stability for tripods with smaller feet.

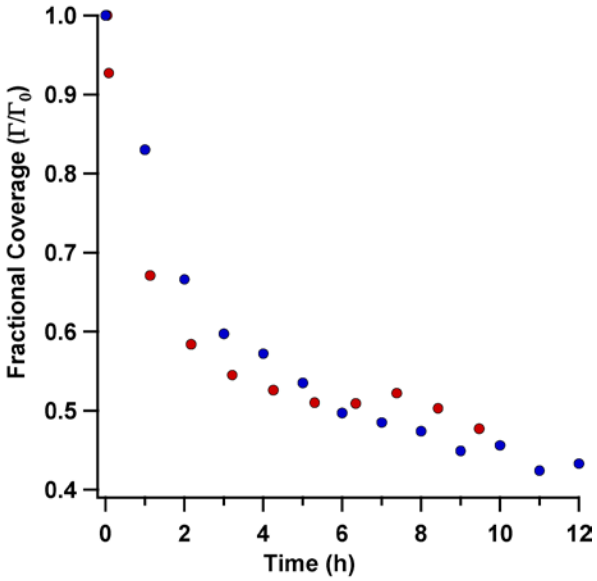

Figure 3.4. Plot of fractional coverage vs time at for monolayers of **7a** (blue) and **7b** (red) after transfer to blank electrolyte (0.1M Bu_4NClO_4 in THF).

We also evaluated the effect of shortening the methylene chains linking the feet to the tetrahedral core on the monolayer coverage and stability to desorption. Ferrocene pyrene tripods **7a** and **7b** both showed saturation coverages of *ca.* 66 pmol cm^{-2}, almost identical to those of $Co(tpy)_2$ pyrene tripod **1a•2PF$_6$**. These coverages indicate that the anchor size, not

the identity of the pendant redox couple, largely determines the molecular footprint and that the single methylene spacer does not affect monolayer density significantly. **7a** and **7b** desorb from SLG with rate constants of 1.1 x 10^{-4} s^{-1} and 2.5 x 10^{-4} s^{-1}, respectively (Figure 3.4). Again, these similar values reflect a tolerance of the shorter linker, and we conclude that the choice of linker length between 1-4 methylenes (and perhaps longer) may be guided by synthetic convenience. It should be noted that both ferrocene tripods desorb more rapidly than **1a•2PF$_6$**, which we attribute to the higher solubility (and therefore, more favorable solvent-solute interactions) of the ferrocene complexes. These results indicate that monolayer stability is not completely independent of the head group, such that larger feet might need to be employed to enhance monolayer stability as demanded by specific application constraints.

3.4 Conclusions

We have shown that tripodal motifs bearing various aromatic anchors form kinetically and chemically stable monolayers from micromolar concentration solutions in organic solvents. The tripodal motif anchors functionality on graphene more efficiently than similar monopodal anchors by forming densely packed monolayers that resist desorption effectively. By preparing and analyzing a series of tripods with different anchor sizes, we demonstrated a linear free energy relationship between anchor area and desorption rate, as well as a linear dependence of packing density with anchor size. In this way, the tripodal design provides a means to access high surface-area contacts needed for stable monolayers. Furthermore, modulation of the core-anchor linker and the redox active moiety, indicated that the binding characteristics are governed primarily, but not exclusively, by the total area of the anchors. Together these results provide a framework for designing and benchmarking new graphene binding motifs. Ongoing work will focus on utilizing tripodal compounds in SLG based

devices and exploring further modification of the tripod structures to enhance their binding characteristics. These binding groups will provide the foundation for the developing SLG as a useful analytical platform.

3.5 Acknowledgements

We acknowledge financial support from Cornell University, a Sloan Research Fellowship, the Research Corporation for Science Advancement, and the Camille and Henry Dreyfus Foundation. We also acknowledge NSF support through use of the Cornell Nanofabrication Facility/NNIN and the Cornell Center for Materials Research facilities. J.A.M. gratefully acknowledges the Integrative Graduate Education and Research Traineeship (IGERT) Program in the Nanoscale Control of Surfaces and Interfaces which is supported under NSF Award DGE-0654193, the Cornell Center for Materials Research, and Cornell University.

REFERENCES

(1) Novoselov, K. S.; Geim, A. K.; Morozov, S. V.; Jiang, D.; Zhang, Y.; Dubonos, S. V.; Grigorieva, I. V.; Firsov, A. A. *Science* **2004**, *306*, 666.

(2) Chen, J.-H.; Jang, C.; Xiao, S.; Ishigami, M.; Fuhrer, M. S. *Nat. Nanotechnol.* **2008**, *3*, 206.

(3) Lee, C.; Wei, X.; Kysar, J. W.; Hone, J. *Science* **2008**, *321*, 385.

(4) (a) Liu, W.; Jackson, B. L.; Zhu, J.; Miao, C.-Q.; Chung, C.-H.; Park, Y. J.; Sun, K.; Woo, J.; Xie, Y.-H. *ACS Nano* **2010**, *4*, 3927; (b) Jang, S.; Jang, H.; Lee, Y.; Suh, D.; Baik, S.; Hong, B. H.; Ahn, J.-H. *Nanotechnology* **2010**, *21*, 425201/1; (c) Nair, R. R.; Blake, P.; Grigorenko, A. N.; Novoselov, K. S.; Booth, T. J.; Stauber, T.; Peres, N. M. R.; Geim, A. K. *Science* **2008**, *320*, 1308.

(5) (a) Yuk, J. M.; Park, J.; Ercius, P.; Kim, K.; Hellebusch, D. J.; Crommie, M. F.; Lee, J. Y.; Zettl, A.; Alivisatos, A. P. *Science* **2012**, *336*, 61; (b) Mohanty, N.; Fahrenholtz, M.; Nagaraja, A.; Boyle, D.; Berry, V. *Nano Lett.* **2011**, *11*, 1270; (c) Nair, R. R.; Blake, P.; Blake, J. R.; Zan, R.; Anissimova, S.; Bangert, U.; Golovanov, A. P.; Morozov, S. V.; Latychevskaia, T.; Geim, A. K.; Novoselov, K. S. *arXiv.org, e-Print Arch., Condens. Matter* **2010**, 1.

(6) Yan, Z.; Lin, J.; Peng, Z.; Sun, Z.; Zhu, Y.; Li, L.; Xiang, C.; Samuel, E. L.; Kittrell, C.; Tour, J. M. *ACS Nano* **2012**, *6*, 9110.

(7) Bae, S.*et al. Nature Nanotech.* **2010**, *5*, 574.

(8) (a) Chen, S.; Cai, W.; Piner, R. D.; Suk, J. W.; Wu, Y.; Ren, Y.; Kang, J.; Ruoff, R. S. *Nano Lett.* **2011**, *11*, 3519; (b) Mattevi, C.; Kim, H.; Chhowalla, M. *J. Mater. Chem.* **2011**, *21*, 3324; (c) Lee, Y.; Bae, S.; Jang, H.; Jang, S.; Zhu, S.-E.; Sim, S. H.; Song, Y. I.; Hong, B. H.; Ahn, J.-H. *Nano Lett.* **2010**, *10*, 490; (d) Li, X.; Cai, W.; An, J.; Kim, S.; Nah, J.; Yang, D.; Piner, R.; Velamakanni, A.; Jung, I.; Tutuc, E.; Banerjee, S. K.; Colombo, L.; Ruoff, R. S. *Science* **2009**, *324*, 1312; (e) Levendorf, M. P.; Ruiz-Vargas, C. S.; Garg, S.; Park, J. *Nano Lett.* **2009**, *9*, 4479; (f) Reina, A.; Jia, X.; Ho, J.; Nezich, D.; Son, H.; Bulovic, V.; Dresselhaus, M. S.; Kong, J. *Nano Lett.* **2008**, *9*, 30.

(9) (a) Laaksonen, P.; Kainlauri, M.; Laaksonen, T.; Shchepetov, A.; Jiang, H.; Ahopelto, J.; Linder, M. B. *Angew. Chem., Int. Ed.* **2010**, *49*, 4946; (b) Kim, S. N.; Kuang, Z.; Slocik, J. M.; Jones, S. E.; Cui, Y.; Farmer, B. L.; McAlpine, M. C.; Naik, R. R. *J. Am. Chem. Soc.*

2011, null; (c) Mannoor, M. S.; Tao, H.; Clayton, J. D.; Sengupta, A.; Kaplan, D. L.; Naik, R. R.; Verma, N.; Omenetto, F. G.; McAlpine, M. C. *Nat Commun* **2012**, *3*, 763; (d) Wang, X.; Tabakman, S. M.; Dai, H. *J. Am. Chem. Soc.* **2008**, *130*, 8152; (e) Wang, Q. H.; Hersam, M. C. *Nature Chem.* **2009**, *1*, 206; (f) Coletti, C.; Riedl, C.; Lee, D. S.; Krauss, B.; Patthey, L.; von Klitzing, K.; Smet, J. H.; Starke, U. *Phys. Rev. B* **2010**, *81*, 235401; (g) Alaboson, J. M. P.; Wang, Q. H.; Emery, J. D.; Lipson, A. L.; Bedzyk, M. J.; Elam, J. W.; Pellin, M. J.; Hersam, M. C. *ACS Nano* **2011**, *5*, 5223; (h) Cheng, H.-C.; Shiue, R.-J.; Tsai, C.-C.; Wang, W.-H.; Chen, Y.-T. *ACS Nano* **2011**, *5*, 2051; (i) Lee, W. H.; Park, J.; Sim, S. H.; Lim, S.; Kim, K. S.; Hong, B. H.; Cho, K. *J. Am. Chem. Soc.* **2011**, *133*, 4447; (j) Jandhyala, S.; Mordi, G.; Lee, B.; Lee, G.; Floresca, C.; Cha, P. R.; Ahn, J.; Wallace, R. M.; Chabal, Y. J.; Kim, M. J.; Colombo, L.; Cho, K.; Kim, J. *ACS Nano* **2012**, *6*, 2722.

(10) (a) Lee, W. H.; Suk, J. W.; Lee, J.; Hao, Y. F.; Park, J.; Yang, J. W.; Ha, H. W.; Murali, S.; Chou, H.; Akinwande, D.; Kim, K. S.; Ruoff, R. S. *ACS Nano* **2012**, *6*, 1284; (b) Colson, J. W.; Woll, A. R.; Mukherjee, A.; Levendorf, M. P.; Spitler, E. L.; Shields, V. B.; Spencer, M. G.; Park, J.; Dichtel, W. R. *Science* **2011**, *332*, 228; (c) Malig, J.; Jux, N.; Kiessling, D.; Cid, J.-J.; Vázquez, P.; Torres, T.; Guldi, D. M. *Angew. Chem. Int. Ed.* **2011**, *50*, 3561; (d) Sabri, S. S.; Guillemette, J.; Guermoune, A.; Siaj, M.; Szkopek, T. *Appl. Phys. Lett.* **2012**, *100*; (e) Yan, C.; Kim, K. S.; Lee, S. K.; Bae, S. H.; Hong, B. H.; Kim, J. H.; Lee, H. J.; Ahn, J. H. *ACS Nano* **2012**, *6*, 2096.

(11) Love, J. C.; Estroff, L. A.; Kriebel, J. K.; Nuzzo, R. G.; Whitesides, G. M. *Chem. Rev.* **2005**, *105*, 1103.

(12) (a) Hofer, R.; Textor, M.; Spencer, N. D. *Langmuir* **2001**, *17*, 4014; (b) Gao, W.; Dickinson, L.; Grozinger, C.; Morin, F. G.; Reven, L. *Langmuir* **1996**, *12*, 6429; (c) Badia, A.; Lennox, R. B.; Reven, L. *Acc. Chem. Res.* **2000**, *33*, 475.

(13) Ulman, A. *Chem. Rev.* **1996**, *96*, 1533.

(14) (a) Georgakilas, V.; Otyepka, M.; Bourlinos, A. B.; Chandra, V.; Kim, N.; Kemp, K. C.; Hobza, P.; Zboril, R.; Kim, K. S. *Chem. Rev.* **2012**, *112*, 6156; (b) Hirsch, A.; Englert, J. M.; Hauke, F. *Acc. Chem. Res.* **2013**, *46*, 87; (c) Johns, J. E.; Hersam, M. C. *Acc. Chem. Res.* **2013**, *46*, 77; (d) Park, J.; Yan, M. D. *Acc. Chem. Res.* **2013**, *46*, 181; (e) Paulus, G. L. C.; Wang, Q. H.; Strano, M. S. *Acc. Chem. Res.* **2013**, *46*, 160.

(15) (a) Sun, Z.; Kohama, S.-i.; Zhang, Z.; Lomeda, J.; Tour, J. *Nano Res.* **2010**, *3*, 117; (b) Lim, H.; Lee, J. S.; Shin, H.-J.; Shin, H. S.; Choi, H. C. *Langmuir* **2010**, *26*, 12278.

(16) (a) Yu, D. S.; Kuila, T.; Kim, N. H.; Khanra, P.; Lee, J. H. *Carbon* **2013**, *54*, 310; (b) Guryel, S.; Hajgato, B.; Dauphin, Y.; Blairon, J. M.; Miltner, H. E.; De Proft, F.; Geerlings, P.; Van Lier, G. *Phys. Chem. Chem. Phys.* **2013**, *15*, 659; (c) Bissett, M. A.; Tsuji, M.; Ago, H. *J. Phys. Chem. C* **2013**, *117*, 3152.

(17) Mann, J. A.; Rodríguez-López, J.; Abruña, H. D.; Dichtel, W. R. *J. Am. Chem. Soc.* **2011**, *133*, 17614.

(18) Rodríguez-López, J.; Ritzert, N. L.; Mann, J. A.; Tan, C.; Dichtel, W. R.; Abruña, H. D. *J. Am. Chem. Soc.* **2012**, *134*, 6224.

(19) Mann, J. A.; Alava, T.; Craighead, H. G.; Dichtel, W. R. *Angew. Chem. Int. Ed.* **2013**, *52*, 3177.

(20) Alava, T.; Mann, J. A.; Théodore, C.; Benitez, J. J.; Dichtel, W. R.; Parpia, J. M.; Craighead, H. G. *Anal. Chem.* **2013**, *85*, 2754.

(21) (a) Keil, R. G. *J. Electrochem. Soc.* **1986**, *133*, 1375; (b) García-Jareño, J. J.; Navarro-Laboulais, J.; Vicente, F. *Electrochim. Acta* **1997**, *42*, 1473.

APPENDIX TWO

Table of Contents

A. Materials. Unless otherwise noted, reagents were purchased from commercial suppliers and used without further purification. 4'-(4-bromophenyl)-2,2':6',2"-terpyridine **4,** 4,4',4"-(prop-2-yne-1,1,1-triyl)tris(methoxybenzene) **3**, terpyridyl triol **5**, monopodal compound **2**, and **1a·2PF$_6$** were prepared using a literature procedure.[21] EtOAc, hexanes, and EtOH (absolute) were purchased from commercial sources and used without further purification. THF, CH_2Cl_2, DMF, and PhMe were purchased from commercial sources and purified using a custom-built activated alumina-based solvent purification system. Graphene electrodes were fabricated by transferring graphene derived from a chemical vapor deposition (CVD) procedure onto SiO_2/Si wafers.[8e] Contacts were formed to the graphene electrodes by pressing stranded hook-up wire (26G Alpha Wire, part # A1853W-100-ND) into a small amount of indium metal which had been pressed onto the graphene surface. Pt wire (20 Gauge - 99.9 % pure) was cleaned in a propane flame before each use. Glassware for electrochemistry was cleaned in a Nochromix™ / H_2SO_4 bath for 12 h, washed with H_2O (HPLC grade), dried in an oven at 150 ^oC for 3 h, and finally cooled in a dessicated chamber under dynamic vacuum.

Instrumentation. Infrared spectra of solid samples were recorded using a Thermo Nicolet iS10 FT-IR spectrometer with a diamond ATR attachment and are uncorrected.

Mass spectra were obtained on a Waters MALDI micro MX MALDI-TOF mass spectrometer using positive ionization in reflectron mode. A saturated solution of dithranol in CH_2Cl_2 was used as the matrix.

NMR spectra were recorded on a Varian INOVA 400 MHz spectrometer using a ^1H/X Z-PFG probe, a Bruker ARX 300 MHz spectrometer using a BBO probe, a Varian INOVA 500MHz spectrometer using a standard $^1H\{^{13}C, ^{15}N\}$ Z-PFG probe, or a Varian INOVA 600 MHz spectrometer using a standard $^1H\{^{13}C, ^{15}N\}$ XYZ-PFG probe with a 20 Hz sample spin rate.

Electrochemistry experiments were performed on a Princeton Applied Research VersaSTAT 3 potentiostat using a standard three electrode configuration with graphene as the working-sense electrode, a Pt wire as the counter, and a Pt wire pseudoreference. The analyses were performed in a custom made Teflon cell (Figure A2.1) that allowed exposure of a controlled area of the graphene electrode (Figure A2.2) (total area *ca.* 2 cm^2, exposed area *ca*. 0.07 cm^2).

B. Synthetic Procedures.

Scheme A2.1. Overall synthesis of the terpyridyl-functionalized graphene binding motif **S7-8**.

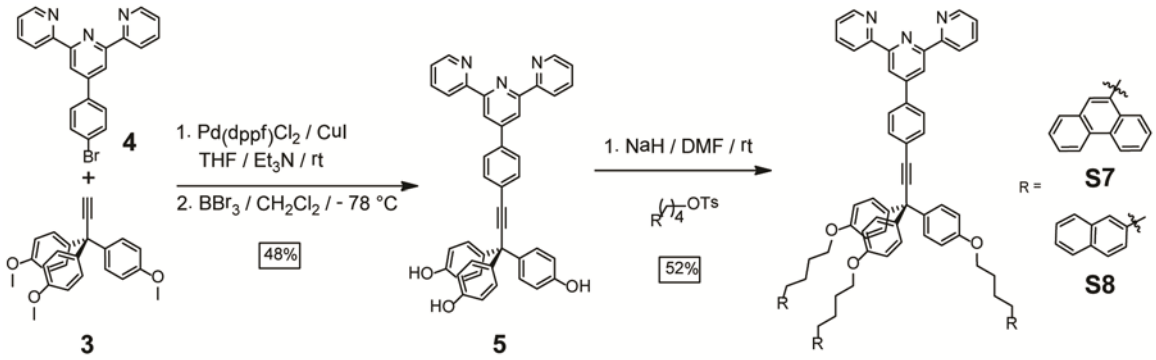

Scheme A2.2. Synthesis of phenanthrene butynol **S1**.

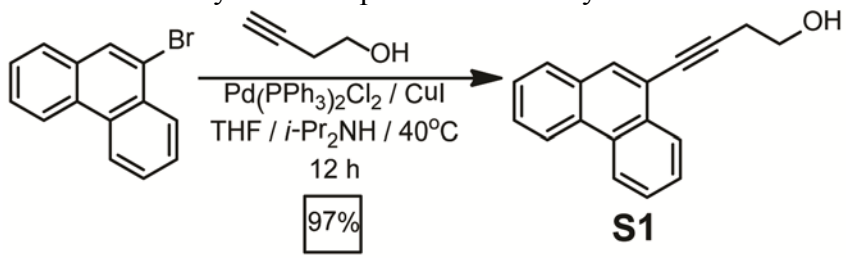

Preparation of phenanthrene butynol S1.

A 250 mL flame dried round bottom flask with stir bar was charged with 9-bromophenanthrene (2.0 g, 7.778 mmol), $Pd(PPh_3)_2Cl_2$ (0.546 mg, 0.778 mmol), CuI (299 mg, 1.556 mmol). The flask was then sealed with a rubber septum and subjected to three cycles of atmosphere replacement with dry nitrogen. To the solids 48 mL of dry THF, 20 mL of freshly distilled *i*-Pr_2NH, and 1.8 mL of 3-butyne-1-ol (1.64 g, 23.33 mmol), all of which were degassed by bubbling with dry nitrogen for 30 min. The mixture was then heated to 40°C for three hours at which time TLC showed complete reaction (SiO_2, 20% EtOAc and 80% hexanes as eluent, R_f=0.2). Reaction was filtered through celite, diluted with EtOAc (100 mL) and washed with H_2O (2 x 50 mL), dried ($MgSO_4$), and the solvent removed under vacuum to give a brown oil. The oil was purified by column chromatography (SiO_2, 20% EtOAc / 80% hexanes) to provide **S1** (1.862 g, 97% yield) as a white solid. ^{1}H NMR (400 MHz, $CDCl_3$) δ 8.72 – 8.66 (m, *4-phenanthrene*, 1H), 8.65 (d, *7-phenanthrene*, J = 8.1 Hz, 1H), 8.48 – 8.38 (m, *5-phenanthrene*, 1H), 7.97 (s, *10-phenanthrene*, 1H), 7.84 (d, *8-phenanthrene*, J = 8.1 Hz, 1H), 7.54 – 7.33(m, *2,3,6,7-naphthalene*, 4H), 3.95 (t, *3-butynyl*, J = 6.3 Hz, 2H), 2.89 (t, *4-butynyl*, J = 6.3 Hz, 2H. ^{13}C NMR (75 MHz, $CDCl_3$) δ 132.14, 131.70, 131.61, 130.51, 130.47, 128.81, 127.71, 127.41, 127.32, 127.26, 123.17, 122.99, 120.10, 91.46, 81.04, 61.76, 24.59. IR (ATR) 3353, 3054, 2938, 1592, 1491, 1450, 1421, 1380, 1332, 1245, 1226, 1163, 1150, 1122, 1093, 1040, 1001, 970, 951, 923 cm^{-1}. EI-MS m/z Calcd. m/z 246.10411 $[M]^+$. Found m/z 246.10447 $[M]^+$.

Scheme A2.3. Synthesis of phenanthrene butanol **S2**.

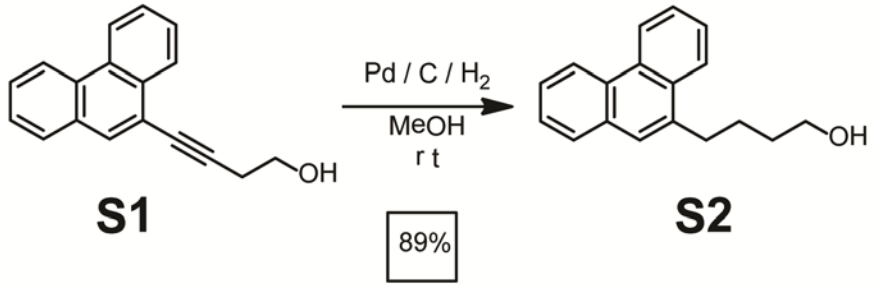

Preparation of phenanthrene butanol S2.

A 250 mL round bottom flask with stir bar and three-way airfree adapter was charged with **S1** (1.69 g, 6.86 mmol) and 0.735 g of 5% Pd on carbon. The flask was cooled on dry ice and MeOH (70 mL) was added. The mixture was then frozen with liquid N_2, the flask evacuated and backfilled with H_2 and the mixture allowed to thaw. The reaction was stirred vigorously for 12 hrs, filtered through celite and concentrated under vacuum to provide **S2** (1.53 g, 89% yield) as a white solid. **S2**:^{1}H NMR (300 MHz, $CDCl_3$) δ 8.80 – 8.70 (m, *4-phenanthrene*, 1H), 8.70 – 8.61 (m, *5-phenanthrene*, 1H), 8.17 – 8.05 (m, *1-phenanthrene*, 1H), 7.86 – 7.79 (m, *8-phenanthrene*, 1H), 7.71 – 7.62 (m, *7,6-phenanthrene*, 2H), 7.62 – 7.55 (m, *2,3,10-phenanthrene*, 3H), 3.72 (t, *J* = 6.4 Hz, *1-butyl*, 2H), 3.16 (t, *J* = 7.7 Hz *4-butyl*, 2H), 1.99 – 1.83 (m, *2-butyl*, 2H), 1.83 – 1.67 (m, *3-butyl*, 2H). ^{13}C NMR (75 MHz, $CDCl_3$) δ 136.78, 132.27, 131.61, 131.13, 130.05, 128.44, 127.02, 126.93, 126.54, 126.36, 124.79, 123.65, 122.84, 63.26, 33.55, 33.20, 26.71. IR (ATR) 3352, 3074, 2934, 2867, 1739, 1602, 1495, 1448, 1428, 1365, 1275, 1265, 1261, 1230, 1217, 1058, 1007, 981 cm^{-1}. MALDI-TOF-MS m/z Calcd. m/z 250.1358 $[M]^+$. Found m/z 250.1304 $[M]^+$.

Scheme A2.4. Synthesis of phenanthrene butanol tosylate **S3**.

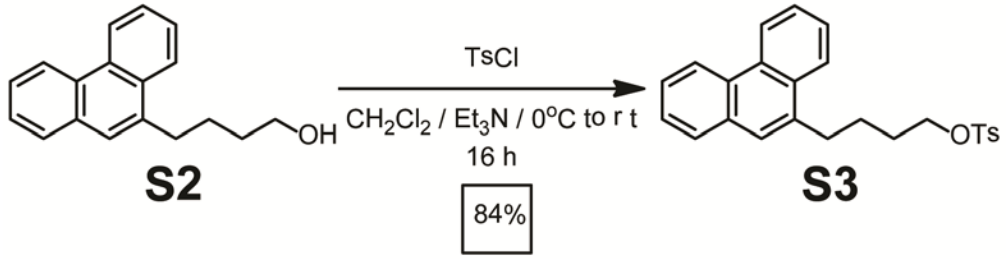

Preparation of phenanthrene butanol tosylate S6.

A 500 mL flame dried round bottom flask with stir bar was charged with **S2** (1.50 g, 6.0 mmol), of anhydrous CH_2Cl_2 (300 mL), and freshly distilled Et_3N (60 mL). The solution was cooled to -10 ^{o}C using a CO_2 (s)/ethylene glycol bath, and p-toluenesulfonyl chloride (2.30 g, 12.1 mmol) was added drop-wise as a solution in anhydrous CH_2Cl_2 (10 mL). The mixture was stirred for 16 hrs under N_2 atmosphere, at which time TLC showed complete reaction (SiO_2, 30% EtOAc and 80% hexanes, R_f=0.25). The reaction mixture was poured into H_2O (50 mL), the organic layer removed and washed with H_2O (3 x 50 mL). The organic layer was then dried ($MgSO_4$) and the solvent removed under vacuum. Purification was accomplished by column chromatography (SiO_2, 30% EtOAc/80% hexanes) to provide **S3** (2.04 g, 84% yield) as an off white solid. **S3**: ^{1}H NMR (300 MHz, $CDCl_3$) δ 8.77 – 8.70 (m, 5-

phenanthrene, 1H), 8.70 – 8.61 (m, *4-phenanthrene*, 1H), 8.10 – 7.96 (m, *1-phenanthrene*, 1H), 7.82 (m, *8-phenanthrene*, 1H), 7.78 (d, *J* = 7.8 Hz, *2-tosyl aryl*, 2H), 7.73 – 7.54 (m, 2,3,6,7-*phenanthrene*, 4H), 7.51 (s, *10-phenanthrene*, 1H), 7.27 (d, *J* = 7.8 Hz, *3-tosyl aryl*, 2H), 4.10 (t, *J* = 5.7 Hz, *1-butyl*, 2H), 3.06 (t, *J* = 6.9 Hz, *4-butyl*, 2H), 2.37 (s, *tosyl methyl*, 3H), 1.89 – 1.72 (m, *2,3-butyl*,4H). ^{13}C NMR (75 MHz, $CDCl_3$) δ 145.15, 136.07, 133.48, 132.17, 131.44, 131.13, 130.25, 130.09, 128.48, 128.28, 127.10, 127.02, 126.66, 126.62, 126.52, 124.67, 123.70, 122.87, 70.82, 32.99, 29.21, 26.22, 22.00. IR (ATR) 3065, 2936, 2868, 1597, 1495, 1449, 1355, 1305, 1291, 1246, 1209, 1188, 1174, 1097, 1039, 1019, 934 cm^{-1}. EI-MS m/z Calcd. m/z 404.14462 $[M]^+$. Found m/z 404.14432 $[M]^+$.

Scheme A2.5. Synthesis of naphthalene butynol **S4**.

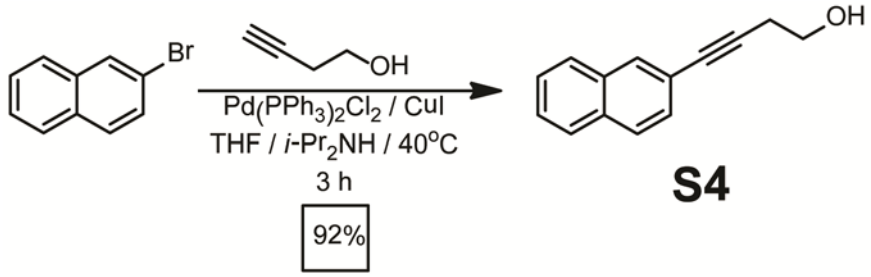

Preparation of naphthalene butynol S4.

A 250 mL flame dried round bottom flask with stir bar was charged with 2-bromonaphthalene (2.0 g, 9.659 mmol), $Pd(PPh_3)_2Cl_2$ (678 mg, 0.966 mmol), CuI (368 mg, 1.932 mmol). The flask was then sealed with a rubber septum and placed under a N_2 atmosphere through three evacuation backfilling cycles. Anhydrous THF (48 mL), freshly distilled *i*-Pr_2NH (20 mL) and 3-butyne-1-ol (2.19 mL, 2.03 g, 28.98 mmol) were added to the reaction vessel. The resulting mixture was degassed by bubbling with N_2 for 30 min. The mixture was then heated to 40 °C for three hours at which time TLC showed complete reaction (SiO_2, 20% EtOAc and 80% hexanes, R_f=0.2). The reaction mixture was filtered through celite, diluted with EtOAc (100 mL) and washed with H_2O (2 x 50 mL), dried ($MgSO_4$), and the solvent removed under vacuum to give a brown oil. The oil was purified by column chromatography (SiO_2, 20% EtOAc / 80% hexanes) to provide **S4** (1.75 g, 92% yield) as a white solid. **S4**: ^{1}H NMR (400 MHz, $CDCl_3$) δ 7.94 (s, *1-naphthalene*, 1H), 7.85 – 7.69 (m, *4,5,8-naphthalene*, *3*H), 7.60 – 7.37 (m, *3,6,7-naphthalene*, 3H), 3.86 (t, *J* = 6.3 Hz, *4*-butynyl, 2H), 2.75 (t, *J* = 6.3 Hz, *2-butynyl*, 2H). ^{13}C NMR (100 MHz, $CDCl_3$) δ 133.45, 133.11, 131.92, 131.85, 131.78, 129.12, 129.05, 128.55, 128.50, 128.45, 128.38, 128.18, 128.09, 128.02, 127.97, 127.07, 126.94, 126.87, 126.82, 126.72, 126.62, 126.41, 121.09, 87.15, 83.32, 61.68, 24.42. IR (ATR) 3285, 3057, 2941, 2880, 1723, 1685, 1626, 1593, 1569, 1558, 1499, 1467, 1430, 1380, 1342, 1290, 1271, 1220, 1184, 1126, 1043, 1019, 963, 950 cm^{-1}.EI-MS m/z Calcd. m/z 196.08882 $[M]^+$. Found m/z 196.08887 $[M]^+$.

Scheme A2.6. Synthesis of naphthalene butanol **S5**.

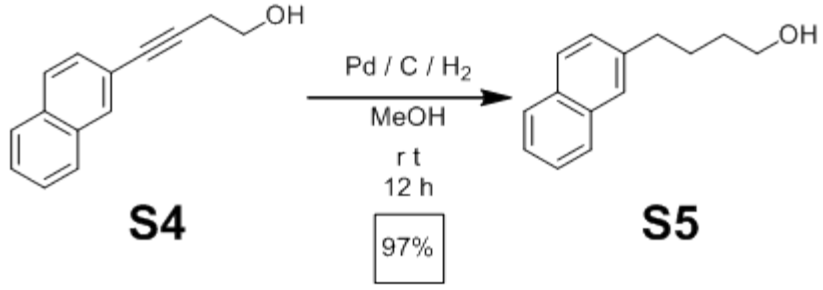

Preparation of naphthalene butanol S5.

A 250 mL round bottom flask with stir bar and three-way airfree adapter was charged with **S4** (1.70 g, 8.67 mmol) and 0.946 g of 5% Pd on carbon. The flask was cooled on dry ice and MeOH (90 mL) was added. The mixture was then frozen with liquid N_2, the flask evacuated and backfilled with H_2 and the mixture allowed to thaw. The reaction was stirred vigorously for 12 hrs, filtered through celite and concentrated under vacuum to provide **S5** (1.69 g, 97% yield) as a white solid. **S5**: ^{1}H NMR (400 MHz,$CDCl_3$) δ 7.81 (d, *J* = 8.4 Hz, *4-naphthalene*, 1H), 7.63 (s, *1-naphthalene*, 1H), 7.44 (pd, J = 6.9, 1.5 Hz, *5,8-naphthalene*, 2H), 7.34 (dd, J = 8.4, 1.7 Hz, *3-naphthalene*, 1H), 3.68 (t, J = 6.2 Hz, *1-butyl*, 2H), 2.82 (t, J = 7.6 Hz, *4-butyl*, 2H), 1.80 (m, *2-butyl*, 2H), 1.65 (m, *3-butyl*, 2H). ^{13}C NMR (100 MHz, $CDCl_3$) δ 139.89, 133.66, 132.02, 127.87, 127.64, 127.44, 127.37, 126.41, 125.92, 125.14, 62.67, 35.80, 32.30, 27.43. IR (ATR) 3570, 3331, 3051, 2934, 2858, 1632, 1600, 1507, 1485, 1365, 1270, 1209, 1144, 1124, 1062, 1030, 982, 959, 945, 888, 854, 817, 746, 709, 692, 686, 676, 669, 663, 653 cm^{-1}. EI-MS m/z Calcd. m/z 200.12012 $[M]^+$. Found m/z 200.12031 $[M]^+$.

Scheme A2.7. Synthesis of naphthalene butanol tosylate **S6**.

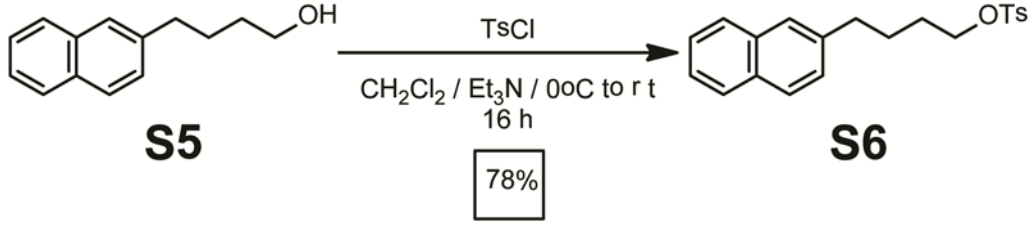

Preparation of naphthalene butanol tosylate S6.

A 500 mL flame dried round bottom flask with stir bar was charged with **S5** (1.5 g, 7.49 mmol), anhydrous CH_2Cl_2 (375 mL), and freshly distilled Et_3N (40mL). The solution was cooled to -10^{o}C using a CO_2 (s)/ethylene glycol bath, and p-toluenesulfonyl chloride (5.71 g, 29.96 mmol) was added drop-wise as a solution in anhydrous CH_2Cl_2 (10 mL). The mixture was stirred for 16 hrs under a N_2 atmosphere, at which time TLC showed complete reaction (SiO_2, 30% EtOAc and 80% hexanes, R_f=0.25). The reaction mixture was poured into H_2O (50 mL), the organic layer removed and washed with H_2O (3 x 50 mL). The organic layer was then dried ($MgSO_4$) and the solvent removed under vacuum. Purification was accomplished by column chromatography (SiO_2, 30% EtOAc/80% hexanes) to provide **S6** (2.07 g, 78% yield) as an off white solid. **S6**: ^{1}H NMR (300 MHz, $CDCl_3$) δ 7.87 – 7.68 (m, *4,5,8-naphthalene*, 3H), 7.76 (d, *J* = 8.5 Hz, *2-tosyl aryl*, 2H) 7.56 (s, *1-naphthalene*, 1H), 7.50 – 7.39 (m, *6,7-naphthalene*, 2H), 7.30 (d, *J* = 8.5 Hz, *3-tosyl aryl*, 1H), 7.28 – 7.20 (m, *3-naphthalene*, 1H), 4.06 (t, *J* = 5.9 Hz, *1-butyl*, 2H), 2.74 (t, *J* = 7.0 Hz, *4-butyl*, 2H), 2.42 (s,

tosyl methyl, 3H), 1.85 – 1.57 (m, *2,3-butyl*, 2H). ^{13}C NMR (75 MHz, $CDCl_3$) δ 145.22, 139.58, 134.05, 133.53, 132.50, 130.33, 128.42, 128.29, 128.10, 127.90, 127.64, 126.90, 126.45, 125.70, 70.96, 35.64, 28.78, 27.39, 22.04. IR (ATR) 3051, 2940, 2859, 1598, 1507, 1494, 1457, 1356, 1306, 1291, 1188, 1175, 1097, 1040, 1019, 934 cm^{-1}. EI-MS m/z Calcd. m/z 354.12897 $[M]^+$. Found m/z 354.12917 $[M]^+$.

Scheme A2.8. Synthesis of phenanthrene tripod ligand **S7**.

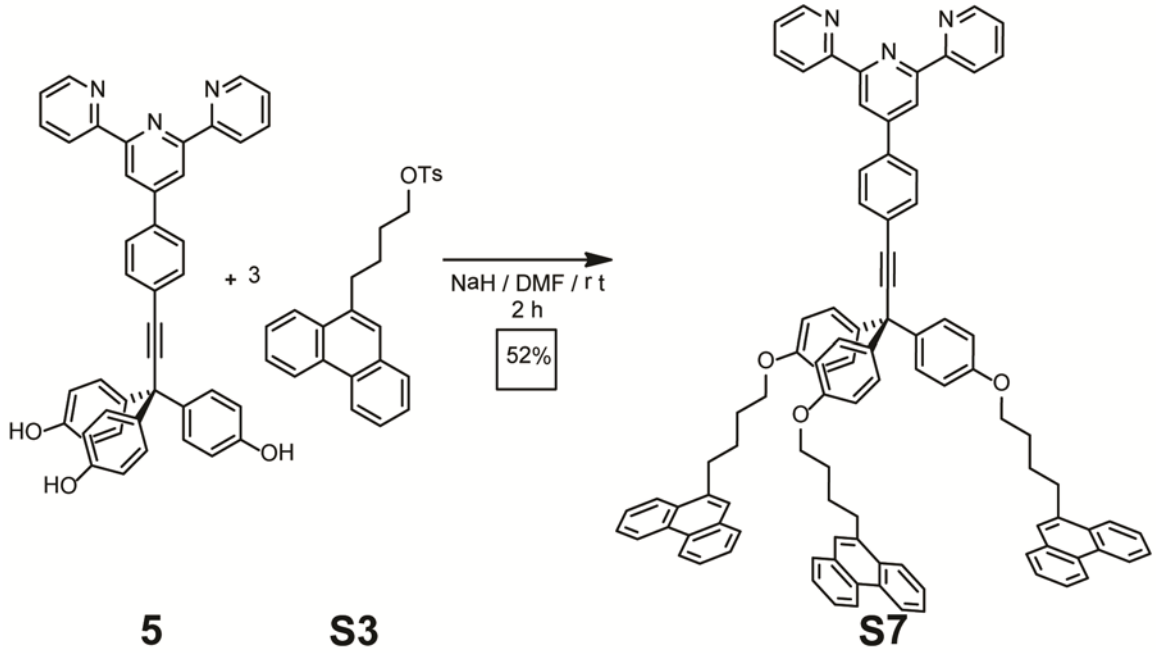

Preparation of phenanthrene tripod ligand S7.

A flame dried 25 mL round bottom flask with a stir bar was charged with **5** (100 mg, 160 mmol) and placed under a N_2 atmosphere. Anhydrous DMF (14 mL) was added to the reaction flask followed by excess NaH (60% suspension in mineral oil), changing the reaction mixture from yellow to green. After 20 min, a solution of tosylate **S3** in anhydrous DMF (0.3 M, 0.227 g, 0.562 mmol) was added. The reaction was determined to be complete after 2 h by TLC (NH_2-SiO_2 , PhMe product R_f = 0.33). The reaction was quenched with water (20 mL), filtered through celite and the celite washed with CH_2Cl_2. The resulting biphasic mixture was transferred to a separatory funnel and the CH_2Cl_2 layer removed and washed with H_2O (3 x 10 mL), dried ($MgSO_4$), and the solvent removed under vacuum. Purification was accomplished by column chromatography (NH_2-SiO_2, gradient elution 50% hexanes / 50% PhMe to 100% PhMe), to provide **S8** (106 mg, 52% yield) as a white powder. **S8**: ^{1}H NMR (600MHz,$CDCl_3$) δ 8.81 (s, *3',5'-pyridyl*, 2H), 8.77 (m, *6,6'-pyridyl*, 2 H), 8.73 (dd, *J* = 7.8, 1.4 Hz, *5-phenanthrene*, 3H), 8.65 (d, *J* = 8.1 Hz, *4-phenanthrene*, 3H), 8.11 (dd, *J* = 8.0, 1.5 Hz, *8-phenanthrene*, 3H), 7.96 (m, *3,3''-pyridyl*, 2H), 7.93 (d, *J* = 7.9 Hz, *2-aryl*, 2H), 7.82 (dd, *J* = 7.7, 1.6 Hz, *1-phenanthrene*, 3H), 7.67 – 7.57 (m, *2,3,6,8,10-phenanthrene*, *3-aryl*, 17H), 7.55 (dd, *J* = 7.0, 1.5 Hz, *4,4''-pyridyl*, 2H), 7.41 (dd, *J* = 7.0, 1.5 Hz, *5,5''-pyridyl*, 2H), 7.24 (d, *J* = 8.9 Hz, *trityl 2-aryl*, 6H), 6.86 (d, *J* = 8.9 Hz, *trityl 3-aryl*, 6H), 4.04 (t, *J* = 6.1 Hz, *1-butyl*, 6H), 3.19 (t, *J* = 7.5 Hz, *4-butyl* 6H), 2.02 (m, *2-butyl*, 6H), 1.97 (m, *3-butyl*, 6H). ^{13}C NMR (125 MHz, $CDCl_3$) δ 138.04, 136.44, 132.36, 132.01, 131.36, 130.87, 130.26, 129.81, 128.19,

127.31, 126.74, 126.67, 126.29, 126.27, 126.08, 124.54, 124.21, 123.37, 122.57, 121.88, 119.21, 114.02, 98.16, 84.35, 67.86, 54.35, 33.19, 29.47, 26.76.IR (ATR) 3061, 2952, 2855, 1723, 1606, 1584, 1567, 1558, 1538, 1505, 1467, 1444, 1432, 1414, 1389, 1365, 1298, 1246, 1176, 1115, 1095, 1069, 1041, 119, 1013, 990, 975, 957, 904 cm^{-1}. MALDI-TOF-MS m/z Calcd. m/z 1319.5965 $[M]^+$. Found m/z 1319.5945 $[M]^+$.

Scheme A2.9 Synthesis of naphthalene tripod ligand **S7**.

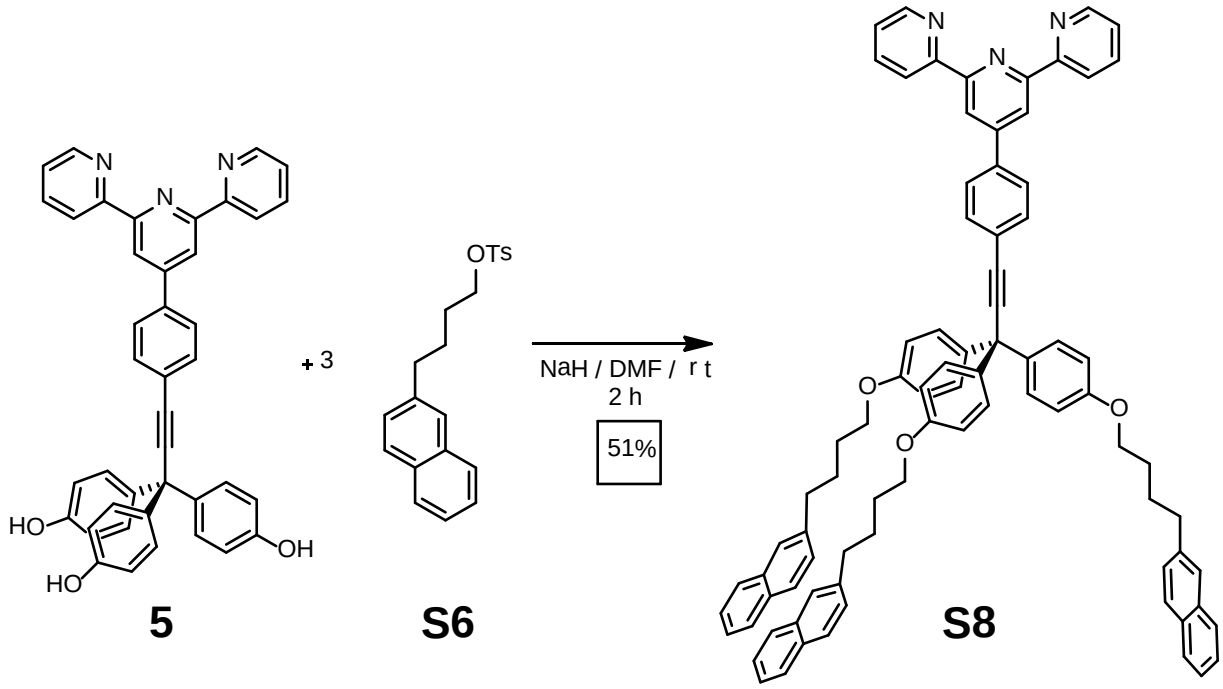

Preparation of naphthalene anchored tripod ligand S8.

To a flame dried 25 mL round bottom flask with a stir bar, added **X** (100 mg, 160 mmol). The powder was dried by cycling vacuum and dry nitrogen three times. Dry DMF (14 mL) was then added to the mixture under nitrogen via syringe, and the mixture was stirred while excess NaH was added as a powder. The suspension was stirred at room temperature for 20 min, at which time the tosylate **X** (0.228 g, 0.642 mmol) was added all at once as a solution in dry DMF (2 mL The reaction was determined to be complete after 2 h by TLC (NH_2-SiO_2 , PhMe product R_f = 0.33). The reaction was quenched with H_2O (20 mL), filtered through celite and the celite washed with CH_2Cl_2 (20mL). The resulting biphasic mixture was transferred to a separatory funnel and the CH_2Cl_2 layer removed and washed with H_2O (3 x 10 mL), dried ($MgSO_4$), and the solvent removed under vacuum. Purification was accomplished by column chromatography (NH_2-SiO_2, gradient elution 50% hexanes / 50% PhMe to 100% PhMe), to provide **S8** (94 mg, 51% yield) as a white powder. **S8**: ^{1}H NMR (400 MHz, $CDCl_3$) δ 8.80 (s, *3',5'-pyridyl*, 2H), 8.78 (d, *J* = 4.1 Hz, *6,6''-pyridyl*, 2H), 8.72 (d, *J* = 7.9 Hz, *2-aryl*, 2H), 7.95 – 7.88 (m, *3,3''-pyridyl*, 4H), 7.87–7.83 (m, *4,5,8-naphthalene*, 9H), 7.68 (d, *J* = 7.9 Hz, *3-aryl*, 2H), 7.68 (s, *1-naphthalene*, 3H), 7.53 – 7.42 (m, *6,7-naphthalene*, 6H), 7.42 – 7.36 (m, *5-pyridyl and 3-naphthalene*, 5H), 7.31 (d, *J* = 8.8 Hz, *trityl 2-aryl*, 6H), 6.90 (d, *J* = 8.8 Hz, *trityl 3-aryl* 6H), 4.02 (t, *J* = 5.8 Hz, *1-butyl*, 6H), 2.89 (t, *J* = 7.0 Hz, *4-butyl*, 6H), 2.00 – 1.84 (m, *2,3-butyl*, 12H). ^{13}C NMR (100 MHz, $CDCl_3$) δ 152.66, 150.79, 150.66, 143.82, 134.54,

132.70, 131.92, 128.43, 127.02, 126.81, 124.95, 123.89, 123.08, 122.71, 122.44, 122.26, 122.17, 121.96, 121.27, 120.73, 120.70, 119.95, 119.47, 118.79, 116.31, 113.55, 108.67, 98.39, 92.78, 79.02, 62.55, 49.03, 30.56, 23.75, 22.60. IR (ATR) 3050, 2938, 2861, 1064, 1583, 1566, 1538, 1505, 1467, 1442, 1411, 1388, 1294, 1244, 1175, 1116, 1060, 1040, 1013, 989, 962 cm^{-1}. ESI-TOF-MS m/z Calcd. m/z 1170.5574 $[M]^+$. Found m/z 1170.5593 $[M]^+$.

Scheme A2.10. Synthesis of phenanthrene anchored tripod complex **1b·2PF$_6$**.

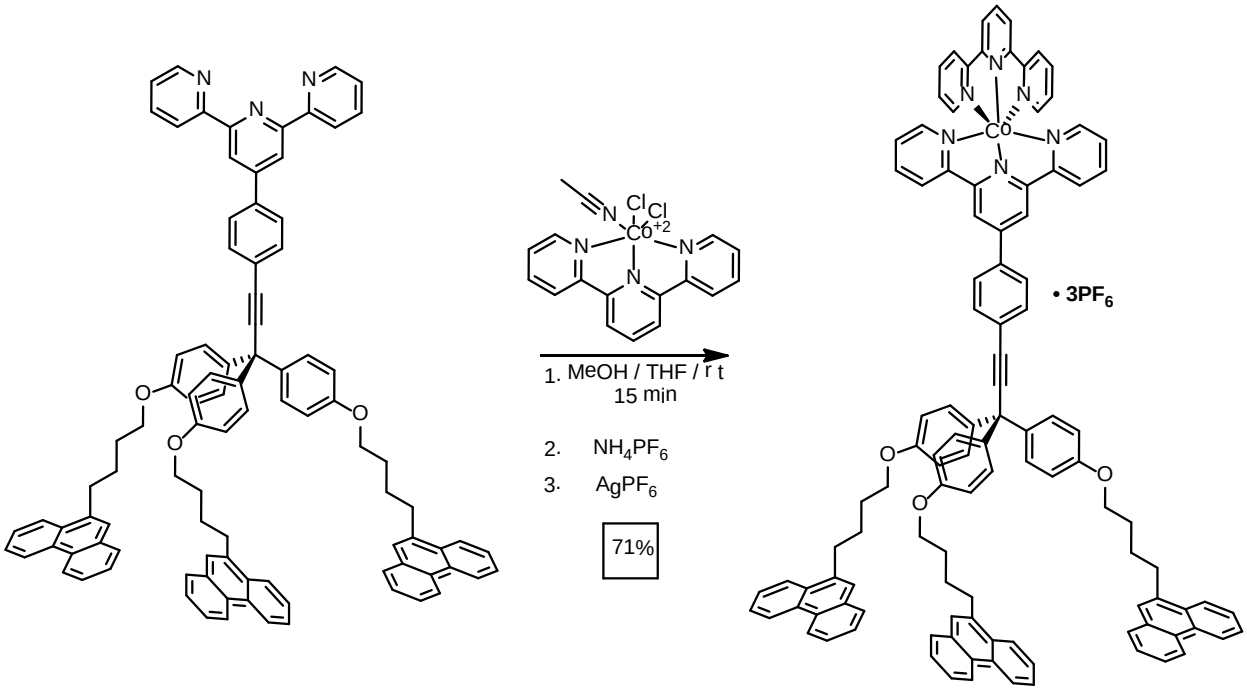

1b • 3PF$_6$

Preparation of phenanthrene anchored tripod complex 1b·2PF$_6$

To a 20 mL scintillation vial with a stir bar added **X** (31 mg, 0.076 mmol) in methanol (3.6 mL). The mixture was stirred to give a suspension to which **X** (50 mg, 0.038 mmol) was added slowly as a solution in THF (1.8 mL). The mixture became soluble and gradually changed a deep red. After 15min of stirring, saturated aqueous NH_4PF_6 was added to precipitate the product which was collected by filtration, and washed with water to give 28 mg of an orange powder in 71% yield. Oxidation with excess $AgPF_6$ in anhydrous THF followed by filtration and removal of the solvent under vacuum afforded the diamagnetic complex as a yellow solid in quantitative yield. **1b·3PF$_6$:** ^{1}H NMR (600 MHz,($CD_3)_2CO$) δ 9.79 (s, *3',5'-pyridyl large*, 2H), 9.42 (dd, *J* = 8.1, 2.3 Hz, *3',5'-pyridyl small*, 2H), 9.31 (t, *J* = 8.1 Hz, *4'- pyridyl small*, 1H), 9.16 (d, *J* = 8.0 Hz, *3,3''-pyridyl large*, 2H), 8.98 (d, *J* = 8.0 Hz, *3,3''-pyridyl small*, 2H), 8.85 (d, *J* = 8.0 Hz, *5-phenanthrene*, 3H), 8.77 (d, *J* = 8.0 Hz, *4-phenanthrene*, 3H), 8.46 (d, *J* = 7.9, *2-aryl*, 2H), 8.44 – 8.36 (m, *4,4''-pyridyl large and small*, 4H), 8.23 (d, *J* = 7.8 Hz, *8-phenanthrene*, 3H), 7.98 (t, *J* = 6.1 Hz, *6,6''-pyridyl large*, 2H), 7.94 (d, *J* = 7.8 Hz, *3-aryl*, 2H), 7.91 (d, *J* = 7.9 Hz, *1-phenanthrene*, 3H), 7.84 (t, *J* = 6.2 Hz, *6,6''-pyridyl small*, 2H), 7.74 (s, *10-phenanthrene*, 3H), 7.71 – 7.56 (m, *5,5''-pyridyl small and large and 2,3,6,7-phenanthrene*, 17H), 7.25 (d, *J* = 8.9 Hz, *trityl 2-aryl*, 6H), 6.96

(d, *J* = 8.9 Hz, *trityl 3-aryl*, 6H), 4.15 (t, *J* = 6.1 Hz, *1-butyl*, 6H), 3.26 (t, *J* = 7.8, *4-butyl*, 6H), 2.04 – 1.96 (m, *2,3-butyl*, 12H). ^{13}C NMR (126 MHz, acetone) δ 158.17, 156.84, 156.69, 156.67, 152.65, 143.27, 143.15, 137.43, 136.58, 132.65, 132.01, 131.20, 131.07, 131.02, 130.75, 129.98, 129.67, 128.69, 128.03, 127.38, 126.68, 126.66, 126.30, 126.07, 126.05, 125.17, 124.51, 123.28, 122.48, 113.97, 100.23, 83.86, 67.53, 54.31, 32.64, 26.65. IR (ATR) 3628, 3437, 3092, 2942, 2867, 1606, 1505, 1484, 1453, 1406, 1257, 1247, 1176, 1131, 1026, 825 cm^{-1}. ESI-TOF-MS m/z Calcd. m/z 1611.499 $[M]^+$. Found m/z 1611.623 $[M]^+$.

Scheme A2.11. Synthesis of naphthalene anchored tripod complex **1c·3PF$_6$**.

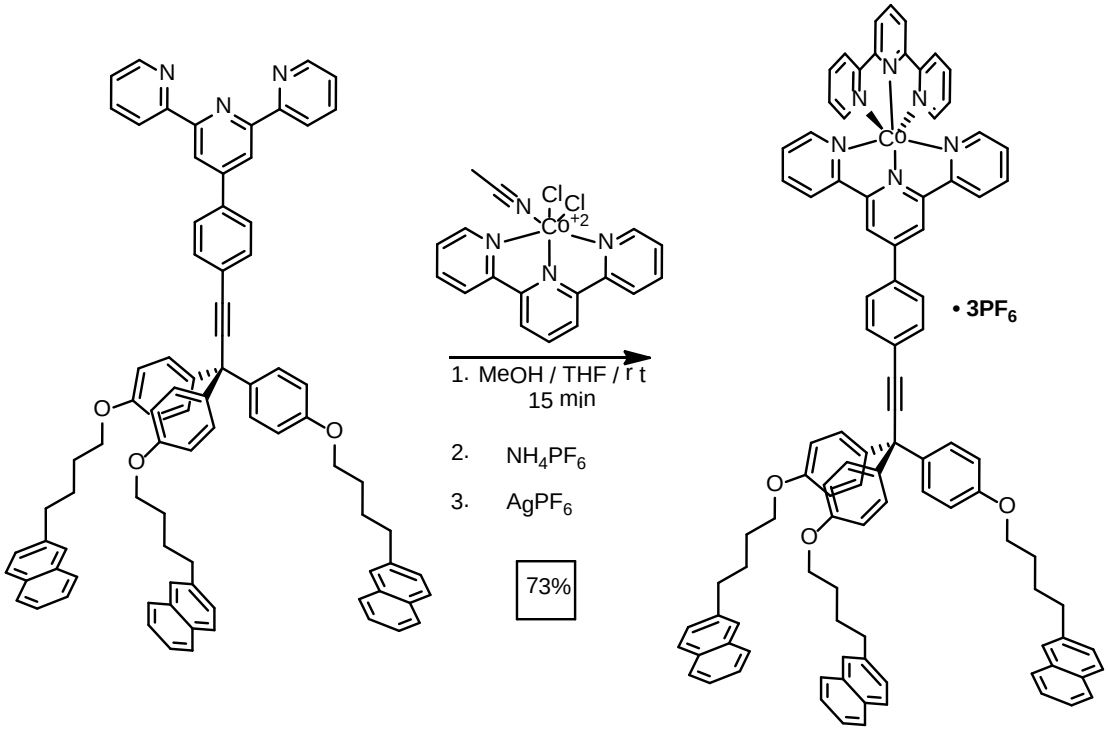

Preparation of naphthalene anchored tripod complex 1c·3PF$_6$.
To a 20 mL scintillation vial with a stir bar added **X** (35 mg, 0.085 mmol) in methanol (3.6 mL). The mixture was stirred to give a suspension to which **X** (50 mg, 0.043 mmol) was added slowly as a solution in THF (1.8 mL). The mixture became soluble and gradually changed a deep red. After 15min of stirring, saturated aqueous NH_4PF_6 was added to precipitate the product which was collected by filtration, and washed with water to give 53 mg of an orange powder in 73% yield. Oxidation with excess $AgPF_6$ in anhydrous THF followed by filtration and removal of the solvent under vacuum afforded the diamagnetic complex as a yellow solid in quantitative yield. **1c·3PF$_6$**:^{1}H NMR (600 MHz, $(CD_3)_2CO$) δ 9.78 (s, *3′,5′-pyridyl large*, 2H), 9.42 (dd, *J* = 8.0, 3.8 Hz, *3′,5′-pyridyl small*, 2H), 9.28 (t, *J* = 8.0 Hz, *4′-pyridyl small*, 1H) 9.19 (d, *J* = 8.0 Hz, *3,3″-pyridyl large*, 2H), 8.99 (d, *J* = 8.1 Hz, *3,3″-pyridyl small*, 2H), 8.54 (d, *J* = 8.0Hz, *2-aryl*, 2H), 8.39 (t, *J* = 7.7 Hz, *4,4″-pyridyl large and small*, 4H), 8.00 (t, *J* = 6.6 Hz, *6,6″-pyridyl large*, 2H), 7.92 (d, *J* = 8.0 Hz, *3-aryl*, 2H), 7.89 –7.78 (m, *4,5,8-naphthalene and 6,6″-pyridyl small*, 11H), 7.74 (s, *1-naphthalene*, 3H), 7.59 (m, *5,5″-pyridyl small and large*, 4H), 7.50 – 7.39 (m, *3,6,7-naphthalene*, 9H), 7.25

(d, *J* = 8.5 Hz, *trityl 2-aryl*, 6H), 6.94 (d, *J* = 8.6 Hz, *trityl 3-aryl*,6H), 4.09 (t, *J* = 6.3 Hz, *1-butyl*, 6H), 2.90 (t, *J* = 7.5 Hz, *4-buty*, 6H), 1.97 – 1.91 (m, *2-butyl*, 6H), 1.88 (m, *3-butyl*, 6H). ^{13}C NMR (125 MHz, $(CD_3)_2CO$) δ 159.03, 157.72, 157.68, 157.56, 157.51, 157.49, 157.47, 157.44, 153.54, 146.81, 144.08, 143.96, 140.86, 138.32, 134.69, 133.45, 133.05, 131.92, 131.86, 130.83, 129.72, 129.04, 129.00, 128.65, 128.36, 128.35, 128.31, 128.21, 128.19, 127.21, 127.19, 126.68, 126.13, 125.91, 125.74, 123.19, 120.64, 118.09, 114.80, 69.37, 68.46, 55.16, 54.48, 36.21, 28.55. IR (ATR) 3491, 3054, 2941, 2863, 2230, 1696, 1603, 1505, 1483, 1434, 1405, 1371, 1245, 1175, 1117, 1049, 1029, 825 cm^{-1}. ESI-TOF-MS m/z Calcd. m/z 1461.5780 $[M]^+$. Found m/z 1461.5723$[M]^+$.

Scheme A2.12. Overall **S**ynthesis of Ferrocene functionalized tripods **7a,b**.

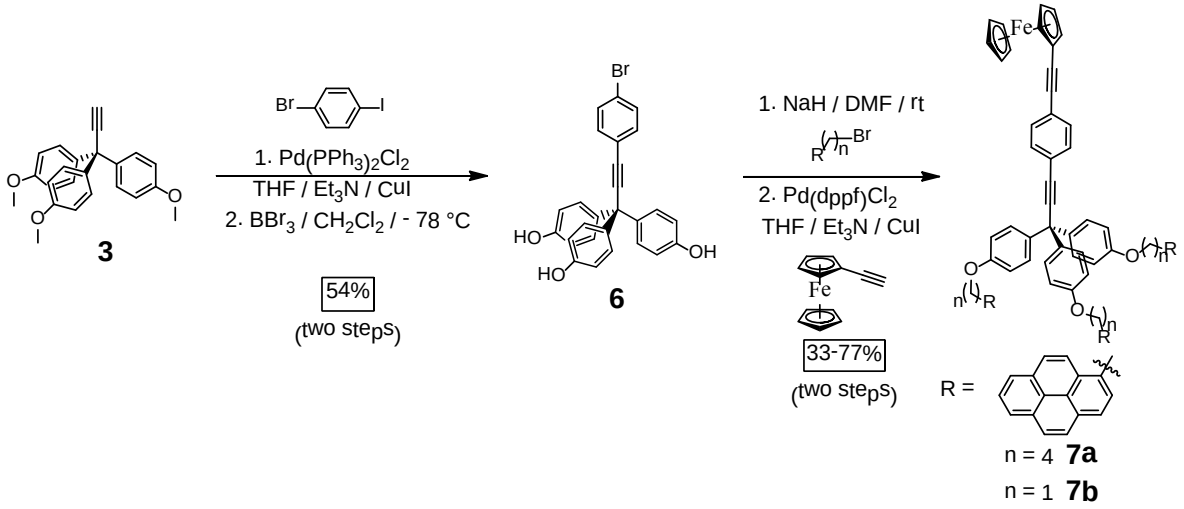

Scheme A2.13. Synthesis of bromophenyl(tris-4-methoxyphenyl)propyne **S9**.

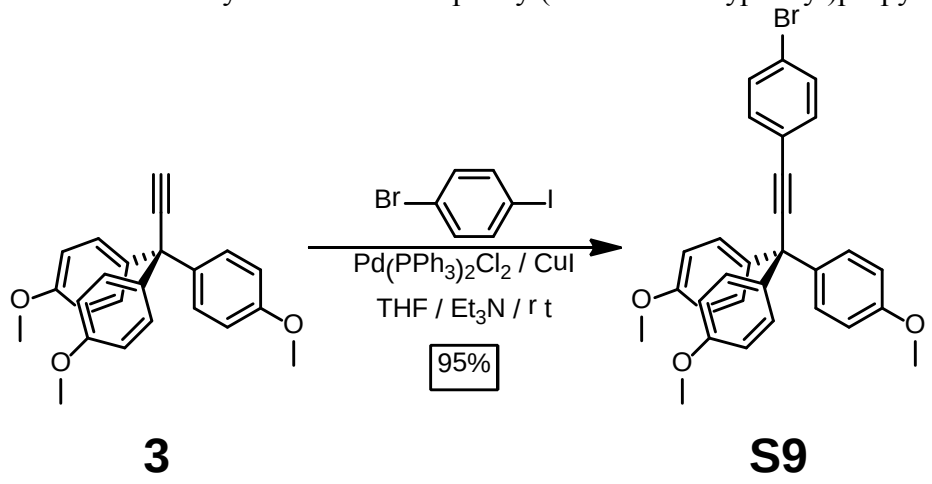

Preparation of bromophenyl(tris-4-methoxyphenyl)propyne S9

A flame dried 25 mL airfree storage tube with 8 mm hi-vac joint was charged with **3**(510 mg, 1.4 mmol), of iodo-4-bromobenzene (670 mg, 2.4 mmol), CuI (24 mg, 0.13 mmol) and $Pd(PPh_3)_2Cl_2$ (47 mg, 0.067 mmol). The solids were placed under an N_2 atmosphere by three cycles of evacuation and backfilling with N_2. Anhydrous THF (10 mL) and Et_3N (5mL) were

degassed by three freeze, pump, thaw cycles and transferred to the reaction vessel using a disposable polypropylene syringe. The reaction mixture was degassed by one freeze, pump, thaw cycle and allowed to warm to room temperature. The mixture was stirred at room temperature for 16 hours at which time the reaction was found to be complete by TLC (SiO_2, 20% EtOAc, 80% hexanes, R_f=0.34). The reaction mixture was filtered through celite and the filter washed with $CHCl_3$ (3 x 10 mL) and the filtrate reduced under vacuum to give a dark brown oil, The oil was adsorbed onto SiO_2 and purified using column chromatography (SiO_2, 20% EtOAc, 80% hexanes) to yield **S9** (0.61 g, 83% yield) as a brown solid. **S9**: ^{1}H NMR (300 MHz, $CDCl_3$) δ 7.45 (d, *J* = 8.5 Hz, *2-aryl*, 2H), 7.34 (d, *J* = 8.5 Hz, *3-aryl*, 2H), 7.20 (d, *J* = 8.8 Hz, *trityl 2-aryl*, 6H), 6.84 (d, *J* = 8.8 Hz, *trityl 3-aryl*, 6H), 3.80 (s, *OMe*, 9H). ^{13}C NMR (75 MHz, $CDCl_3$) δ 158.70, 138.21, 131.84, 130.44, 123.05, 122.44, 113.69, 97.82, 83.86, 55.67, 54.47. IR (ATR) 3000, 2928, 2834, 1962, 1606, 1582, 1506, 1485, 1462, 1441, 1414, 1392, 1298, 1248, 1175, 1115, 1070, 1035, 1010, 825 cm^{-1}. EI-MS Calcd. m/z 512.09871 $[M]^+$. Found m/z 512.09909 $[M]^+$

Scheme A2.14. Synthesis of bromophenyl(tris-4-hydroxyphenyl)propyne **6**.

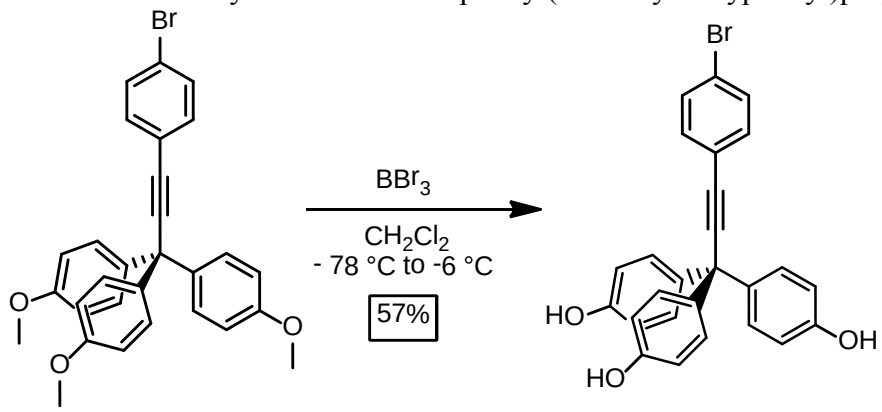

Preparation of bromophenyl(tris-4-hydroxyphenyl)propyne 7

A flame dried 500 mL round bottom flask was charged with **S9** (1.6 g, 3.1 mmol) and anhydrous CH_2Cl_2 (300 mL). The resulting solution was cooled to -78 ^{o}C using a CO_2 (s)/*i*-PrOH bath and a solution of BBr_3 in CH_2Cl_2 (77 mL, 1M, 77 mmol) added slowly over 30 min and the resulting mixture was warmed to -6 ^{o}C. The reaction was determined to be complete by TLC (SiO_2, 50% EtOAc, 50% hexanes, R_f=0.4) after 18 hrs, at which time the reaction was quenched by the addition of MeOH (5mL). The resulting mixture was adsorbed onto SiO2 and purified by column chromatography (SiO_2, gradient elution from 10% EtOAc, 90% hexanes to 50% EtOAc, 50% hexanes) to yield **6** (0.85 g, 57% yield) as a red solid. **6**: ^{1}H NMR (300 MHz, $(CD_3)_2SO$) δ 9.32 (s, *OH*, 3H), 7.91 (d, *J* = 8.4 Hz, *2-aryl*, 2H), 7.58 (d, *J* = 8.4 Hz, *3-aryl*, 2H), 6.98 (d, *J* = 8.7 Hz, *trityl 2-aryl*,6H), 6.69 (d, *J* = 8.7 Hz, *trityl 3-aryl*,6H). ^{13}C NMR (75 MHz, $(CD_3)_2SO$) δ 166.92, 147.61, 147.58, 143.99, 142.47, 142.44, 142.42, 140.81, 140.78, 133.75, 132.39, 125.38, 108.90, 93.76, 64.80. IR (ATR) 3301, 1696, 1605, 1560, 1506, 1437, 1365, 1231, 1173, 1109, 1015, 860 cm^{-1}. MALDI-TOF-MS m/z Calcd. m/z 470.0518 $[M]^+$. Found m/z 470.1023 $[M]^+$.

Scheme A2.15. Synthesis of 4-bromophenyl butylpyrene tripod **S10**.

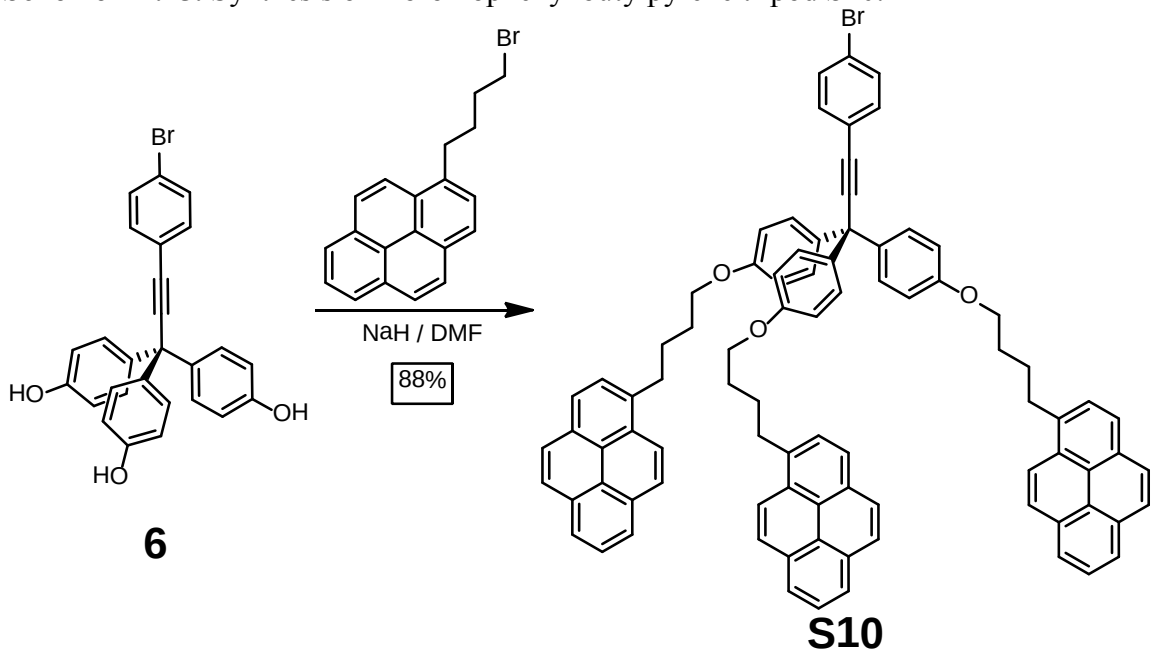

6 **S10**

Preparation of 4-bromophenyl butylpyrene tripod S10.

A flame dried 25 mL round bottom flask with a stir bar was charged with **6** (400 mg, 0.85 mmol) and 4-bromobutylpyrene (892 mg, 2.65 mmol), and the solids placed under a N_2 atmosphere. NaH (99%, 300 mg, 13 mmol) was then added to the stirring mixture slowly as a solid. anhydrous DMF (8 mL). The suspension was stirred at room temperature for 10 h, at which time the reaction was determined to be complete by TLC (SiO_2 , 80% Hexanes / 20% EtOAc product R_f = 0.44). The reaction was quenched with H_2O (20 mL), filtered through celite and the celite washed with CH_2Cl_2 (20 mL). The resulting biphasic mixture was transferred to a separatory funnel and the CH_2Cl_2 layer removed and the aqueous layer extracted with fresh CH_2Cl_2 (3 x 20 mL). The combined organic layers were washed with H_2O (3 x 20 mL), dried ($MgSO_4$), and the solvent removed under vacuum. Purification was accomplished by column chromatography (SiO_2, gradient elution hexanes to 50% hexanes / 50% EtOAc), to provide **S10** (830 mg, 88% yield) as a dark yellow powder. **S10**:^{1}H NMR (300 MHz, $CDCl_3$) δ 8.27 (d, *J* = 9.3 Hz, *10-pyrene*, 3H), 8.18 – 7.93 (m, *3,4,5,6,7,8,9-pyrene*, 21H), 7.87 (d, *J* = 7.8 Hz, *2-pyrene*, 3H), 7.42 (d, *J* = 8.5 Hz, *2-aryl*, 2H), 7.34 (d, *J* = 8.5 Hz, 3-*aryl*, 2H), 7.20 (d, *J* = 8.9 Hz, *trityl 2-aryl*, 6H), 6.82 (d, *J* = 8.9 Hz, *trityl 3-aryl*, 6H). ^{13}C NMR (75 MHz, $CDCl_3$) δ 158.21, 138.14, 136.93, 133.46, 131.83, 131.82, 131.28, 130.45, 130.21, 129.02, 127.91, 127.65, 127.00, 126.20, 125.48, 125.41, 125.26, 125.19, 125.09, 123.78, 123.10, 122.40, 114.24, 97.95, 83.81, 68.08, 54.51, 33.55, 29.67, 28.68. IR (ATR) 3038,2922, 2852, 1919,1726, 1639, 1603, 1586, 1505, 1485, 1465, 1434, 1415, 1376, 1295, 1244, 1175, 1110, 1069, 1041, 1010, 960, 841, 825, 780, 755, 736, 719, 708, 680 cm^{-1}. MALDI-TOF-MS m/z Calcd. m/z 1238.4274 $[M]^+$. Found m/z 1238.4268 $[M]^+$.

Scheme A2.16. Synthesis of bromophenyl methylpyrene tripod **S11**.

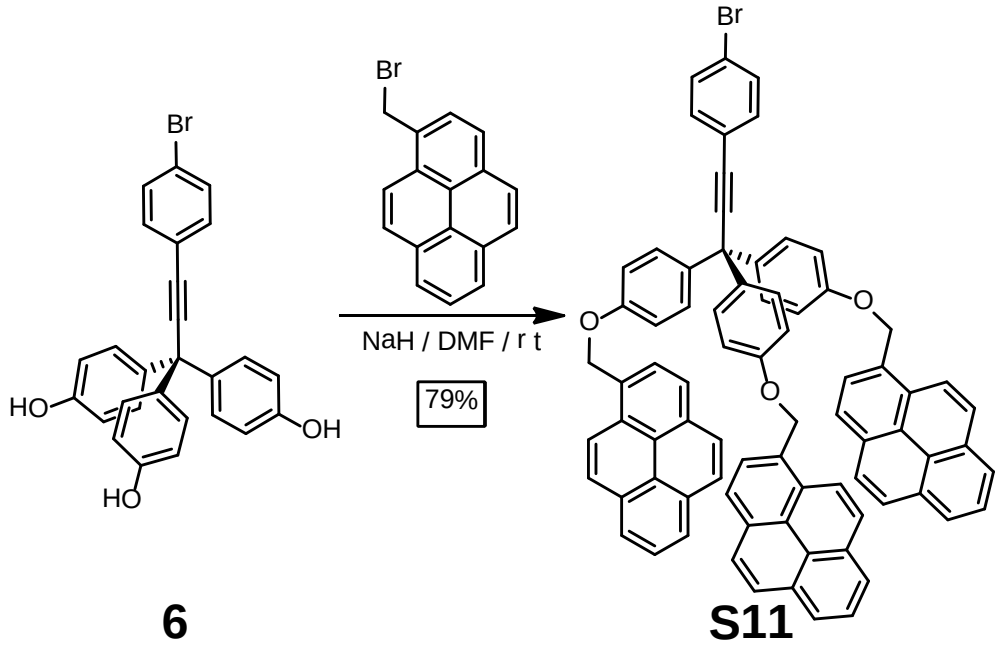

Preparation of 4-bromophenyl methylpyrene tripod S11.

A flame dried 5 mL round bottom flask with a stir bar was charged with **6** (50 mg, 0.11 mmol) and 4-bromomethylpyrene (103 mg, 0.038 mmol), and the solids placed under a N_2 atmosphere. NaH (99%, 100 mg, 4.3 mmol) was then added to the stirring mixture slowly as a solid. anhydrous DMF (1 mL). The suspension was stirred at room temperature for 10 h, at which time the reaction was determined to be complete by TLC (SiO_2 , 80% Hexanes / 20% EtOAc product R_f = 0.44). The reaction was quenched with H_2O (20 mL), filtered through celite and the celite washed with CH_2Cl_2 (20mL). The resulting biphasic mixture was transferred to a separatory funnel and the CH_2Cl_2 layer removed and washed with H_2O (3 x 10 mL), dried ($MgSO_4$), and the solvent removed under vacuum. Purification was accomplished by column chromatography (SiO_2, gradient elution hexanes to 50% hexanes / 50% EtOAc), to provide **S11** (105 mg, 79% yield) as a yellow powder. **S11**: ^{1}H NMR (300 MHz, $CDCl_3$) δ 8.32 (d, *J* = 9.2 Hz, *10-pyrene*, 3H), 8.25 – 7.97 (m, *2,3,4,5,6,7,8,9-pyrene*, 24H), 7.41 (d, *J* = 8.7 Hz, *2-aryl*, 2H), 7.37 (d, *J* = 8.7 Hz, *3-aryl*, 2H), 7.29 (d, *J* = 8.9 Hz, *trityl 2-aryl*, 6H), 7.06 (d, *J* = 8.9 Hz, *trityl 3-aryl*, 6H), 5.76 (s, *OCH*$_2$, 6H). ^{13}C NMR (75 MHz, $CDCl_3$) δ 158.16, 138.60, 133.49, 133.48, 132.01, 131.86, 131.62, 131.14, 130.59, 130.14, 129.74, 128.50, 128.09, 127.78, 127.39, 126.45, 125.84, 125.80, 125.37, 125.09, 123.48, 114.78, 69.27. IR (ATR) 3350, 3041, 2922, 2849, 1918, 1718, 1604, 1582, 1502, 1485, 1458, 1416, 1392, 1379, 1293, 1263, 1234, 1173, 1138, 1116, 1063, 1009, 903, 841, 825, 781, 757, 735, 710, 702, 681cm^{-1}. MALDI-TOF-MS m/z Calcd. m/z 1112.2865 $[M]^+$. Found m/z 1112.2098 $[M]^+$.

Scheme A2.17. Synthesis of tripod **7a**.

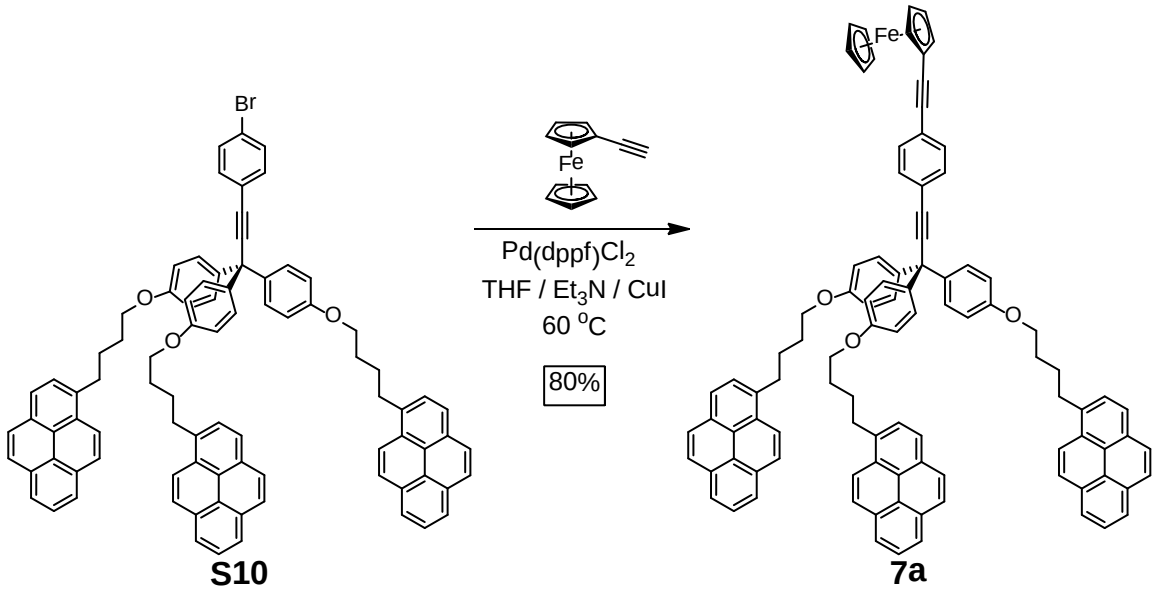

Preparation of ferrocene tripod 7a.

A flame dried 5 mL round bottom flask fitted with an airfree adapter joint was charged with **S10** (52 mg, 0.042 mmol), ethynylferrocene (35 mg, 0.12 mmol), CuI (5 mg, 0.026 mmol) and Pd(dppf)Cl_2 (3 mg, 4 μmol). The solids were placed under an N_2 atmosphere by three cycles of evacuation and backfilling with N_2. Anhydrous THF (0.4 mL) and Et_3N (0.4 mL) were degassed by three freeze, pump, thaw cycles and transferred to the reaction vessel using a disposable polypropylene syringe. The reaction mixture was degassed by one freeze, pump, thaw cycle and allowed to warm to room temperature. The mixture was then stirred at 60 °C for 24 hours, at which time the reaction was complete by TLC (SiO_2, 20% EtOAc, 80% hexanes, R_f =0.44, product spot is orange). The reaction mixture was filtered through celite and the filter washed with CH_2Cl_2 (3 x 5 mL) and the filtrate washed with aqueous HCl (1M, 10 mL). The aqueous layer was extracted with CH_2Cl_2 (3 x 2 mL) and the combined organic layer washed with H_2O (10 mL) and dried ($MgSO_4$). The solvent was reduced under vacuum to give a dark brown oil. The oil was adsorbed onto SiO_2 and purified using column chromatography (SiO_2, step gradient elution, 10% EtOAc, 90% hexanes to 20% EtOAc / 80% Hexanes to PhMe) to yield **7a** (0.044 g, 80% yield) as a brown solid. **7a**: ^{1}H NMR (300 MHz, $CDCl_3$) δ 8.28 (d, *J* = 9.3 Hz, *10-pyrene*, 3H), 8.19 – 7.93 (m, *3,4,5,6,7,8,9-pyrene*, 21H), 7.87 (d, *J* = 7.8 Hz, *2-pyrene*, 3H), 7.47 (d, *J* = 8.5 Hz, *2-aryl*, 2H), 7.44 (d, *J* = 8.5 Hz, 3-*aryl*, 2H), 7.26 (d, *J* = 8.9 Hz, *trityl 2-aryl*, 6H), 6.85 (d, *J* = 8.9 Hz, *trityl 3-aryl*, 6H), 4.53 (t, *J* = 1.8 Hz, *ferrocene 2,5-alkynecyclopentadiene*, 2H), 4.26 (m, *ferrocene 3,4-alkynecyclopentadiene and cyclopentadiene*, 7H), 4.00 (t, *J* = 6.0 Hz, *1-butyl*, 6H), 3.40 (t, *J* = 7.4 Hz, *4-butyl*, 6H), 2.25 – 1.84 (m, *2,3-butyl*, 12H). ^{13}C NMR (75 MHz, $CDCl_3$) δ 158.18, 142.98, 142.55, 142.14, 138.30, 136.96, 131.83, 131.63, 131.29, 130.46, 130.22, 129.03, 127.92, 127.66, 127.01, 126.21, 125.49, 125.42, 125.27, 125.20, 125.11, 123.80, 114.23, 68.08, 54.49, 33.55, 29.66, 28.68. IR (ATR) 3038, 2936, 2867, 2246, 2203, 1716, 1603, 1581, 1505, 1468, 1433, 1416, 1390, 1294, 1245, 1175, 1105, 1041, 1012, 957, 905 cm^{-1}. ESI-TOF-MS m/z Calcd. m/z 1368.5144 $[M]^+$. Found m/z 1368.5138 $[M]^+$.

Scheme A2.18. Synthesis of tripod **7b**.

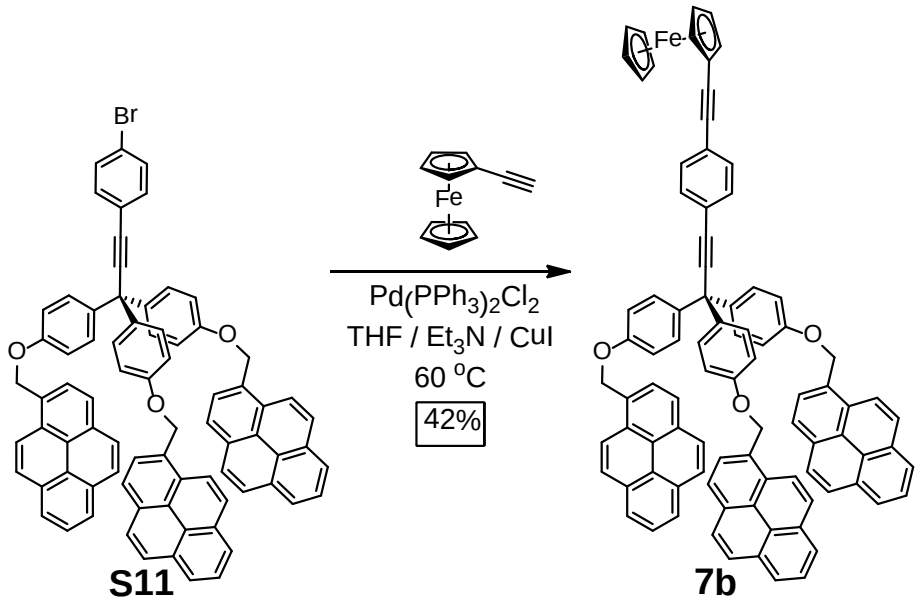

Preparation of ferrocene tripod 7b.

A flame dried 5 mL round bottom flask fitted with an airfree adapter joint was charged with **S11** (27 mg, 0.024 mmol), ethynylferrocene (14 mg, 0.05 mmol), CuI (5 mg, 0.026 mmol) and Pd(dppf)Cl_2 (3 mg, 4 μmol). The solids were placed under an N_2 atmosphere by three cycles of evacuation and backfilling with N_2. Anhydrous THF (0.4 mL) and Et_3N (0.4 mL) were degassed by three freeze, pump, thaw cycles and transferred to the reaction vessel using a disposable polypropylene syringe. The reaction mixture was degassed by one freeze, pump, thaw cycle and allowed to warm to room temperature. The mixture was then stirred at 60 ^oC for 24 hours, at which time the reaction was complete by TLC (SiO_2, 20% EtOAc, 80% hexanes, R_f =0.44, product spot is orange). The reaction mixture was filtered through celite and the filter washed with CH_2Cl_2 (3 x 5 mL) and the filtrate washed with aqueous HCl (1M, 10 mL). The aqueous layer was extracted with CH_2Cl_2 (3 x 2 mL) and the combined organic layer washed with H_2O (10 mL) and dried ($MgSO_4$). The solvent was reduced under vacuum to give a dark brown oil. The oil was adsorbed onto SiO_2 and purified using column chromatography (SiO_2, step gradient elution, 10% EtOAc, 90% hexanes to 20% EtOAc / 80% Hexanes to PhMe) to yield **7b** (0.014 g, 42% yield) as a brown solid. **7b**: ^{1}H NMR (600 MHz, $CDCl_3$) δ 8.33 (d, *J* = 9.2 Hz, *10-pyrene*, 4H), 8.23 – 8.20 (m, *6,8-pyrene*, 6H), 8.19 (d, *J* = 7.8 Hz, 2-*pyrene*, 3H), 8.16 (d, *J* = 9.2 Hz, *9-pyrene*, 3H), 8.13 (d, *J* = 7.8 Hz, *3-pyrene*, 3H), 8.08 (d, *J* = 9.0 Hz, *5-pyrene*, 3H), 8.07 (d, *J* = 9.0 Hz,*4-pyrene*, 3H), 8.03 (t, *J* = 7.6 Hz, *7-pyrene*, 3H), 7.46 (d, *J* = 8.6 Hz, *2-aryl*, 2H), 7.42 (d, *J* = 8.6 Hz, *3-aryl*, 2H), 7.32 (d, *J* = 8.9 Hz, 6H), 7.07 (d, *J* = 8.8 Hz, 6H), 5.76 (s, 6H), 4.51 (t, *J* = 1.8 Hz, *ferrocene 2,5-alkynecyclopentadiene*, 2H), 4.25 (m, *ferrocene 3,4-alkynecyclopentadiene and cyclopentadiene*, 7H). ^{13}C NMR (100 MHz, $CDCl_3$) δ 152.54, 133.15, 126.38, 126.31, 126.01, 125.95, 125.54, 125.02, 124.58, 124.12, 122.86, 122.45, 122.17, 121.76, 120.82, 120.18, 119.75, 119.47, 117.87, 109.18, 66.23, 64.78, 63.72, 63.65. IR (ATR) 3039, 2922, 2852, 1727, 1662, 1650, 1603, 1582, 1503, 1458, 1417, 1378, 1293, 1275, 1262, 1235, 1175, 1106, 1062, 1002, 958 cm^{-1}. ESI-MS m/z Calcd. m/z 1242.3735 [M]+. Found m/z 1242.5227 $[M]^+$.

C. NMR Spectra

Figure A2.3. ^{1}H NMR of phenanthrene butynol **S1** (400 MHz, $CDCl_3$, 298K).

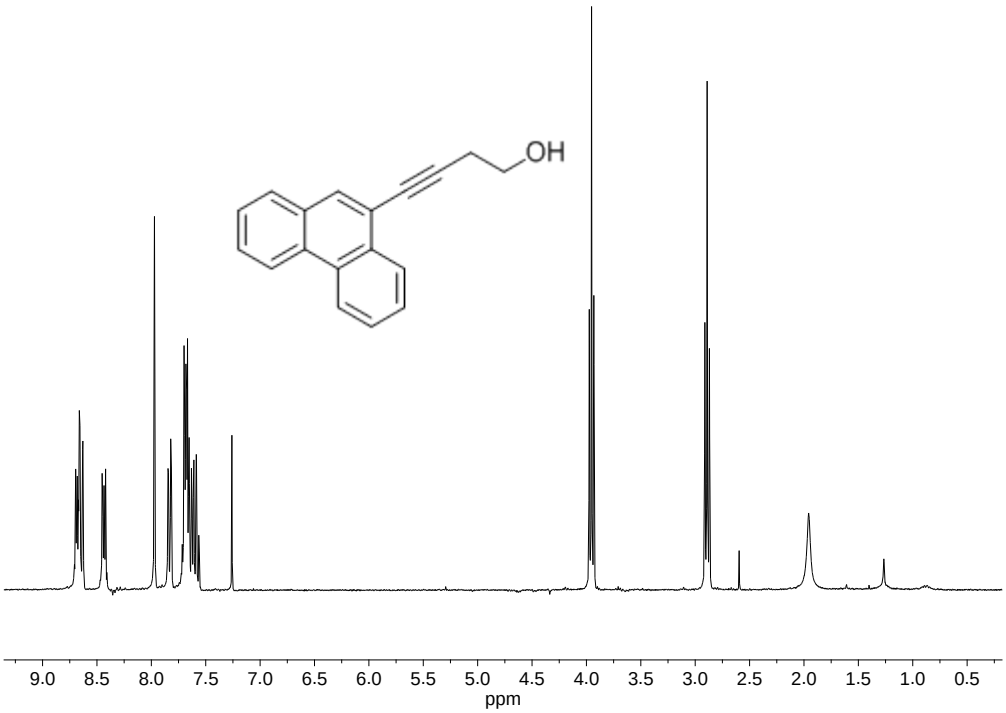

Figure A2.4. ^{13}C NMR of phenanthrene butynol **S1**(75 MHz, $CDCl_3$, 298K).

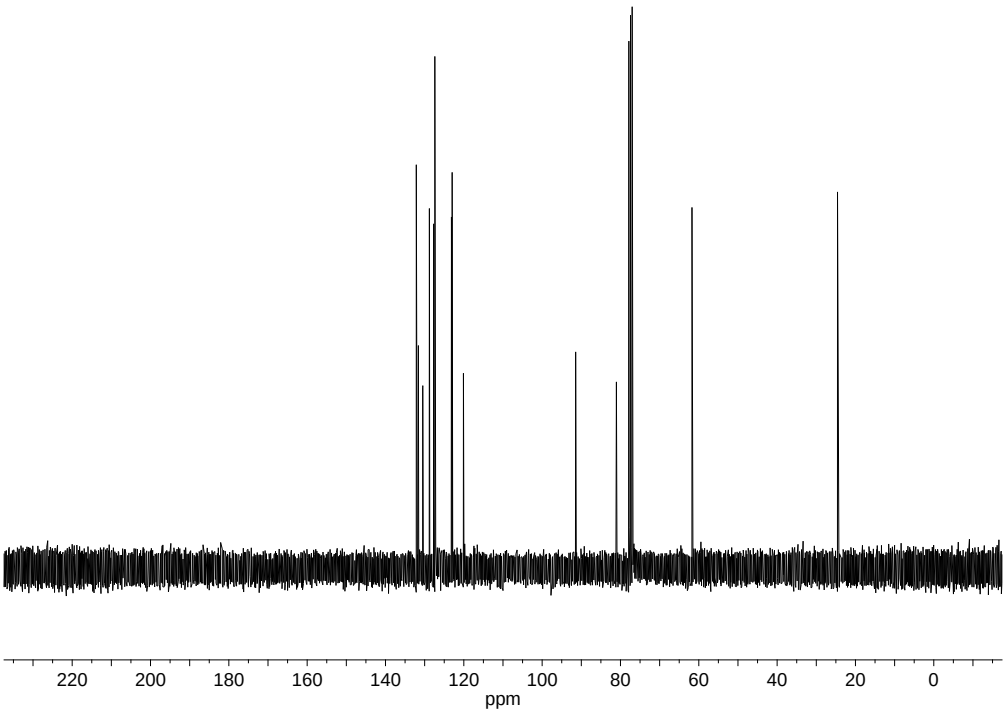

Figure A2.5. ^{1}H NMR of phenanthrene butanol **S2** (300 MHz, $CDCl_3$, 298K).

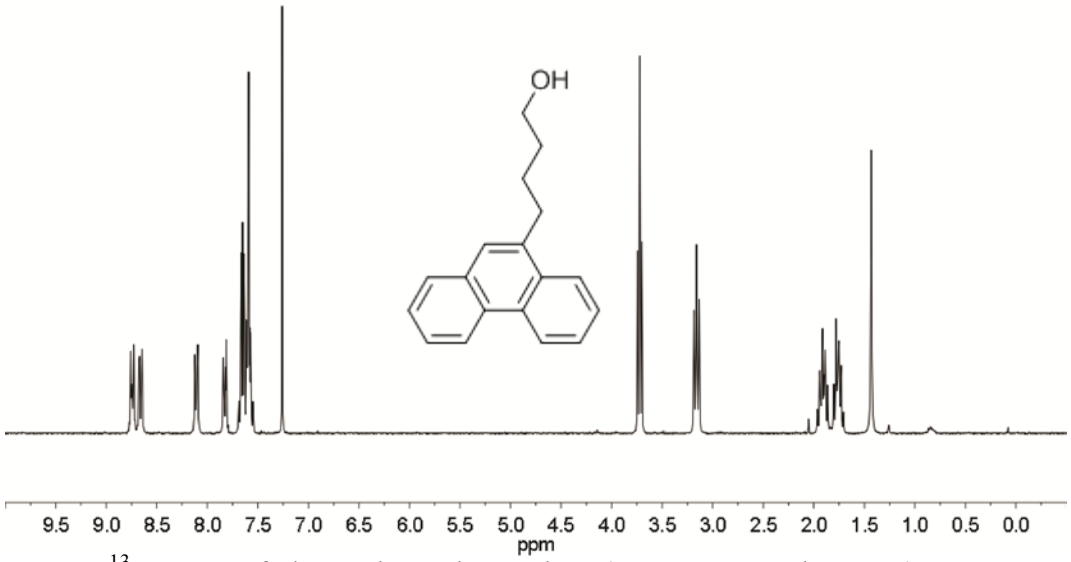

Figure A2.6. ^{13}C NMR of phenanthrene butanol **S2** (75 MHz, $CDCl_3$, 298K).

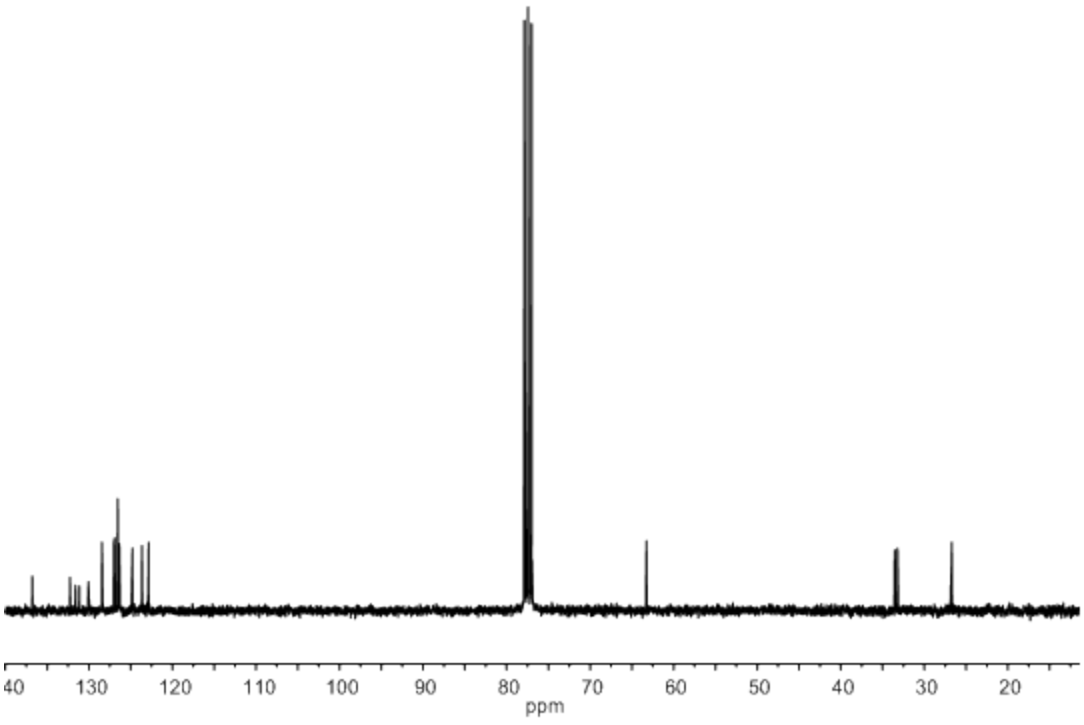

Figure A2.7. ^{1}H NMR of phenanthrene butanol tosylate **S3** (300 MHz, $CDCl_3$, 298K).

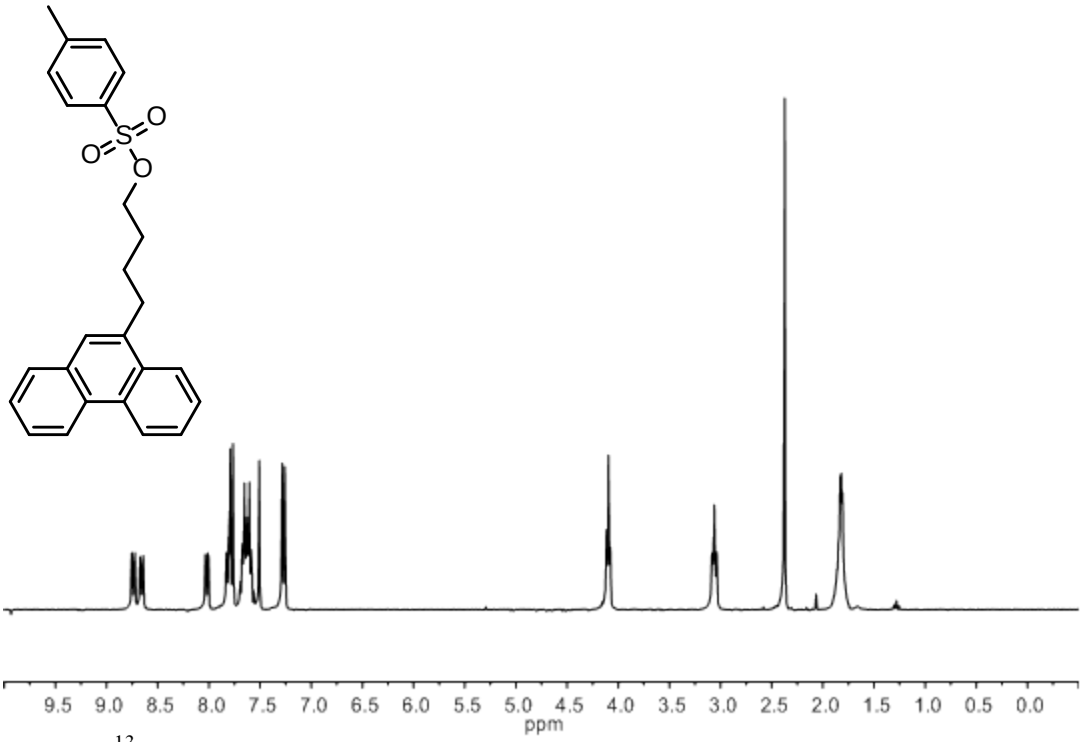

Figure A2.8. ^{13}C NMR of phenanthrene butanol tosylate **S3** (75 MHz, $CDCl_3$, 298K).

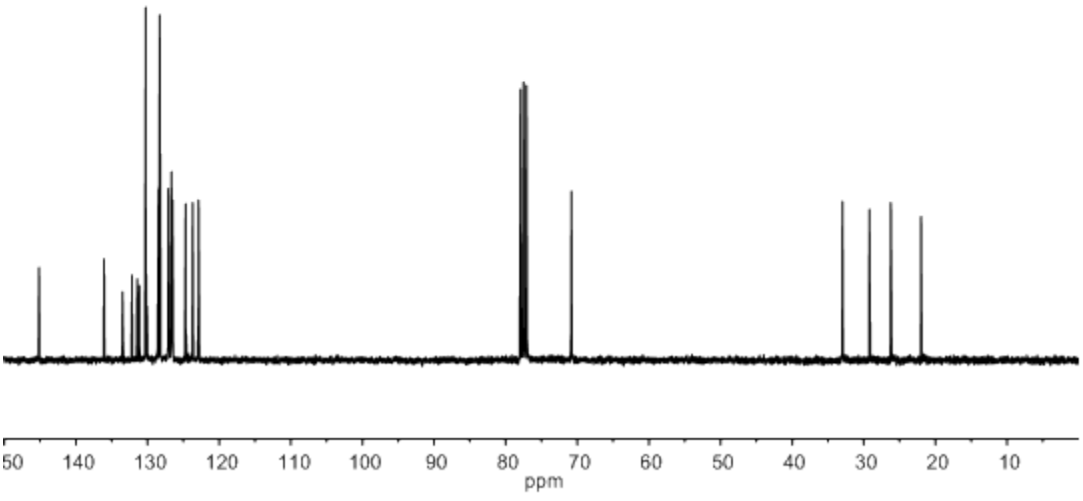

Figure A2.9. ^{1}H NMR of naphthalene butynol **S4** (400 MHz, $CDCl_3$, 298K).

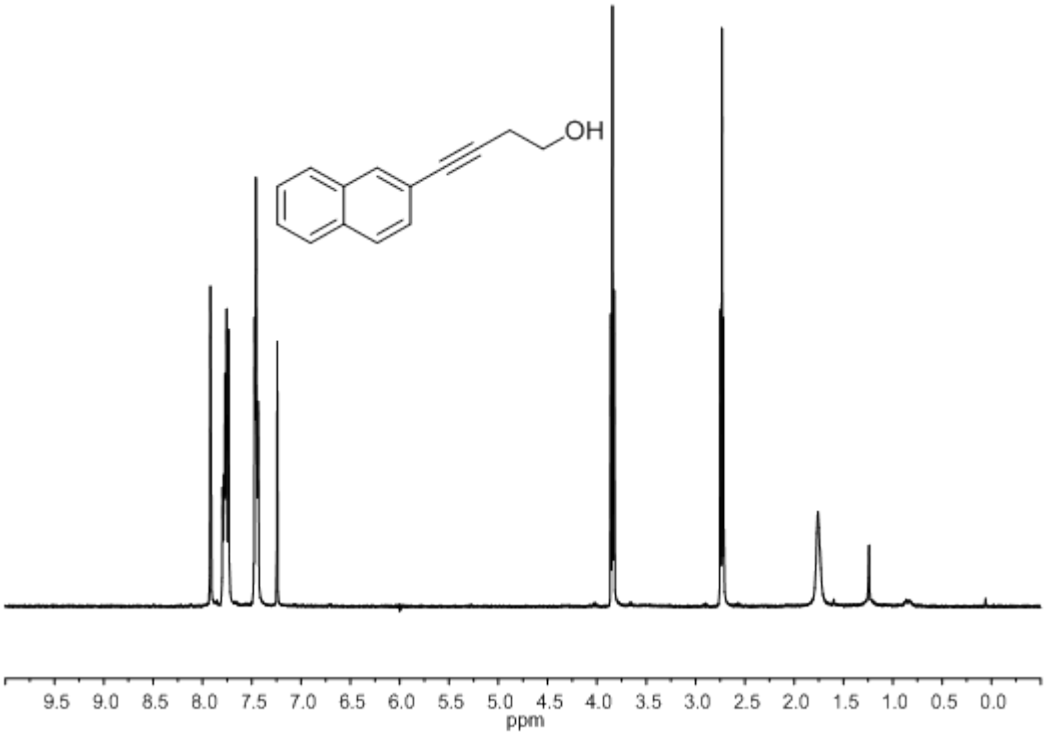

Figure A2.10. ^{13}C NMR of naphthalene butynol **S4** (100 MHz, $CDCl_3$, 298K).

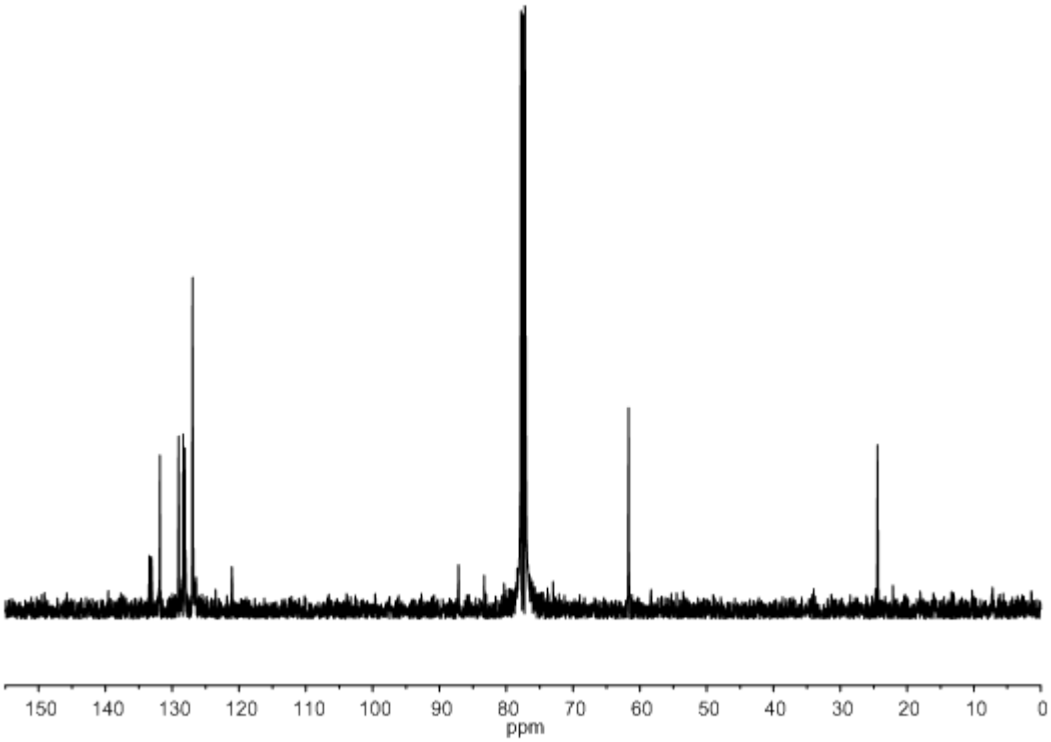

Figure A2.11. ^{1}H NMR of naphthalene butanol **S5** (400 MHz, $CDCl_3$, 298K).

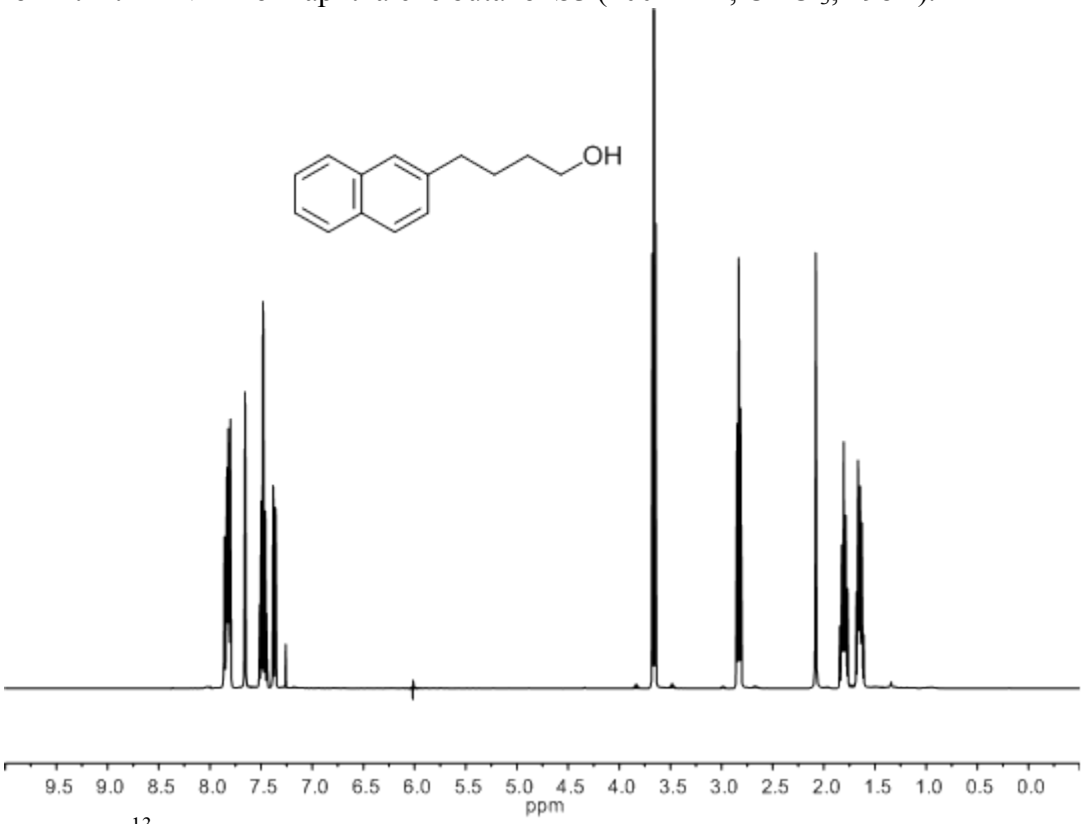

Figure A2.12. ^{13}C NMR of naphthalene butanol **S5** (100 MHz, $CDCl_3$, 298K).

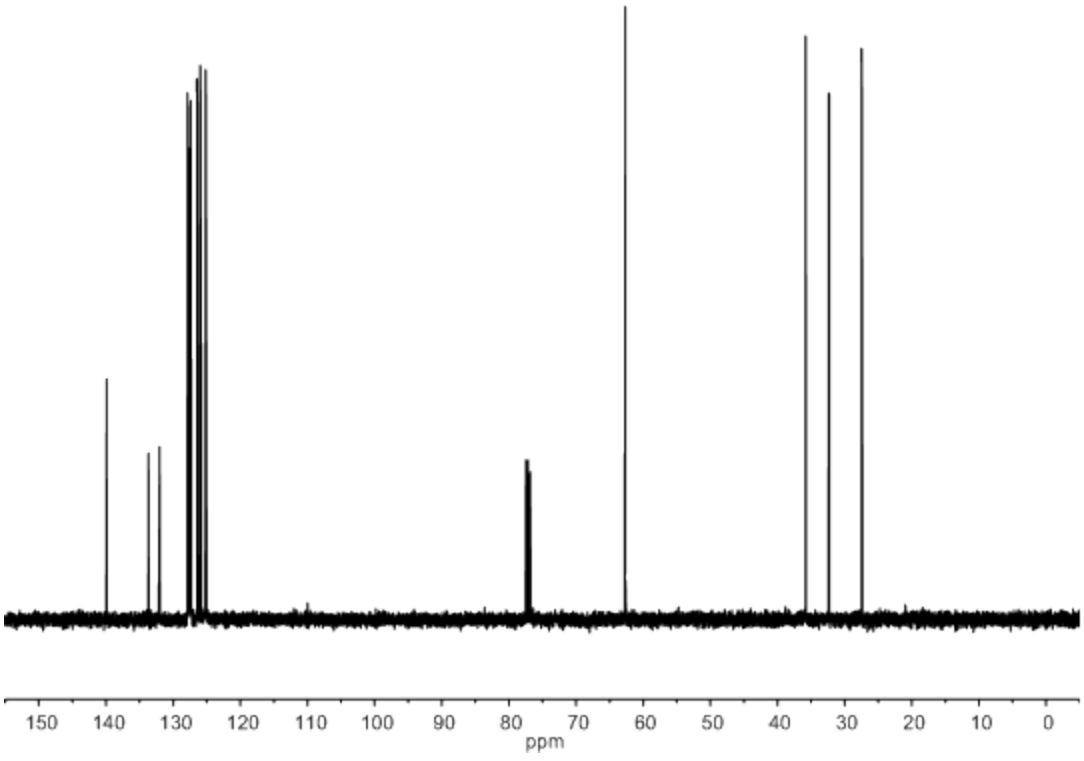

Figure A2.13. ^{1}H NMR of naphthalene butanol tosylate **S6** (300 MHz, $CDCl_3$, 298K).

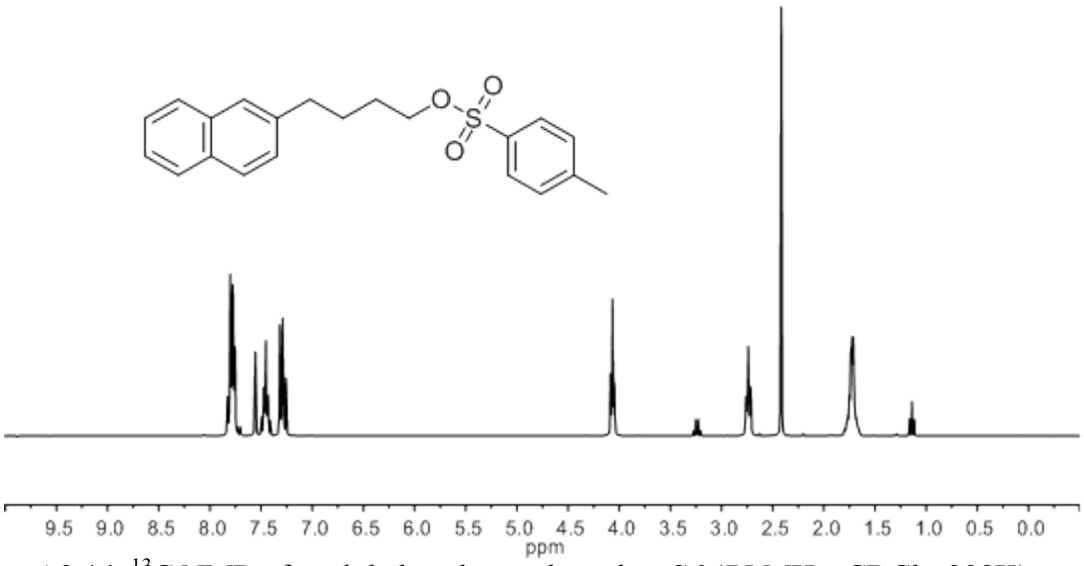

Figure A2.14. ^{13}C NMR of naphthalene butanol tosylate **S6** (75 MHz, $CDCl_3$, 298K).

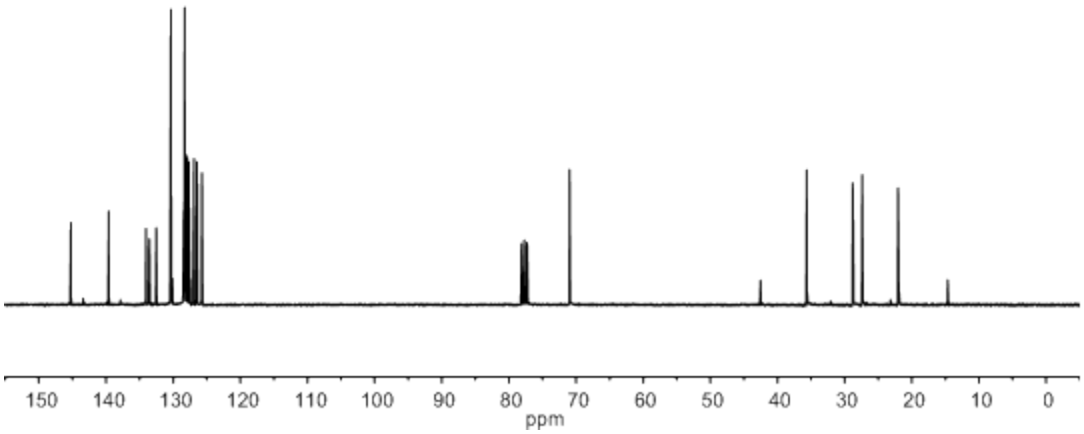

Figure A2.15. ^{1}H NMR of phenanthrene tripod ligand **S7** (600 MHz, $CDCl_3$, 298K).

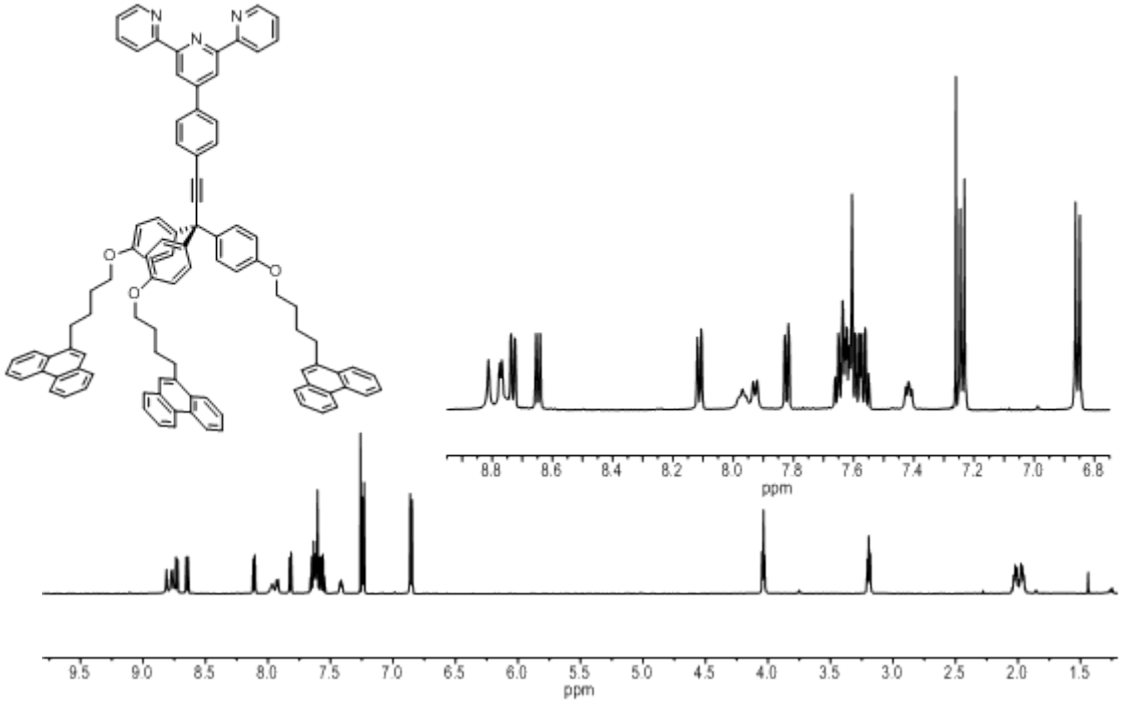

Figure A2.16. ^{13}C NMR of phenanthrene tripod ligand **S7** (125 MHz, $CDCl_3$, 298K).

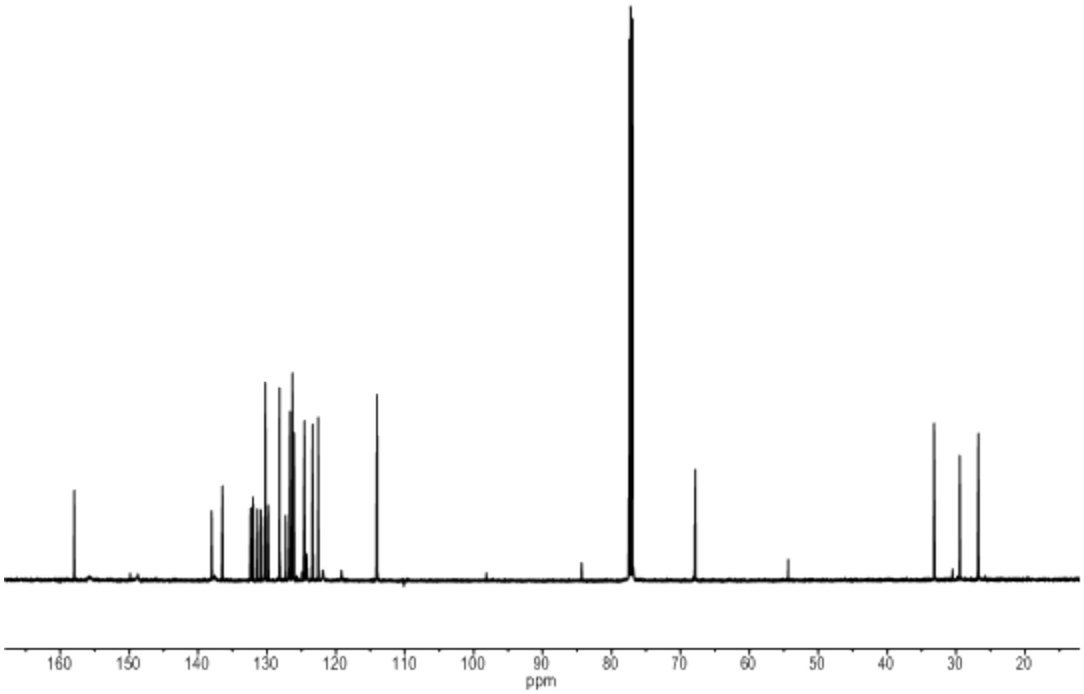

Figure A2.17. ^{1}H NMR of naphthalene tripod ligand **S8** (400 MHz, $CDCl_3$, 298K).

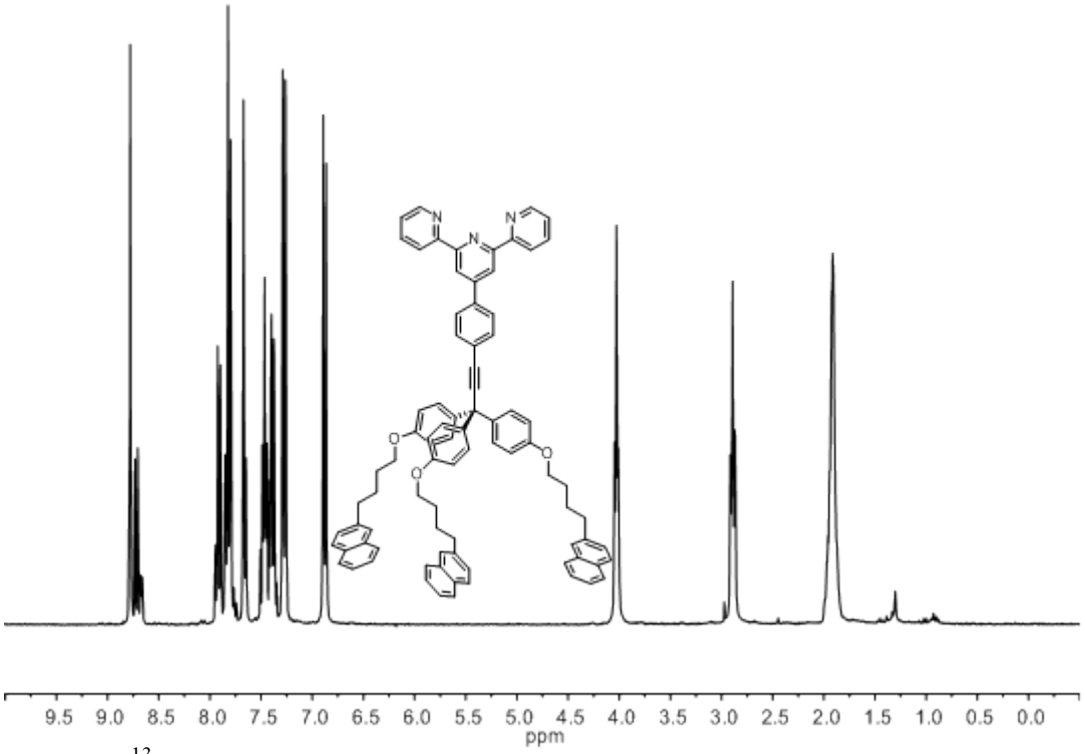

Figure A2.18. ^{13}C NMR of naphthalene tripod ligand **S8** (100 MHz, $CDCl_3$, 298K).

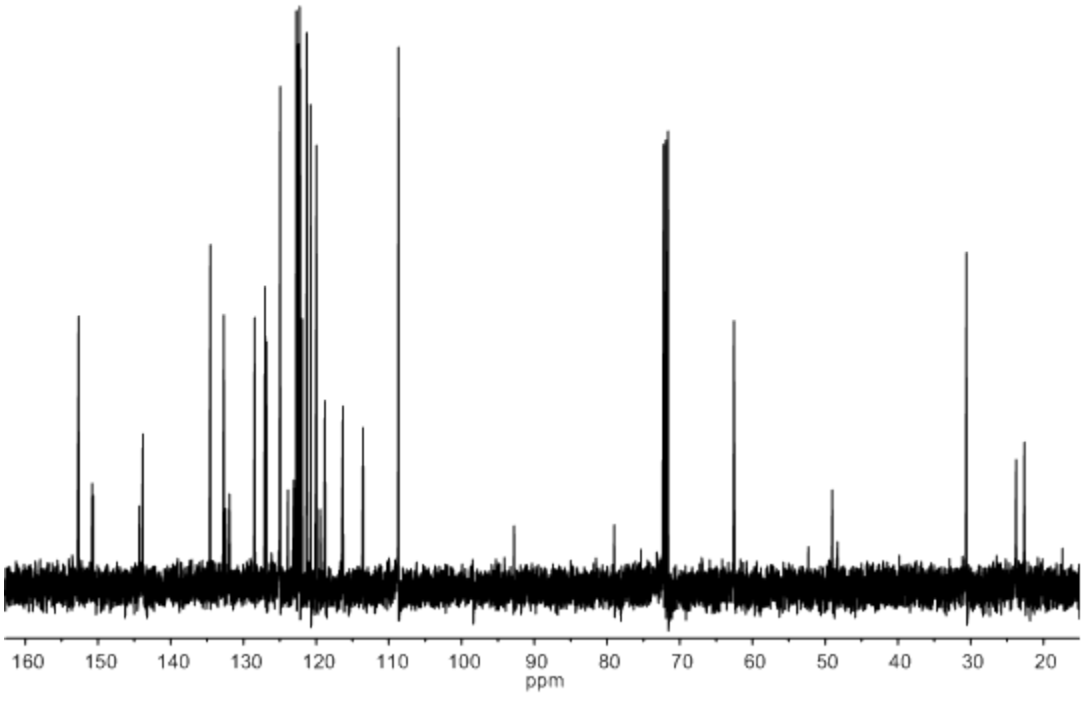

Figure A2.19. ^{1}H NMR of complex **1b·3PF$_6$** (600 MHz, $(CD_3)_2CO$, 298K).

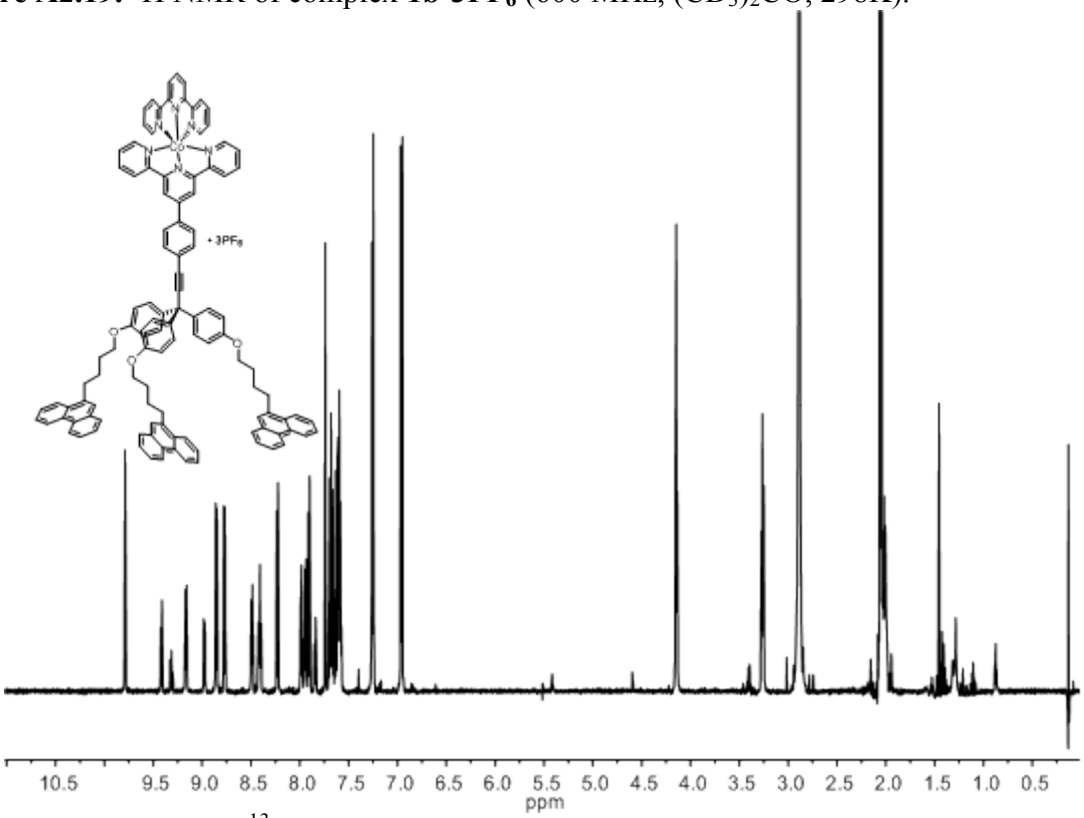

Figure A2.20. ^{13}C NMR of complex **1b·3PF$_6$** (125 MHz, $(CD_3)_2CO$, 298K).

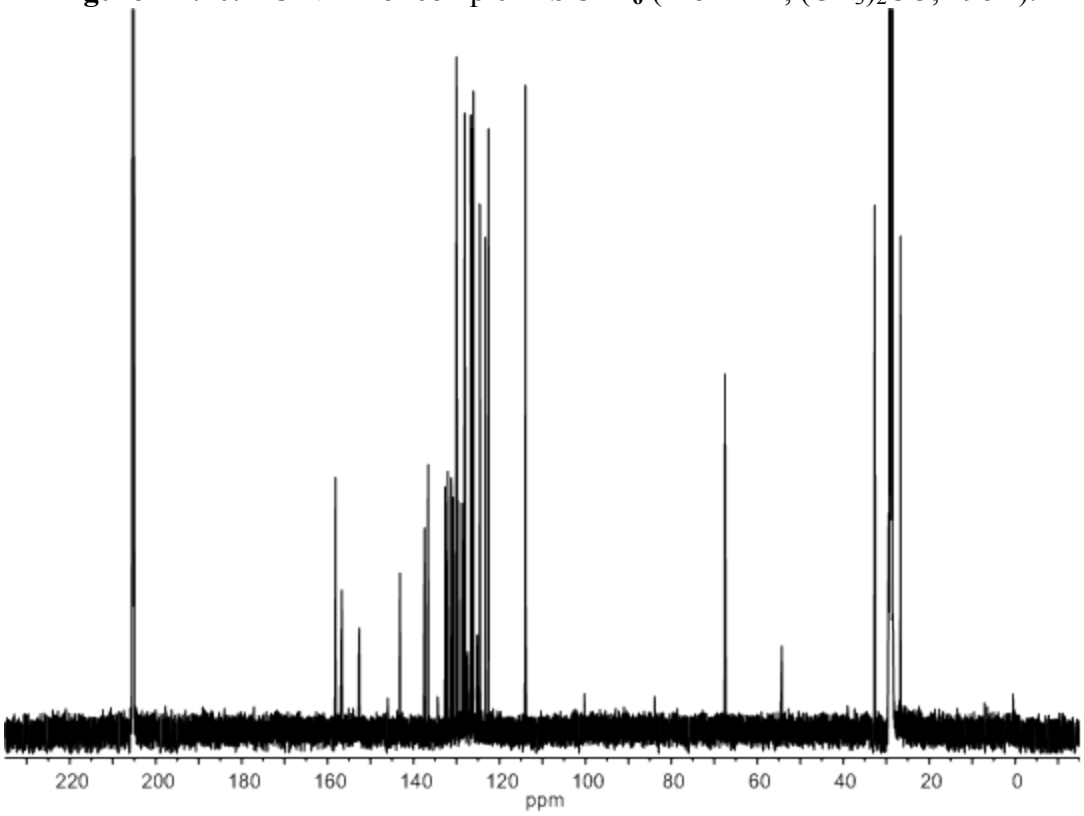

Figure A2.21. ^{1}H NMR of complex **1c·3PF$_6$** (600 MHz, $(CD_3)_2CO$, 298K).

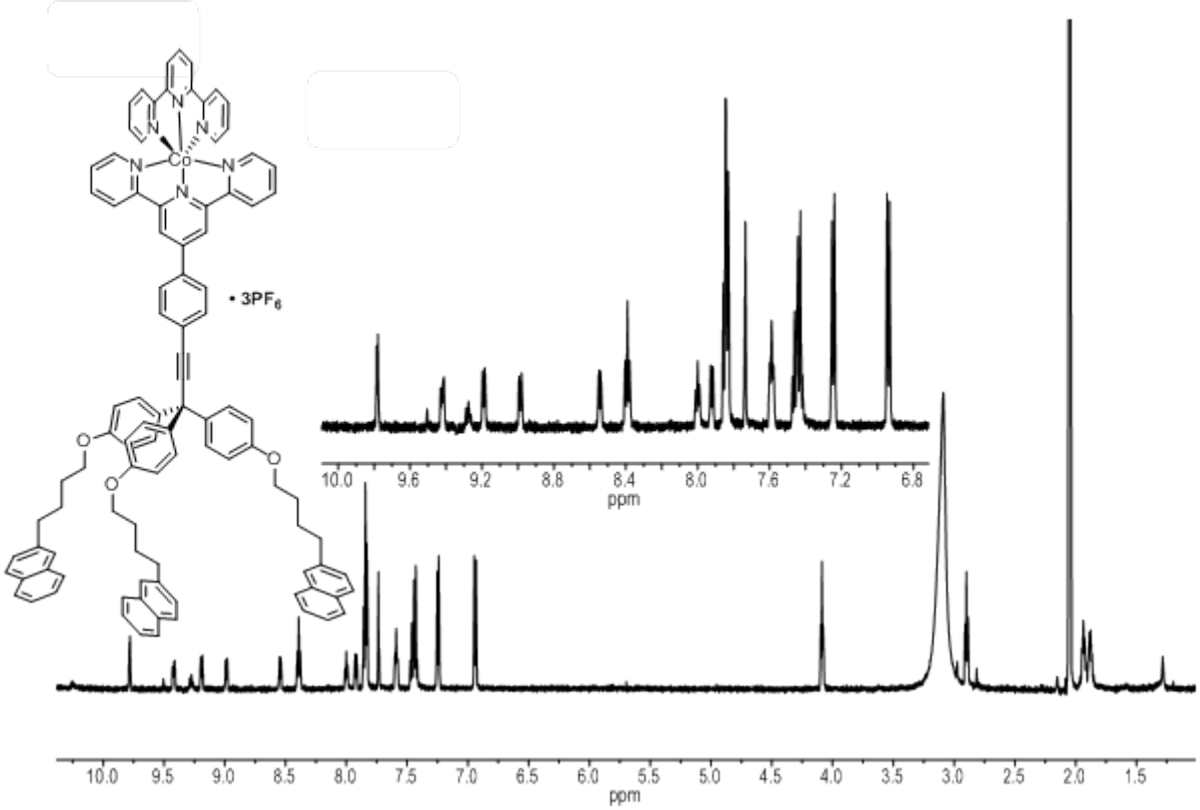

Figure A2.22. ^{13}C NMR of complex **1c·3PF$_6$** (125 MHz, $(CD_3)_2CO$, 298K).

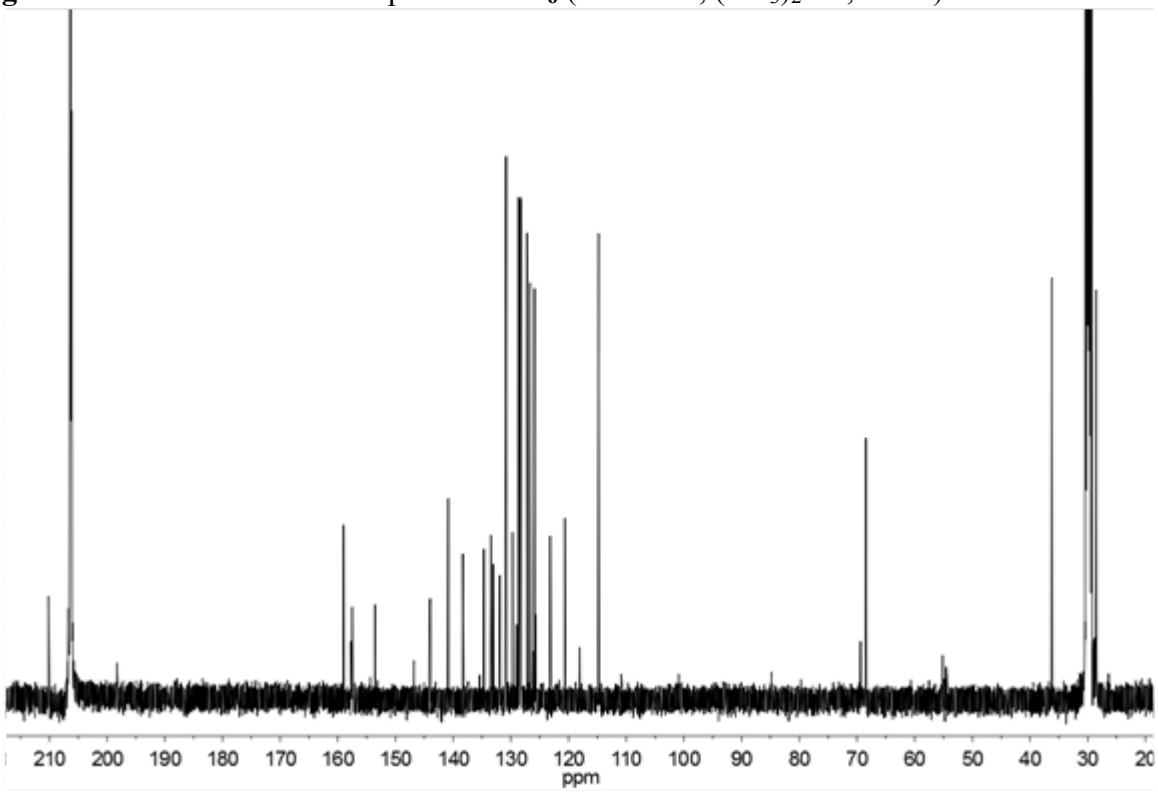

Figure A2.23. ^{1}H NMR of aryl bromide **S9** (300 MHz, $CDCl_3$, 298K).

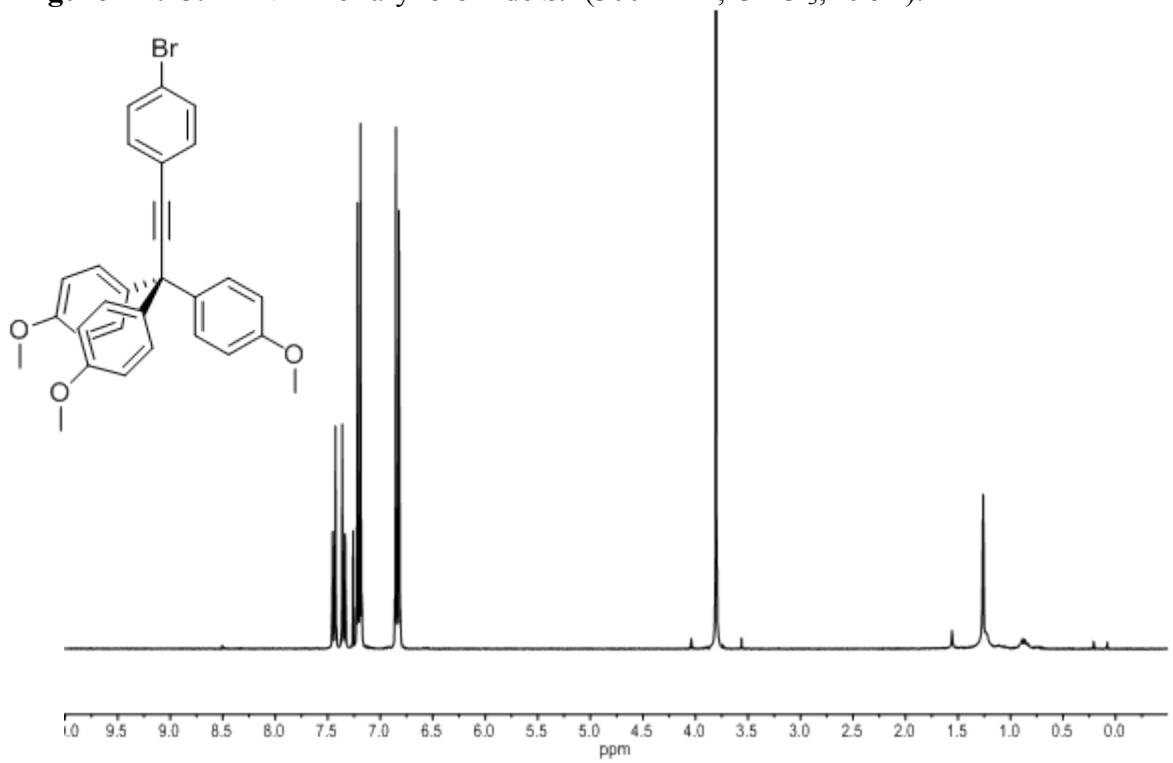

Figure A2.24. ^{13}C NMR of aryl bromide **S9** (75 MHz, $CDCl_3$, 298K).

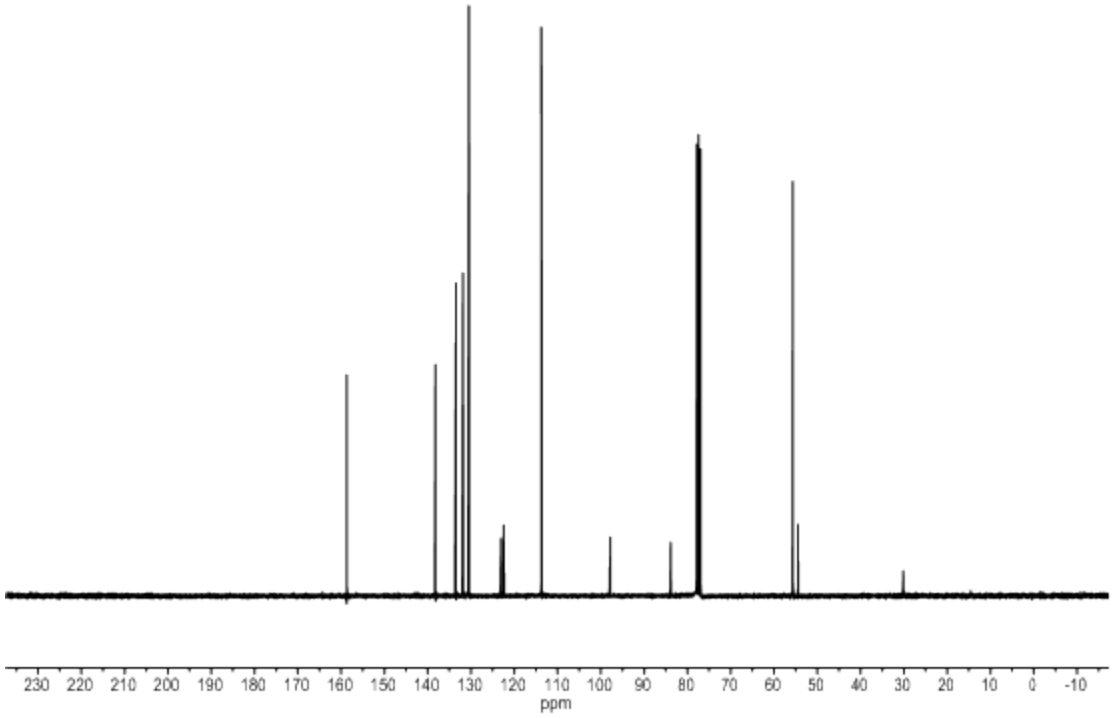

Figure A2.25. ^{1}H NMR of aryl bromide **6** (300 MHz, $CDCl_3$, 298K).

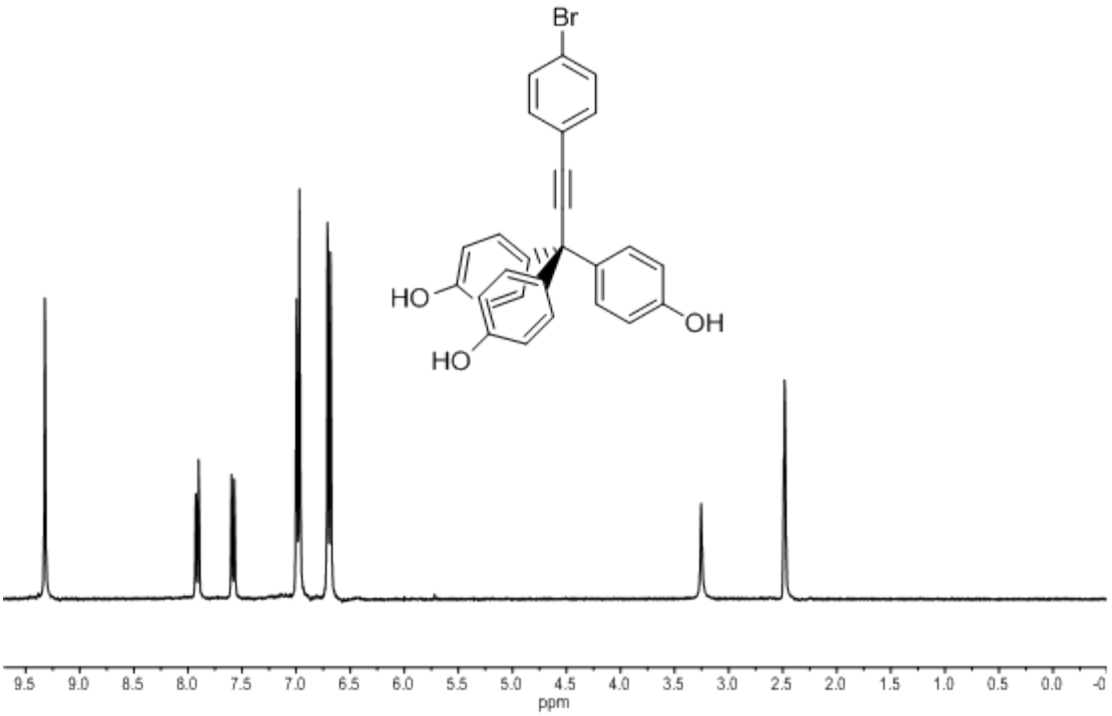

Figure A2.26. ^{13}C NMR of aryl bromide **6** (75 MHz, $CDCl_3$, 298K).

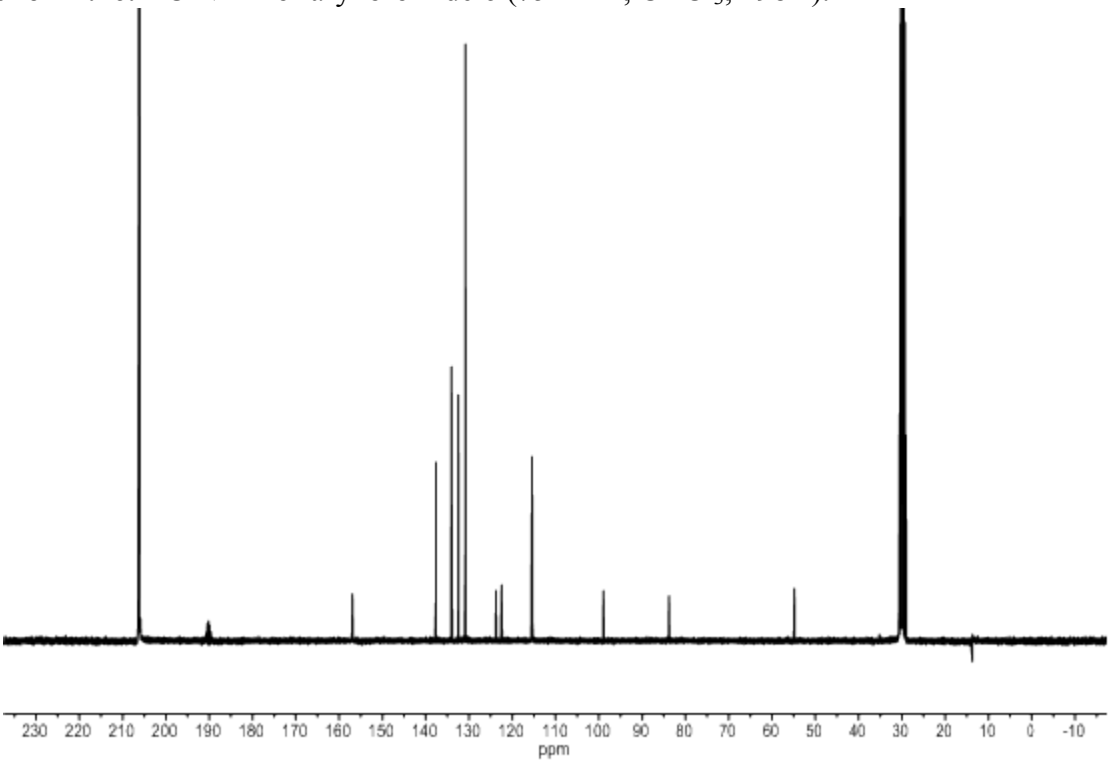

Figure A2.27. ^{1}H NMR of aryl bromide **S10** (300 MHz, $CDCl_3$, 298K).

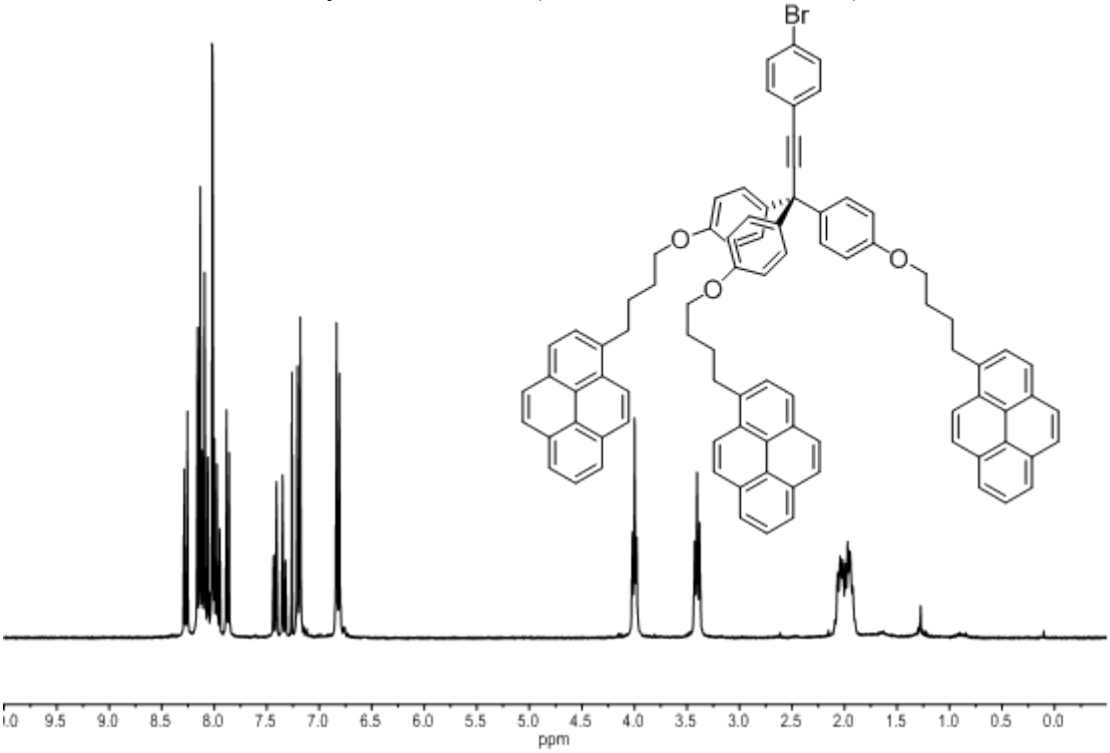

Figure A2.28. ^{13}C NMR of aryl bromide **S10** (75 MHz, $CDCl_3$, 298K).

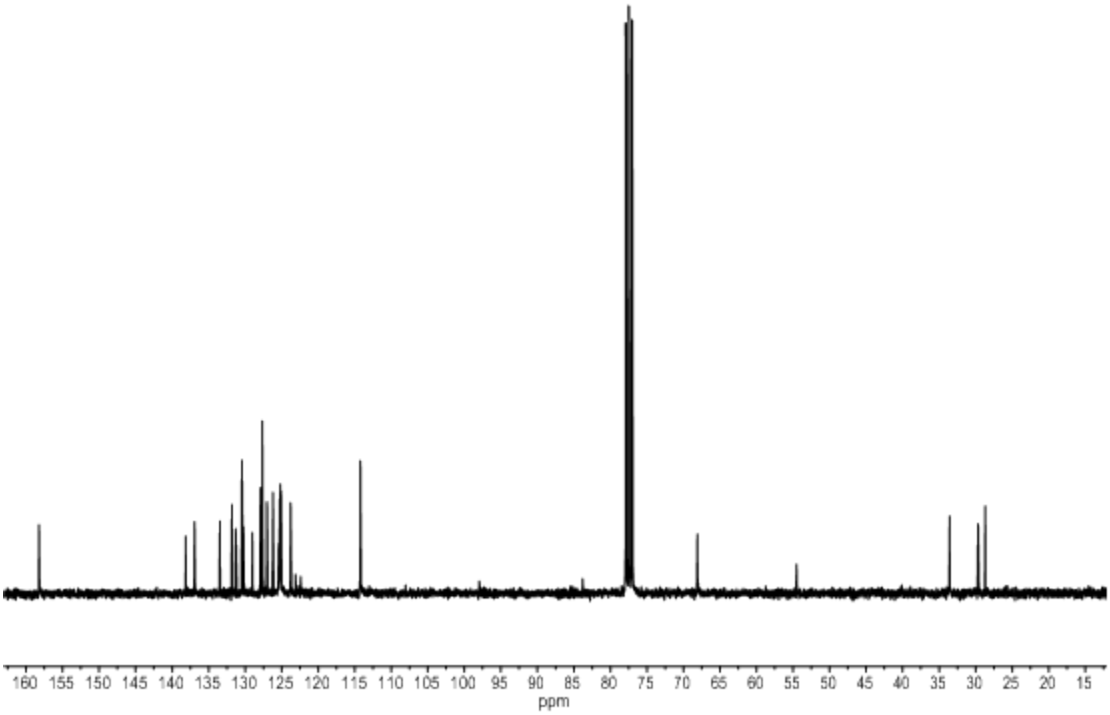

Figure A2.29. ^{1}H NMR of aryl bromide **S11** (300 MHz, $CDCl_3$, 298K).

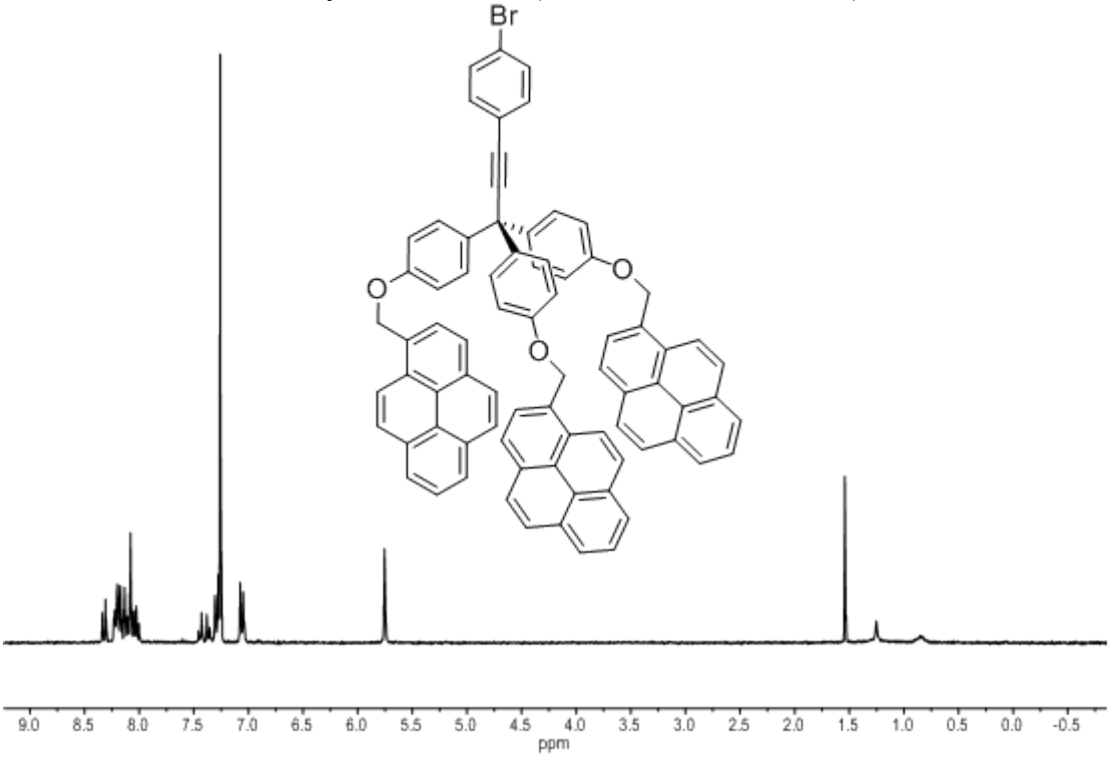

Figure A2.30. ^{13}C NMR of aryl bromide **S11** (75 MHz, $CDCl_3$, 298K).

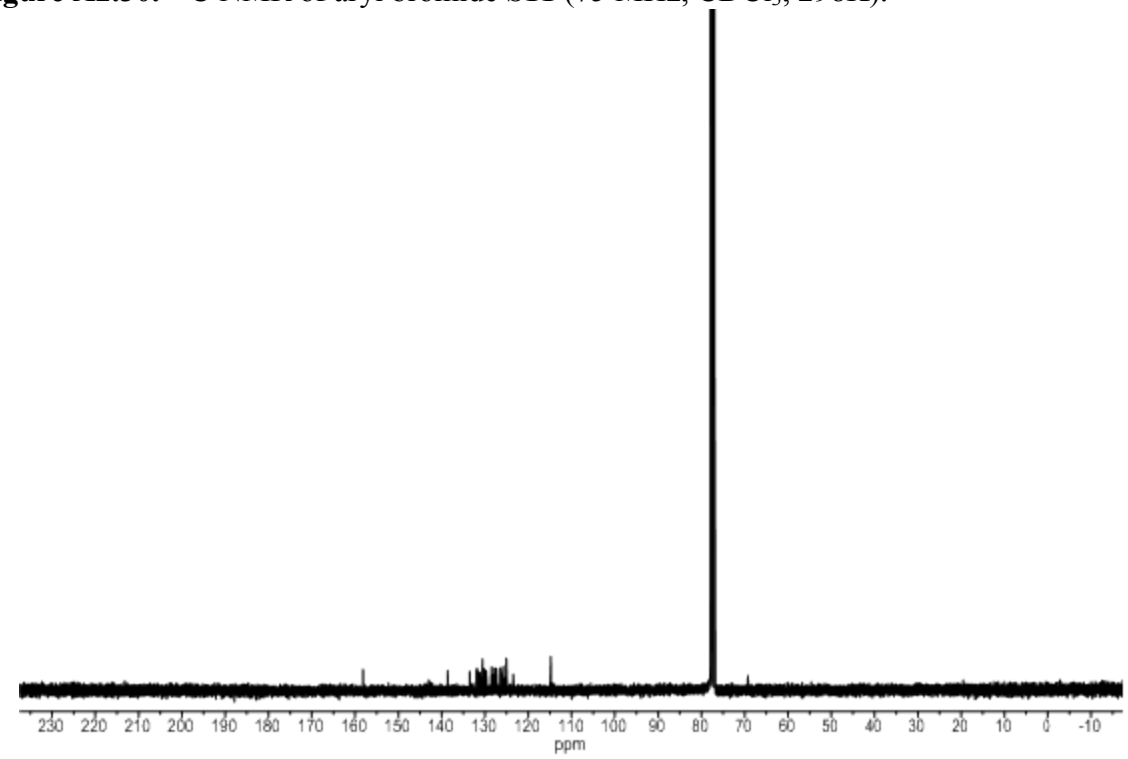

Figure A2.31. ^{1}H NMR of ferrocene tripod **7a** (300 MHz, $CDCl_3$, 298K).

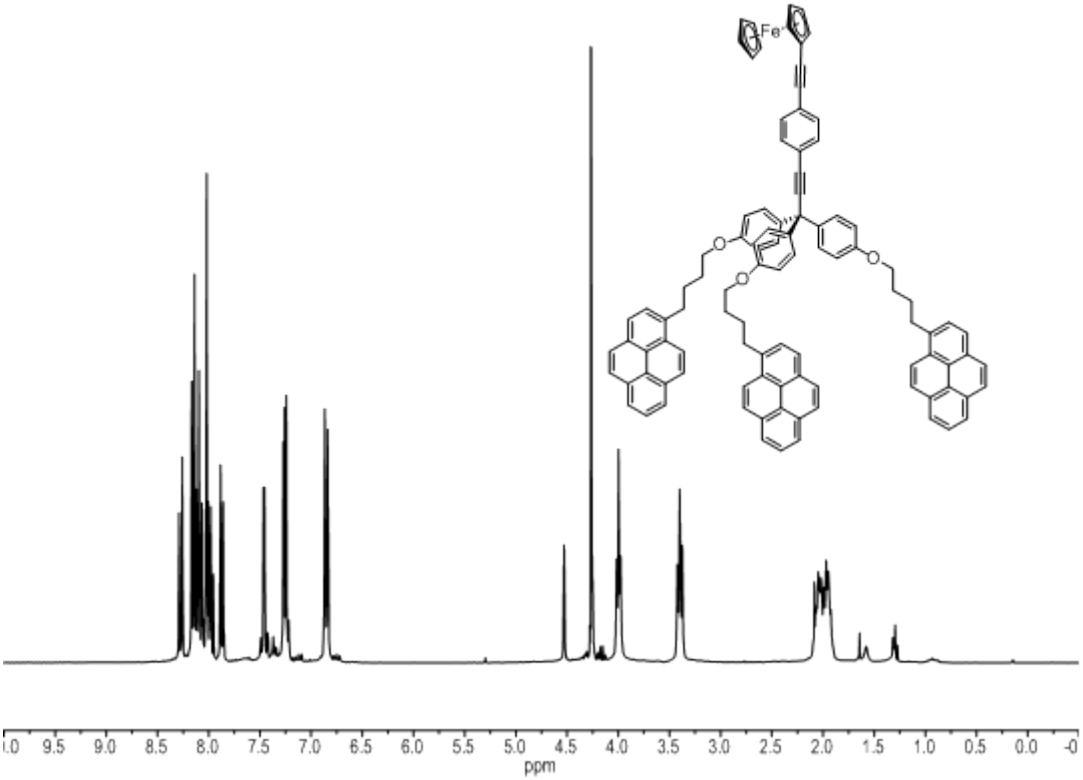

Figure A2.32. ^{13}C NMR of ferrocene tripod **7a** (75 MHz, $CDCl_3$, 298K).

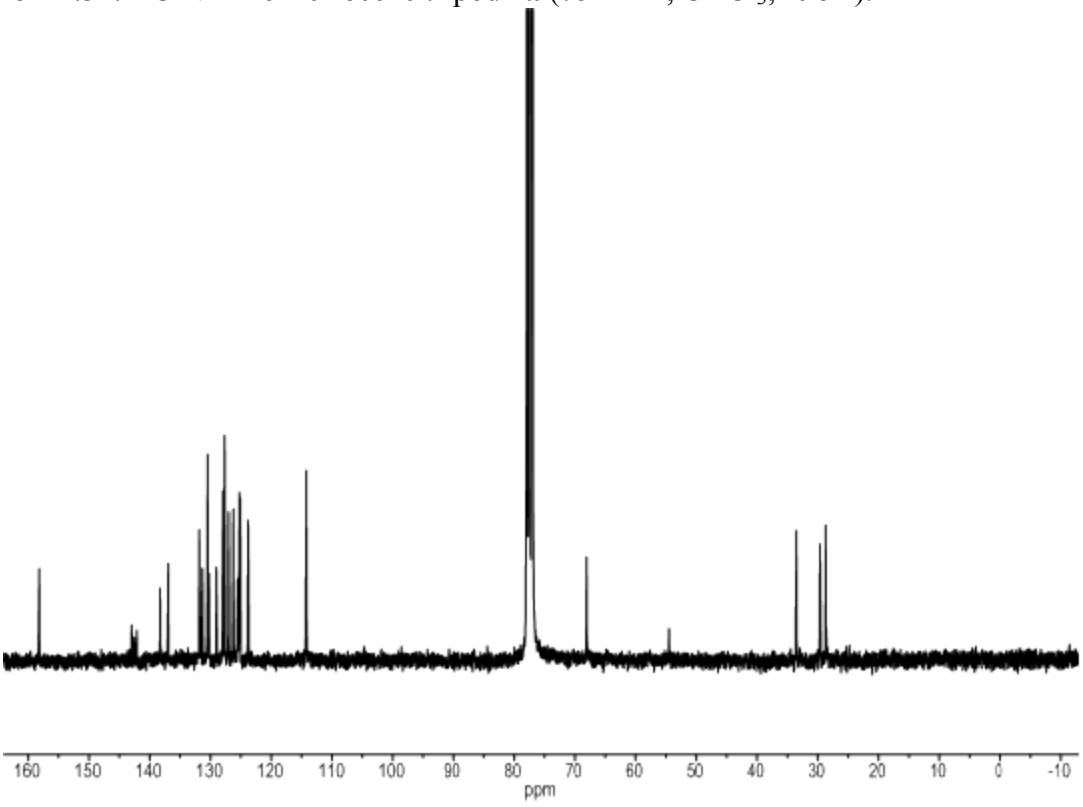

Figure A2.33. ^{1}H NMR of ferrocene tripod **7b** (600 MHz, $CDCl_3$, 298K).

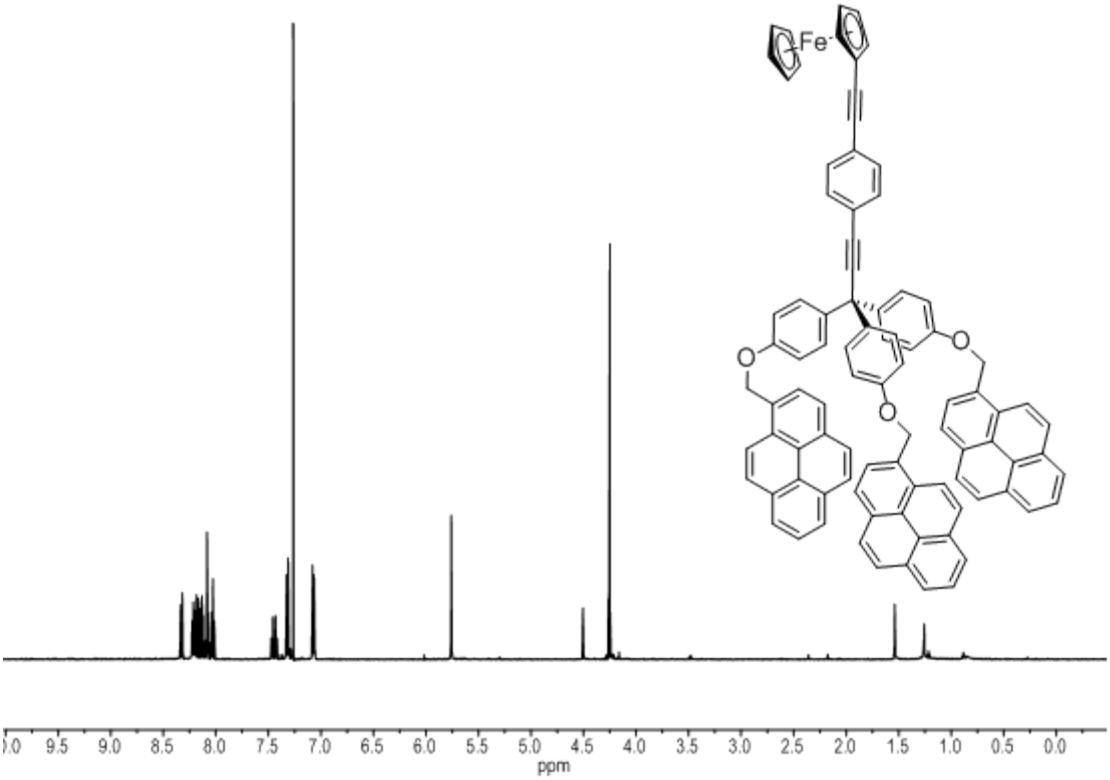

Figure A2.34. ^{13}C NMR of ferrocene tripod **7b** (100 MHz, $CDCl_3$, 298K).

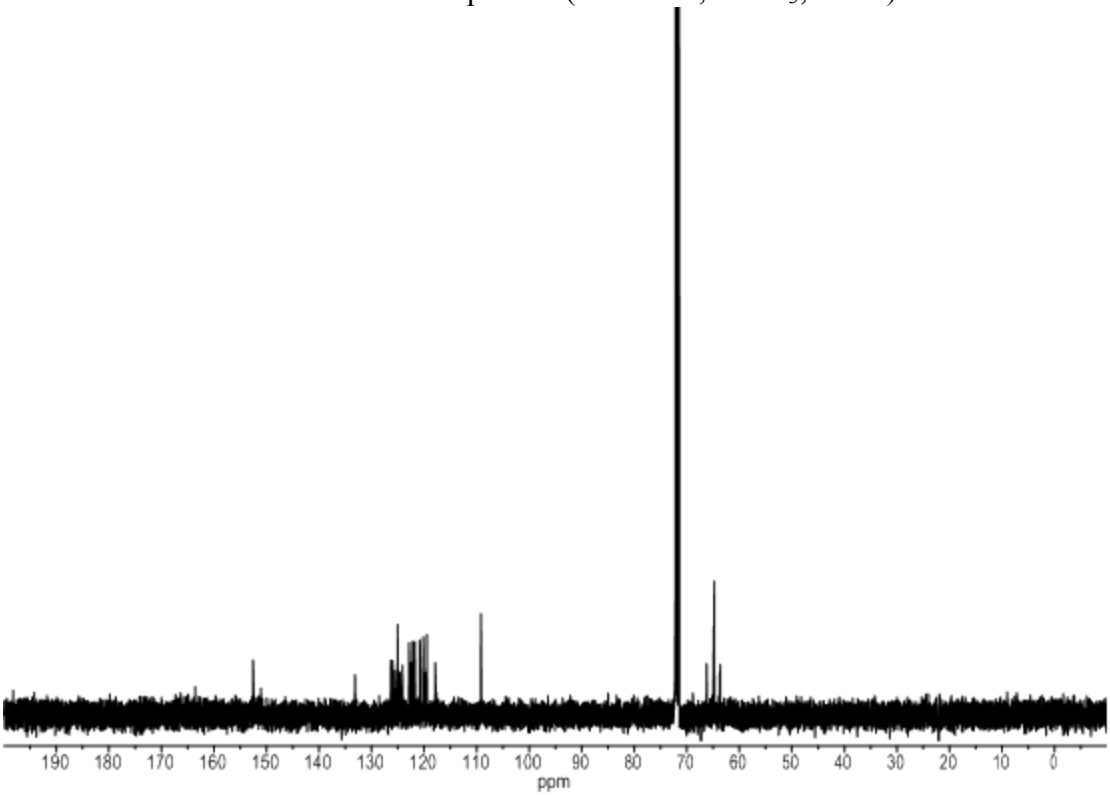

D. Raman Spectroscopy

Figure A2.33. Representative Raman spectrum of a graphene electrode.

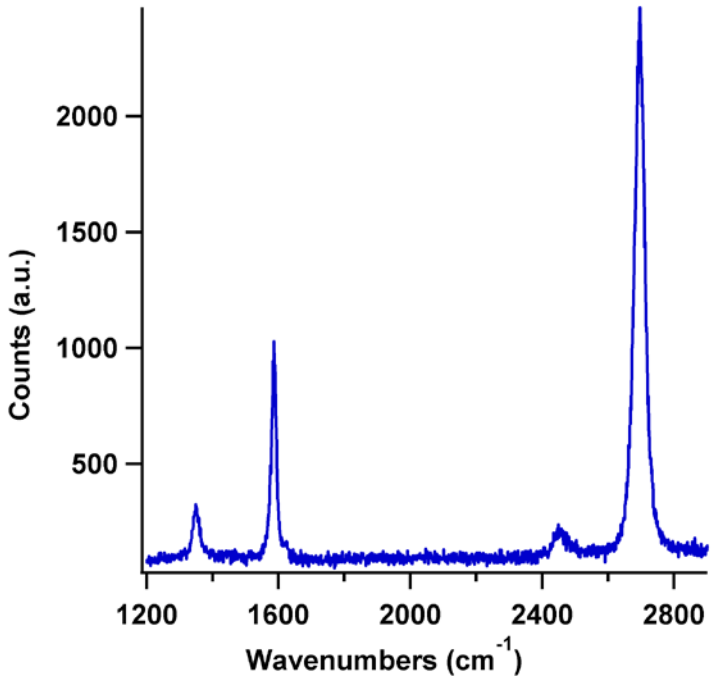

Figure A2.34. Representative Raman spectrum of a graphene electrode.

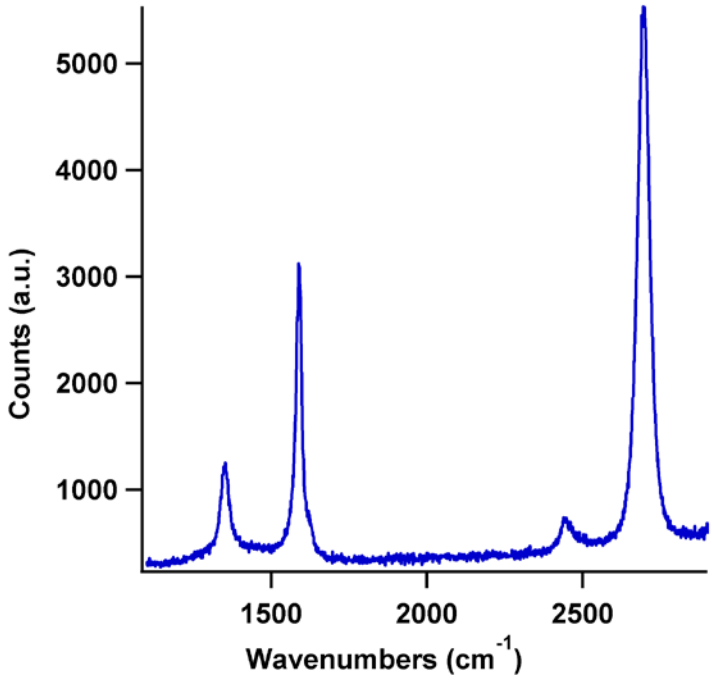

Figure A2.35. Representative Raman spectrum of a graphene electrode.

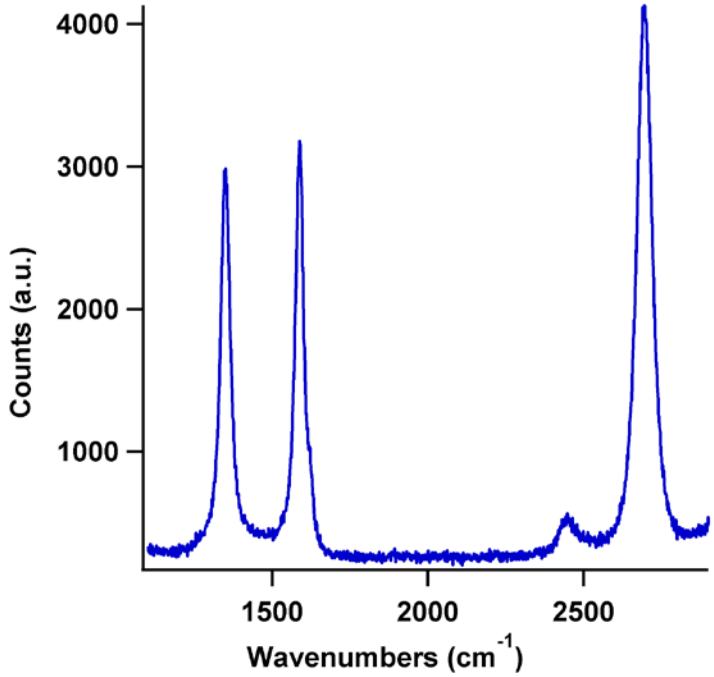

Figure A2.36. Representative Raman spectrum of a graphene electrode.

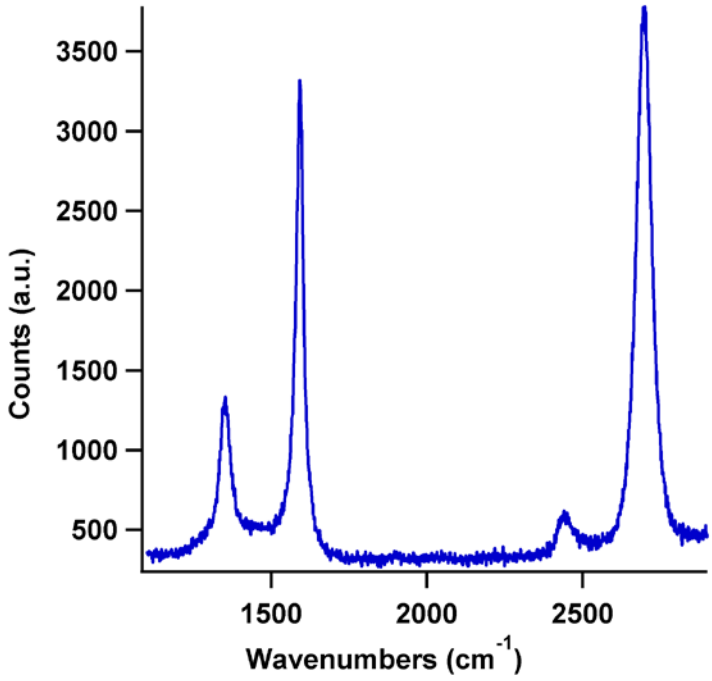

Figure A2.37. Representative Raman spectrum of a graphene electrode.

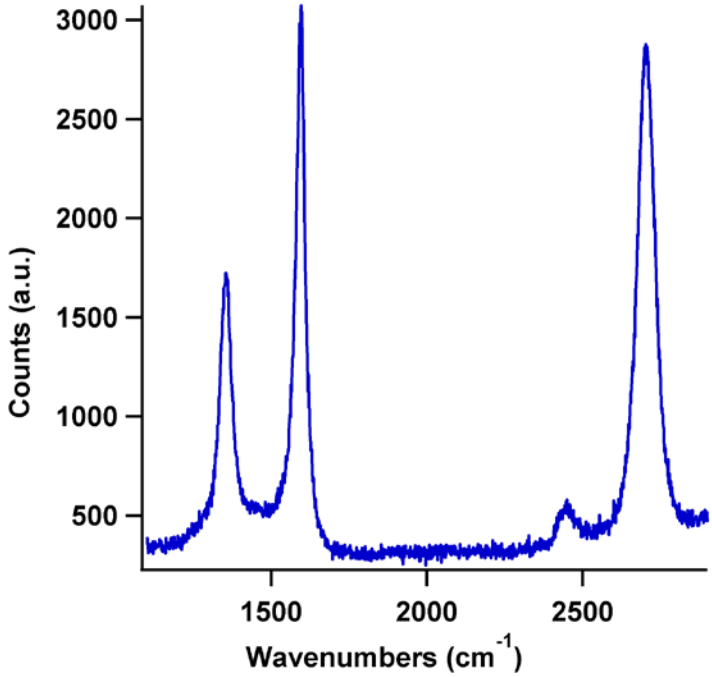

Figure A2.38. Representative Raman spectrum of a graphene electrode.

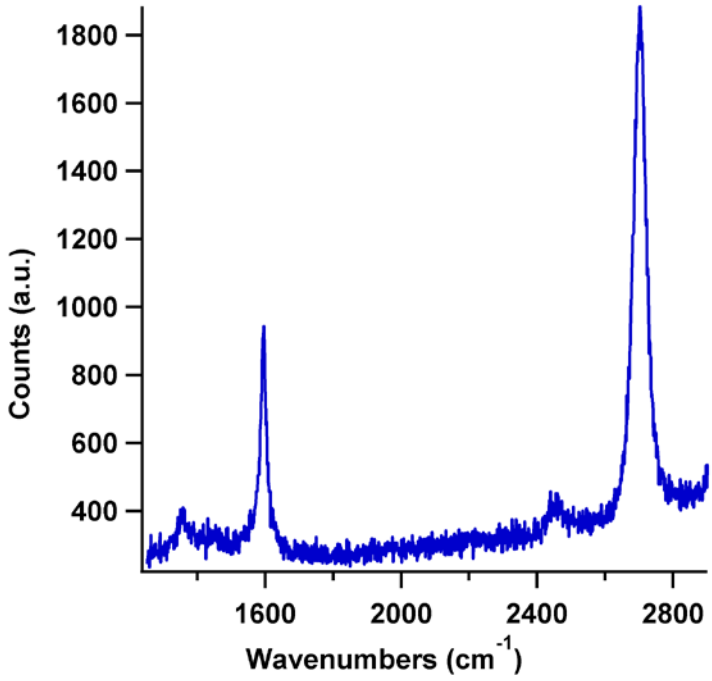

Figure A2.39. Representative Raman spectrum of a graphene electrode.

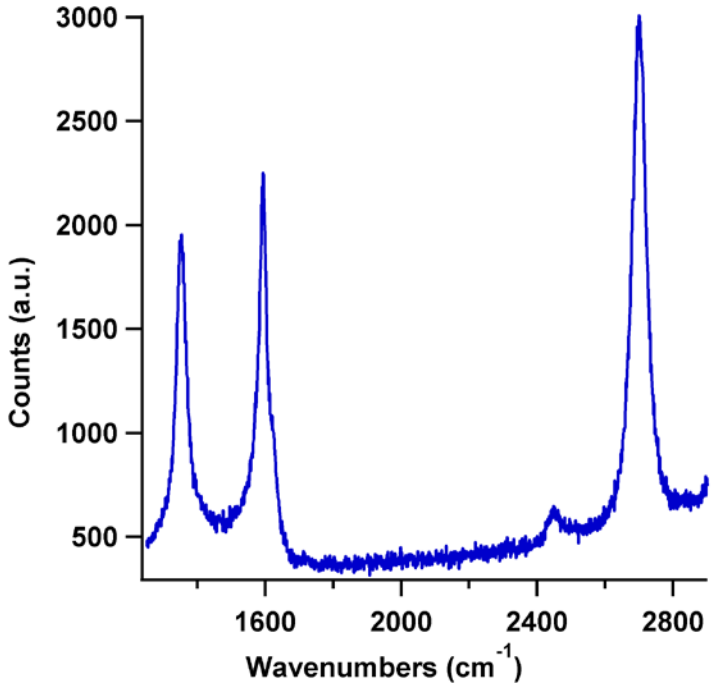

Figure A2.40. Representative Raman spectrum of a graphene electrode.

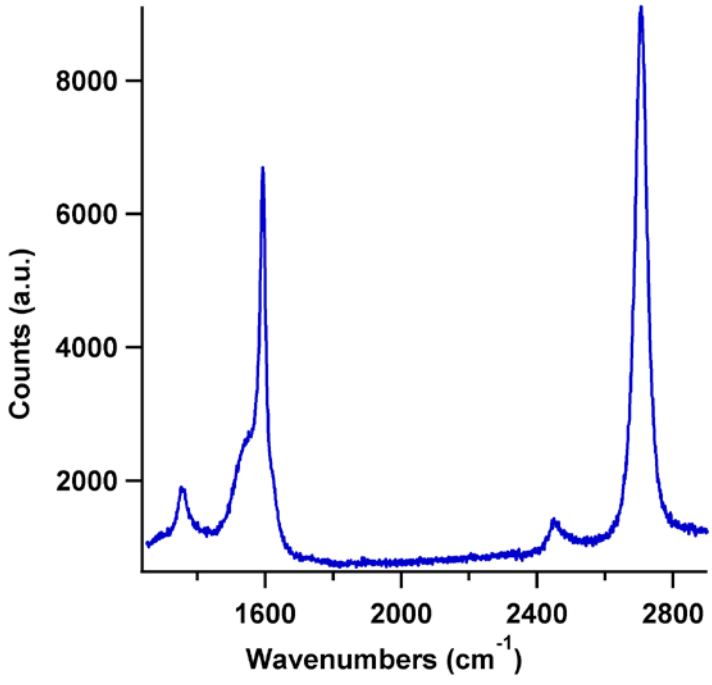

Figure A2.41. Representative spatial map of the intensity of the D band of a graphene electrode.

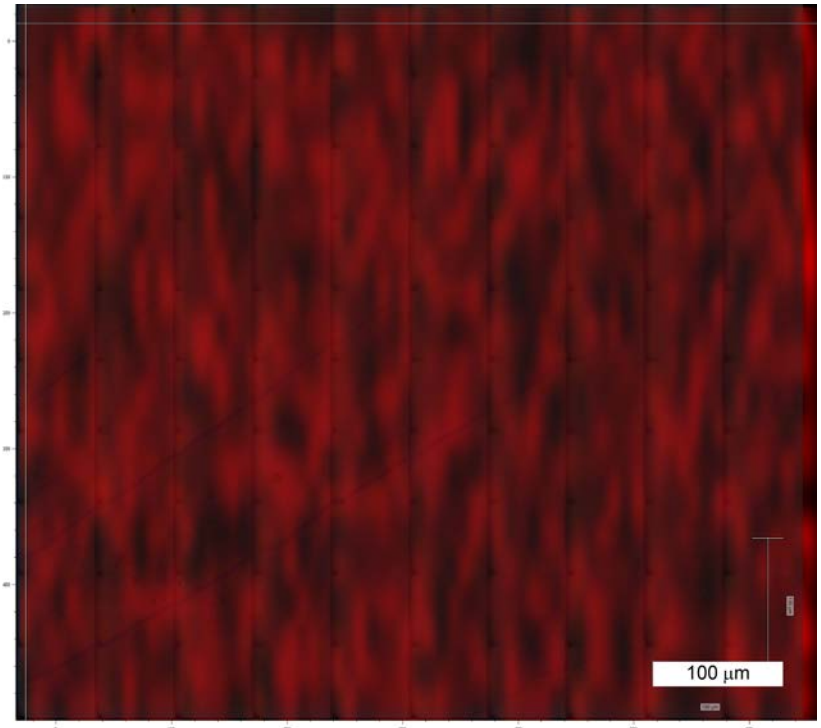

Figure A2.42. Representative spatial map of the intensity of the G band of a graphene electrode.

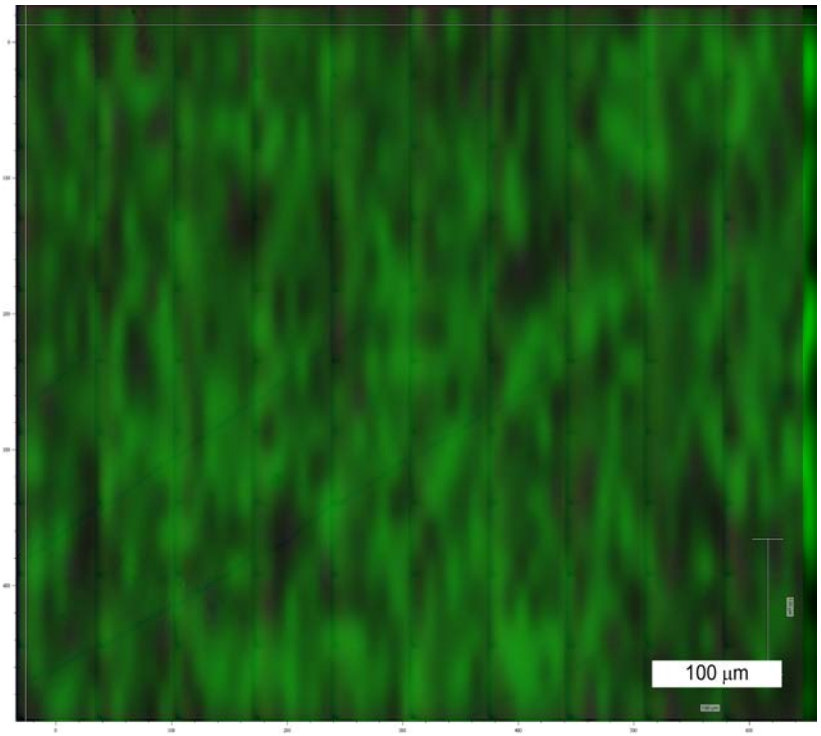

E. Electrochemical Characterization

Electrochemistry on graphene. All electrochemical experiments were carried out in 0.1M NBu_4ClO_4 in THF as supporting electrolyte under ambient conditions (i.e. oxygen and trace water). Graphene electrodes were prepared by transferring single-layer graphene grown on Cu foil by chemical vapor deposition onto Si/SiO_2 wafers.[8e] Electrical contact was made to the graphene by pressing a contact wire into a bead of In metal placed on the graphene surface outside of the electroactive region. All measurements used 1 mL of analyte solution. The electrochemical cell consisted of a custom made Teflon cell with a single compartment. Pt counter and pseudoreference electrodes were used. Cyclic voltammagrams were recorded in analyte solution in every case, except desorption experiments, which used supporting electrolyte only.

Table A2.1. ΔG_{ads} for compounds **1a-c•2PF$_6$** and **2•3PF$_6$** from the fit to the Langmuir model in Figure 3.1A

Table A3.1	
Compound	ΔG_{ads} **(kJ mol^{-1})**
1a•2PF$_6$	−38.8 ± 0.2
1b•2PF$_6$	−38.9 ± 0.46
1c•2PF$_6$	−40.7 ± 0.7
2•3PF$_6$	−38.3 ± 0.5

Figure A2.43. Cyclic voltammagram of tripod complex **1b·2PF$_6$** adsorbed on a graphene (0.1M NBu_4ClO_4 in THF, 0.1 V s^{-1}).

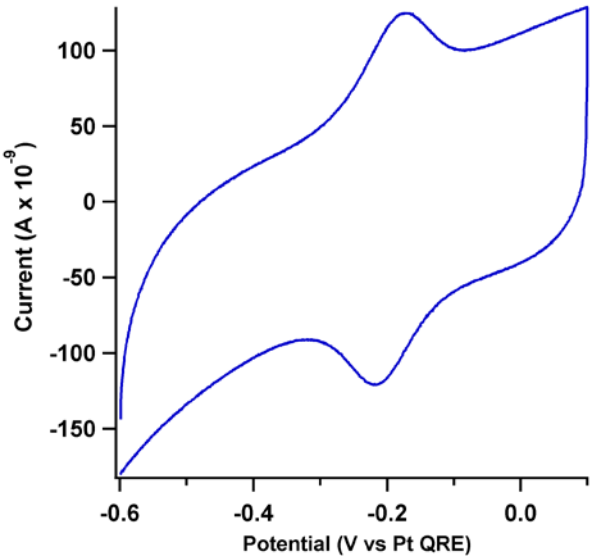

Figure A2.44. Plot of peak current with varying scan rate for tripod complex **1b·2PF$_6$** adsorbed on a graphene electrode (1.0 µM **1b·2PF$_6$**, 0.1M NBu_4ClO_4 in THF, 0.1 V s^{-1}).

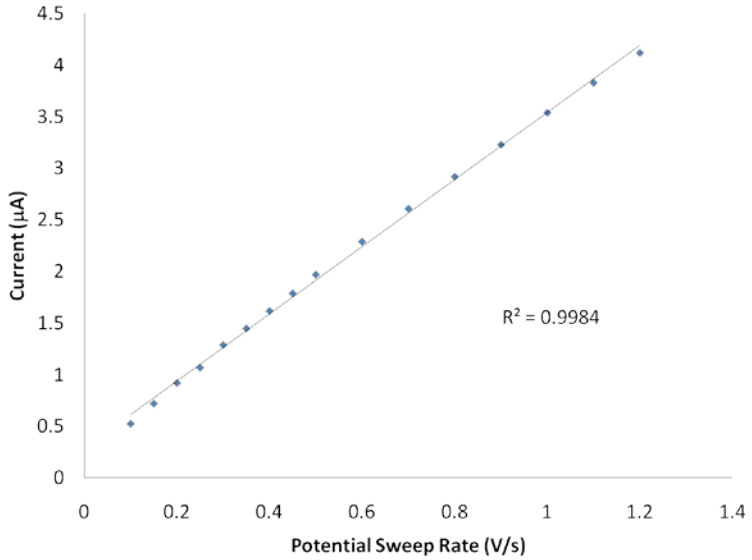

Figure A2.45. Cyclic voltammagram of tripod complex **1c·2PF$_6$** adsorbed on a graphene electrode in blank electrolyte (0.1M NBu_4ClO_4 in THF, 0.1 V s^{-1}).

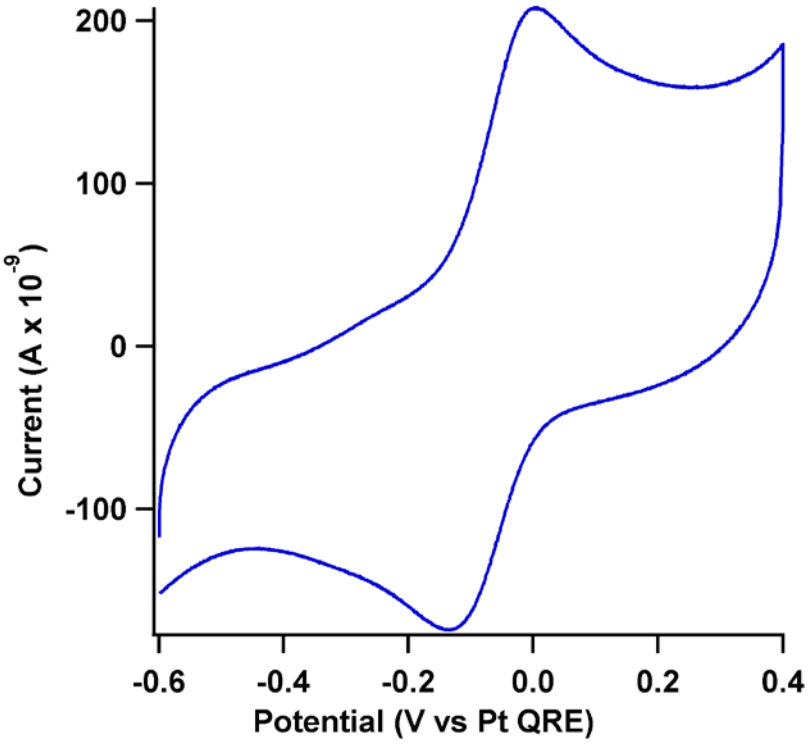

Figure A2.46. Plot of peak current with varying scan rate for tripod complex **1c·2PF$_6$** adsorbed on a graphene electrode (1.0 µM **1c·2PF$_6$**, 0.1M NBu_4ClO_4 in THF, 0.1 V s^{-1}).

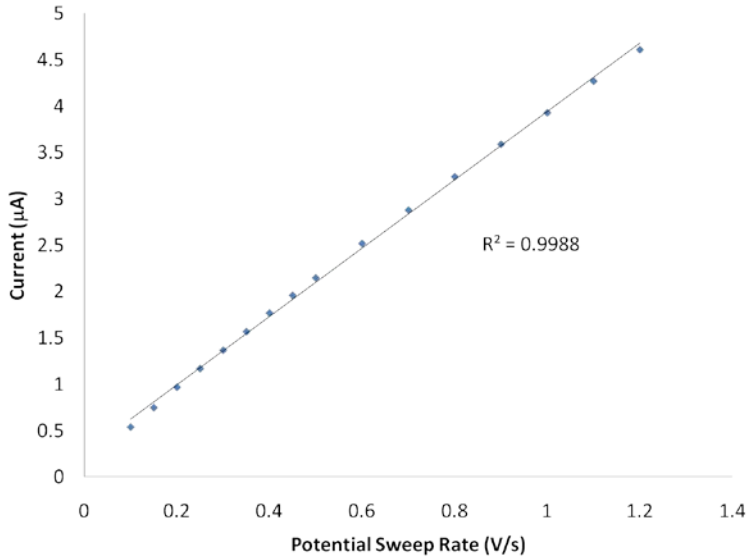

Figure A2.47. Cyclic voltammagram of tripod complex **7a** adsorbed on a graphene electrode in blank electrolyte (0.1M NBu_4ClO_4 in THF, 0.1 V s^{-1}).

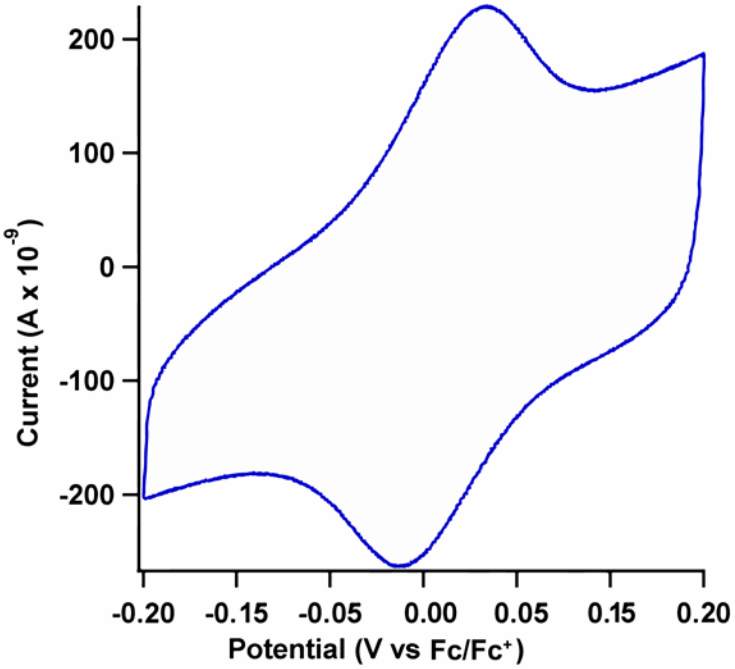

Figure A2.48. Cyclic voltammagram of tripod complex **7b** adsorbed on a graphene electrode in blank electrolyte (0.1M NBu_4ClO_4 in THF, 0.1 V s^{-1}).

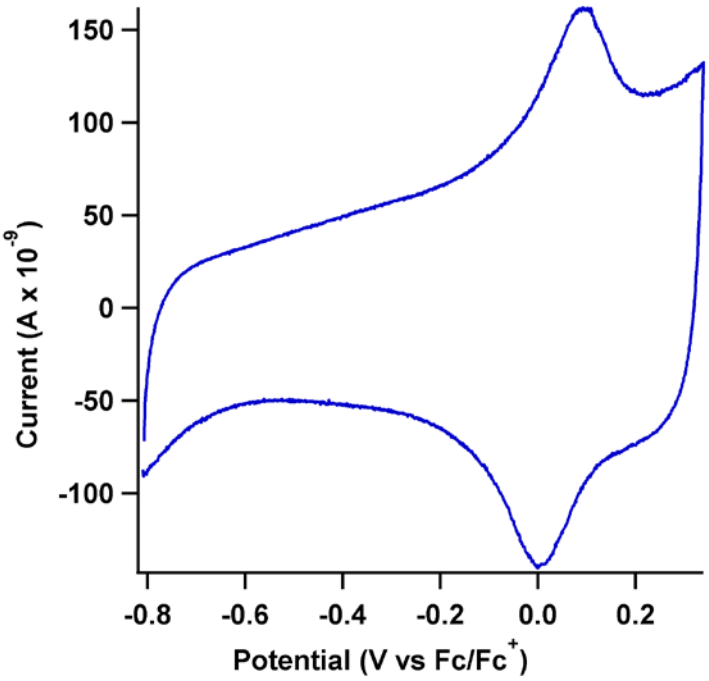

F. References

(1) (a) Wang, J.; Hanan, G. S. *Synlett* **2005**, *2005*, 1251; (b) Glass, T. E. *J. Am. Chem. Soc.* **2000**, *122*, 4522. (c) Mann, J. A.; Rodríguez-López, J.; Abruña, H. D.; Dichtel, W. R. *J. Am. Chem. Soc.* **2011**, *133*, 17614.

(2) Levendorf, M. P.; Ruiz-Vargas, C. S.; Garg, S.; Park, J. *Nano Lett.* **2009**, *9*, 4479.

(3) Laviron, E. J. *Electroanal. Chem.* **1979**, *101*, 19.

G. Complete references from chapter body

(2a) Bae, S.; Kim, H.; Lee, Y.; Xu, X.; Park, J.-S.; Zheng, Y.; Balakrishnan, J.; Lei, T.; Ri Kim, H.; Song, Y. I.; Kim, Y.-J.; Kim, K. S.; Ozyilmaz, B.; Ahn, J.-H.; Hong, B. H.; Iijima, S. *Nature Nanotech.* **2010**, *5*, 574.

(13m) Pollard, A. J.; Perkins, E. W.; Smith, N. A.; Saywell, A.; Goretzki, G.; Phillips, A. G.; Argent, S. P.; Sachdev, H.; Müller, F.; Hüfner, S.; Gsell, S.; Fischer, M.; Schreck, M.; Osterwalder, J.; Greber, T.; Berner, S.; Champness, N. R.; Beton, P. H. *Angew. Chem. Int. Ed.* **2010**, *49*, 1794.

(29b) Yu, Q.; Jauregui, L. A.; Wu, W.; Colby, R.; Tian, J.; Su, Z.; Cao, H.; Liu, Z.; Pandey, D.; Wei, D.; Chung, T. F.; Peng, P.; Guisinger, N. P.; Stach, E. A.; Bao, J.; Pei, S.-S.; Chen, Y. P. *Nature Mater.* **2011**, *10*, 443.

CHAPTER FOUR

QUANTIFICATION OF THE SURFACE DIFFUSION OF TRIPODAL BINDING MOTIFS ON GRAPHENE USING SCANNING ELECTROCHEMICAL MICROSCOPY

4.1 Abstract

The surface diffusion of a cobalt *bis*-terpyridine, $Co(tpy)_2$-containing tripodal compound (**1·2PF$_6$**), designed to noncovalently adsorb to graphene through three pyrene moieties, has been studied by scanning electrochemical microscopy (SECM) on single-layer graphene (SLG). An initial boundary approach was designed in which picoliter droplets (radii ≈15−50 μm) of the tripodal compound were deposited on an SLG electrode, yielding microspots in which a monolayer of the tripodal molecules is initially confined. The time evolution of the electrochemical activity of these spots was detected at the aqueous phosphate buffer/SLG interface by SECM, in both generation/collection (G/C) and feedback modes. The tripodal compound microspots exhibit differential reactivity with respect to the underlying graphene substrate in two different electrochemical processes. For example, during the oxygen reduction reaction, adsorbed **1·2PF$_6$** tripodal molecules generate more H_2O_2 than the unfunctionalized graphene surface. The product was detected with spatial and temporal resolution using the SECM tip. The tripodal compound also mediates the oxidation of an Fe(II) species, generated at the SECM tip, under conditions in which SLG exhibits slow interfacial charge transfer. In each case, SECM images, obtained at longer times, show a gradual decrease in the electrochemical response due to radial diffusion of the adsorbed molecules outward from the microspots onto the

unfunctionalized areas of the SLG surface. This response was to a simple surface diffusion model, which yielded excellent agreement between the two experiments for the effective diffusion coefficients: D_{eff} = 1.6 (± 0.9) × 10^{-9} cm^2/s and D_{eff} = 1.5 (± 0.6) × 10^{-9} cm^2/s for G/C and feedback modes, respectively. Control experiments ruled out alternative explanations for the observed behavior, such as deactivation of the Co(II/III) species or of the SLG, and verified that the molecules do not diffuse when confined to obstructed areas. The noncovalent nature of the surface functionalization, together with the surface reactivity and mobility of these molecules, provides a means to couple the superior electronic properties of graphene to compounds with enhanced electrochemical performance, a key step toward developing dynamic electrode surfaces for sensing, electrocatalysis, and electronic applications. The work described in this chapter was performed in collaboration with Dr. Joaquín Rodrígues López., Ms. Nicole Ritzert, and Ms. Cen Tan under the direction of Prof. H. D. Abruña and Prof. W. R. Dichtel and was published in the *Journal of the American Chemical Society* (Rodríguez-López, J.; Ritzert, N. L.; Mann, J. A.; Tan, C.; Dichtel, W. R.; Abruña, H. D. *J. Am. Chem. Soc.* **2012**, *134*, 6224.)

4.2 Introduction

Here, we demonstrate that single layer graphene (SLG) allows the mobility of redox-enhancing molecular binders at its surface in an electrolytic medium. The superb physical, optical, and electronic properties[1–4] of single- and multilayer graphene motivate its fundamental study and development for applications including transparent electrodes,[5–8] resonators,[9,10] transistors,[11–16] and others. However, within an electrochemical context, SLG exhibits slow interfacial charge transfer kinetics at

the graphene/solvent interface with many redox mediators, as do highly oriented pyrolytic graphite (HOPG) and carbon nanotubes.[17–21] This reactivity increases with the intentional generation of oxygenated defects,[22] nitrogen incorporation,[23] and in graphene oxide samples with abundant reactive edges and oxide sites.[24–29] However, these modifications disrupt graphene's conjugation.[25] In contrast, noncovalent functionalization couples the superior electronic properties of SLG to adsorbed molecules with enhanced electrochemical activity. In Chapter 2, we introduced[30] the tripodal compound **1·2PF$_6$**, which consists of a Co(II) *bis*-terpyridine [Co(tpy)$_2$] redox center attached to a tetrahedral core bearing three pyrene "feet". The pyrene moieties interact strongly with the graphene surface[31] (Figure 4.1A), and this multivalent design results in kinetically stable monolayers that resist desorption under infinite dilution conditions.[30]

Although **1·2PF$_6$** molecules do not desorb readily from SLG, we hypothesized that they might diffuse over the two dimensional carbon surface. Here we explore the surface mass transport properties of **1·2PF$_6$** on SLG by detecting its differential electrochemical activity with spatial and temporal resolution. Thus we designed two strategies, each based on the scanning electrochemical microscope (SECM),[32–34] for the electrochemical detection of the **1·2PF$_6$** surface concentration in real time, allowing its surface diffusion coefficient to be measured. In this work, we demonstrate the ability of adsorbed functionalities to modify the electrochemical activity of graphene and exploit the dynamic nature of noncovalent π-stacking interactions.

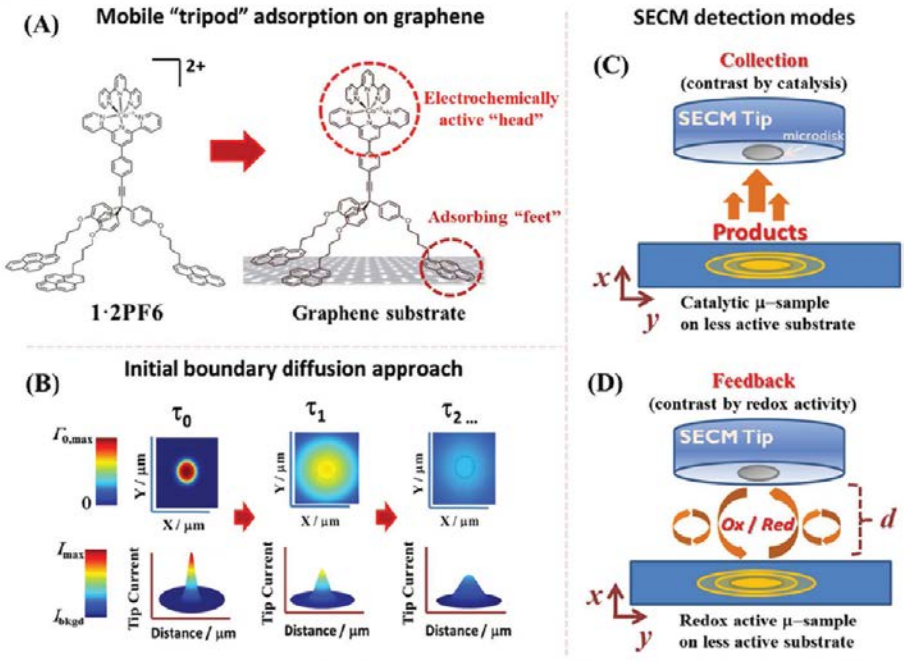

Figure 4.1. Strategy for characterizing the surface diffusion of a tripodal compound on graphene using SECM. (A) Chemical structure of tripodal compound **1·2PF$_6$** and its proposed mode of adsorption onto SLG. (B) Initial boundary approach for measuring the surface diffusion of **1·2PF$_6$**, initially confined to a few micrometers-sized spot, by detecting a decrease in its electrochemical activity as a result of radial diffusion onto the bulk surface. Schematics of the complementary substrate generation/tip collection (C) and feedback modes (D) of SECM. In each case, the SECM microelectrode (radius a) is positioned at a distance d from the substrate and scanned in the *x* and *y* directions to produce a spatially and temporally resolved reactivity image.

Controlling the surface diffusion of molecular electrocatalysts[35] on a model carbon support, such as graphene, is an intriguing possibility for designing efficient catalytic platforms and studying association phenomena,[35,36] for which dynamic interactions between electrocatalysts may benefit the product selectivity or catalytic performance. These and other cooperative properties might emerge from the ability of the surface to present dynamic combinations of functional groups. Finally, functionalizing graphene with [Co(tpy)$_2$] or other redox couples using motifs that bind with predictable and well-defined orientations might also facilitate future studies of molecular electronic

phenomena.[37,38] Relatively few techniques can measure surface diffusion coefficients at the solid/liquid or solid/electrolyte interface. Electrochemical scanning tunneling microscopy (EC-STM) may be used in principle,[39,40] but this technique is uncommon because of the difficulty of imaging in liquids at room temperature.[41] In most instances, only qualitative data are obtained or inferred.[42] STM has been used at cryogenic temperatures to study molecular adsorption on graphene under more favorable conditions.[43,44] Nuclear magnetic resonance spectroscopy has been applied to a limited subset of samples, such as lipid bilayers[45,46] or to suspended samples of nanoparticle electrocatalysts. [47,48] Fluorescence measurements,[49,50] such as the widely used fluorescence recovery after photobleaching method (FRAP),[51−53] in which the time dependence of the fluorescence restoration of a small photobleached spot is monitored, might also be used. However graphene oxide, reduced graphene oxide, and pristine SLG strongly quench organic dyes[54−57] and semiconductor nanocrystals,[58] likely rendering these surfaces incompatible with the FRAP approach. The limitations of the above techniques motivated us to develop an electrochemical method for characterizing the surface diffusion of **1·2PF$_6$** on SLG. The use of SECM for measuring surface diffusion coefficients was pioneered by Unwin[59] and co-workers at the water/air interface, first by taking advantage of acid−base equilibria[60−62] to use the generation/collection modes to study proton diffusion along Langmuir monolayers and later through feedback measurements using redox-active amphiphiles.[63] Effective diffusion coefficients for charge transfer across thin redox-active layers were also measured using an electrochemical analogue of FRAP experiments.[64−66] These electrochemical experiments require an inert supporting interface because it is

otherwise difficult to deconvolve the SECM response to the background activity and lateral conductivity of the electrode[67,68] from charge transport or molecular diffusion. The low interfacial activity of graphene for several redox mediators provides the requisite low background over which the electrochemically active tripod molecules can be readily detected. Other complications that might obscure a linear SECM response to variations in the molecular surface concentration, such as a large self-exchange rate between adjacent redox centers,[69] were circumvented in this work through the judicious choice of the Co(II/III) redox couple, whose slow self-exchange rate[70,71] originates from an unfavorable spin conversion.[72,73] Likewise, as discussed in Chapter 2, we previously found that **1·2PF$_6$** exhibits Langmurian adsorption onto the SLG surface, which suggests that interactions between adjacent molecules are sufficiently weak to not complicate the surface diffusion analysis.[30]

Our experimental approach (Figure 4.1B) relies on characterizing the diffusion of the tripodal compound **1·2PF$_6$** radially outward from a monoloayer initially deposited as a small microspot. A droplet of the **1·2PF$_6$** solution of appropriate concentration to form a monolayer is dispensed as a microspot of radius b onto the graphene surface, forming an initial boundary with (ideally) a uniform concentration of the tripod upon drying. When immersed in an electrolyte ($t = \tau_0$) that disfavors the desorption of the tripod but allows some degree of solvation of the [Co(tpy)$_2$] complex, the molecule diffuses outward onto the bare graphene surface. The SECM tip interrogates the electrochemical activity of the surface, or of products flowing outward from it, with spatial resolution and records "electrochemical snapshots" that describe the time evolution of the microspot. The microspot's activity decreases over

time ($t = \tau 1, \tau 2, ..., \tau x$) due to the radial dilution of the mobile **1·2PF$_6$** molecules on the surface. The decrease in the analytical signal at the center of the spot is fit to a surface diffusion model, yielding a macroscopic effective surface diffusion coefficient, D_{eff}.

Two complementary modes of SECM were used to differentiate the activity of **1·2PF$_6$** from the unfunctionalized SLG electrode. In the first mode (Figure 4.1C), a catalytic reaction triggered by the Co(tpy)$_2$ moiety generates homogeneous products that are collected at the tip.[74] Specifically, we used the oxygen reduction reaction (ORR) under kinetic control, eqs 1 and 2,[75] and showed that adsorbed **1·2PF$_6$** is able to generate more H_2O_2 [35,76] than the bare SLG. The Pt tip detects this peroxide through the inverse electrochemical process. H_2O_2 imaging using SECM has been used previously to characterize immobilized enzymes[77–80] and to evaluate the activity of electrocatalysts.[81–83]

$$O_2 + 2e^- + 2H^+ \rightarrow H_2O_2 \qquad (1)$$

$$O_2 + 4e^- + 4H^+ \rightarrow H_2O \qquad (2)$$

In the second mode (Figure 4.1D), feedback measurements directly assess the electrochemical activity of the tripodal molecules at the graphene/solution interface. Such feedback measurements of molecular species have been obtained at diverse interfaces, including self-assembled monolayers,[84] enzyme reactive sites,[85] intercalated DNA,[86] dye-sensitized solar cells,[87] and biological cells.[88] Here, a redox mediator in solution is activated at the tip, e.g. Ox + e^- → Red, where Ox and Red are the oxidized and reduced mediator species, respectively. The substrate is held at a constant oxidizing potential such that each of the adsorbed Co(tpy)$_2$ redox centers are in the

Co(III) oxidation state. The activated mediator, Red, diffuses to the surface, where it is oxidized by the Co(III) tripodal molecules to form Ox and a bound Co(II) species that is rapidly reoxidized to Co(III) by the activated surface. Ox diffuses back to the tip, where it is reactivated, and the repetition of these processes establishes a feedback current, which is measured at the tip. This feedback current is quantitatively related to an effective exchange rate constant that is directly proportional to the surface concentration of the adsorbed species.[84] The time evolution of the surface concentration is modeled to obtain D_{eff} as described for the above generation/collection scheme. Fe(II/III) complexes were chosen as mediators since they are relatively insensitive to electrochemical activation at the basal plane of HOPG[89,90] and have shown good chemical identification of adsorbed species in contrast to the competing electrode activation.[91]

4.3 Experimental Methods

Chemicals. The tripodal compound **1·2PF$_6$** (Figure 4.1A) was synthesized as reported in Chapter 2 (see Scheme 2.1).[30] Aqueous experiments were carried out with deionized water from a Millipore system. Chemicals used as received were potassium phosphate monobasic, potassium chloride (KCl), isopropanol (IPA), dimethylformamide (DMF), dichloromethane (DCM), glycerol (GLY), ethanol (EtOH), and acetone from Mallinckrodt; agar and ethylenediamine-tetraacetic acid ferric sodium salt (FeEDTA) from Sigma; potassium phosphate dibasic trihydride, tetrahydrofuran (THF), and anisole from Aldrich; potassium hexacyanoferrate (ferricyanide) and nitric acid from Fisher; tetrabutylammonium perchlorate (TBAP) from Fluka; hydroxymethylferrocene and Cu foil (0.025 mm thick, 99.8%) from Alfa;

glacial acetic acid, acetone, and isopropanol for graphene synthesis from VWR. For the fabrication of SECM tip electrodes, soft glass capillaries (FHC, Inc.) and 25 μm diameter platinum (99.99%) microwire (Goodfellow) were used and polished on microcloth polishing pads (Buehler). Silver, gold, tungsten, and indium wires were supplied by Sure Pure metals. The electrochemically active copolymer poly(vinylpyridine)/poly(vinylferrocene)[92] (PVP/PVF) 2:1 was used from an available batch. Reference electrodes were homemade Ag/AgCl in saturated KCl, and all potentials are quoted versus this reference. The reference was used with disposable 3% agar jelly/0.2 M potassium nitrate salt bridges to prevent silver ion and chloride contamination in the electrochemical cell. Gold was used as counter electrode and was sonicated in acetone and rinsed with water before use. For experiments with highly oriented pyrolytic graphite, HOPG SPI-2 grade (Structure Probe Inc.) was freshly cleaved before experiments using adhesive tape and then rinsed in the electrochemical cell using IPA. Graphene was obtained through chemical vapor deposition on Cu substrates and later transferred onto Si/SiO2 chips (see Appendix, Figure A3.1).

Electrochemical Measurements. All electrochemical and SECM measurements were performed with a CHI 900 SECM station. A homemade Teflon electrochemical cell with an active window of 0.2 cm^2, in which the graphene or HOPG substrate electrodes were sandwiched between an O-ring in the Teflon body and the PMMA base, was used for SECM and three-electrode measurements. For conventional three electrode experiments in organic solvents, either graphene or HOPG was used as the working electrode, with a Ag wire as a reference and a Au wire as counter electrode. Experiments in which **1·2PF$_6$** adsorption was monitored, with the

electrode later transferred to an aqueous environment, consisted in using <5 μM tripod in THF or DMF with 0.1 M TBAP as supporting electrolyte and running cyclic voltammograms (CV) to verify the adsorption of the tripod and to calculate its coverage. In order to study the behavior of the tripod in an aqueous environment, the cell was thoroughly rinsed with blank solvent (THF or DMF) to remove excess tripod and organic supporting electrolyte, then rinsed with IPA at least once (to recreate the conditions of the blank electrodes), and then thoroughly rinsed with deionized water to remove excess solvents. Finally phosphate buffer (0.2 M, pH 7) was introduced as the aqueous electrolyte. While inevitable losses were observed during this procedure, **1·2PF$_6$** could be detected and quantified using CV in the aqueous solution. Adsorption of PVP/PVF for feedback and control experiments was carried out by exposing the substrate electrodes to a solution of 0.1 mg/mL of the polymer in EtOH and then rinsing with copious amounts of H_2O.

Tripod Microspots on Graphene and HOPG. Microarrays of drops of **1·2PF$_6$** solution were dispensed on graphene and HOPG using a picoliter dispenser with a 30-μm diameter orifice (Microfab Inc. Plano, Texas) controlled by a homemade circuit with output gain of 20X using two OPA445AP High Voltage FET-Input operational amplifiers (Burr-Brown products from Texas Instruments).[93] The dispenser was operated using a synthesized function generator model DS345 (Stanford Research Systems) and an oscilloscope model TDS 210 (Tektronics) and powered by two batteries at ± 30 V. **1·2PF$_6$** was dissolved in a mixture of DMF/GLY 10:1 (intended to dissolve the tripod with a workable viscosity and low evaporation rate at room temperature) and was deposited by applying two consecutive pulses of 25 μs (20

kHz) at 44 V (input of 2.2 V). This deposition procedure typically yielded droplets of radius $b \approx 50$ μm as determined by optical microscopy. A calibration experiment (same solvent and parameters) that dispensed a solution of hydroxymethylferrocene (0.1 M) 100 times into a droplet (50 μL) of phosphate buffer was analyzed by steady state voltammetry using a 25-μm microelectrode in a two-electrode configuration. This calibration showed that each dispensing cycle produced droplets of 177 ± 8 pL, i.e., flattened hemispheres with radius $b \approx 50$ μm and height $h \approx 35$ μm. Using this information, the concentration of **1·2PF$_6$** was chosen to deliver the desired amount of adsorbate to the SLG surface. For example, [**1·2PF$_6$**] = 45 μM provides an approximate coverage of 104 pmol/cm^2 within each spot, which exceeds the ≈70 pmol/cm^2 required for the first plateau observed in the isotherm for **1·2PF$_6$** on graphene but is lower than a more compact layer observed at ≈ 140 pmol/cm^2. A slight excess is desirable to account for possible losses in the dispensing process[94] but much larger excesses, e.g., five-fold monolayer equivalents, caused precipitation of **1·2PF$_6$** on the SLG surface and the inability to perform SECM measurements (i.e., a lower activity of spots is observed compared to the SLG substrate). Typical arrays of tripod spots were deposited on graphene or HOPG electrodes with interspot distances between 300 and 600 μm. The arrays were dried at 50 °C in an oven at ambient pressure for ≈1 h before imaging. Successful images were typically obtained from arrays where no residue was evident on the graphene substrate upon microscopic inspection.

SECM Experiments. SECM experiments used a four electrode configuration. All SECM experiments were performed using a sharpened 25-μm diameter Pt

microdisk SECM tip with an $R_G \approx 7$ (closest approach on glass $d_0 \approx 1.5$ μm) sealed in soft glass using reported procedures.[33] For imaging experiments, the time at which the solution was introduced into the cell and wetted the substrate electrode was defined as $t = 0$. The SECM tip was approached to the surface and positioned at a tip/surface distance of 10 μm. A first extended image or several lateral scans were performed at relatively high scan rate (e.g., 125 μm/s in steps of ≈15−25 μm) to locate an active spot. Subsequent images were obtained at more moderate scan rates and higher resolution (e.g., 50 μm/s in steps of 6−10 μm). An accumulated uncertainty in the time assigned to each image (i.e., the maximum intensity of the image) is estimated to be ≈100 s because of changes in the position of the spot due to a slight drift in the motors. All times shown in images are thus rounded to the nearest 100 s. All approach curves and tip positioning procedures were analyzed using reported expressions.[95]

For H_2O_2 collection experiments, the electrolyte was air-saturated aqueous phosphate buffer (0.2 M, pH = 7).[96] The tip was positioned in the negative feedback mode using O_2 as mediator (typical $i_{T,inf} = 7$ nA). Unless otherwise noted, for H_2O_2 collection experiments, the substrate was biased to a potential $E_S = -0.6$ V vs Ag/AgCl and the tip to $E_T = 0.6$ V vs Ag/AgCl (i.e., ≈1.22 V vs RHE, an optimum potential for H_2O_2 collection at Pt).[81] Occasional cleaning of the tip was performed between images by cycling between 0.8 and −0.6 V vs Ag/ AgCl to prevent fouling, although no significant improvement was observed in relatively clean environments. Potassium ferricyanide (1− 2 mM) dissolved in aqueous phosphate buffer (0.2 M, pH 7) was used for feedback imaging experiments. For graphene electrodes, the tip, $E_T = -0.1$ V vs Ag/AgCl, was positioned by a negative feedback-like approach curve obtained with

the substrate at open circuit (Appendix Figure A3.2).[97] For feedback experiments on HOPG, a positive feedback approach curve was also used to verify adequate positioning. During imaging, the substrate electrodes were biased to E_S = 0.4 V vs Ag/AgCl unless otherwise noted. Conditions for the supporting experiments with FeEDTA as mediator are described in the Appendix.

Simulations and Experimental Considerations. Digital simulations of the surface diffusion problem coupled to the SECM conditions were performed using the COMSOL Multiphysics 3.5a software, which implements the finite element method to solve the required kinetic and diffusion coupled equations. A complete description of the simulation conditions for the G/C and feedback schemes is given in the Appendix.

Figure A3.2 shows the temporal evolution of the surface concentration of a species with a homogeneous surface concentration (Γ_0) that is radially diffusing from an initially confined circular microspot (radius b). The microspot is surrounded by a semi-infinite blank surface with radius 20b and the diffusing species exhibits a uniform surface diffusion coefficient D (i.e., independent of coverage and intermolecular interactions). The response is modeled using a radial coordinate r, where r = 0 represents the center of the microspot. The results of these simulations are displayed as a series of master curves that describe the temporal evolution of the surface concentration of the diffusing species relative to its initial value at the center of the microspot (Γ/Γ_0) at each of several normalized distances r/b from the center. A dimensionless time τ is introduced as shown in eq 3:

$$\tau = \frac{\sqrt{Dt}}{b} \qquad (3)$$

where D is the diffusion coefficient of the species, t is time, and b is the radius of the microspot. The conditions tested include 1×10^{-4} cm^2/s > D > 1×10^{-16} cm^2/s (1 cm^2/s = 1×10^{-4} m^2/s), 1000 μm > b >0.001 μm (1 μm = 1×10^{-6} m), and their respective times (s) such that $5 > \tau > 0$. Figure 4.2A,B shows the concentration profiles for the coordinates inside and outside the original area of the microspots, respectively. The concentration inside of the spot shows a continuous decrease as a consequence of radial diffusion, whereas the positions outside of the spot show a concentration front that increases and then vanishes upon further radial dilution.

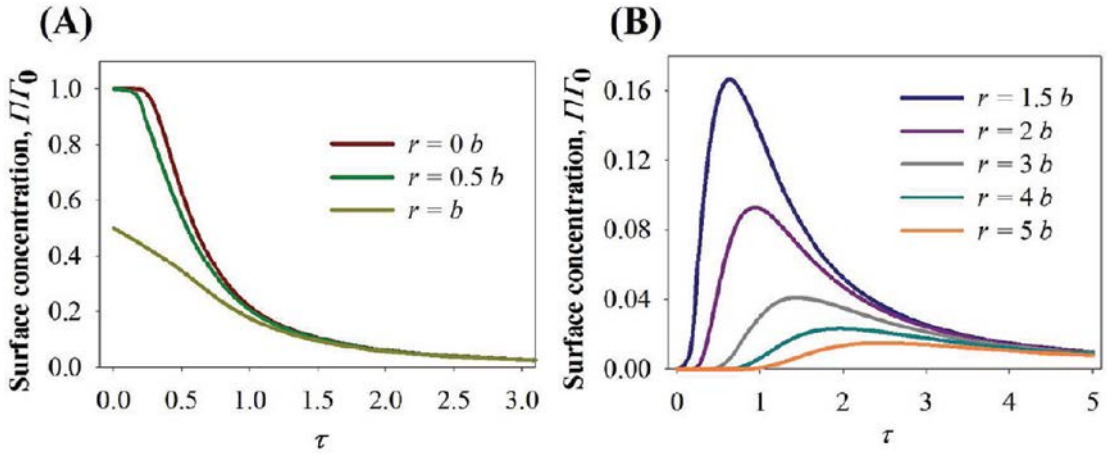

Figure 4.2. Master curves for the surface concentration changes associated with the two-dimensional diffusion of adsorbed molecules from a circular area with uniform initial concentration Γ_0 and radius b outward onto a blank, bulk surface. The different curves indicate selected positions in the radial coordinate r, and the horizontal axis represents the normalized time τ (eq 3). The curves in panel A correspond to coordinates within the initial boundary, and the curves in panel B correspond to coordinates outside the initial boundary.

Two observations relevant to our SECM measurements warrant further discussion. First, the steepest change in concentration and therefore electrochemical signal occurs

at the center of the microspot, where the concentration drops to ≈ 25% of its original value in one time period. This finding suggests that measuring the surface concentration as a function of time at the center of the microspot is likely to be the most effective strategy for characterizing the molecular diffusion process. Second, the changes within the original area of the spot follow closely those of the center while the changes outside the original area of the spot are not sufficient to supply more than ≈10% of the original concentration to radii larger than 2*b* as a consequence of radial dilution of the species. Therefore, it is expected that only a modest broadening of the signal will be observed. In utilizing the dimensionless time parameter (τ), these simulations also highlight the interplay between the size of the spot deposited, the expectations on the value of *D*, and the absolute time and time resolution available for the experiment. For example, for $D = 1 \times 10^{-9}$ cm^2/s (a value between a typical solution diffusion coefficient, $D = 1 \times 10^{-5}$ cm^2/s, and that of a low surface diffusion coefficient, $D = 1 \times 10^{-13}$ cm^2/s, approaching diffusion in solids)[47] with a spot of radius $b = 50$ μm and for times $\tau < 1$, the absolute measuring time would conveniently be 25,000 s (e.g., enough for positioning the tip and obtaining several images), in contrast to 2.5 s if $b = 500$ nm, which would be experimentally difficult to probe through SECM imaging. Finally, in SECM experiments, the size of the tip affects the spatial and temporal resolution of the measurement. Scans performed with relatively large tips, e.g., $a > 5$ μm, allow for a fast screening of a given area (e.g., if $b = 50$ μm) at the expense of a convoluted signal from the area that is projected below the tip. Smaller tips could directly correlate the concentration profile at the substrate to the tip response but are more challenging to implement in a time-sensitive experiment. In this

study we opted for the former option and solved the convoluted tip response by fitting to widely implemented computer simulations for SECM studies.

4.4 Results and Discussion

H_2O_2 Collection Experiments. In Chapter 2 we discussed the characterization of monolayer formation, desorption, and the electrochemical behavior of the pyrene-containing tripodal compound **1·2PF$_6$** on SLG.[30] Its Co(II/III) redox center exhibits quasi-reversible electrochemical kinetics at scan rates between 0.1 and 3.0 V/s with a standard potential E_0 = −0.2 V vs ferrocene. The slower rate of electron transfer between graphene and **1·2PF$_6$** (standard rate constant k_0 = 13.5 s^{-1}) relative to that of a model compound bearing a single pyrene moiety (k_0 = 18 s_{-1}) suggested that the tripodal motif projects its [Co(tpy)$_2$] complex away from the graphene surface. Finally, monolayers of **1·2PF$_6$** resist desorption when transferred to fresh THF/ NH_4PF_6 electrolyte solution. Here, our SECM experiments are performed in aqueous electrolyte, in which **1·2PF$_6$** is insoluble and the strength of aromatic stacking interactions is maximized, making its desorption from SLG even less favorable. As such, our measurements of the surface diffusion dynamics of **1·2PF$_6$** are minimally complicated by transport mechanisms other than lateral translation across the graphene surface (e.g., desorption-convection). Preliminary experiments performed at the basal plane of freshly cleaved HOPG electrodes (analogous to the graphene surface) confirm that **1·2PF$_6$** remains strongly bound to the surface in aqueous electrolyte (Figure 4.3). At the same scan rate (0.1 V/s), a similar peak splitting $\Delta E_p \approx 100$ mV is observed in both THF and aqueous phosphate buffer, suggesting that the adsorption mode and orientation of the tripod is similar in both solvents.

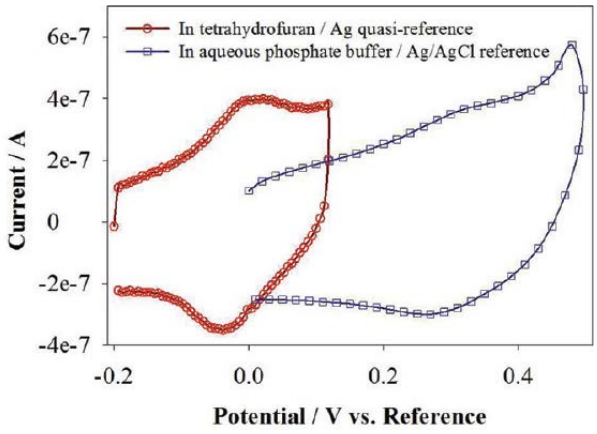

Figure 4.3. Cyclic voltammograms of **1·2PF$_6$** adsorbed on the basal plane of HOPG (initial surface concentration = 20 pmol/cm^2). The left voltammogram (red curve) was obtained in a 0.1 M TBAP in THF supporting electrolyte. The right voltammogram (blue curve) was obtained in phosphate buffer (0.2M, pH = 7) after rinsing the surface with THF, IPA, and H_2O.

A differential electrochemical response between adsorbed **1·2PF$_6$** and bare SLG is necessary to detect **1·2PF$_6$** using SECM. Qualitative collection of H_2O_2 at a Pt SECM tip originating from the ORR over HOPG and SLG electrodes in the presence and absence of **1·2PF$_6$** monolayers showed sufficient activity differences to provide this contrast (Figure 4.4). The onset for ORR on Pt in phosphate buffer occurs at ~0.15 V vs Ag/AgCl (~0.77 V vs RHE), and thus the reaction presents a considerable overpotential on both bare SLG and HOPG. Inconsistencies in the rising portion of the curves for oxygen reduction (lower panels) were observed in different batches of graphene (Appendix Figure A3.3), which can be attributed to the presence of small amounts of residual metal ions from the fabrication process (e.g., Cu, Fe). Nevertheless, the output of H_2O_2 on both graphene and HOPG always increased following adsorption of **1·2PF$_6$**. This increase was not observed when the electrodes were exposed to organic electrolyte lacking **1·2PF$_6$**. Furthermore, Co complexes are known to form H_2O_2 during the ORR.[35,75,76]

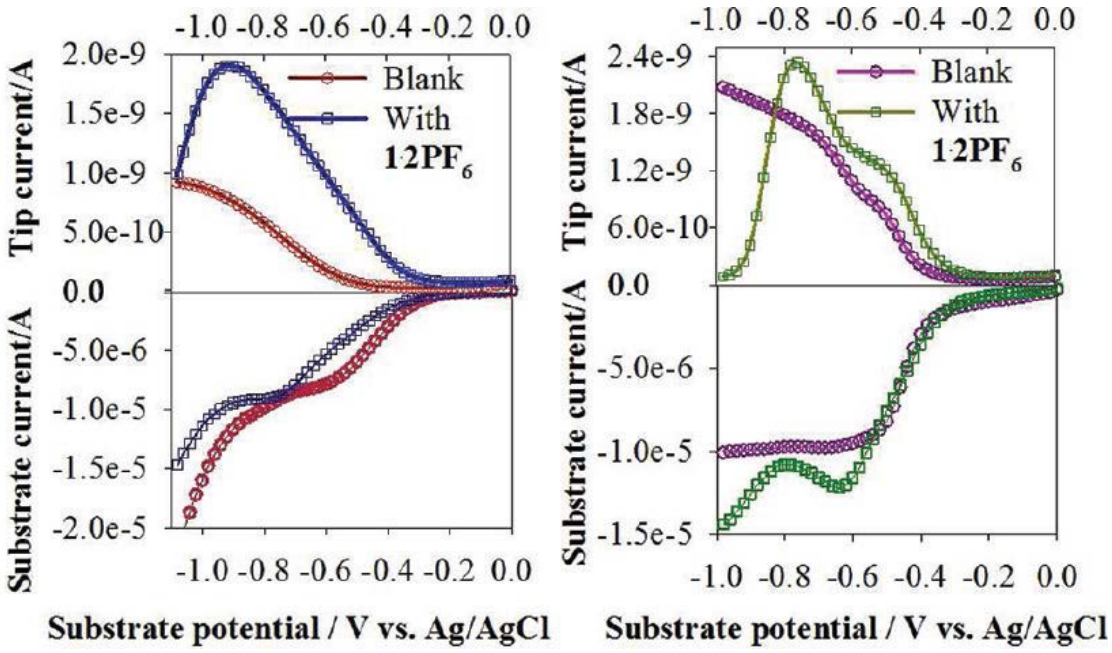

Figure 4.4. Substrate generation/tip collection curves for H_2O_2 generated during the oxygen reduction reaction performed in an air saturated phosphate buffer (0.2 M, pH = 7) at a large-area (left) graphene electrode (**1·2PF$_6$** coverage =23 pmol/cm^2) or (right) HOPG electrode (**1·2PF$_6$** coverage = 28 pmol/cm^2). H_2O_2 collection at the SECM tip (a = 12.5 μm Pt, $R_G \approx 7$) was performed at ET = 0.6 V vs Ag/AgCl at an interelectrode distance d = 10 μm. The linear sweep of the substrate voltage was performed at 10 mV/s.

The H_2O_2 output curves (Figure 4.4) for graphene and HOPG show common features when **1·2PF$_6$** is present. Each curve shows a rise to a maximum H_2O_2 output, followed by a sharp decrease at increased overpotentials, which likely reflects a change in the predominant mechanism from the two-electron (eq 1) to the four-electron route (eq 2). In order to use H_2O_2 generation/collection to describe changes in the distribution of **1·2PF$_6$** on the electrode surface, the electrochemical reaction must operate under kinetic control, i.e., at low overpotentials, such that the rate of reaction is proportional to the molecular surface concentration. Compared to a bare glassy carbon surface (Appendix Figure A3.4), both **1·2PF$_6$** -modified SLG and HOPG produce less H_2O_2 at potentials positive of E_S = −0.8 V vs Ag/AgCl ($i_{T,max}$ = 3 nA

under similar conditions), which suggests kinetic control below this potential. Furthermore, a graphene microelectrode experiment designed to estimate the percentage of H_2O_2 output (Appendix Figure A3.5), i.e., the contribution of eq 1 to the ORR process,[74] over this potential region indicates that the total ORR current is less than 0.25 times the limiting current (assuming the limiting 4-electron route) at potentials more positive than E_S = −0.6 V vs Ag/AgCl. Under these conditions, the $\%H_2O_2$ is less than ≈ 20% for unfunctionalized graphene, while that of tripod-adsorbed graphene shows higher values of ≈ 40%. Under these kinetic limitations and although likely dominated by convection of O_2 toward the graphene substrate, a steady background suitable for imaging on a bare SLG electrode is obtained (Appendix Figure A3.6, E_S = −0.6 V vs Ag/AgCl).

After establishing that adsorbed **1·2PF$_6$** presents a differential reactivity during the ORR on graphene, we employed a "microspot" approach to evaluate the mobility of the tripods on the SLG surface (Figure 4.1). A piezoelectric dispenser (Figure 4.5A) was used to deliver small droplets of a solution of **1·2PF$_6$** in DMF/GLY (10:1 v/v), forming an initial boundary with monolayer coverage of the species after solvent evaporation. The droplets form well-defined areas that were observed by optical microscopy. The ORR occurs on the entire substrate, yielding a background level of H_2O_2 collection (Figure 4.5B) over unfunctionalized regions of the electrode, as well as larger collection currents over areas where the tripod is adsorbed. Figure 4.5C shows an array of tripod microspots deposited on HOPG (b = 50 and 300 μm center to center). The areas where tripod spots were deposited are clear, and their sizes correspond well to those observed by optical microscopy.

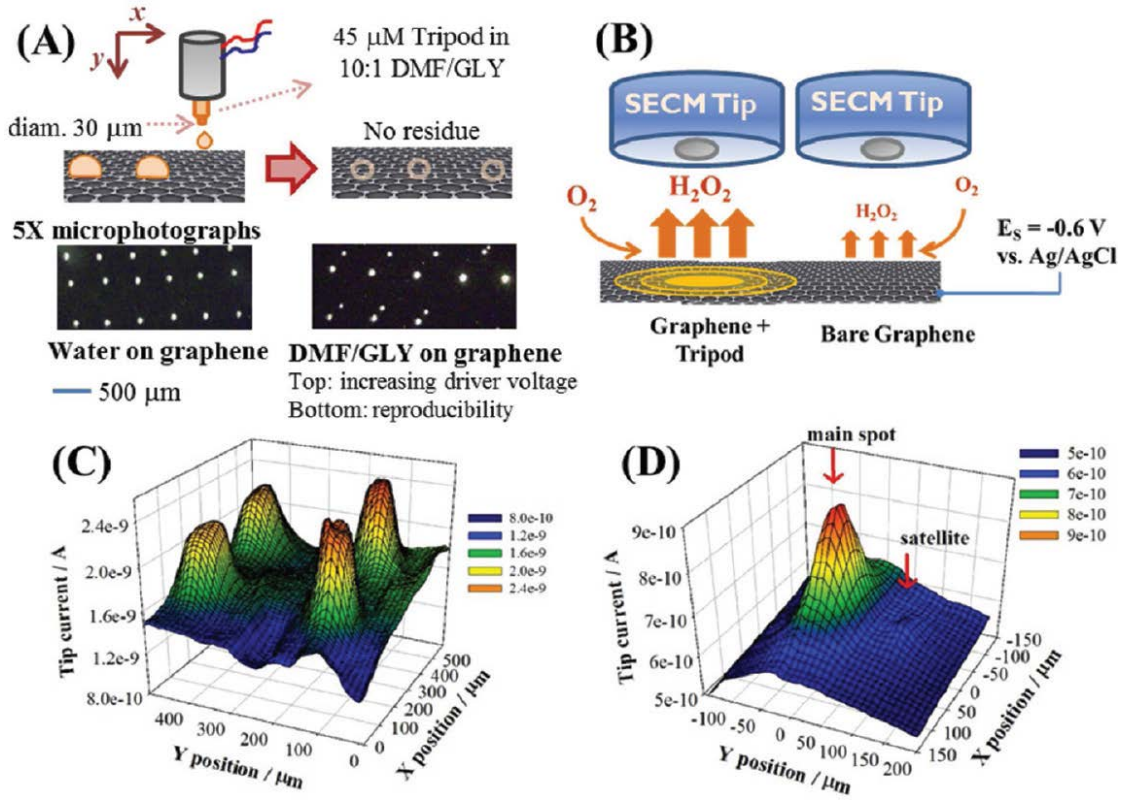

Figure 4.5. Tripod microspot deposition on graphene and HOPG. (A) Schematics of microdroplet deposition on the graphene surface from an organic precursor solution using a piezoelectric dispenser. Optical micrographs show satellite spots during droplet dispensing of DMF/GLY solutions that are not observed when aqueous solutions are deposited, but good reproducibility of overall size and shape in both cases. (B) Schematics of imaging tripod microspots by collecting H_2O_2 produced at the substrate during ORR. (C, D) SECM H_2O_2 substrate generation/tip collection experiments for (C) an array of **1·2PF$_6$** microspots (100 pmol/cm^2, b = 50 µm) on HOPG (recorded at t = 2 400 s) and (D) a **1·2PF$_6$** microspot (100 pmol/cm^2, b = 50 µm) on SLG (recorded at t = 6 300 s) that shows a satellite spot seen in panel A. For each experiment, H_2O_2 collection at the SECM tip (a = 12.5 µm Pt, $R_G \approx 7$) was performed at E_T = 0.6 V vs Ag/AgCl, interelectrode distance d = 10 µm, and E_S = −0.6 V vs Ag/AgCl.

Figure 4.5D shows a microspot on a SLG electrode, where a satellite spot, created by an irregular deposition from the dispenser, is also observed. The observation of these irregularities further confirms the ability of the SECM to detect **1·2PF$_6$** deposited on SLG. The spots in Figure 4.5C,D are also well below the maximum H_2O_2 collection observed for glassy carbon (Appendix Figures A4.4 and A4.7). Experiments in which

blank solvent was deposited did not show any activity over the background.

We postulated that the necessary conditions to allow mobility of **1·2PF$_6$** from its initial confinement toward the bulk graphene surface are present once the electrode is completely immersed in the electrolytic environment. The tip current observed due to collection of H_2O_2 over microspots of **1·2PF$_6$** on SLG decreases with time in a manner consistent with surface diffusion. Figure 4.6 and Appendix Figure A3.8 show a typical progression of this change in activity. It should be noted that an approximate background of ~0.85 nA is present throughout the experiment even as the spot activity decreases, indicating that potential complications, such as fouling of the SECM tip, are unimportant (occasional cleaning of the tip was performed with similar results). The collection intensities observed for an approximate initial monolayer coverage of **1·2PF$_6$** and for the SLG background are well below that observed for blank glassy carbon, confirming that the requisite kinetic control for modeling surface diffusion response is followed at E_S = −0.6 V vs Ag/AgCl. An approximate calibration of the H_2O_2 output in b = 50 μm spots for selected initial surface concentrations is also shown in Appendix Figure A3.9 and indicates the decreasing trend in activity at lower surface concentrations. The time dependence of the collection intensity at the center of a microspot expected for surface diffusion, normalized to its initial intensity, was simulated with respect to the normalized time τ (Figure 4.7).

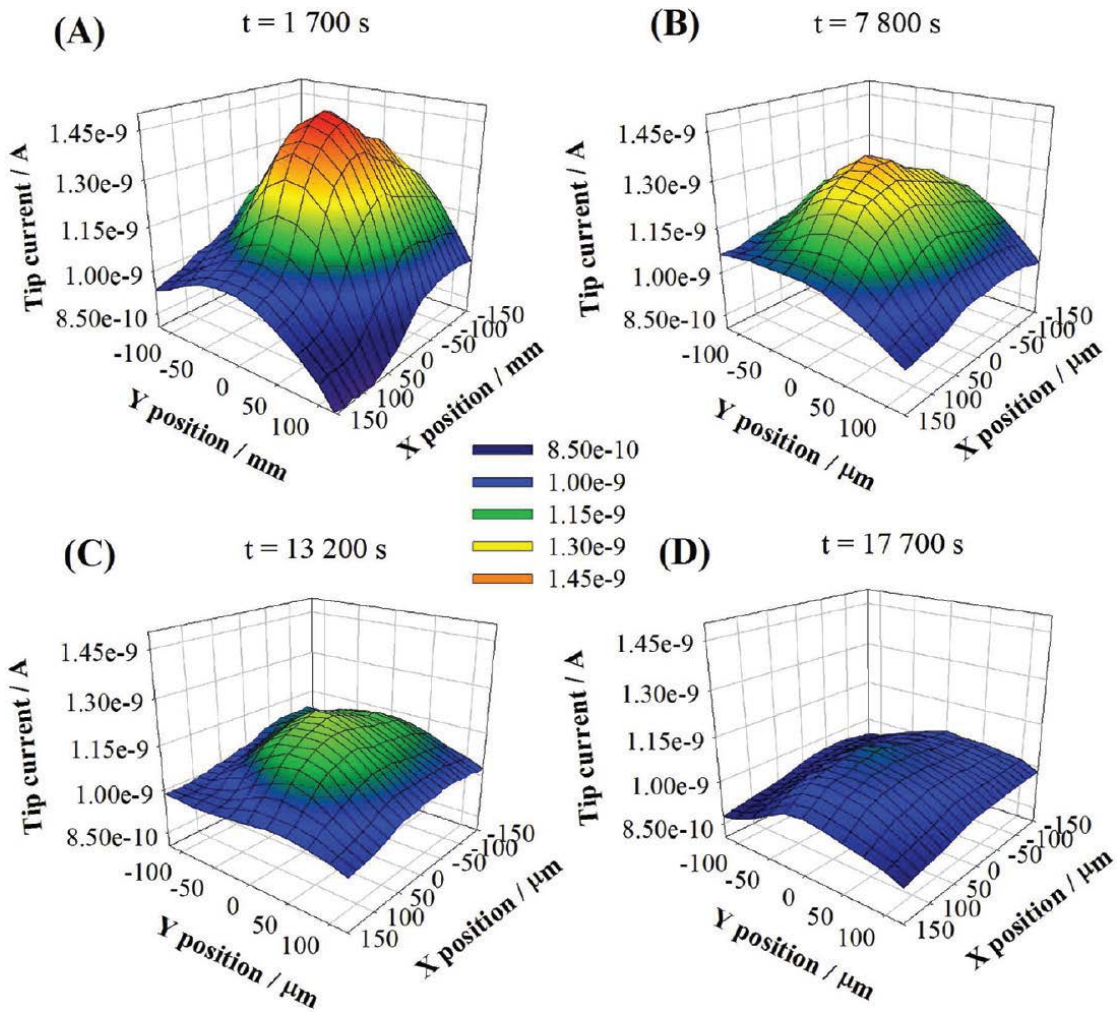

Figure 4.6. Progression of SECM hydrogen peroxide substrate generation/tip collection images for a representative **1·2PF$_6$** microspot on graphene (100 pmol/cm^2, b = 50 µm). Images A−D were obtained at the indicated times. H_2O_2 collection at the SECM tip (a = 12.5 µm Pt, $R_G \approx 7$) was performed at E_T = 0.6 V vs Ag/AgCl, interelectrode distance d = 10 µm, and E_S = −0.6 V vs Ag/AgCl. The substrate potential E_S was −0.6 V vs Ag/ AgCl throughout the experiment.

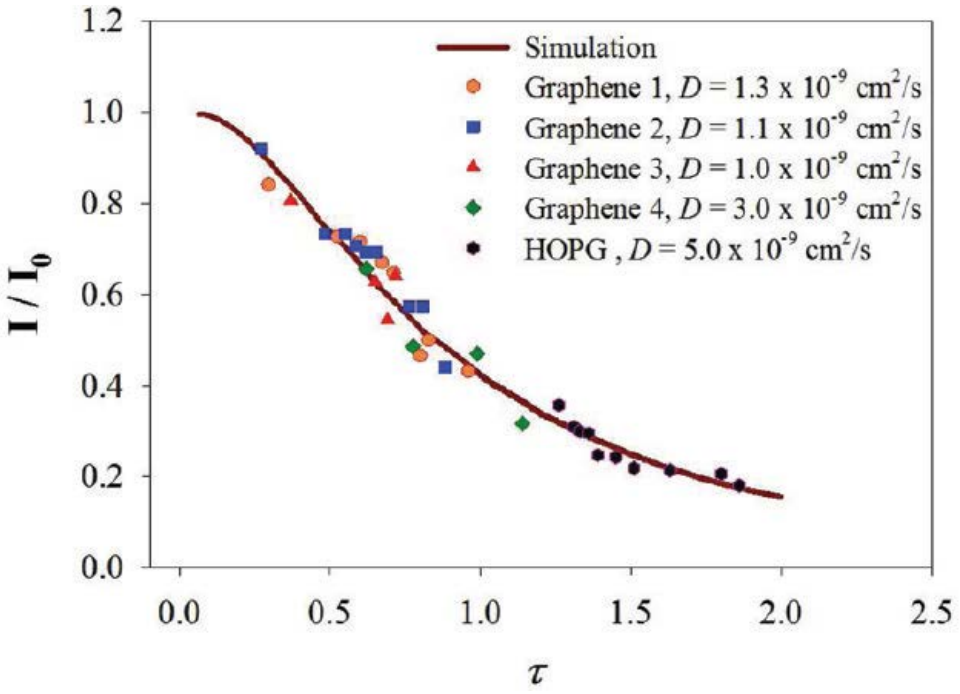

Figure 4.7. Comparison of simulation and experiment for H_2O_2 collection experiments performed over the center of **1·2PF$_6$** microspots (r = 0). The experimental data were background subtracted and fitted to the simulation by choice of D (implicit in τ) as explained in the text. All conditions as in Figure 4.6.

This simulation is analogous to the concentration profile shown for the surface species in Figure 4.2 for $r = 0b$ and also accounts for the contribution of the tip and substrate geometries to the electrochemical signal. Data from many **1·2PF$_6$** microspots were fit to this curve, and the experimental responses (after background subtraction to provide the changes in the peak intensities) were adjusted to the main curve by the choice of D in the normalized time axis (eq 3).[98] An excellent agreement to the simulation was observed over the steep region of the curve ($\tau < 1$). Averaging these data yields D = 1.6 (± 0.9) × 10^{-9} cm^2/s, a value fully consistent with surface diffusion. Differences between graphene substrates may occur because of heterogeneous distribution of defects, grain boundaries, and inconsistencies in

transferring graphene to the Si/SiO_2 support (e.g., presence of nanometer-scale ripples). Nonetheless, all samples display surface diffusion values within the same order of magnitude.

A variety of control experiments support our interpretation of the above data as the diffusion of **1·2PF$_6$** on the SLG surface and preclude many plausible alternative explanations. Stirring the solution between experiments did not appreciably change the SECM response except for small changes in the graphene background current. This indicates that convective transport of the adsorbed tripod does not contribute significantly to the decrease in the activity of the microspots. In addition, an oxygen depletion effect cannot account for the observed decrease in the activity of the microspot, because the SECM was also open to air saturation throughout the experiment. We also confirmed that the SLG remains stable under the experimental conditions and potentials for long periods of time. For example, even at a higher overpotential (E_S = −1.0 V vs Ag/AgCl) than was used above, an SLG microelectrode consisting of graphene surrounded by cured photoresist exhibits only a ± 2.5% current variation over a period of 8000 s (Appendix Figure A3.10). Next, we designed an experiment to interrupt the diffusion of **1·2PF$_6$** on the SLG surface. In this situation, no decrease of its electrochemical response over time would be expected. Figure 4.8A−D shows a progression of images of a **1·2PF$_6$** microspot on an SLG electrode treated with an electroactive thin layer of poly(vinylpyridine) / poly(vinylferrocene) (PVP/PVF) so as to disrupt the mobility of the tripod on the surface without damaging the SLG. The presence of the polymer is confirmed by its electrochemical response (Figure 4.8E, process 2 and 2′), in addition to the **1·2PF$_6$** signal (process 1 and 1′).

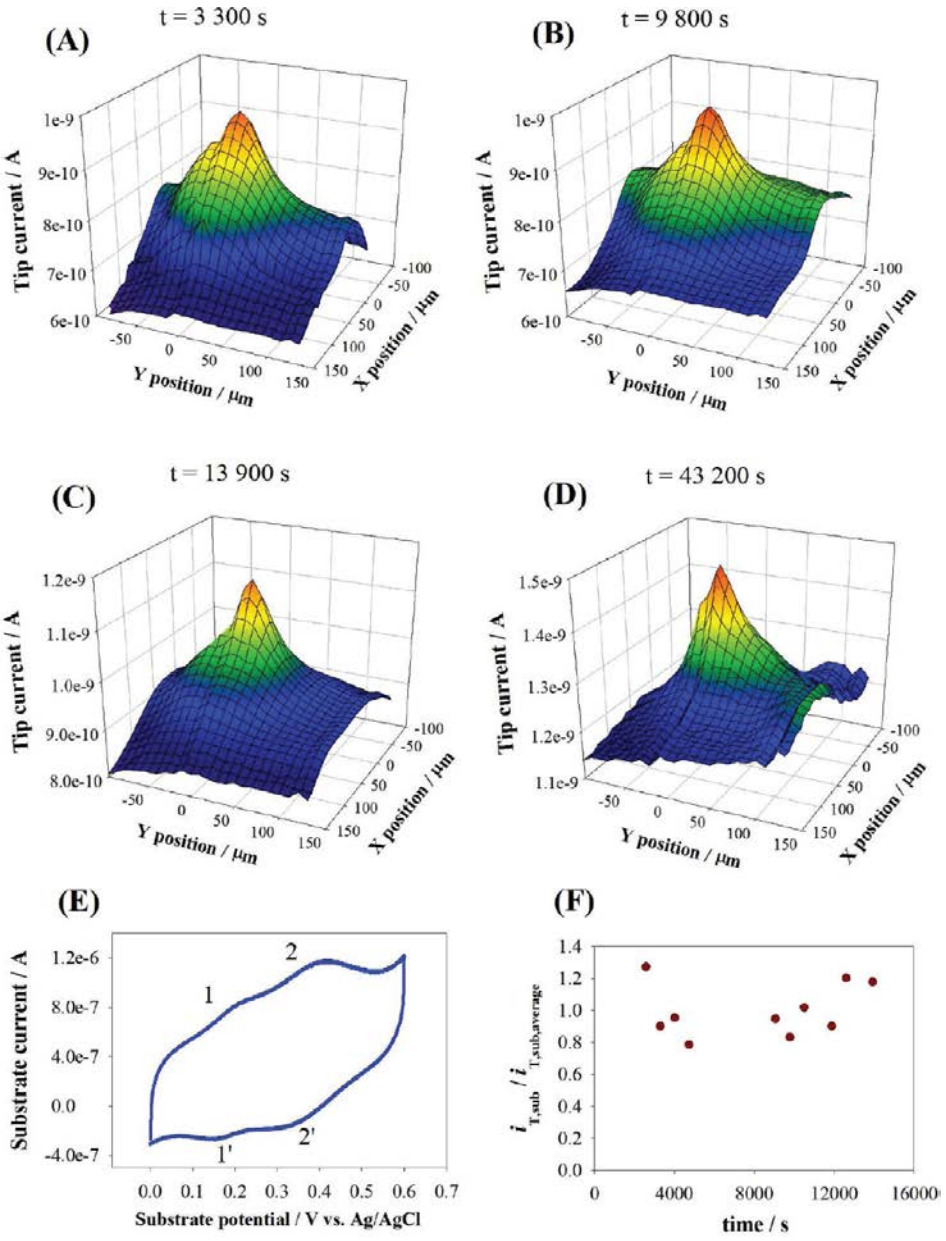

Figure 4.8. Representative SECM H_2O_2 substrate generation/tip collection images for a **1·2PF$_6$** microspot (~100 pmol/cm^2, $b \approx 40$ µm) on a surface disrupted SLG electrode. The graphene was pretreated with a 0.1 mg/mL ethanolic solution of PVP/PVF copolymer 2:1 to a final coverage of ~90 pmol/cm^2 of ferrocene redox centers. Images A−D were obtained at the indicated times. H_2O_2 collection at the SECM tip (a = 12.5 µm Pt, $R_G \approx 7$) was performed at E_T = 0.6 V vs Ag/AgCl, interelectrode distance d = 10 µm, and E_S = −0.6 V vs Ag/AgCl. The surface potential was held at E_S throughout the experiment except for image D. (E) Cyclic voltammogram showing adsorption of PVP/PVF and tripod spots (from the entire array), v = 100 mV/s. (F) Plot of background subtracted collection currents, normalized to the average measured current vs time (<16,000 s).

Although H_2O_2 collection measurements over a **1·2PF$_6$** microspot show some variability in their electrochemical response over 43,000 s (Figure 4.8F), no clear decreasing trend in activity is observed, in contrast to the continuous decrease in activity of the microspots observed in the absence of the PVP/PVF diffusion barrier (compare to Figure 4.7). The presence of the co-adsorbed PVP/PVF polymer introduces a physical barrier ≈ 5−10 nm high over lengths of hundreds of micrometers (Appendix Figure A3.11) where **1·2PF$_6$** is unlikely to traverse or displace the adsorbed polymeric units. This prevents mass transfer diffusion of **1·2PF$_6$** out of its initial confinement, although individual molecules may still preserve mobility within much smaller domains. Taken together, the above control experiments strongly suggest that surface diffusion is the main mechanism for the observed decrease in the analytical signal of **1·2PF$_6$** microspots on SLG.

Feedback Experiments. The H_2O_2 collection experiments described above measure the activity of the underlying surface indirectly by detecting the product of an electrocatalytic reaction at the SECM tip. We also probed the activity of **1·2PF$_6$** at the SLG surface more directly using the feedback mode of SECM (Figure 4.9A). In this experiment, a dissolved redox mediator is used to continuously generate, at steady state, a reactive species at the SECM tip. The tip is moved toward the surface to a distance comparable to that of its active microdisk (described by the normalized distance $L = d/a$ where d is the tip−substrate distance), and the reactive form of the mediator diffuses to the substrate, which is typically biased to a potential where it can perform the reverse of the reaction occurring at the tip.[33] For example, if the SECM tip reduces the soluble redox mediator, the mediator is regenerated by oxidation at the

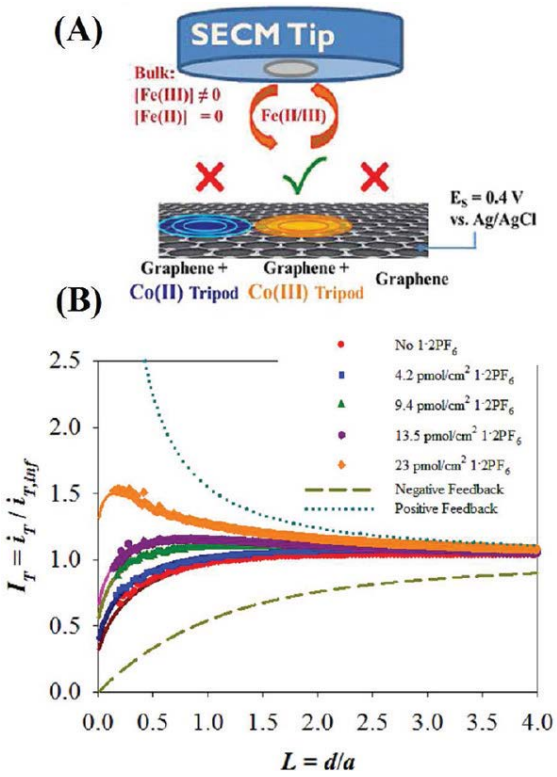

Figure 4.9. Use of SECM feedback for the detection of adsorbed, activated Co(III) tripod at graphene using a Fe(II/III) mediator couple. (A) Schematic of the use of SECM feedback to detect the Co(III) oxidation state of the tripodal compound adsorbed on graphene. The reduced Fe(II) complex reacts more quickly with the Co(III) tripod than the unfunctionalized SLG substrate. (B) Approach curves on HOPG with increasing coverages of adsorbed **1·2PF$_6$** (as indicated) in a potassium ferricyanide (1.65 mM) phosphate buffer solution (0.2 M, pH 7); E_S = 0.4 V vs Ag/AgCl, E_T = −0.1 V vs Ag/ AgCl. The SECM tip had a = 12.5 μm Pt with $R_G \approx$ 7. Solid lines based on theory for heterogeneous kinetics (rates shown in Supplementary Figure A3.12).

bulk substrate electrode. For typical conductive substrates, such as metal electrodes and glassy carbon, most electrochemically reversible mediators react rapidly at the surface. In this situation, the current read at the SECM tip increases at distances $L < 1$ because the mass transfer coefficient of the redox mediator increases as the tip-substrate separation decreases, a phenomenon known as positive feedback. In contrast, an insulating or inactive surface causes the tip current to decrease as the tip approaches the surface, a negative feedback effect. Furthermore, the kinetics of

electron transfer between the electrodes and the redox mediator may be evaluated within the context of these two feedback regimes. Although SLG is highly conductive over its basal plane, its rate of interfacial charge transfer to the Fe(II/III) complex ferro/ferricyanide is expected to be similar to that of HOPG. Adsorbed **1·2PF$_6$** increases the electrochemical activity of the SLG electrode (see below), and this differential reactivity between functionalized and nonfunctionalized SLG provides contrast in the SECM measurement that allows the surface diffusion of the tripodal binding motif to be measured.

Figure 4.9B shows approach curves (i.e., steady-state current vs L curves, from which the value of the heterogeneous charge transfer rate constant can be extracted) generated using the ferri/ferrocyanide $Fe(CN)_6^{3-/4-}$ couple (E^0 = 0.16 V vs Ag/ AgCl) as the soluble redox mediator and an HOPG bulk electrode at a constant E_S = 0.4 V vs Ag/AgCl. Under these conditions noble metal substrates (e.g., Pt and Au) would show almost complete positive feedback, but the approach curve for the unfunctionalized HOPG electrode (Figure 4.9B, red) indicates negative feedback-like behavior with a small yet measurable charge transfer rate constant. The slow rate of electron transfer between ferri / ferrocyanide and HOPG electrodes is well-known[17,18] and is attributable to the low density of states on the material relative to metallic electrodes, [99] effects of the self-exchange rate constants of the mediator,[89] and effects of oxygenated defects.[90] The approach curves for HOPG electrodes functionalized with **1·2PF$_6$** show a clear increase in the rate of charge transfer for the ferrocyanide mediator (Figure 4.9B), as reflected by the higher currents observed at smaller tip/sample distances (L) and by their characteristic shape in this intermediate kinetic

regime. A linear relationship between the heterogeneous electron transfer rate constant and the tripod surface concentration (Appendix Figure A3.12) was observed, corresponding to a second order electron transfer rate constant k_{ex} = 1.6 × 10^8 mol^{-1} cm^3 s^{-1} between the Co(III) tripod and $Fe(CN)_6^{4-}$. Although higher exchange rate constants have been observed for highly electrochemically reversible systems (≈10^{10} mol^{-1} cm^3 s^{-1}),[84] this value is similar to that measured for electron transfer between the iron active site of cytochrome c and ferricyanide (k_{ex} = 2 × 10^8 mol^{-1} cm^3 s^{-1})[85] and exceeds that of complex oxide reduction mechanisms involving additional proton transfers (k_{ex} < 1 × 10^8 mol^{-1} cm^3 s^{-1}).[91] It is also likely that the relatively low k_{ex} value also reflects the low self-exchange rate constant for Co(II/III) terpyridine and bipyridine couples.[70–73] Nevertheless, the increased electrochemical activity of the bulk electrode upon adsorption of **1·2PF$_6$** provides a means to characterize molecular diffusion by measuring the time dependence of the feedback current obtained over **1·2PF$_6$** microspots.

Figure 4.10 shows a progression of feedback images for a **1·2PF$_6$** microspot (b ≈ 15 μm) deposited on graphene with the substrate potential held at E_S = 0.4 V vs Ag/AgCl and interrogated using tip generated $Fe(CN)_6^{4-}$ in phosphate buffer. A decrease in the peak intensity of the feedback current with respect to time was observed, similar to the trend observed in the H_2O_2 collection experiments. A small increase in the electrochemical activity of the surrounding SLG was also observed over the course of the experiment. We attribute this increase to the diffusion of **1·2PF$_6$** from the microspots into the surrounding unfunctionalized area of the SLG, although it is difficult to deconvolve this small change from other sources of background drift.

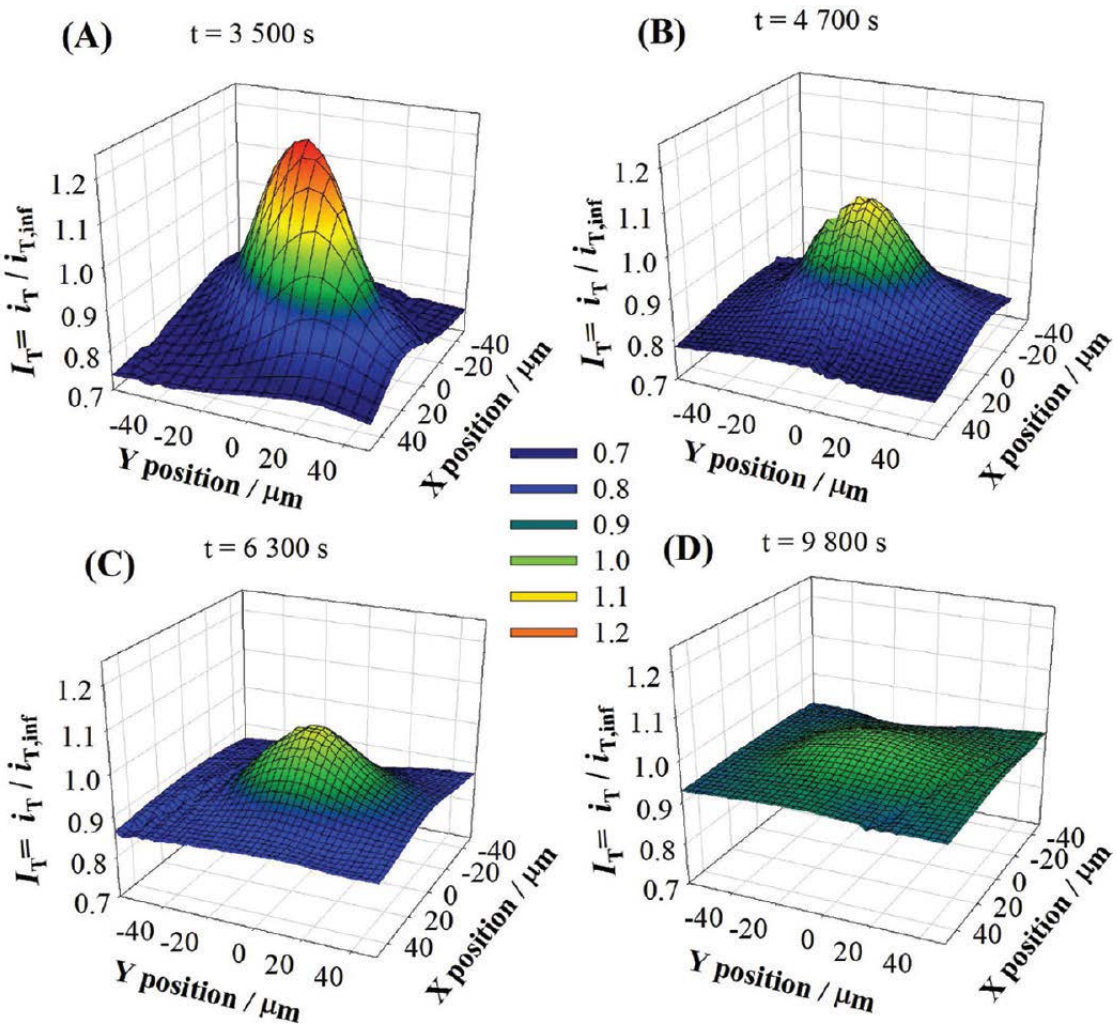

Figure 4.10. Progression of SECM feedback images for a representative **1·2PF$_6$** microspot (≈140 pmol/cm^2, b = 15 µm) on SLG. The experiment used a potassium ferricyanide mediator (2 mM) in phosphate buffer (0.2 M, pH = 7). Images A−D were obtained at the indicated times. The SECM tip was a = 12.5 µm Pt, $R_G \approx 7$ with an interelectrode distance d = 10 µm. Feedback was carried out at E_T = −0.1 V vs Ag/AgCl and E_S = 0.4 V vs Ag/AgCl. The substrate potential was held at E_S throughout the experiment.

We also observed similar behavior at a larger microspot (Appendix Figure A3.13) and performed control experiments to support our interpretation of the feedback measurments. First, images obtained at open circuit (Appendix Figure A3.13), at which the Co(III) species is not deliberately formed on the SLG surface, show almost no difference in the feedback current as compared to unfunctionalized

graphene. The stability of the SLG electrode at oxidizing potentials was also confirmed by measuring the average collection current associated with generating the hydroxymethylferricenium ion (E_S = 0.4 V vs Ag/AgCl) over a period of 6,000 s. These collection currents varied up to ±8%, but no degrading trend for the electrode was observed (Appendix Figure A3.14). Furthermore, no significant formation of oxygenated defects on the SLG is expected at the potentials used for these measurements.[22] It was also possible to detect the **1·2PF$_6$** microspots using other Fe redox mediators, such as FeEDTA (E^0 = −0.08 V vs Ag/ AgCl, Appendix Figure A3.15). The use of Fe(II/ III)EDTA was not pursued further because it would require that these time-sensitive measurements be performed in an inert atmosphere.

The peak feedback currents measured at the center of the microspot were fit to a diffusion model (Figure 4.11) whose input parameters included the measured exchange rate between the adsorbed Co(III) complex and $Fe(CN)_6^{4-}$, the initial surface concentration of **1·2PF$_6$**, and the charge transfer rate constant of the unfunctionalized SLG electrode (see Appendix). Two microspot sizes (15 and 50 μm diameter) were analyzed to confirm the model's applicability. The diffusion coefficient obtained by fitting the absolute feedback measurements (D_{eff} = 1.5 (± 0.6) × 10^{-9} cm^2/s) is in good agreement with that derived from the H_2O_2 collection measurements (D_{eff} = 1.6 (±0.9) × 10^{-9} cm^2/s). Finally, the improved lateral resolution of feedback measurements enabled further inspection of the electrochemical response of the SLG surface away from the center of the **1·2PF$_6$** microspots, which provide further qualitative confirmation of our surface diffusion model.

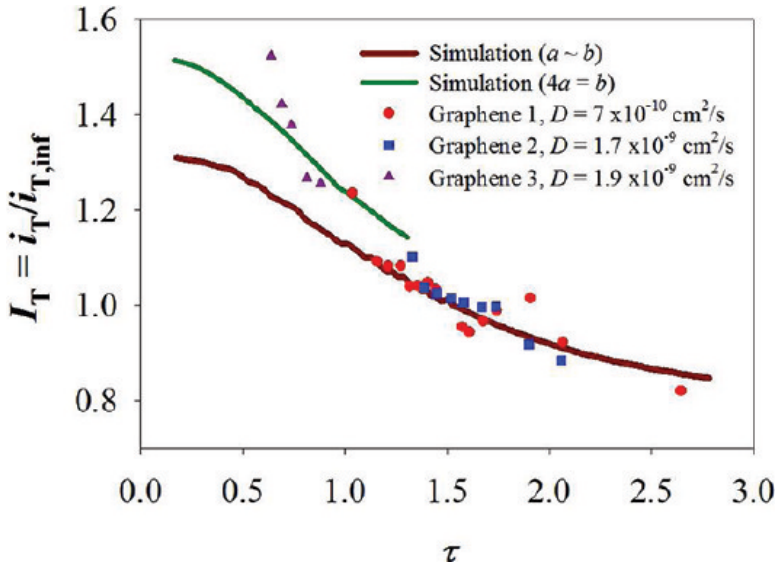

Figure 4.11. Comparison of simulation and experiment for ferrocyanide feedback experiments performed over the center of **1·2PF$_6$** microspots (140 pmol/cm^2, r = 0). The experimental data were fitted to simulation by the choice of D (implicit in τ) as explained in the text. Conditions as in Figure 4.10. The simulations assume a Co(III)- ferrocyanide exchange constant k_{ex} of 1.6 × 10^8 mol/cm^{3}s and an SLG background constant k_{back} of 0.8 × 10^{-3} cm/s. The simulated D for ferri/ferrocyanide was 7.2 × 10^{-6} cm^2/s for both forms of the redox pair. Two sets of data are shown, one for microspots $b \approx 15$ μm (red circles and blue squares) and another for $b \approx 50$ μm. (purple triangles). The first point of each experimental series was obtained at a higher tip scan rate (see Experimental Section) and may reflect some advective effects.

We compared the results of three-dimensional simulations (Appendix Figure A3.16), in which a nonuniform surface concentration profile is translated into a tip response, to the experimental lateral tip currents from the experiment shown in Figure 4.10. A reasonable agreement between simulation and experiment was obtained, which reproduces the concurrent decrease of the peak response, close to the center of the microspot, and increased response in the surrounding graphene material associated with diffusion of the tripods from the microspots. Although the SECM tip size is not necessarily optimal for this analysis, these simulations do confirm that the broadening

of the signal at longer times is a much less sensitive measure of diffusion than the decrease in the peak intensity of the microspot (see above).

The similarity of the surface diffusion values obtained from either G/C or feedback measurements is remarkable, considering the fundamental mechanistic differences, as well as the ≈1 V difference in substrate potential, associated with the two experiments. The potential of zero charge (PZC) of the basal plane of HOPG has been reported[89] to be ≈ −0.2 V vs Ag/AgCl and recent charge carrier measurements on solution-gated graphene field effect transistors show a minimum conductivity, carrier concentration, and shift in carrier entity at ≈ −0.4 V vs Ag/AgCl,[14] which might be closely related to the PZC of graphene. The substrate potentials employed in our studies lie on either side of these values, suggesting that the diffusion of the tripodal binding motif is relatively insensitive to excess charge from adsorbed ions at the graphene/solution interface. Thus, the rate of tripod diffusion might instead be limited by solvent displacement processes or by decreased mobility at graphene defects and edges. The description of these effects lies outside the scope of this manuscript, but their further study is relevant for designing new mobile adsorbates on SLG and other technologically relevant surfaces.

This study represents a macroscopic approach to measuring the diffusion coefficient of the tripodal compounds on SLG and provides an effective value that applies over large distances and times, similar to those obtained by fluorescence in FRAP experiments. These values are distinct from those obtained through single molecule experiments.[49] We have not yet considered the effects of the surface roughness on the response. Scanning probe experiments have found that graphene

transferred onto SiO_2 partially adapts to the morphology of the underlying substrate,[100] with root-mean-square roughness of ≈ 3 nm over 100 μm^2. This roughness is approximately three to four times the graphene layer thickness of 0.8 nm[101] and is less pronounced in high-quality HOPG.[102] This difference in surface roughness is one explanation for the larger surface diffusion coefficient for HOPG shown in Figure 4.7. Reduced diffusion along defects and grain boundaries in our SLG samples[103] may also reduce the measured effective diffusion coefficients. However, it has been observed that favorable π- stacking interactions are relatively insensitive to these features, including steps in single to bilayer graphene.[43] **1·2PF$_6$** is designed to adsorb onto the pristine sp^2 surface of graphene, unlike other aromatic molecules that prefer adsorption at defects on HOPG.[104] However, we cannot discount that favorable interactions between defects and the tripod could account for slowing down its surface mobility. The value obtained here is also at least three orders of magnitude lower than that computationally predicted in vacuum for adsorbed aromatics,[105,106] although this discrepancy can be explained by the lack of description of ion and solvent displacement in such theoretical treatments. Intuitively, the obtained value fits well a middle region between diffusion in solution and in solids.

4.5 Conclusions

Scanning electrochemical microscopy was used to detect the activity and quantify the surface diffusion of tripodal compound **1·2PF$_6$** adsorbed onto SLG and the basal plane of HOPG using two complementary methods. The first method used the substrate generation/tip collection (G/C) mode of SECM to exploit the electrocatalytic properties of the adsorbed tripod, which produced larger amounts of

H_2O_2 than the bare graphene surface in the oxygen reduction reaction. A second method used the feedback mode, in which the tripod mediates the oxidation of ferrocyanide produced at the tip faster than the bare graphene electrode. For each measurement, the increased electrochemical activity of the adsorbed molecules relative to the SLG electrode provided sufficient contrast to image microspots of the tripodal molecules with spatial and temporal resolution. We attribute the decreased electrochemical response of the tripodal microspots over time to diffusion of the molecules onto the unfunctionalized regions of the SLG electrode. A framework for describing this diffusion in terms of the decrease of the peak intensity of the microspots due to radial dilution, as detected by SECM, was successfully implemented. The two imaging strategies yielded similar values of the macroscopic surface diffusion (D_{eff}) of the tripod on the graphene surface: D_{eff} = 1.6 (±0.9) × 10^{-9} cm^2/s at E_S = −0.6 V vs Ag/AgCl and D_{eff} = 1.5 (±0.6) × 10^{-9} cm^2/s at E_S = 0.4 V vs Ag/AgCl for G/C and feedback modes, respectively. Control experiments, in which the stability of graphene was tested, as well as experiments in which the mobility of the tripodal molecules was disrupted by coadsorption of a polymer, strongly support our surface diffusion hypothesis. The development of an SECM-based technique for quantifying molecular surface diffusion on electrodes, specifically on graphene as a model carbon surface, is an important addition to the understanding and control of molecular electrocatalysis for sensing and energy conversion systems. It also presents interesting possibilities in the field of molecular electronics, where the coupling of the unique electronic and mechanical properties of graphene together with its surface mass transfer properties can now be studied and quantitatively described. We are currently

working to image graphene using SECM at higher resolution in order to describe this material and its interactions in better detail. For instance, we hope to explore the impact of grain boundaries, single crystallites (ranging from a few to tens of micrometers), reactive defects, and heteroatom substitutions on the electrochemical reactivity of this promising material.

4.6 Acknowledgements

The authors acknowledge NSF CCI-phase I (0847926) for financial support. The authors thank CNF (ECS 0335765) and CCMR (DMR 1120296) for providing fabrication facilities and instrumentation; Professor Paul L. McEuen, Professor Jiwoong Park, and Kevek Innovations for help with graphene growth; and Dr. Eric Rus for helpful discussions. N.L.R., C.T., and J.A.M. gratefully acknowledge the Integrative Graduate Education and Research Traineeship (IGERT) Program in the Nanoscale Control of Surfaces and Interfaces, which is supported under NSF Award DGE-0654193, the Cornell Center for Materials Research, and Cornell University.

REFERENCES

(1) Novoselov, K. S.; Geim, A. K.; Morozov, S. V.; Jiang, D.; Zhang, Y.; Dubonos, S. V.; Crigorieva, I. V.; Firsov, A. A. *Science*, **2004**, *306*, 666-669.

(2) Stankovich, S.; Dikin, D. A.; Dommett, G. H. B.; Kohlhaas, K. M.; Zimney, E. J.; Stach, E. A.; Piner, R. D.; Nguyen, S. T.; Ruoff, R. S. *Nature*, **2006**, *442*, 282-286.

(3) Geim, A. K.; Novoselov, K. S. *Nat. Mater.*, **2007**, *6*, 183-191.

(4) Geim, A. K. *Science,* **2009**, *324*, 1530-1534.

(5) Li, W.; Tan, C.; Lowe, M. A.; Ralph, D. C.; Abruña, H. D. *ACS Nano,* **2011**, *5*, 2264-2270.

(6) Wang, X.; Zhi, L.; Müllen, K. *Nano Lett.*, **2007**, *8*, 323-327.

(7) Kumar, A.; Zhou, C. *ACS Nano.*, **2010**, *4*, 11-14.

(8) Li, X.; Zhu, Y.; Cai, W.; Borysiak, M.; Han, B.; Chen, D.; Piner, R. D.; Colombo, L.; Ruoff, R. S. *Nano Lett.*, **2009**, *9*, 4359-4369.

(9) Bunch, J. S.; van der Zande, A. M.; Verbridge, S. S.; Frank, I. W.; Tanenbaum, D. M.; Parpia, J. M.; Craighead, H. G.; McEuen, P. L. *Science*, **2007**, *315*, 490-493.

(10) Van der Zande, A. M.; Barton, R. A.; Alden, J. S.; Ruiz-Vargas, C. S.; Whitney, W. S.; Pham, P.H.-Q.; Park, J.-W.; Parpia, J. M.; Craighead, H. G.; McEuen, P. L. *Nano Lett.*, **2010**, *10*, 4869-4873.

(11) Lee, W. H.; Park, J.; Sim, S. H.; Lim, S.; Kim, K. S.; Hong, B. H.; Cho, K. *J. Am. Chem. Soc.*, **2011**, *133*, 4447-4454.

(12) Liu, W.; Jackson, B. L.; Zhu, J.; Miao, C.-Q.; Chung, C.-H.; Park, Y. J.; Sun, K.; Woo, J.; Xie, Y.-H. *ACS Nano*, **2010**, *4*, 3927-3932.

(13) Jang, S.; Jang, H.; Lee, Y.; Suh, D.; Baik, S.; Hong, B. H.; Ahn, J.- H. *Nanotechnology*, **2010**, *21*, 425201/1-425201/5.

(14) Dankerl, M.; Hauf, M. V.; Lippert, A.; Hess, L. H.; Birner, S.; Sharp, I. D.; Mahmood, A.; Mallet, P.; Veuillen, J-.Y.; Stutzmann, M.; Garrido, J. A. *Adv. Funct. Mater.* **2010**, *20*, 3117-3124.

(15) Cheng, H.-C.; Shiue, R.-J.; Tsai, C.-C.; Wang, W.-H.; Chen, Y.- T. *ACS Nano*, **2011**, *5*, 2051-2059.

(16) Coletti, C.; Riedl, C.; Lee, D. S.; Krauss, B.; Patthey, L.; von Klitzing, K.; Smet, J. H.; Starke, U. *Phys. Rev. B*, **2010**, *81*, 235401/1- 235401/8.

(17) McCreery, R. L. *Chem. Rev.*, **2008**, *108*, 2646-2687.

(18) McCreery, R. L. Carbon Electrodes: Structural Effects on Electron Transfer Kinetics. *In Electroanalytical Chemistry*; Bard, A. J., Ed.; Marcel Dekker: New York, **1991**; *Vol.17*, pp 221-374.

(19) Edwards, M. A.; Bertoncello, P.; Unwin, P. R. *J. Phys. Chem. C*, **2009**, *113*, 9218-9223.

(20) Dumitrescu, I.; Dudin, P. V.; Edgeworth, J. P.; Macpherson, J. V.; Unwin, P. R. *J. Phys. Chem. C*, **2010**, *114*, 2633-2639.

(21) Heller, I.; Kong, J.; Heering, H. A.; Williams, K. A.; Lemay, S. G.; Dekker, C. *Nano Lett.*, **2005**, *5*, 137-142.

(22) Lim, C. X.; Hoh, H. Y.; Ang, P. K.; Loh, K. P. *Anal. Chem.*, **2010**, *82*, 7387-7393.

(23) Qu, L.; Liu, Y.; Baek, J-.B.; Dai, L. *ACS Nano*, **2010**, **4**, 1321-1326.

(24) Scida, K.; Stege, P. W.; Haby, G.; Messina, G. A.; Garcia, C. D. *Anal. Chim. Acta*, **2011**, *691*, 6-17.

(25) Ratinac, K. R.; Yang, W.; Gooding, J. J.; Thordarson, P.; Braet, F. *Electroanalysis*, **2011**, *23*, 803-826.

(26) Pumera, M. *Chem. Rec.*, **2009**, *9*, 211-223.

(27) Brownson, D. A. C.; Banks, C. E. *Analyst*, **2010**, *135*, 2768-2778.

(28) Hasin, P.; Alpuche-Avile.s, M. A.; Wu, Y. *J. Phys. Chem. C*, **2010**, *114*, 15857-15861.

(29) Shao, Y.; Wang, Y.; Wu, H.; Liu, J.; Aksay, I. A.; Lin, Y. *Electroanalysis*, **2010**, *22*, 1027-1036.

(30) Mann, J. A.; Rodriguez-Lo.pez, J.; Abruña, H. D.; Dichtel, W. R. *J. Am. Chem. Soc.*, **2011**, *133*, 17614-17617.

(31) Tasis, D.; Tagmatarchis, N.; Bianco, A.; Prato, M. *Chem. Rev.*, **2006**, *106*, 1105-1136.

(32) *Scanning Electrochemical Microscopy*; Bard, A. J., Mirkin, M. V., Eds.; Marcel Dekker: New York, **2001**.

(33) Bard, A. J.; Fan, F.-R. F.; Mirkin, M. V. Scanning Electrochemical Microscopy. In Electroanalytical Chemistry; Bard, A. J., Ed.; Marcel Dekker: New York, 1993, Vol. 18, pp 243.373.

(34) Bard, A. J.; Denuault, G.; Lee, C.; Mandler, D.; Wipf, D. O. *Acc. Chem. Res.*, **1990**, *23*, 357-363.

(35) Save.ant, J-.M. *Chem. Rev.*, **2008**, *108*, 2348-2378.

(36) McCrory, C. C. L.; Devadoss, A.; Ottenwaelder, X.; Lowe, R. D.; Stack, D. P.; Chidsey, C. E. D. *J. Am. Chem. Soc.*, **2011**, *133*, 3696-3699.

(37) Park, J.; Pasupathy, N.; Goldsmith, J. I.; Chang, C.; Yaish, Y.; Petta, J. R.; Rinkoski, M.; Sethna, J. P.; Abrun.a, H. D.; McEuen, P. L.; Ralph, D. C. *Nature*, **2002**, *417*, 722-725.

(38) Metzger, R. M. *J. Mater. Chem.*, **2008**, *18*, 4364-4396.

(39) Marek Szklarczyk, M.; Strawski, M.; Bieńkowski, K. 25 years of the Scanning Tunneling Microscopy . 20 Years of Application of STM in Electrochemistry. *In Modern Aspects of Electrochemistry*; Vayenas, C. G.; White, R. E.; Gamboa-Aldeco, M. E., Eds.; Springer: New York, **2008**; Vol. *42*, pp 303-368.

(40) Wang, D.; Wan, L-.J. *J. Phys. Chem. C*, **2007**, *111*, 16109-16130.

(41) Kolb, D. M. *Angew. Chem., Int. Ed.*, **2001**, *40*, 1162-1181.

(42) Itaya, K. *Prog. Surf. Sci.*, **1998**, *58*, 121-248.

(43) Emery, J. D.; Wang, Q. H.; Zarrouati, M.; Fenter, P.; Hersam, M. C.; Bedzyk, M. *J. Surf. Sci.*, **2011**, *605*, 1685-1693.

(44) Wang, Q. H.; Hersam, M. C. *Nat. Chem.*, **2009**, *1*, 206-211.

(45) Kornberg, R. D.; McConnell, H. M. *Proc. Natl. Acad. Sci. U.S.A.*, **1971**, *68*, 2564-2568.

(46) Ko.chy, T.; Bayerl, T. M. *Phys. Rev. E*, **1993**, *47*, 2109-2116.

(47) Kobayashi, T.; Babu, P. K.; Gancs, L.; Chung, J. H.; Oldfield, E.; Wieckowski, A. *J. Am. Chem. Soc.*, **2005**, *127*, 14164-14165.

(48) Tong, Y. Y.; Oldfield, E.; Wieckowski, A. *Faraday Discuss.*, **2002**, *121*, 323-330.

(49) Sigaut, L.; Ponce, M. L.; Colman-Lerner, A.; Ponce Dawson, S. *Phys. Rev. E*, **2010**, *82*, 051912.

(50) Naito, K.; Tachikawa, T.; Fujitsuka, M.; Majima, T. J. *Phys. Chem. C*, **2008**, *112*, 1048-1059.

(51) Reits, E. A.J.; Neefjes, J. J. *Nat. Cell Biol.*, **2001**, *3*, E145-E147.

(52) Axelrod, D.; Koppel, D. E.; Schlessinger, J.; Elson, E.; Webb, W. W. *Biophys. J.* **1976**, *16*, 1055-1067.

(53) Lore.n, N.; Nyde.n, M.; Hermansson, A.-M. *Adv. Colloid Interface Sci.* **2009**, *150*, 5-15.

(54) Lu, C-.H.; Yang, H-.H.; Zhu, C-.L.; Chen, X.; Chen, G-.N. *Angew. Chem., Int. Ed.*, **2009**, *48,* 4785-4787.

(55) Ramakrishna Matte, H. S. S.; Subrahmanyam, K. S.; Rao, K. V.; George, S. J.; Rao, C. N. R. *Chem. Phys. Lett.*, **2011**, *506*, 260-264.

(56) Kim, J.; Cote, L. J.; Kim, F.; Huang, J. *J. Am. Chem. Soc.*, **2010**, *132*, 260-267.

(57) He, S.; Song, B.; Li, D.; Zhu, C.; Qi, W.; Wen, Y.; Wang, L.; Song, S.; Fang, H.; Fan, C. *Adv. Funct. Mater.*, **2010**, *20*, 453-459.

(58) Chen, Z.; Berciaud, S.; Nuckolls, C.; Heinz, T. F.; Brus, L. *ACS Nano*, **2010**, *4*, 2964-2968.

(59) Unwin, P. R.; Bard, A. J. *J. Phys. Chem.*, **1992**, *96*, 5035-5045.

(60) Slevin, C. J.; Unwin, P. R. *J. Am. Chem. Soc.*, **2000**, *122*, 2597- 2602.

(61) Zhang, J.; Unwin, P. R. *J. Am. Chem. Soc.*, **2002**, *124*, 2379.

(62) Zhang, J.; Slevin, C.; Morton, C.; Scott, P.; Walton, D. J.; Unwin, P. R. *J. Phys. Chem. B*, **2001**, *105*, 11120-11130.

(63) Zhang, J.; Unwin, P. R. *Phys. Chem. Chem. Phys.*, **2002**, *4*, 3814-3819.

(64) O. F. Mullane, A. P.; Macpherson, J. V.; Unwin, P. R.; Cervera- Montesinos, J.; Manzanares, J. A.; Frehill, F.; Vos, J. G. J. *Phys. Chem. B* , **2004**, *108*, 7219-7227.

(65) Mandler, D.; Unwin, P. R. *J. Phys. Chem. B*, **2003**, *107*, 407-410.

(66) Bertoncello, P.; Ciani, I.; Li, F.; Unwin, P. R. *Langmuir*, **2006**, *22*, 10380-10388.

(67) Whitworth, A. L.; Mandler, D.; Unwin, P. R. *Phys. Chem. Chem. Phys.*, **2005**, *7*, 356-365.

(68) Zhang, J.; Barker, A. L.; Mandler, D.; Unwin, P. R. *J. Am. Chem. Soc.*, **2003**, *125*, 9312-9313.

(69) Charych, D. H.; Landau, E. M.; Majda, M. *J. Am. Chem. Soc.*, **1991**, *113*, 3340-3346.

(70) Takada, K.; Storrier, G. D.; Goldsmith, J. I.; Abruña, H. D. *J. Phys. Chem. B*, **2001**, *105*, 2404-2411.

(71) Buttry, D. A.; Anson, F. C. *J. Am. Chem. Soc.*, **1983**, *105*, 685-689.

(72) Farina, R.; Wilkins, R. G. *Inorg. Chem.*, **1968**, *7*, 514-518.

(73) Chow, H. S.; Constable, E. C.; Housecroft, C. E.; Kulicke, K. J.; Tao, Y. *Dalton Trans.*, **2005**, 236-237.

(74) Sanchez-Sanchez, C. M.; Rodriguez-Lopez, J.; Bard, A. J. *Anal. Chem.*, **2008**, *80*, 3254-3260.

(75) Yeager, E. *Electrochim. Acta*, **1984**, *29*, 1527-1537.

(76) Durand, R. R.; Anson, F. C. J. *Electroanal. Chem.*, **1982**, *134*, 273-289.

(77) Horrocks, B. R.; Schmidtke, D.; Heller, A.; Bard, A. J. *Anal. Chem.*, **1993**, *65*, 3605-3614.

(78) Wittstock, G.; Schuhmann, W. *Anal. Chem.*, **1997**, *69*, 5059-5066.

(79) Ge, F.; Tenent, R. C.; Wipf, D. O. *Anal. Sci.*, **2001**, *17*, 27-35.

(80) Wittstock, G.; Wilhelm, T. *Anal. Sci.*, **2002**, *18*, 1199-1204.

(81) Sanchez-Sanchez, C. M.; Bard, A. J. *Anal. Chem.*, **2009**, *81*, 8094-8100.

(82) Eckhard, K.; Schuhmann, W. *Electrochim. Acta*, **2007**, *53*, 1164-1169.

(83) Pust, S. E.; Maier, W.; Wittstock, G. *Z. Phys. Chem.*, **2008**, *222*, 1463-1517.

(84) Liu, B.; Bard, A. J.; Mirkin, M. V.; Creager, S. E. *J. Am. Chem. Soc.*, **2004**, *126*, 1485-1492.

(85) Holt, K. B. *Langmuir*, **2006**, *22*, 4298-4304.

(86) Wain, A. J.; Zhou, F. *Langmuir*, **2008**, *24*, 5155-5160.

(87) Tefashe, U. M.; Loewenstein, T.; Miura, H.; Schlettwein, D.; Wittstock, G. J. *Electroanal. Chem.*, **2010**, *650*, 24-30.

(88) Liu, B.; Rotenberg, S. A.; Mirkin, M. V. *Anal. Chem.*, **2002**, *74*, 6340-6348.

(89) Kneten, K. R.; McCreery, R. L. *Anal. Chem.*, **1992**, *64*, 2518-2524.

(90) McDermott, C. A.; Kneten, K. R.; McCreery, R. L. *J. Electrochem. Soc.*, **1993**, *140*, 2593-2599.

(91) Rodríguez-López, J.; Minguzzi, A.; Bard, A. J. *J. Phys. Chem. C*, **2010**, *114*, 18645-18655.

(92) Hurrell, H. C.; Abrun.a, H. D. *Anal. Chem.*, **1988**, *60*, 254.

(93) OPA445 High Voltage FET-Input Operational Amplifier, Texas Instruments technical note. SBOS156B . March 1987 . Revised April 2008.

(94) These coverages are similar to others observed on cobalt complexes in related materials. McQueen, E.; Goldsmith, J. I. *J. Am. Chem. Soc.*, **2009**, *131*, 17554-17556.

(95) Lefrou, C.; Cornut, R. *ChemPhysChem*, **2010**, *11*, 547-556.

(96) Cobalt (II) *bis*-terpyridine is labile in highly acidic medium but shows negligible decomposition at neutral pH. Farina, R.; Hogg, R.; Wilkins, R. G. *Inorg. Chem.*, **1968**, *7*, 170-172.

(97) Experiments (not shown) where reversible mediators (e.g., methyl viologen) that show quantitative positive feedback were used together with sluggish Fe (II/III) couples to calibrate their feedback response demonstrate that this positioning method is valid; a maximum error of $\approx \pm 1$ μm can be conceded.

(98) In this procedure, all experimental tip currents within a run were also divided by an arbitrary constant in order to fit them in the vertical axis. The overall procedure is equivalent (and was checked to be so) to comparing the normalized simulated result to a normalized experimental result at a fixed absolute time, except that in this case it is necessary to obtain a simulated curve for any possible value of D; this is less convenient than fitting the data by choice of D to the master curve.

(99) Kneten Cline, K.; McDermott, M. T.; McCreery, R. L. *J. Phys. Chem.*, **1994**, *98*, 5314-5319.

(100) Ishigami, M.; Chen, J. H.; Cullen, W. G.; Fuhrer, M. S.; Williams, E. D. *Nano Lett.*, **2007**, 7, 1643-1648.

(101) Reina, A.; Jia, X.; Ho, J.; Nezich, D.; Son, H.; Bulovic, V.; Dresselhaus, M. S.; Kong, J. *Nano Lett.*, **2008**, *9*, 30-35.

(102) Gewirth, A. A.; Bard, A. J. *J. Phys. Chem.*, **1988**, *92*, 5563-5566.

(103) Huang, P. Y.; Ruiz-Vargas, C. S.; van der Zande, A. M.; Whitney, W. S.; Levendorf, M. P.; Kevek, J. W.; Garg, S.; Alden, J. S.; Hustedt, C. J.; Zhu, Y.; Park, J.; McEuen, P. L.; Muller, D. A. *Nature*, **2011**, *469*, 389-392

APPENDIX THREE

Table of Contents

A.Graphene growth

CVD Graphene. The CVD graphene was fabricated according to literature procedures[1,2] and was grown on Cu foil. Copper foils were treated with acetone (10 s), water, glacial acetic acid (10 min), water (deionized), acetone (10 s), and isopropanol (10 s) before growth. The Cu foil was then loaded in a quartz tube in a tube furnace. The system was pumped down to 8.0×10^{-5} torr. After reaching base pressure, 6 sccm of H_2 (99.999%, Airgas) were flowed. Then the system was heated at 1000 °C for 10 min followed by 157.5 sccm of CH_4 (99.999%, Airgas) for 13 min and then let to cool down to room temperature. For support during graphene transfer, 8% PMMA in anisole (Nano^{TM} 495 PMMA series resists in anisole, MicroChem) was spin coated on graphene at 4000 RPM for 60 sec. The Cu-graphene-PMMA was then floated on a ferric chloride etch solution (CE-100 grade, Transene Company) to remove the Cu. The graphene-PMMA membrane was transferred into fresh DI water 6 times to remove the residual impurities. Finally, the membrane was scooped out of DI water with a piece of plasma-cleaned Si/SiO_2 substrate (SiO_2 thickness 300 nm, prime grade, Silicon Quest International). The chip was blow-dried using N_2 (99.999%, Airgas). To remove the PMMA, the chip was soaked in anisole (2 h), dichloromethane:acetone (1:1, 4 h), and isopropanol (2 h), then blow-dried again. The quality of the graphene was characterized using a Renishaw InVia Confocal Raman microscope (Renishaw, Gloucestershire, UK) with a 488 nm laser. A typical Raman spectrum of the SLG used, shown in Figure A3.1, shows the expected characteristics for single layer graphene of the desired quality on Si/SiO_2: the ratio of the G band peak (~ 1585 cm^{-1}) to 2D band peak (~ 2697 cm^{-1}), I(G)/I(2D) < 0.5, a relatively small D band (~ 1350 cm^{-1}) and a narrow, single Lorentzian-like 2D band (FWHM 33 cm^{-1}).[2-4] Graphene microelectrodes for control and supporting experiments were fabricated as follows: Al_2O_3 (1000 Å, CVC SC4500 e-gun evaporator) and Parylene (~500nm, PDS 2010 Labcoter deposition system, Specialty Coating Systems, Indianapolis, IN) were evaporated on the entire graphene surface to prevent contamination. A layer of p20 was spin casted to remove the moisture on the substrate followed by a layer of photo resist (microposit S1813, Dow Chemical Company) for patterning. A hole of 15μm or

50 μm in radius was patterned upon UV exposure for 7.5 s using a contact aligner (ABM, Inc., San Jose, CA). To expose the graphene, parylene was removed using oxygen plasma (5 min., Oxford PlasmaLab 80+ RIE System, Oxford Instruments, Oxfordshire, UK) and the Al_2O_3 was removed using AZ 726MIF developer (AZ Electronic Materials USA Corp., Branchburg, NJ). Finally, the photo resist was removed using Shipley microposit remover (1165, Dow Chemical Company).

Electric contacts to graphene electrodes were made by either direct contact of a small piece of indium to the edge of the graphene sheet (which is visible on the SiO_2 substrate) followed by contact to conductive copper tape (Saint-Gobain performance plastics) or by depositing gold contacts to which copper tape could be attached. For the deposition of gold, 20Å of Ti (99.995%, Kurt J. Lesker Company) were evaporated onto one end of the single-layer graphene electrode as an adhesion layer followed by 1000 Å of Au (99.999%, Kurt J. Lesker Company) for contacts using a CVC SC4500 e-gun evaporator. Either contact method is satisfactory except that the gold contacts are more robust at the expense of an additional fabrication step.

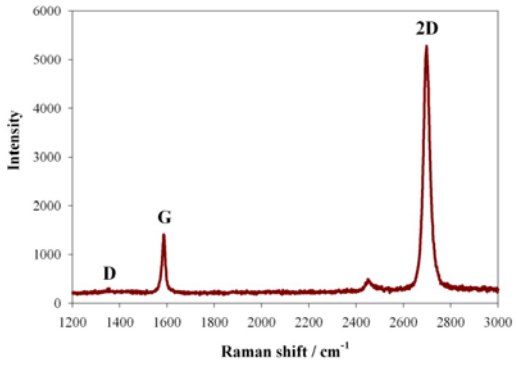

Figure A3.1. Raman spectrum of typical single layer graphene used in the electrochemical experiments described here.

B. Additional Electrochemical Characterization.

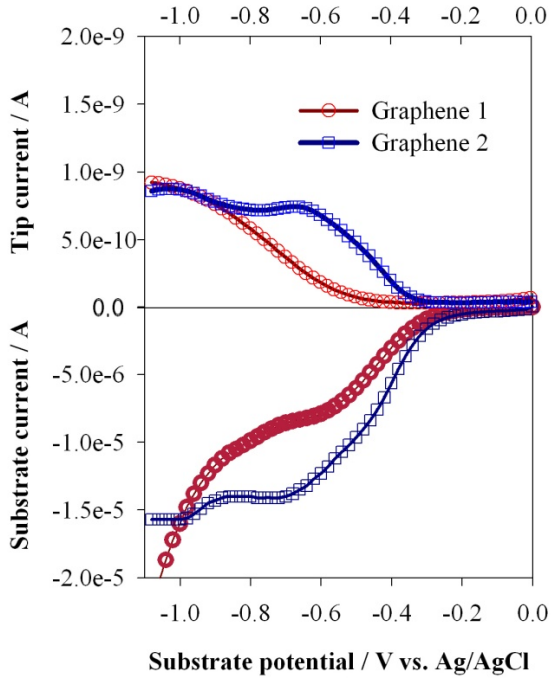

Figure A3.2. Substrate generation / tip collection curves for hydrogen peroxide generated during the oxygen reduction reaction at a macroelectrode in air-saturated 0.2 M phosphate buffer pH 7 for two samples of graphene; Graphene 2 shows the most active electrode observed in terms of oxygen reduction onset potential and peroxide output. Tip was a = 12.5 μm Pt, RG ~ 7 and collection was carried out at E_T = 0.6 V vs. Ag/AgCl and interelectrode distance d = 10 μm. Linear sweep at the substrate was carried out at 10 mV/s.

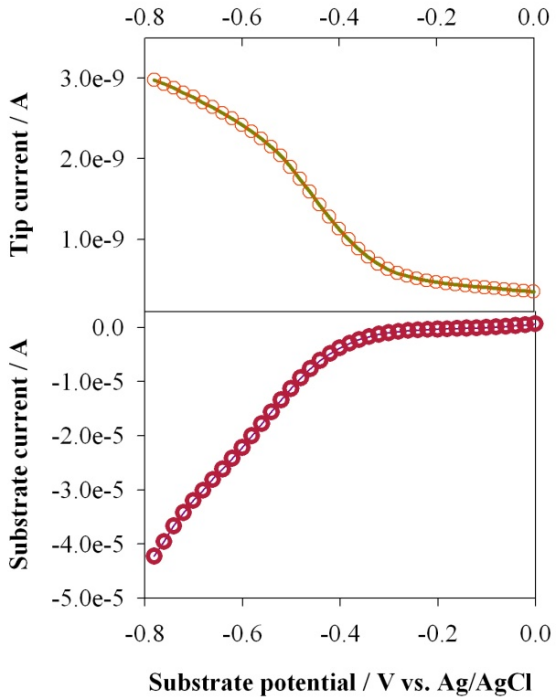

Figure A3.3. Substrate generation / tip collection curves for hydrogen peroxide generated during the oxygen reduction reaction at a macroelectrode in air-saturated 0.2 M phosphate buffer pH 7 for glassy carbon; Tip was a = 12.5 µm Pt, RG ~ 7 and collection was carried out at E_T = 0.6 V vs. Ag/AgCl and interelectrode distance d = 10 µm. Linear sweep at the substrate was carried out at 10 mV/s.

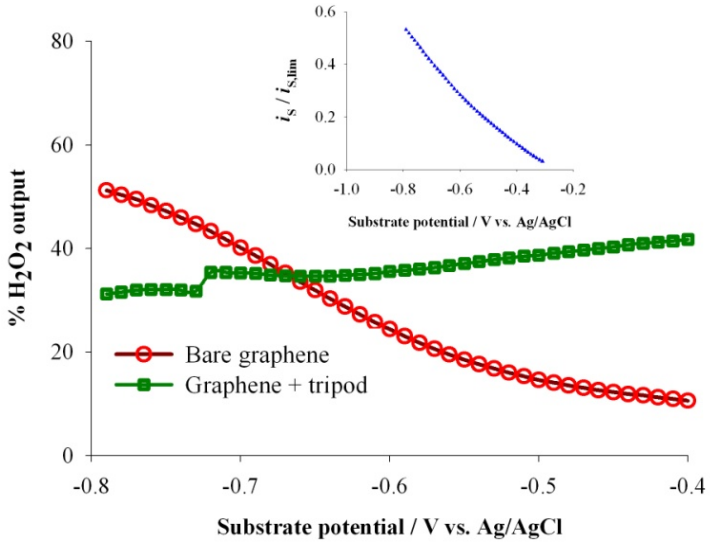

Figure A3.4. Hydrogen peroxide quantification at steady state on a b = 50 µm graphene microelectrode before and after exposure to 5 µM tripod solution in THF followed by thorough cell rinsing. Quantification was done according to the method proposed in Ref. 76 in the main text: The SECM tip (a = 12.5 µm Pt, RG ~ 7) was

coaligned to the graphene microelectrode using hydroxymethylferrocene as mediator and the collection efficiency of the system verified. Peroxide measurements done with E_T = 0.6 V vs. Ag/AgCl and interelectrode distance d = 10 μm. Inset shows the bare graphene current as a function of the diffusion limited current attainable if assuming a 4-electron route (~28 nA for the electrode used) for oxygen reduction.

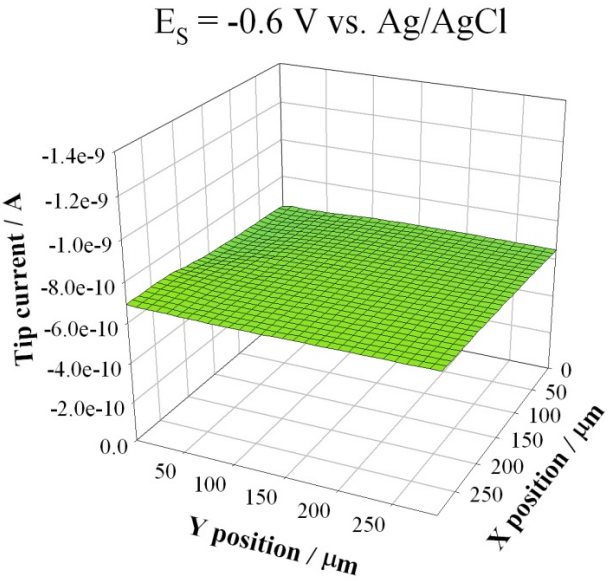

Figure A3.5. Typical hydrogen peroxide background observed on bare graphene. Tip was a = 12.5 μm diameter Pt, RG ~ 7 and collection was carried out at E_T = 0.6 V vs. Ag/AgCl and E_S = -0.6 V vs. Ag/AgCl; interelectrode distance d = 10 μm.

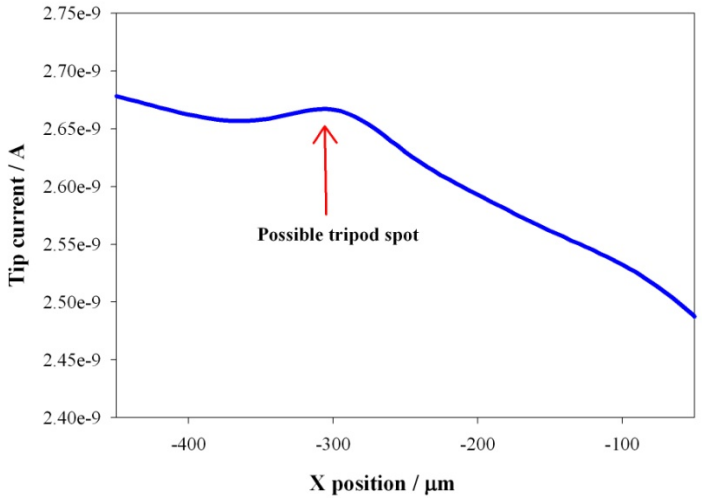

Figure A3.6. Hydrogen peroxide linescan observed on a glassy carbon electrode with tripod microspots deposited onto it. Tip was a = 12.5 μm diameter Pt, RG ~ 7 and collection was carried out at E_T = 0.6 V vs. Ag/AgCl and E_S = -0.6 V vs. Ag/AgCl; interelectrode distance d = 10 μm.

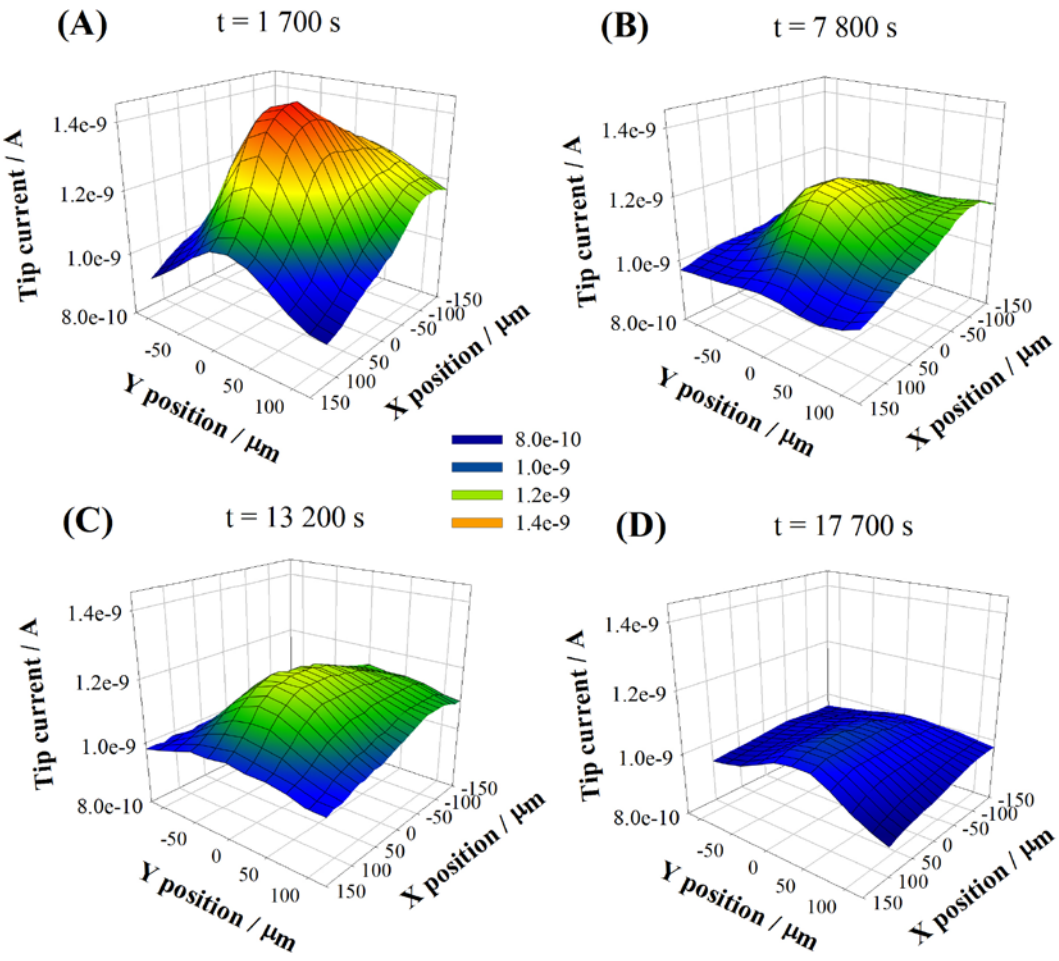

Figure A3.7. Progression of SECM hydrogen peroxide substrate generation / tip collection images for a representative tripod microspot on graphene, b = 50 µm. Images (A) to (D) obtained at indicated times. Tip was a = 12.5 µm diameter Pt, RG ~ 7 and collection was carried out at E_T = 0.6 V vs. Ag/AgCl and E_S = -0.6 V vs. Ag/AgCl; interelectrode distance d = 10 µm. Tripod was deposited in sufficient amount to yield ~ 100 pmol/cm^2. Potential held at E_S throughout the experiment.

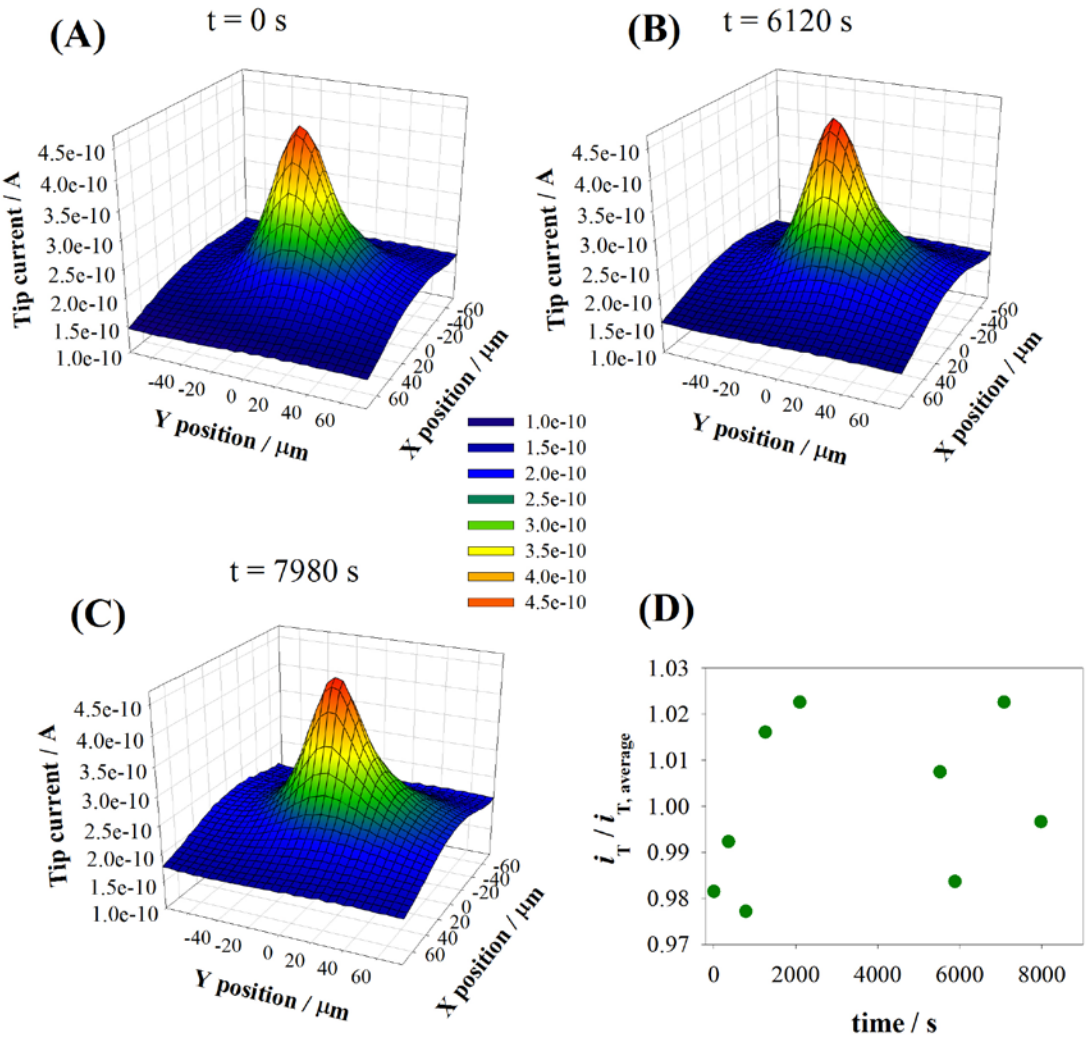

Figure A3.8. Progression of SECM hydrogen peroxide substrate generation / tip collection images for a microfabricated graphene electrode, b = 15 µm. Images (A) to (C) obtained at indicated times. Tip was a = 12.5 µm diameter Pt, RG ~ 7 and collection was carried out at E_T = 0.6 V vs. Ag/AgCl and E_S = -1.0 V vs. Ag/AgCl; interelectrode distance d = 10 µm. Potential held at E_S throughout the experiment. (D) Plot of background subtracted peak collection currents, normalized to the average measured current vs. time.

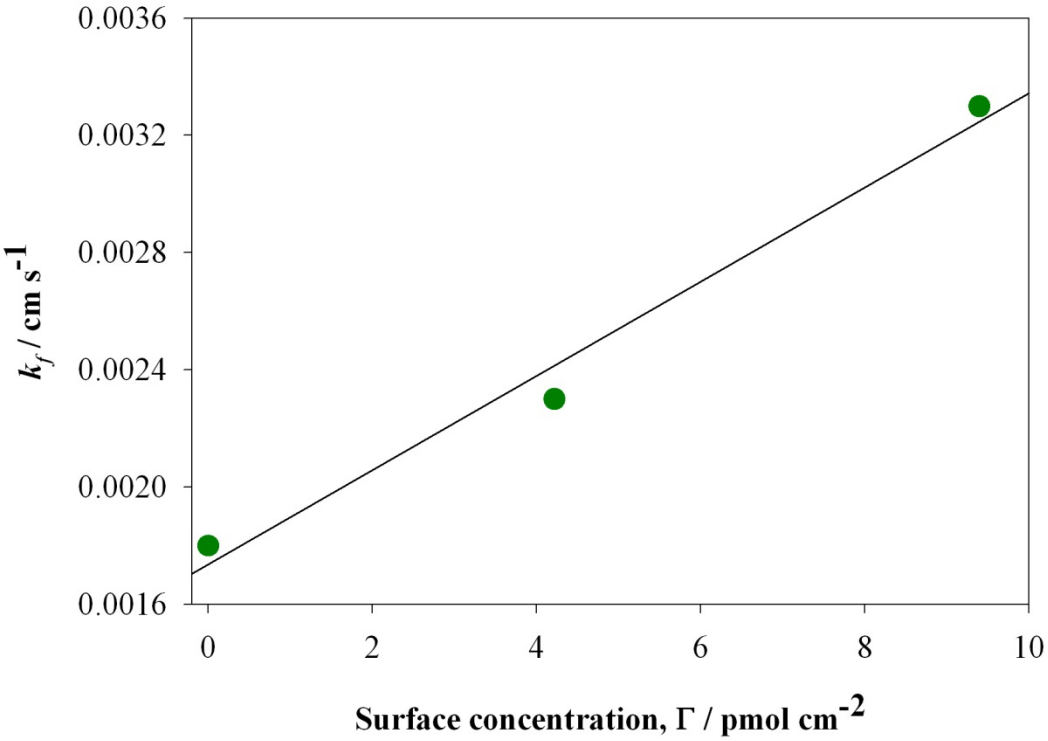

Figure A3.9. Estimation of the exchange rate constant between the **1· 2PF6** tripod and ferrocyanide. k_{ex} for the approach curves presented in Figure 4.9 in the main text. At complete activation of the tripod to Co(III), the pseudo-first order electrochemical rate constant can be written as $k_{el} = k_{ex} \Gamma$, where a linear plot of k_{el} with respect to Γ should give a line with slope k_{ex}. Estimated $k_{ex} = 1.6 \times 10^8$ mol/cm^{3}s.

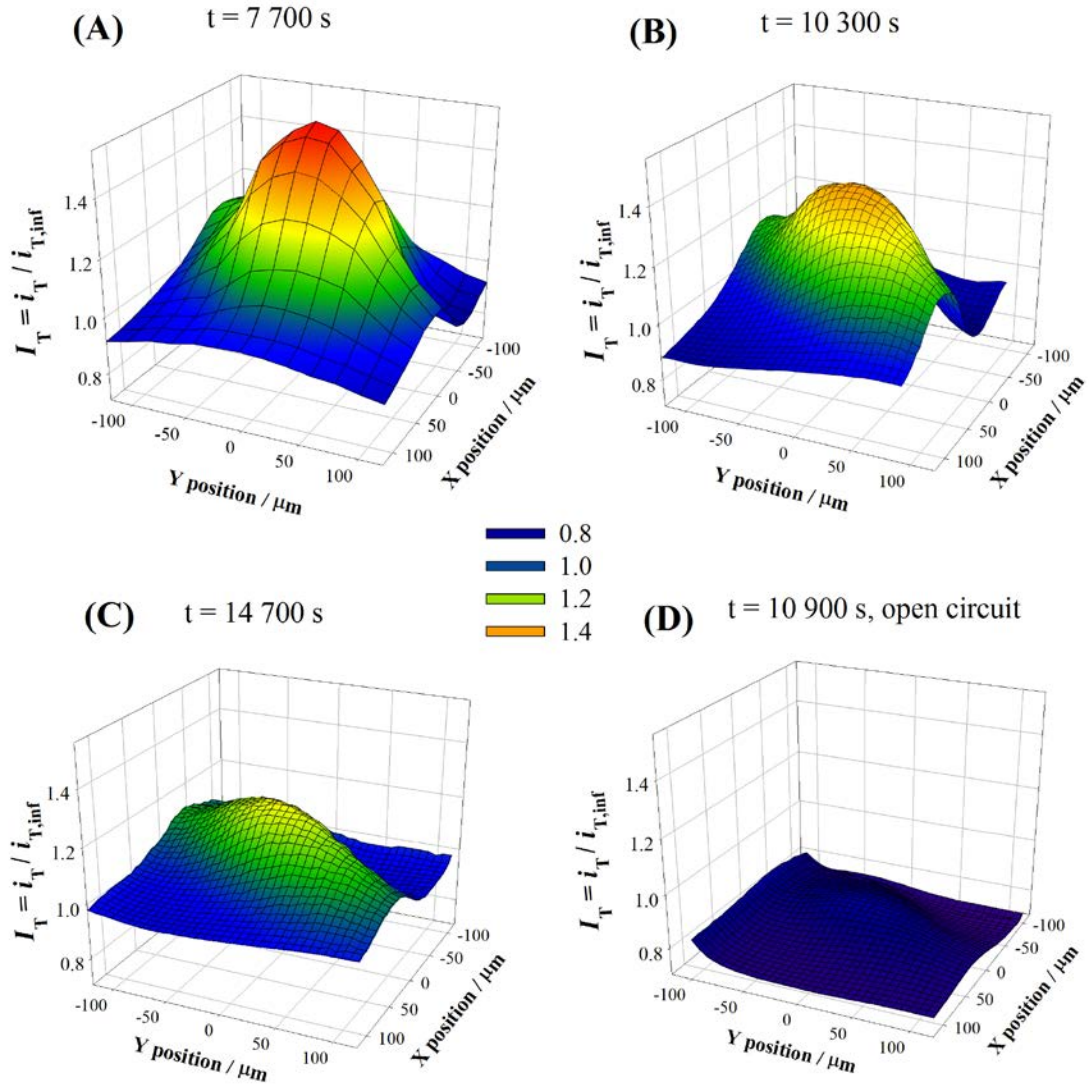

Figure A3.10. Progression of SECM feedback images for a representative tripod microspot on graphene, b = 50 µm using 2 mM potassium ferricyanide as mediator in 0.2 M phosphate buffer pH 7. Images (A) to (C) obtained at indicated times. Tip was a = 12.5 µm Pt, RG ~ 7 and feedback was carried out at E_T = -0.1 V vs. Ag/AgCl and E_S = 0.4 V vs. Ag/AgCl; interelectrode distance d = 10 µm. Image (D) obtained with substrate at open circuit under similar conditions to image (B). Tripod was deposited in sufficient amount to yield ~ 140 pmol/cm^2. Potential held at E_S throughout the experiment except for Figure (D).

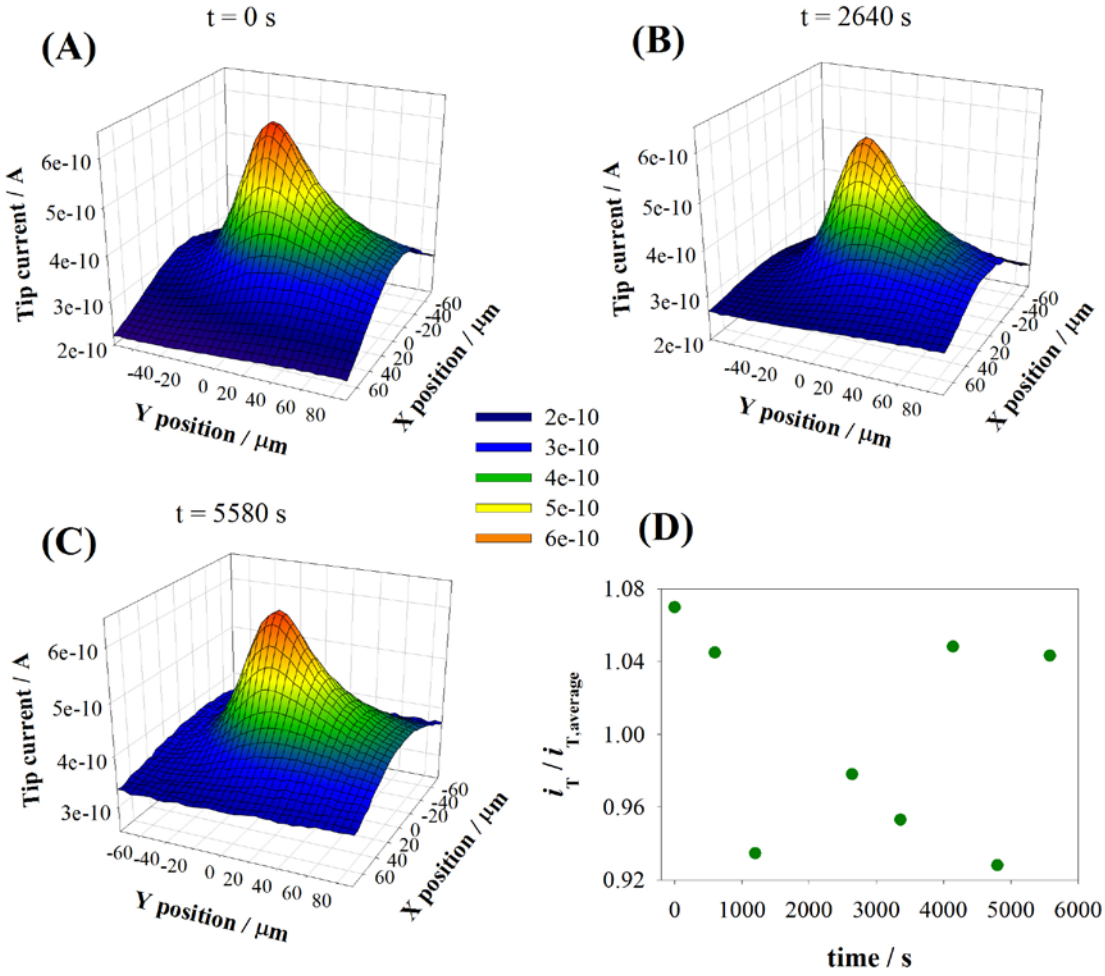

Figure A3.11. Progression of SECM hydroxymethylferrocenium substrate generation / tip collection images for a microfabricated graphene electrode, b = 15 µm. Images (A) to (C) obtained at indicated times. Tip was a = 12.5 µm diameter Pt, RG ~ 7 and collection was carried out at E_T = 0.1 V vs. Ag/AgCl and E_S = 0.4 V vs. Ag/AgCl; interelectrode distance d = 10 µm. Potential held at E_S throughout the experiment. (D) Plot of peak collection currents, normalized to the average measured current vs. time.

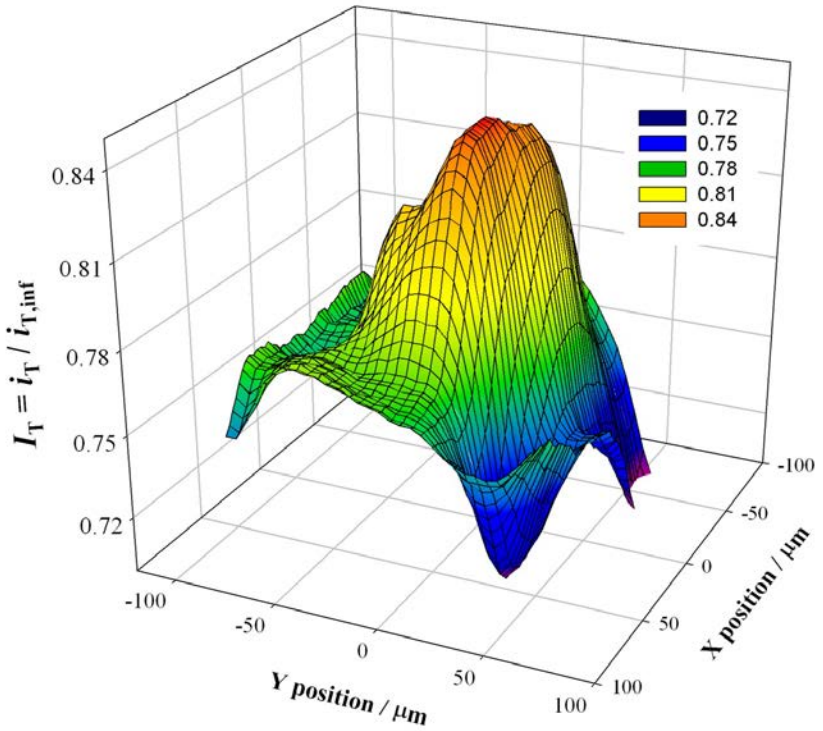

Figure A3.12. SECM feedback image for a representative tripod microspot on graphene, b = 50 μm using 1 mM FeEDTA as mediator in 0.2 M phosphate buffer pH 7; deareated solution with constant nitrogen flow. Tip was a = 12.5 μm Pt, RG ~ 7 and feedback was carried out at E_T = -0.5 V vs. Ag/AgCl and E_S = 0.4 V vs. Ag/AgCl; interelectrode distance d = 10 μm. Tripod was deposited in sufficient amount to yield ~ 140 pmol/cm^2.

C. Digital simulations

Computer simulations were run using the COMSOL Multiphysics v3.5a software, which uses the finite element method to solve the diffusive and kinetic problem coupled to the geometry required to model the SECM response. Two simulation models were used depending on the geometric constraints of the problem. For the description of the changes in SECM signal at the center of the tripod microspots, the geometry and conditions shown in Figure A3.13 were used. An additional simulation was constructed to describe the feedback response of the tip when scanned over different lateral positions along x (radial coordinate r on a microspot); this 3-D simulation is shown in Figure A3.14.

General description of the 2D SECM -1D surface simulation

When the cylindrical SECM tip and the circular microspot are co-aligned, it is possible to model the system using an axis of symmetry as shown in Figure A3.13, which also describes the initial conditions for tripod surface concentration, Γ_T. Tripod Fickian diffusion was modeled as shown in equation S1:

$$\frac{\partial \Gamma_T}{\partial t} = D_T \nabla^2 \Gamma_T \qquad \text{(S1)}$$

where D_T represents the diffusion coefficient of the tripod on the surface. The model does not take into account changes in D_T with respect to Γ_T or any other dependency. All simulations were performed on transient mode, to describe the tip signal changes as diffusion occurs at the substrate. For the results shown in Figure 2 in the main text where the tripod surface concentration profiles described, only the axial 1-D component of this simulation was used under the following conditions: 1×10^{-4} $cm^2/s > D_T > 1 \times 10^{-16}$ cm^2/s, 1×10^{-3} m $> b > 1 \times 10^{-9}$ m and their respective times such that the normalized time (equation 3 in the main text) $5 > \tau > 0$. These values were tested to conform to the main curves shown in Figure 2 in the main text, which they respect for concentrations $\Gamma_T / \Gamma_{T,0} > 0.01$ with no more than 1% discrepancy between radically different conditions. To allow for sufficient space for the establishment of semi-infinite conditions, $m = 20\ b$ as shown in Figure A3.13 for the 1-D geometry. Surface diffusion simulations were coupled to the collection and feedback approaches that follow.

Substrate generation / tip collection simulations

For the simulation of hydrogen peroxide collection, a simple model based on the reaction of molecule A (e.g. oxygen), initially present in the bulk of the solution, to B (e.g.hydrogen peroxide) produced at the graphene surface was done; the diffusion of these species was modeled using equation S1 applied to them. In Figure A3.13, species A and B are only present in the 2-D representation, while the tripod is present only in the 1-D representation. The production of B was modeled as shown in equation S2, where the outward flux of B into the 2-D subdomain was calibrated by adequate

choice of the reaction constant k_{het}. This parameter was chosen such that at the initial (i.e. maximum) tripod concentration $\Gamma_{T,0}$, no more than 10% of the maximum collection efficiency at the tip was reached (close to the experimental conditions); this imposed a kinetic control where the activity of the surface is dependent on the concentration of tripod at any given point. The rate of reaction is linear with respect to the tripod concentration. The tip reaction collects B and regenerates A (H_2O_2 oxidation to O_2) as shown in equation S3, where k_{coll} is large enough to maintain a zero B concentration at the surface of the tip microdisk. The boundary conditions in Figure A3.13 are shown in table S1.

$$-J_A = J_B = k_{het}\Gamma_T \text{ A} \qquad \text{S2}$$

$$J_A = -J_B = k_{coll}\text{B} \qquad \text{S3}$$

Boundary / Species	**T**	**A**	**B**
i (bulk)	T* = 0	A* = 1 mM	B* = 0
ii	--	Insulation	Insulation
iii	--	Flux, eq. S3	Flux, eq. S3
iv	Axial symmetry	Axial symmetry	Axial symmetry
v	Continuity	--	--
Projected substrate	T(τ)	Flux, eq. S2	Flux, eq. S2

Table A3.1. Boundary conditions for substrate generation / tip collection model of A/B system.

The projected substrate in Table A3.1 and indicated in Figure A3.13 was modeled in the COMSOL simulation using the concentrations of T, A and B as projected coupling variables. Two constraints are important in order to collapse the simulations results to a master curve (Figure 4.2 in the main text) and to fit the experimental data. First, $D_T << D_A, D_B$ in such a way that changes in the surface are adequately reflected by the diffusing B species. For these simulations, a value $D_A = D_B = 1 \times 10^{-5}$ cm^2/s and the minimum tested value for the tripod was $D_T = 1 \times 10^{-6}$ cm^2/s (~ 1000 times larger than the one obtained experimentally). For larger values of D_T, a different SECM would have to be pursued. Seconly, the collection efficiency and distribution of the

species generated at the substrate will change importantly with the ratio a/b; we solved this experimentally by choosing strictly spots where b ~ 50 μm, such that all simulations used to validate the master curve in Figure 7 in the main text were obtained with $rg = 7a$, $a = 12.5$ μm and $b = 50$ μm, as defined in Figure A3.13. To allow sufficient space for the establishment of semi-infinite conditions, $m = 20\ b$ and $n = 10\ b$; $d = 10$ μm in all experiments and simulations.

Feedback simulations

For the simulation of ferri/ferrocyanide feedback, the initially present ferricyanide species, A, reacted at the microdisk of the tip to produce ferrocyanide, B, at a diffusion limited rate and at steady state; the diffusion of these species was modeled using equation S1 applied to them. In Figure A3.13, species A and B are only present in the 2-D representation, while the tripod is present only in the 1-D representation. Species B produced at the tip diffuses to the substrate where it reacts with the tripod and regenerates A through a second order process with constant $k_{ex} = 1.6 \times 10^8$ mol/cm^{3}s. We assumed that electron transfer from the electro to the tripod species is fast, such that it is unnecessary to specify the oxidation state of the tripod, instead, the rate of formation of A (and consumption of B) at the substrate is given in equation S4, where an electrochemical background term with constant $k_{back} = 0.8 \times 10^{-3}$ cm/s was also used as experimentally determined at $E_S = 0.4$ V vs. Ag/AgCl on graphene. The rate of reaction is linear with respect to the tripod concentration. Table A3.2 shows all boundary conditions used according to the geometry in Figure A3.13.

$$J_A = -J_B = k_{ex}\Gamma_T B + k_{back} B \qquad \text{S4}$$

Boundary / Species	**T**	**A**	**B**
i (bulk)	T* = 0	A* = 2 mM	B* = 0
ii	--	Insulation	Insulation
iii	--	A = 0	B = 2 mM
iv	Axial symmetry	Axial symmetry	Axial symmetry
v	Continuity	--	--
Projected substrate	T(τ)	Flux, eq. S4	Flux, eq. S4

Table A3.2. Boundary conditions for feedback model of A/B system in 1-D/2-D

The projected substrate in table S2 and indicated in Figure A3.13 was modeled in the COMSOL simulation using the concentrations of T, A and B as projected coupling variables. The discussion done for the collection experiments with respect to the relative values of the tripod and mediator diffusion coefficients is applicable in there also. For the ferri/ferrocyanide system a value $D_A = D_B = 7.2 \times 10^{-6}$ cm^2/s and the minimum tested value for the tripod was $D_T = 1 \times 10^{-6}$ cm^2/s (~ 1000 times larger than the one obtained experimentally). We simulated two sizes of microspots, as shown in Figure 11 in the main text with $rg = 7a$, $a = 12.5$ μm and the micrsopot radius either $b = 50$ μm or $b = 15$ μm , as defined in Figure A3.13. To allow sufficient space for the establishment of semi-infinite conditions, $m = 20\ b$ and $n = 10\ b$; $d = 10$ μm in all experiments and simulations. Feedback results are presented in terms of the normalized tip current i_T divided by the tip current in the bulk solution, $i_{T,inf}$ which was obtained both experimentally and in the simulation by making $d > 500$ μm. An initial tripod concentration for these simulations was $\Gamma_{T,0} = 140$ pmol/cm^2.

3-D feedback simulations

The feedback approach discussed in the previous section was used to obtain 3-D simulations where the tip current was obtained as a function of the lateral displacement on the *x* coordinate (i.e. *r* in the 1-D/2-D simulations) as shown in Figure A3.14 for a microspot with $b = 15$ μm. Table S3 shows the boundary conditions used in this geometry, with all other conditions kept equal to the previous section.

Boundary / Species	**T**	**A**	**B**
i (bulk)	--	A* = 2 mM	B* = 0
ii	--	Insulation	Insulation
iii	--	A = 0	B = 2 mM
iv	Continuity	--	--
v (bulk)	T* = 0	--	--
Projected substrate	T(τ)	Flux, eq. S4	Flux, eq. S4

Table A3.3. Boundary conditions for feedback model of A/B system in 2-D/3-D.

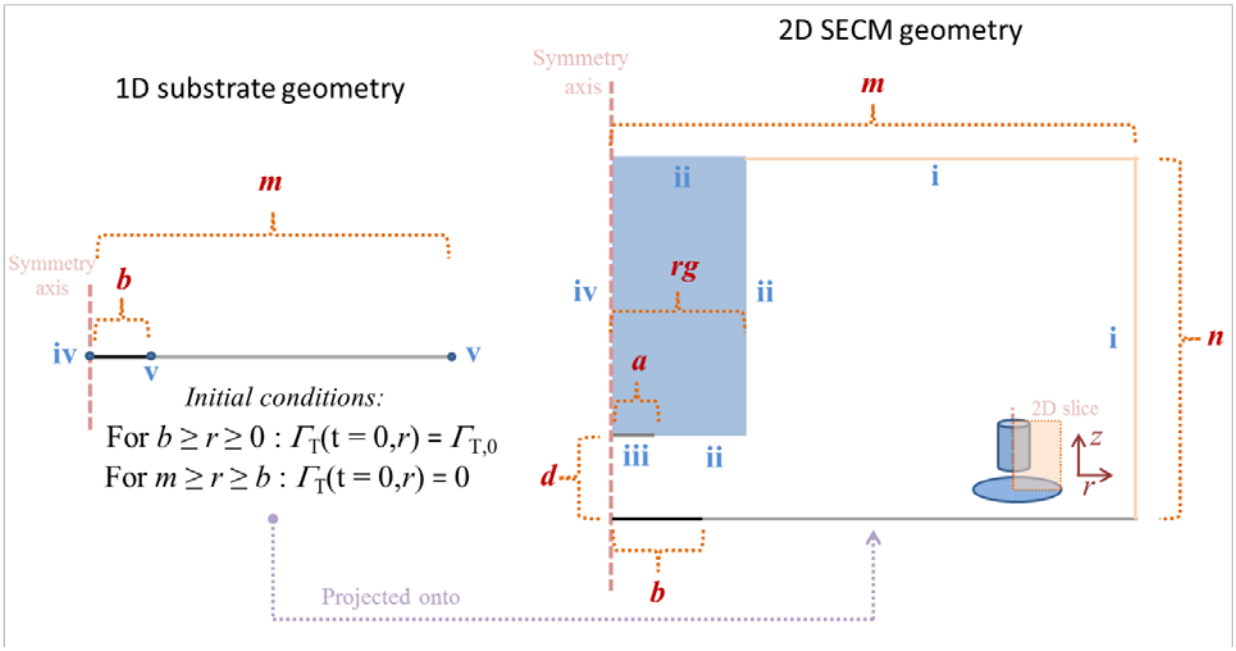

Figure A3.13. Geometry, initial tripod conditions and boundary designation for the 1-D/2-D framework used for substrate generation / tip collection and feedback experiments. All geometric elements were kept fixed in the simulations.

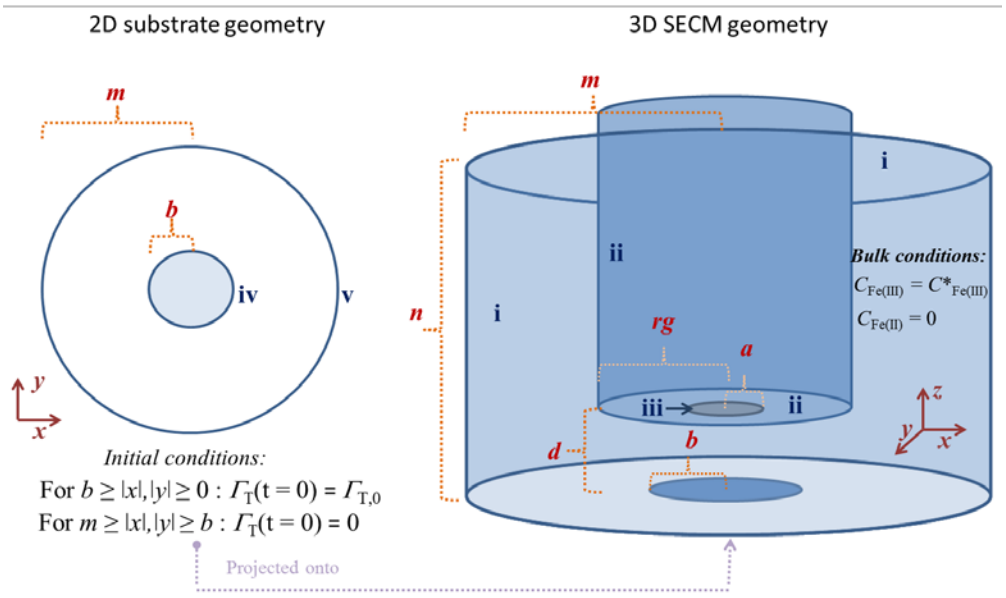

Figure A3.14. Geometry, initial tripod conditions and boundary designation for the 2-D/3-D framework used for feedback experiments. The tip and microdisk geometries were displaced in the *x* coordinate to obtain feedback readings at different lateral positions in increments of 5 μm.

Tip currents

All SECM tip currents were obtained by integrating the flux of the reacting species at the microdisk boundary. Equations S5, S6 and S7 were used for the generation/collection, 2-D feedback and 3-D feedback approaches respectively, where F = 96 485 C/mol :

$$i_T = 2\pi FD_B \int_0^a \frac{\partial B(z=d)}{\partial z} r dr \qquad \text{(S5)}$$

$$i_T = 2\pi FD_A \int_0^a \frac{\partial A(z=d)}{\partial z} r dr \qquad \text{(S6)}$$

$$i_T = FD_A \iint_{iii} \frac{\partial A(z=d)}{\partial z} dxdy \qquad \text{(S7)}$$

D. References

1. Li, X.; Cai, W.; An, J.; Kim, S.; Nah, J.; Yang, D.; Piner, R.; Velamakanni, A.; Jung, I.; Tutuc, E.; Banerjee, S.K.; Colombo, L.; Ruoff, R.S. *Science*, **2009**, *324*, 1312-1314.

2. Lee, D.S.; Riedl, C.; Krauss, B.; von Klitzing, K.; Starke, U.; Smet, J.H. *Nano Lett*. **2008**, *8*, 4320-4325.

3.Wang, Y.Y.; Ni, Z.H.; Yu, T.; Shen, Z.X.; Wang, H.M.; Wu, Y.H.; Chen, W.; Wee, A.T.S. *J. Phys. Chem. C* **2008**, *112*, 10637-10640.

4.Casiraghi, C.; Pisana, S.; Novoselov, K. S.; Geim, A. K.; Ferrari, A. C. *Appl. Phys. Lett.* **2007**, *91*, 233108.

CHAPTER FIVE

PRESERVATION OF ANTIBODY SELECTIVITY ON GRAPHENE BY CONJUGATION TO A TRIPOD MONOLAYER

5.1 Introduction

Interfacing biomolecules and cells to electronic materials is a longstanding challenge to manufacturing sensitive biosensors and inexpensive diagnostic devices.[1] Single layer graphene (SLG) has emerged as a promising material for this purpose because of its transparency, conductivity, robust mechanical properties, and high surface area.[2] Recent developments in its synthesis using chemical vapor deposition methods[3] provide large-area, high quality SLG that is easily transferred to a variety of substrates. For example, SLG supported on reconstituted silk formed the basis of a wireless biosensor that was adsorbed onto tooth enamel and detected pathogens in saliva.[4] The function and specificity of such biosensors relies on assembling active recognition elements on the SLG surface, ideally through noncovalent interactions that preserve its superior electronic properties.

Noncovalent functionalization strategies to attach biomolecules to SLG are therefore of significant interest. Small peptides and nucleic acids bind to graphene and have been used to detect proteins,[5, 6] polynucleotides,[7] changes in pH,[8] nanoparticles,[9] and cells.[4] In contrast, the activity and selectivity of proteins whose function relies on specific tertiary or quaternary structure, including antibodies and enzymes, have not been demonstrated unambiguously when they are adsorbed to SLG.[10, 11] Furthermore, significant conformational changes of proteins adsorbed to SLG have been noted in both experiments[12] and simulations,[13] as well as loss of function.[14] Here we demonstrate

that an anti-*E.coli* antibody (aEAB) readily adsorbs onto SLG but loses its specific recognition ability. In contrast, when the antibody is supported on a self-assembled monolayer (SAM) of tripodal graphene binding molecules, it retains its ability to recognize *E. coli* cells. The captured cells divide normally on the aEAB/tripod SAM and form a biofilm on the SLG surface. These findings demonstrate the importance of engineering the graphene-biomolecule interface in order to preserve protein function and that multivalent binding motifs provide a solution to this challenge. The work described in this chapter was performed in collaboration with Dr. Thomas Alava under the direction of Prof. H. G. Craighead and Prof. W. R. Dichtel and was published in the *Angewandte Chemie International Edition* (Mann, J. A.; Alava, T.; Craighead, H. G.; Dichtel, W. R. *Angew. Chem. Int. Ed.* **2013**, *52*, 3177.)

5.2 Results and Discussion

The graphene-binding tripod **3** that we used for antibody conjugation is based on a design we used in Chapters 2-4 to functionalize SLG with redox-active moieties.[15, 16] Tripod **3** features a multivalent design in which three pyrene-SLG interactions provide exceptional SAM stability in both aqueous and organic solvents. As discussed in Chapters 2 and 3, electrochemical studies of redox-active tripods with identical binding groups indicated self-limiting monolayer formation upon exposure to dilute tripod solutions (μM concentration) and suggested that the tripods project their active functionality away from the SLG surface.[16] For biofunctionalization experiments, **3** incorporates an N-hydroxysuccinimidyl (NHS) active ester, which has been used extensively for protein conjugation at exposed lysine residues. The core of **3** was

established through a Sonogashira cross-coupling reaction between 4-bromoethyl benzoate and triarylpropyne **1** (Figure 5.1). Subsequent demethylation using BBr_3 provided the tris(phenol) derivative **2**, onto which three pyrene moieties were incorporated under Williamson etherification conditions. Finally, the ethyl ester was saponified and subsequently elaborated to an NHS ester using a carbodiimide-mediated esterification procedure to provide the NHS ester tripod **3**. We also evaluated SAMs comprised of pyrene butyrate NHS ester **4**, which has been used extensively to functionalize SLG,[6, 10] graphene oxide,[17] and carbon nanotubes.[18] As a monovalent pyrene binding group, **4** also serves to evaluate the importance of the multivalent tripodal design for effective bioconjugation. Despite the frequent use of **4** for graphene functionalization, the performance of aEAB conjugated to its SAMs suggests that individual pyrene moieties do not prevent antibody denaturation on SLG (see below).

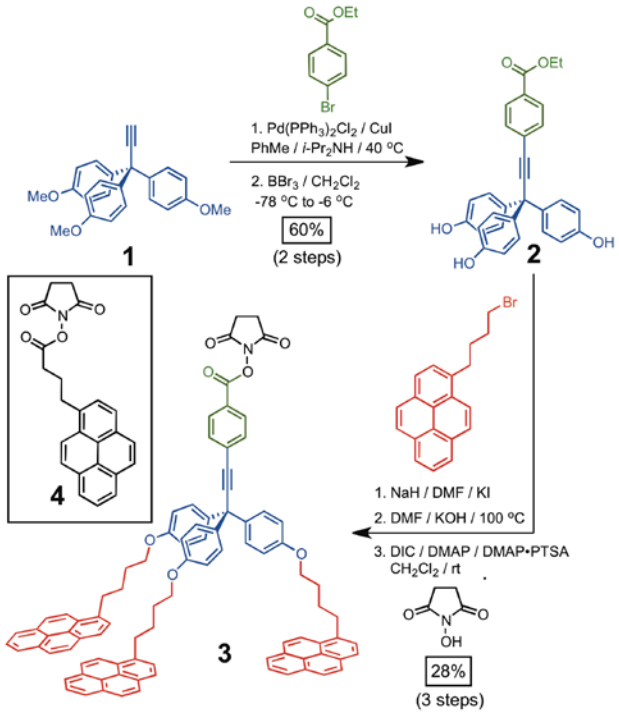

Figure 5.1. Synthesis of NHS-ester tripod **3** and structure of NHS-pyrene butyrate **4**.

We first compared the adsorption of aEAB onto pristine, pyrene-modified, and tripod-modified SLG using a graphene-functionalized quartz crystal microbalance (GQCM). Antibodies were chosen because of their importance in biosensors and because they offer highly selective analyte binding specificity that relies on maintaining their native conformation. Furthermore, *E. coli* is a relevant capture/immobilization target for biosensors because it is a known foodborne pathogen. The QCM is a piezoelectric mechanosensor whose resonant frequency is sensitive to changes in mass adsorbed on the surface, and whose resistance is related to both deposition of mass and the type of mechanical coupling between the surface and the adsorbed mass. The change in resonant frequency (Δf) is related to mass of the antibody deposited on the quartz surface (Δm) using the Sauerbrey equation, $\Delta f = -C_f \Delta m$, in which C_f is a constant dependent on the quartz properties, 56.6 $Hz \cdot \mu g^{-1} \cdot cm^2$ for the 5 MHz AT-cut quartz used here.[19] All three substrates (tripod- and pyrene-functionalized and bare GQCM) exhibit exponential frequency decreases upon introduction of the aEAB and reach an equilibrium $\Delta f \approx$ -50 Hz after 10 min, corresponding to approximately 20 pmol cm^{-2} of adsorbed antibody (Figure 5.1, Figure A4.18). There is little difference among the mass change traces for the pyrene-functionalized, tripod-functionalized, and bare GQCM surfaces. After the frequency stabilized, the cell was rinsed with blank PBS buffer for 25 min, which caused almost no desorption of the antibody. Atomic force microscopy of each functionalized graphene surface showed no evidence of aggregation (see Appendix).

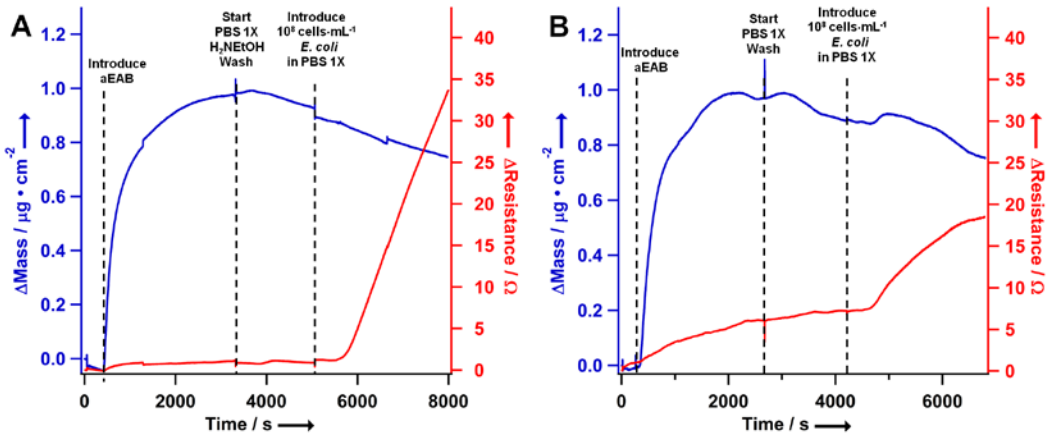

Figure 5.1. (A) GQCM trace showing the frequency (blue) and resistance (red) response to the introduction of aEAB to a surface functionalized with a SAM of **3** and subsequent introduction of *E.coli*. (B) The corresponding GQCM trace for aEAB adsorbed onto bare SLG.

As an additional control, we formed a monolayer of a tripod in which the NHS ester had been displaced by ethanolamine (Appendix compound **S3**), thus lacking the ability to form covalent bonds to aEAB. These monolayers showed reduced frequency responses to antibody introduction compared to monolayers of **3**, further suggesting that covalent bond formation occurs between the antibody and **3** (see Appendix Figure A4.18). Overall, these results indicate that similar amounts of aEAB are deposited on NHS tripod-functionalized and bare SLG and that both types of antibody-graphene films are stable to washing.

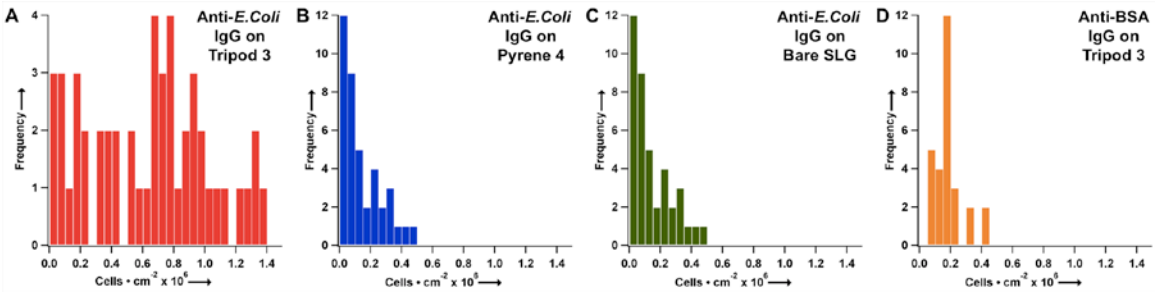

Figure 5.2. Cell count histograms for (A) aEAB on tripod SAMs of **3** (B) aEAB adsorbed on monopod SAMs of **4** (C) aEAB adsorbed on bare SLG, and (D) aBSA conjugated to tripod SAMs of **3**.

After aEAB film formation, *E. coli* cells that were resuspended in PBS buffer and introduced to the GQCM induced an apparent increase in the frequency response, which usually indicates a loss of mass from the surface. However, the resistance (ΔR) of the GQCM simultaneously increased, which is inconsistent with this interpretation. We attribute these observations to viscoelastic coupling between the bacterial cells and the GQCM, a phenomenon that was noted previously for bacterial cell adsorption to a SAM-modified QCM.[20] Although it is possible in principle to quantify cell binding through analysis of ΔR, such measurements require careful calibration and are quite susceptible to environmental noise. We instead quantified *E. Coli* binding directly through fluorescence microscopy of appropriately stained cells (Figure 5.2).

The bound *E. coli* cell density was determined for the following three antibody-functionalized graphene surfaces: aEAB on bare SLG, aEAB conjugated to pyrene butyrate **4**, and aEAB conjugated to tripod **3**. We also performed two additional control experiments: The first utilized a mismatched antibody, anti-bovine serum albumin (aBSA), which does not recognize *E. coli* cells, conjugated to a SAM of **3**. The second employed the tripod monolayer incapable of bioconjugation (**S3**) that had been exposed to aEAB. Each surface was incubated with a solution of the bacterium (10^8 cfu·mL^{-1} in lysogeny broth) for 10 min and then rinsed to remove weakly bound cells. The remaining surface-bound cells were stained with propidium iodide and their density was measured repeatedly using a fluorescence microscope. Notably, surfaces in which aEAB was immobilized on the tripodal SAM showed a nearly five-fold higher density ($7.8 \pm 1 \times 10^5$ cells·cm^{-2}) than when aEAB was supported on the monovalent pyrene butyrate SAM ($1.4 \pm 0.4 \times 10^5$ cells·cm^{-2}) or on bare SLG ($1.7 \pm 0.3 \times 10^5$ cells·cm^{-2}). The aBSA conjugated

to the tripod SAM also showed nearly identical bound cell density ($1.9 \pm 0.3 \times 10^5$ cells·cm^{-2}) as the aEAB films that were not interfaced to the tripodal SAMs. Since aBSA does not recognize *E. coli*, we attribute the lower density value to nonspecific cell adsorption. These results therefore suggest that aEAB exhibits little or no specific *E. coli* recognition when it is adsorbed on bare graphene or conjugated to pyrene **4**, yet retains this function when conjugated to tripod **3**. The **S3** monolayers incapable of bioconjugation also showed quite low bound cell density ($1.8 \pm 0.5 \times 10^4$ cells·cm^{-2}), indicating that covalent attachment between the SAM and antibody are necessary for cell capture. Collectively, these differences in bound cell density suggest that the nature of the SLG/antibody interface is crucial for antibodies to retain their desirable specific binding function (Figure 5.3).

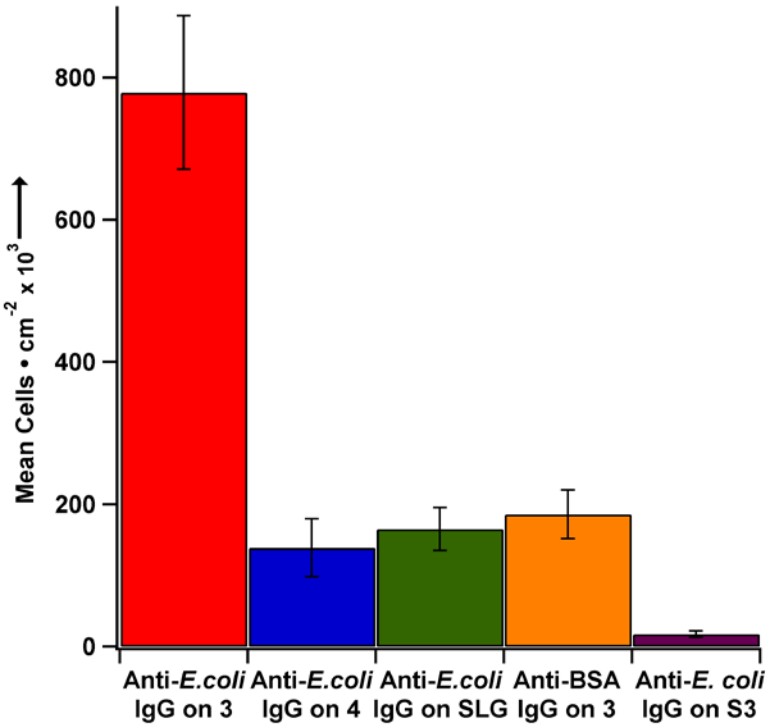

Figure 5.3. Captured *E. coli* binding densities for aEAB on SAMs of **3** (red), on SAMs of **4** (blue), on bare SLG (green), and on SAMs of **S3** (purple). *E. coli* binding density for aBSA on SAMs of **3** (orange).

Finally, we confirmed that *E. coli* cells captured by aEAB on tripodal SAMs are viable by monitoring their division on the SLG surface (Figure 5.4). The immobilized cells replicate exponentially and remain attached to the surface, eventually forming a graphene-conjugated biofilm (Figure 5.4A, red). In contrast, *E. coli* cells that were immobilized on aEAB on bare SLG did not remain attached to the graphene surface, and biofilm coherence was lost above a colony size of two individuals (Figure 5.4B, green). *E. coli* cells responsible for biofilm growth on tripod-conjugated aEAB divided with a doubling time of only 50% longer than cells grown in solution under similar conditions (Figure 5.4). These observations further confirm that the nature of the antibody/graphene interface strongly influences antibody function and suggest that immobilizing biomolecules on tripod SAMs will enable studies of cell growth and differentiation. SLG is an intriguing analytical platform for such investigations, in part because it can serve as a transparent barrier material, as was shown by Alivisatos for imaging nanoparticles within bilayer graphene pockets.[21]

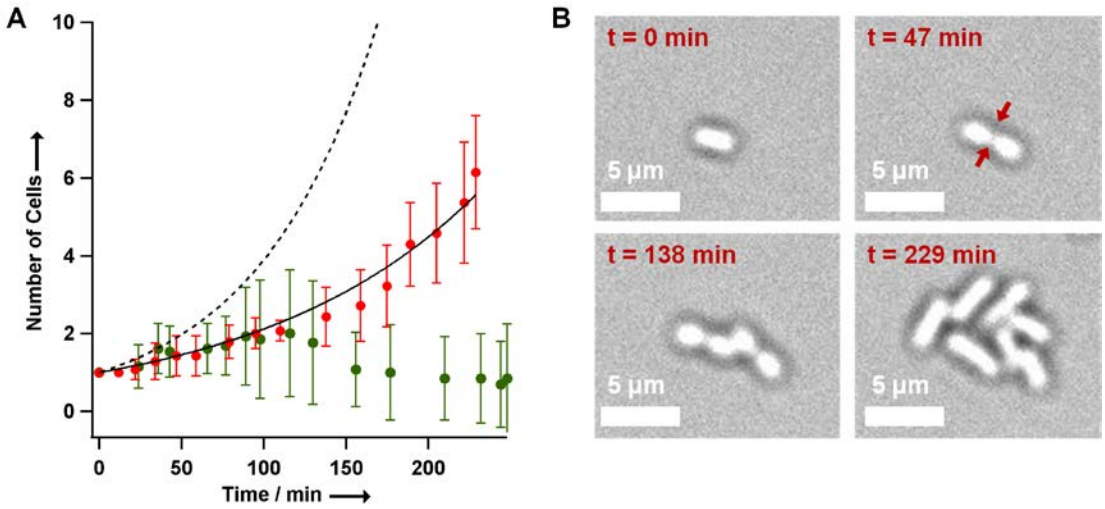

Figure 5.4. A. Growth curves for *E. coli* in solution (dashed line), on aEAB on SAMs of **3** (red), and on aEAB on bare SLG (green). B. Optical images of *E.coli* division on aEAB/tripod SAMs that indicate the progression of biofilm formation.

5.3 Conclusions

In conclusion, we have shown that similar masses of anti-*E. coli* antibodies deposit onto both bare SLG and NHS-functionalized aromatic SAMs. The binding specificity of the antibody depends strongly on the nature of SLG functionalization method. The antibodies retain their specificity when conjugated to tripodal SAMs, but exhibit poor *E. coli* recognition when immobilized onto the monovalent binding group or bare SLG. Antibody activity on tripodal SAMs was further confirmed by the observations that captured bacterial cells readily divide, remain bound to the graphene surface, and form biofilms. This work answers fundamental questions about interfacing biomolecules to SLG that are relevant to both biosensor applications and fundamental studies at the abiotic/biotic interface. Further work in this area will elaborate on the functionality and orientational control that we have demonstrated through the use of site-selective bioconjugation strategies and will investigate practical SLG-based biosensors.

5.4 Acknowledgements

We acknowledge NSF support through use of the Cornell Nanofabrication Facility/NNIN and the Cornell Center for Materials Research facilities. J.A.M. gratefully acknowledges the Integrative Graduate Education and Research Traineeship (IGERT) Program in the Nanoscale Control of Surfaces and Interfaces, which is supported under NSF Award DGE-0654193, the Cornell Center for Materials Research, and Cornell University. T.A. acknowledges funding through a grant from the National Science Foundation under ECCS-1001742 and through support from Analog Devices.

REFERENCES

[1] M. Medina-Sanchez, S. Miserere, A. Merkoci, *Lab Chip* **2012**, *12*, 1932-1943.

[2] a) A. Bonanni, A. H. Loo, M. Pumera, *Trends Anal. Chem.* **2012**, *37*, 12-21; b) Y. Liu, X. Dong, P. Chen, *Chem. Soc. Rev.* **2012**, *41*, 2283-2307; c) S. Song, Y. Qin, Y. He, Q. Huang, C. Fan, H.-Y. Chen, *Chem. Soc. Rev.* **2010**, *39*, 4234-4243; d) W. Yang, K. R. Ratinac, S. P. Ringer, P. Thordarson, J. J. Gooding, F. Braet, *Angew. Chem.* **2010**, *122*, 2160-2185; *Angew. Chem. Int. Ed.* **2010**, *49*, 2114-2138.

[3] a) S. Bae, et al., *Nature Nanotech.* **2010**, *5*, 574-578; b) X. Li, et al., *Science* **2009**, *324*, 1312-1314; c) M. P. Levendorf, C. S. Ruiz-Vargas, S. Garg, J. Park, *Nano Lett.* **2009**, *9*, 4479-4483; d) A. Reina, X. Jia, J. Ho, D. Nezich, H. Son, V. Bulovic, M. S. Dresselhaus, J. Kong, *Nano Lett.* **2008**, *9*, 30-35.

[4] M. S. Mannoor, H. Tao, J. D. Clayton, A. Sengupta, D. L. Kaplan, R. R. Naik, N. Verma, F. G. Omenetto, M. C. McAlpine, *Nat. Commun.* **2012**, *3*, 763.

[5] L. Wang, C. Zhu, L. Han, L. Jin, M. Zhou, S. Dong, *Chem. Commun.* **2011**, *47*, 7794-7796.

[6] Y. Ohno, K. Maehashi, K. Matsumoto, *J. Am. Chem. Soc.* **2010**, *132*, 18012-18013.

[7] a) E. Dubuisson, Z. Yang, K. P. Loh, *Anal. Chem.* **2011**, *83*, 2452-2460; b) X. Dong, Y. Shi, W. Huang, P. Chen, L.-J. Li, *Adv. Mater.* **2010**, *22*, 1649-1653.

[8] Z. Cheng, Q. Li, Z. Li, Q. Zhou, Y. Fang, *Nano Lett.* **2010**, *10*, 1864-1868.

[9] Y. Cui, S. N. Kim, S. E. Jones, L. L. Wissler, R. R. Naik, M. C. McAlpine, *Nano Lett.* **2010**, *10*, 4559-4565.

[10] a) S. Okamoto, Y. Ohno, K. Maehashi, K. Inoue, K. Matsumoto, *Jpn. J. Appl. Phys.* **2012**, *51*, 06FD08/01-06FD08/04; b) V. K. Kodali, J. Scrimgeour, S. Kim, J. H. Hankinson, K. M. Carroll, H. W. A. de, C. Berger, J. E. Curtis, *Langmuir* **2011**, *27*, 863-865; c) Y. Huang, X. Dong, Y. Liu, L.-J. Li, P. Chen, *J. Mater. Chem.* **2011**, *21*, 12358-12362.

[11] a) P. K. Ang, A. Li, M. Jaiswal, Y. Wang, H. W. Hou, J. T. L. Thong, C. T. Lim, K. P. Loh, *Nano Lett.* **2011**, *11*, 5240-5246; b) Y. Ohno, K. Maehashi, Y. Yamashiro, K. Matsumoto, *Nano Lett.* **2009**, *9*, 3318-3322.

[12] a) J. Katoch, S. N. Kim, Z. Kuang, B. L. Farmer, R. R. Naik, S. A. Tatulian, M. Ishigami, *Nano Lett.* **2012**, *12*, 2342-2346; b) Y. Zhang, J. Zhang, X. Huang, X.

Zhou, H. Wu, S. Guo, *Small* **2012**, *8*, 154-159; c) M. De, S. S. Chou, V. P. Dravid, *J. Am. Chem. Soc.* **2011**, *133*, 17524-17527.

[13] a) K. Balamurugan, E. R. A. Singam, V. Subramanian, *J. Phys. Chem. C* **2011**, *115*, 8886-8892; b) G. Zuo, X. Zhou, Q. Huang, H. Fang, R. Zhou, *J. Phys. Chem. C* **2011**, *115*, 23323-23328; c) L. Ou, Y. Luo, G. Wei, *J. Phys. Chem. B* **2011**, *115*, 9813-9822; d) G. Gianese, V. Rosato, F. Cleri, M. Celino, P. Morales, *J. Phys. Chem. B* **2009**, *113*, 12105-12112.

[14] T. Alava, J. A. Mann, C. Theodore, J. J. Benitez, W. R. Dichtel, J. M. Parpia, H. G. Craighead, *Anal. Chem.* Submitted.

[15] J. Rodríguez-López, N. L. Ritzert, J. A. Mann, C. Tan, W. R. Dichtel, H. D. Abruña, *J. Am. Chem. Soc.* **2012**, *134*, 6224-6236.

[16] J. A. Mann, J. Rodríguez-López, H. D. Abruña, W. R. Dichtel, *J. Am. Chem. Soc.* **2011**, *133*, 17614-17617.

[17] a) F. Liu, K. S. Choi, T. J. Park, S. Y. Lee, T. S. Seo, *BioChip J.* **2011**, *5*, 123-128; b) W. Song, D.-W. Li, Y.-T. Li, Y. Li, Y.-T. Long, *Biosens. Bioelectron.* **2011**, *26*, 3181-3186.

[18] a) D. Tasis, N. Tagmatarchis, A. Bianco, M. Prato, *Chem. Rev.* **2006**, *106*, 1105-1136; b) R. J. Chen, Y. Zhang, D. Wang, H. Dai, *J. Am. Chem. Soc.* **2001**, *123*, 3838-3839.

[19] D. A. Buttry, in *Electroanalytical Chemistry: A Series of Advances, Vol. 17* (Ed.: A. J. Bard), Marcel Dekker, New York, **1990**, pp. 1-82.

[20] a) C. Poitras, N. Tufenkji, *Biosens. Bioelectron.* **2009**, *24*, 2137-2142; b) R. D. Vaughan, C. K. O'Sullivan, G. G. Guilbault, *Enzyme Microb. Tech.* **2001**, *29*, 635-638.

[21] J. M. Yuk, J. Park, P. Ercius, K. Kim, D. J. Hellebusch, M. F. Crommie, J. Y. Lee, A. Zettl, A. P. Alivisatos, *Science* **2012**, *336*, 61-64.

APPENDIX FOUR

Table of Contents

A. Materials and Instrumentation

Materials. Unless otherwise noted, reagents were purchased from commercial suppliers and used without further purification. 4,4',4''-(prop-2-yne-1,1,1-triyl)tris(methoxybenzene) **1** was prepared using a literature procedure.[1] EtOAc, hexanes, and Et_2O were purchased from commercial sources and used without further purification. THF, CH_2Cl_2, DMF, and PhMe were purchased from commercial sources and purified using a custom-built activated alumina-based solvent purification system.

Graphene on quartz crystal microbalance sensors (G-QCM) were fabricated by transferring graphene derived from a chemical vapor deposition (CVD) procedure onto Stanford Research Systems O100RX3 quartz resonators. Graphene on SiO_2/Si wafers and quartz coverslips were prepared similarly according to a literature procedure.[2]

Stock bacterial solutions (*Escherichia coli* K-12 strain, *Bacilus subtilis* and *Lactobacillus casei* ATCC n°334) were cultured by aseptic inoculation of 200 mL of Lysogeny Broth (LB) medium with a colony of the desired bacterium and 12 h incubation at 37 °C and 8.5% $CO_2$with continuous shaking. For the *E.coli*, the grown media was supplemented with ampiciline (100 $\mu g \cdot mL^{-1}$) as the strain used was ampiciline resistant. Fresh secondary cultures were prepared before each experiment by inoculating 5 mL of LB medium with 100 µL of stock growth solution, and incubating until the optical density at 600 nm reached 0.6. The cells were then resuspended in 1X phosphate buffered saline (PBS 1X) solution through centrifugation (3000 rpm, 10 min) and supernatant buffer exchange. Microbial concentrations were estimated using a heamocytometer. Solutions were diluted with PBS 1X to 10^8 cfu $\cdot$ mL^{-1} for use in cell capture experiments.

Goat polyclonal anti-*E. coli* antibodies were purchased from Abcam (Cambridge, MA) and chosen for their affinity towards the O and K antigens of the bacteria. Aliquots were prepared by dilution in PBS 1X to a concentration of 50 $\mu g \cdot ml^{-1}$. The anti-bovine serum albumin IgG (rabbit, polyclonal) used for negative control were purchased from Invitrogen (Grand Island, NY) and diluted in PBS 1X to a concentration of 50 $\mu g \cdot mL^{-1}$.

Instrumentation. Infrared spectra of solid samples were recorded using a Thermo Nicolet iS10 FT-IR spectrometer with a diamond ATR attachment and are uncorrected.

Mass spectra were obtained on a Waters MALDI micro MX MALDI-TOF mass spectrometer using positive ionization in reflectron mode.

NMR spectra were recorded on a Varian INOVA 400 MHz spectrometer using a ^{1}H/X Z-PFG probe, a Bruker ARX 300 MHz spectrometer using a BBO probe, a Varian INOVA 500MHz spectrometer using a standard ^{1}H{^{13}C, ^{15}N} Z-PFG probe, or a Varian INOVA 600 MHz spectrometer using a standard ^{1}H{^{13}C, ^{15}N} XYZ-PFG probe with a 20 Hz sample spin rate.

Atomic force microscopy (AFM) analysis was performed in non-contact mode on a Veeco DI 3100 AFM using diamond-like-carbon coated silicon cantilevers (Tap150DLC) purchased from Budget Sensors (Sofia, Bulgaria).

In-flow mass grafting was performed with G-QCM mounted in a Stanford Research Systems (Sunnyvale, CA) model O100FC flow cell. The monitoring of the resonator frequency and the resistance was accomplished using a universal frequency counter and a voltmeter connected to a QCM E-100 system (Stanford Research Systems) and controlled by a computer running Labview.

An Olympus AX-70 microscope equipped with a Photometrics Cascade II EMCCD camera was used to image surfaces. The free image processing software Image J was used to analyze the resulting images.[3]

B. Synthetic Procedures.

Scheme A4.1. Overall synthesis of a N-Hydroxysuccinimide-functionalized graphene binding motif **3**.

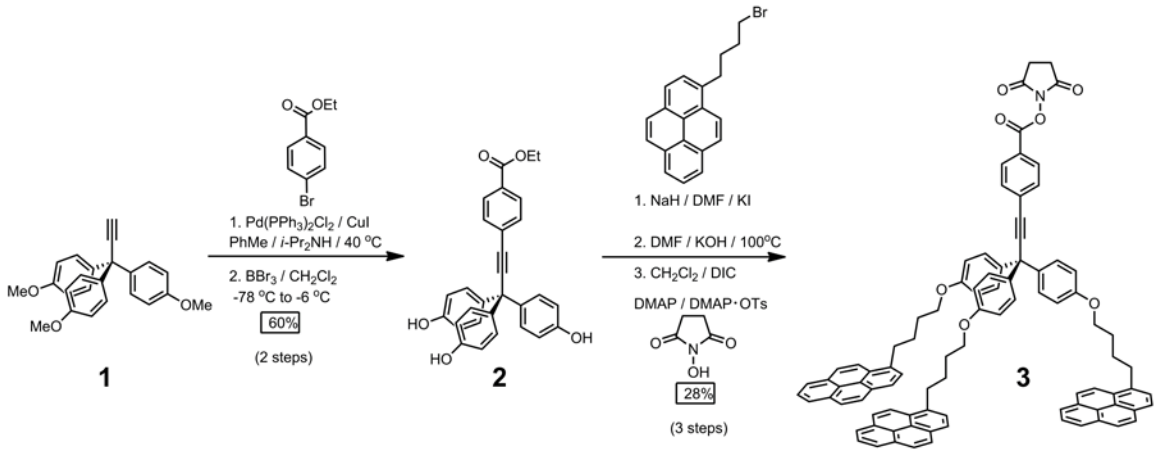

Scheme A4.2. Synthesis of S**1**.

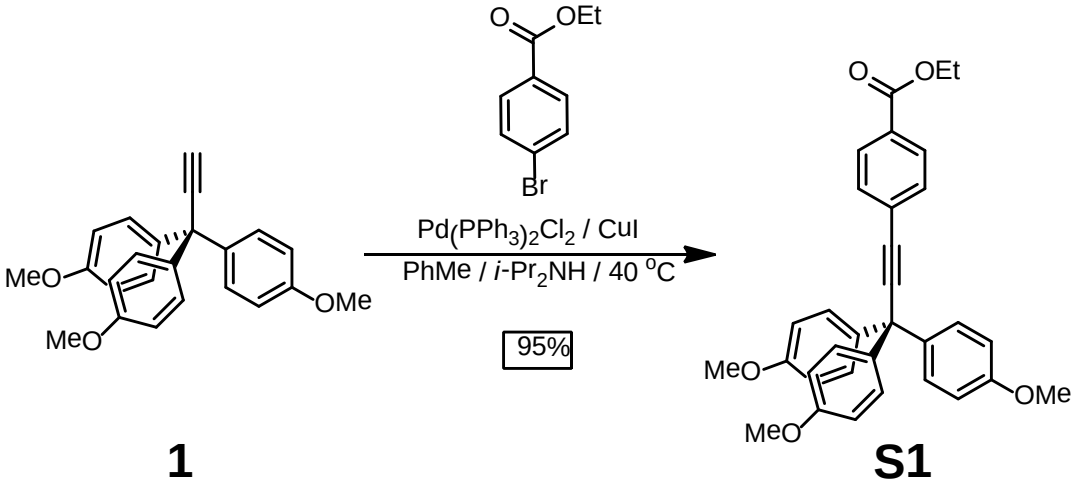

Preparation of trityl-functionalized ester S1. A 25 mL round bottom flask containing a stir bar was charged with **1** (0.522 g, 1.455 mmol), CuI (21.1 mg, 0.111 mmol), and $Pd(PPh_3)_2Cl_2$ (39.7 mg, 0.056 mmol). These solids were placed under a N_2 atmosphere through three evacuation and backfilling cycles. Anhydrous PhMe (22 mL), *i*-Pr_2NH (1.0 mL), and 4-bromoethylbenzoate (0.280 g, 1.222 mmol) were added to the reaction flask. The reaction mixture was heated to 40 ^oC for 10 h, after which the reaction was judged to have proceeded to completion by TLC (SiO_2, 10% EtOAc / hexanes, product $R_f = 0.1$). The reaction mixture was filtered through celite, and the solvent removed over silica gel. The mixture was then purified by column chromatography (SiO_2, 20% EtOAc / 80% hexanes, product $R_f = 0.25$) to provide **2** (0.621 g, 99% yield). **2**: ^1H NMR (500 MHz, $CDCl_3$, 298K) δ 8.00 (d, J = 8.0 Hz, *2*-

aryl, 2H), 7.55 (d, J = 8.0 Hz, *3-aryl*, 2H), 7.23 (d, J = 8.8 Hz, *trityl-2-aryl,* 6H), 6.85 (d, J = 8.8 Hz, *trityl-3-aryl*, 6H), 4.39 (q, J = 7.1 Hz, *ester 1-ethyl*, 2H), 3.81 (s, *4-OCH_3*, 9H), 1.41 (t, J = 7.1 Hz, *ester 2-ethyl*, 3H). ^{13}C NMR (101 MHz, $CDCl_3$, 298K) δ 166.26, 158.48, 137.83, 131.60, 130.18, 129.69, 129.49, 128.46, 113.46, 99.48, 84.07, 61.23, 55.39, 54.29. IR (solid, ATR) 3036, 2997, 2954,2904, 2835, 2222, 1716, 1605, 1582, 1560, 1506, 1462, 1441, 1405, 1366, 1273, 1248, 1175, 1106, 1034, 827, 769 cm^{-1}. EI-MS m/z Calcd. m/z 506.20932 $[M]^+$. Found m/z506.20944 $[M]^+$.

Scheme A4.3. Demthylation of **S1** to tris(phenol) **2**.

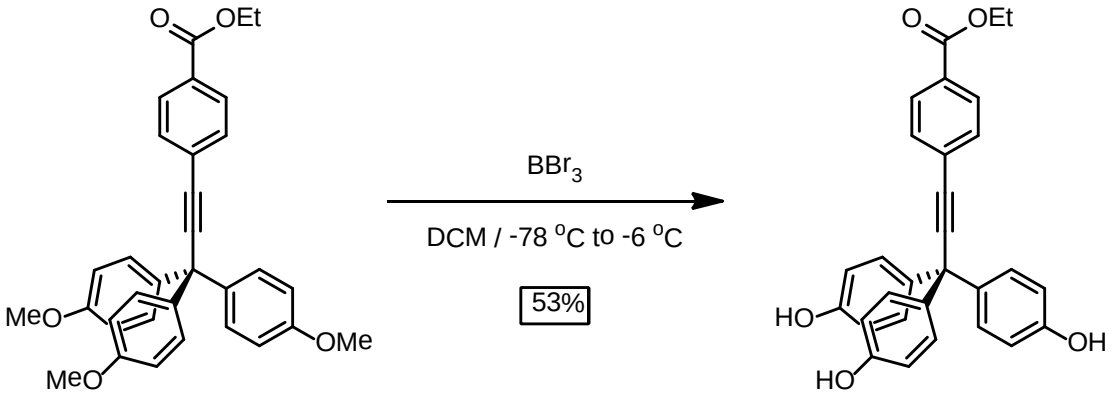

S1 **2**

Preparation of tris(phenol) 5: A flame-dried 250 mL round bottom flask was charged with **S1** (473 mg, 0.934 mmol) and placed under a N_2 atmosphere. Anhydrous CH_2Cl_2 (50 mL) $CH_2Cl_2$was added, and the solution was cooled to -78 °C. A solution of BBr_3 in CH_2Cl_2 (1.0M, 25 mL, 25 mmol) was added using a gastight syringe, and the reaction mixture was warmed to -6 °C by placing the sealed flask in a chemical freezer. The reaction was determined to be complete after 23 h by TLC (SiO_2, 50% EtOAc / hexanes, product R_f = 0.33). The reaction mixture was cooled to -78 °C and MeOH was added slowly (10 mL). The solvent was removed under vacuum and the resulting solid was redissolved in EtOAc (25 mL) and washed with water (2 x 10 mL). The aqueous layer was washed with EtOAc (3 x 25 mL). The combined organic layers were dried ($MgSO_4$), and the solvent was evaporated over silica gel. The mixture purified by flash chromatography (SiO_2, 50% EtOAc / hexanes, product R_f = 0.33) to provide **2** (0.216 g, 53% yield) as a red solid. **2**: ^{1}H NMR (500 MHz, $(CD_3)_2CO$) δ 8.41 (s, *phenol-OH*, 3H), 8.03 (d, J = 8.5 Hz, *2-aryl*, 2H), 7.67 (d, J = 8.5 Hz, *3-aryl*, 2H), 7.14 (d J = 8.6 Hz, *trityl-2-aryl,* 6H), 6.82 (d, J = 8.6 Hz, *trityl-3-aryl* 6H), 4.37 (q, J = 7.1 Hz, *ester 1-ethyl*, 2H), 1.38 (t, J = 7.1 Hz, *ester 2-ethyl*, 3H). ^{13}C NMR (126 MHz, $(CD_3)_2CO$) δ 166.17, 157.08, 156.97, 137.55, 132.34, 132.30, 130.86, 130.65, 130.22, 130.19, 129.23, 115.53, 115.44, 100.82, 84.32, 61.64, 54.96, 14.54. IR (solid, ATR) 3369, 2219, 1696, 1604, 1507, 1440, 1369, 1275, 1173, 1110, 1016, 833, 770 cm^{-1}. ESI-TOF-MS: Calcd. m/z 465.1702 $[M+H]^+$. Found m/z 465.1706 $[M+H]^+$

Scheme A4.4. Synthesis of carboxylic acid tripod **S2**.

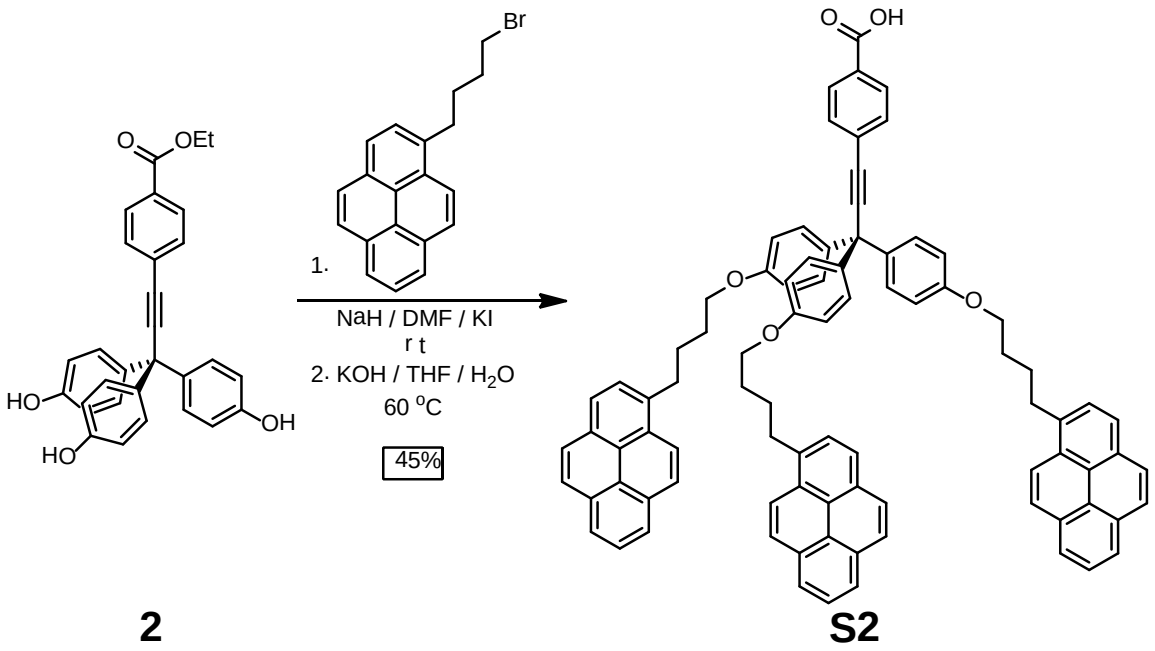

Preparation of carboxylic acid tripod S2. A flame-dried 10 mL round bottom flask was charged with **2** (0.097 g, mmol) and placed under a N_2 atmosphere. Anhydrous DMF (1 mL) was added to the reaction flask followed by excess NaH (95%), changing the solution from red to purple. The reaction was determined to be complete after 12 h by TLC (SiO_2, 10% MeOH / 90% CH_2Cl_2 R_f = 0.8). The reaction mixture was poured into H_2O (20 mL), filtered through celite and the celite washed with CH_2Cl_2 (10 mL x 3). The resulting biphasic mixture was transferred to a separatory funnel and the CH_2Cl_2 layer removed and washed with H_2O (3 x 10 mL). The aqueous layer was extracted with CH_2Cl_2 (10 mL x 3) and the combined organic portions were dried ($MgSO_4$) and the solvent removed under vacuum. The resulting solids were purified by flash chromatography (SiO_2, 100% CH_2Cl_2 to 10% MeOH / 90% CH_2Cl_2). The purified ester was then dissolved in THF (10 mL) and saturated aqueous KOH (2 mL) and refluxed for 2 h when the reaction was complete by TLC (SiO_2, 10% MeOH / 90% CH_2Cl_2 R_f = 0.5). The solvent was removed under vacuum and the mixture resuspended in Et_2O (20 mL), filtered and washed with H_2O (10 mL x 3) and Et_2O (10 mL x 3) affording **S2** (0.120 g, 45% yield) as a white solid. **S2:** ^{1}H NMR (500 MHz, $(CD_3)_2SO$, 298 K) δ 8.35 (d, J = 9.3 Hz, *2-pyrenyl*, 3H), 8.23 (d, J = 7.6 Hz, *5-pyrenyl and 7-pyrenyl*, 6H), 8.20 (d, J = 7.8 Hz, *9-pyrenyl*, 3H), 8.17 (d, J = 9.3 Hz, *1-pyrenyl*, 3H), 8.11 (d, J = 9.0 Hz, *3-pyrenyl* 3H), 8.09 (d, J = 9.0, *4-pyrenyl*, Hz, 3H), 8.02 (t, J = 7.6 Hz, , *6-pyrenyl*, 3H), 7.95 (d, J = 7.8 Hz, , *1-pyrenyl*, 3H), 7.91 (d, J = 8.4 Hz, *2-aryl*, 2H), 7.59 (d, J = 8.4 Hz, *3-aryl*, 2H), 7.07 (d, J = 8.8 Hz, *trityl-2-aryl*, 6H), 6.88 (d, J = 8.9 Hz, *trityl-3-aryl*, 6H), 4.01 (t, J = 6.0 Hz, *1-butyl*, 6H), 3.38 (t, J = 7.2 Hz, *4-butyl*, 7H), 2.06 – 1.76 (m, *2-butyl and 3-butyl*, 14H). ^{13}C NMR (126 MHz, $(CD_3)_2SO$, 298 K) δ 171.92, 162.64, 142.06, 141.99, 136.66, 136.07, 135.59, 134.71, 134.44, 133.26, 132.65, 132.39, 131.66, 131.30, 130.12, 129.42, 129.34, 128.71, 119.23, 72.82, 72.46, 64.93, 58.80, 52.06, 38.57, 37.40, 37.04, 33.79, 33.39,

33.19, 31.21. IR (solid, ATR) 3048, 2947, 2864, 2321, 1678, 1601, 1507, 1246, 1179, 842 cm^{-1} ESI-TOF-MS: Calcd. m/z 1227.4964 $[M+Na]^+$. Found m/z 1227.4956 $[M+Na]^+$

Scheme A4.5. Synthesis of NHS ester Tripod **3**.

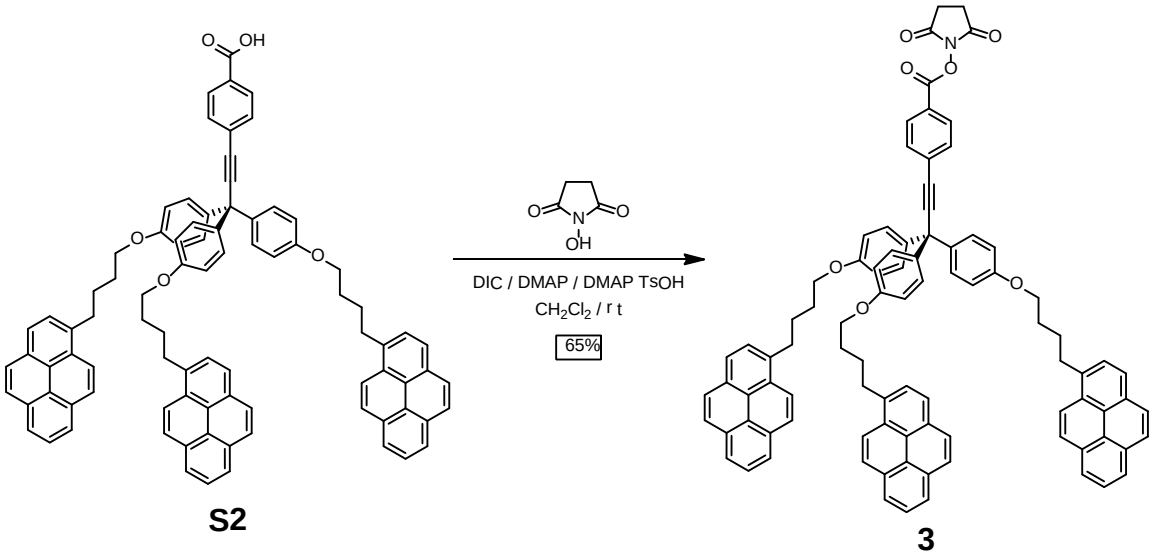

Preparation of NHS ester Tripod 3. A 5 mL flame-dried round bottom flask was charged with **S2** (35 mg, 0.029 mmol), N-hydroxy succinimide (16 mg, 0.14 mmol), N,N-dimethylaminopyridine (2 mg, 0.016 mmol), N,N-dimethylaminopyridinium p-toluenesulphonate(2 mg, 0.007 mmol) and placed under a N_2 atmosphere. Anhydrous CH_2Cl_2 (1 mL) was added to the reaction flask followed by N,N'-diisopropylcarbodiimide (0.05 mL, 0.32 mmol). The resulting suspension was stirred at room temperature for 2 h until homogenous at which point the reaction was complete by TLC (SiO_2, CH_2Cl_2, product R_f = 0.6). The reaction mixture was then filtered through SiO_2 eluted with CH_2Cl_2,and the solvent removed under vacuum to afford **3** (24 mg, 65% yield) as an off-white powder. **1:** ^{1}H NMR (500 MHz, $CDCl_3$, 298 K) δ 8.27 (d, J = 9.2 Hz, *2-pyrenyl,* 3H), 8.14 (d, J = 7.6 Hz, *5-pyrenyl and 7-pyrenyl*, 6H), 8.10 (d, J = 7.8 Hz, *9-pyrenyl*, 3H), 8.08 (d, J = 9.3 Hz, *1-pyrenyl*, 3H), 8.05 (d, J = 8.3 Hz, *2-aryl*, 2H), 8.03 (d, J = 8.9 Hz, *3-pyrenyl*, 3H), 8.00 (d, J = 8.9 Hz, *4-pyrenyl*, 3H), 7.97 (t, J = 7.6 Hz, *6-pyrenyl*, 3H), , 7.87 (d, J = 7.8 Hz, 8-*pyrenyl*, 3H), 7.58 (d, J = 8.3 Hz, *3-aryl*, 2H), 7.18 (d, J = 8.8 Hz, *trityl-2-aryl,* 6H), 6.83 (d, J = 8.8 Hz, *trityl-3-aryl,* 6H), 4.01 (t, J = 6.2 Hz, *1-butyl*, 6H), 3.41 (t, J = 7.6 Hz, *4-butyl*, 6H), 2.89 (s, 4H), 2.04 (m, *2-butyl*, 6H), 2.00 – 1.89 (m, *3-butyl*, 6H). ^{13}C NMR (126 MHz, $CDCl_3$, 298 K) δ 169.16, 161.43, 157.91, 137.37, 136.52, 131.89, 131.41, 130.88, 130.71, 130.37, 130.04, 129.82, 128.62, 127.50, 127.25, 126.60, 125.80, 125.09, 125.01, 124.86, 124.79, 124.69, 123.92, 123.37, 113.93, 101.29, 83.47, 67.71, 54.26, 33.15, 29.25, 28.28, 25.67. IR (solid, ATR) 3039, 2941, 2866, 2248, 1769, 1739, 1603, 1581, 1505, 1243, 1202, 1176, 1043, 996, 906, 844, 729 cm^{-1}. ESI-TOF-MS Calcd. m/z 1302.5309. Found m/z 1302.5286 $[M+H]^+$

Scheme A4.6. Synthesis of Amide Tripod **S3**.

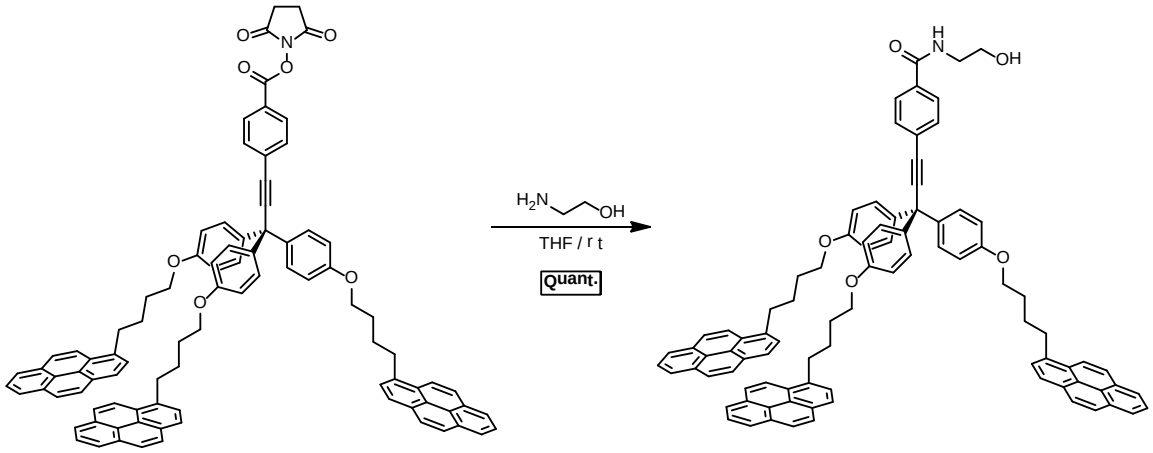

3 **S3**

Preparation of Amide Tripod S3. A 20 mL flame-dried vial with stir bar was charged with **3** (10 mg, 7 μmol) and anhydrous THF (4 mL) and placed under a N_2 atmosphere. Freshly distilled ethanolamine (50.6 mg, 0.83 mmol) was then added and the mixture stirred at room temperature for 1 h when TLC (SiO_2, EtOAc, product R_f = 0.25). The solvent was removed under vacuum and the residue redissolved in $CHCl_3$ (10 mL), washed with 2 M HCl (3 x 2 mL), followed by saturated NaCl (2 mL). The organic layer was then dried using $MgSO_4$, filtered and the solvent removed under vacuum to afford S**3** (10 mg, quantitative yield) as an off-white powder. **S3**: ^{1}H NMR (500 MHz, $CDCl_3$, 298 K) δ 8.31 – 7.87 (m, *pyrene*, 21H), 7.72 (d, *J* = 8.2 Hz, *2-aryl*, 2H), 7.54 (d, *J* = 8.2 Hz, *3-aryl*, 2H), 7.19 (d, *J* = 8.7 Hz, *trityl-2-aryl*, 6H), 6.83 (d, *J* = 8.7 Hz, *trityl-3-aryl*, 6H), 4.02 (t, *J* = 6.2 Hz, *1-butyl*, 6H), 3.86 (t, *J* = 4.8 Hz, *1-ethyl*, 2H), 3.65 (t, *J* = 4.8 Hz, *2-ethyl*, 2H), 3.42 (t, *J* = 6.2 Hz, *4-butyl*, 6H), 2.05 (m, *2-butyl*, 6H), 1.97 (m, *3-butyl*, 6H). ^{13}C NMR (126 MHz, $CDCl_3$, 298 K) δ 136.52, 131.74, 131.42, 130.04, 129.82, 128.62, 127.49, 127.23, 126.83, 126.58, 125.78, 125.09, 124.84, 124.78, 124.67, 123.36, 113.88, 110.00, 67.71, 62.37, 54.10, 42.91, 33.13, 29.26, 28.27. IR (solid, ATR) 3321, 3043, 2923, 2851, 1718, 1640, 1605, 1544, 1505, 1467, 1295, 1246, 1063, 844, 759 cm^{-1}.

C. NMR Spectra

Figure A4.1. ^{1}H NMR of **S1** (400 MHz, $CDCl_3$, 298K).

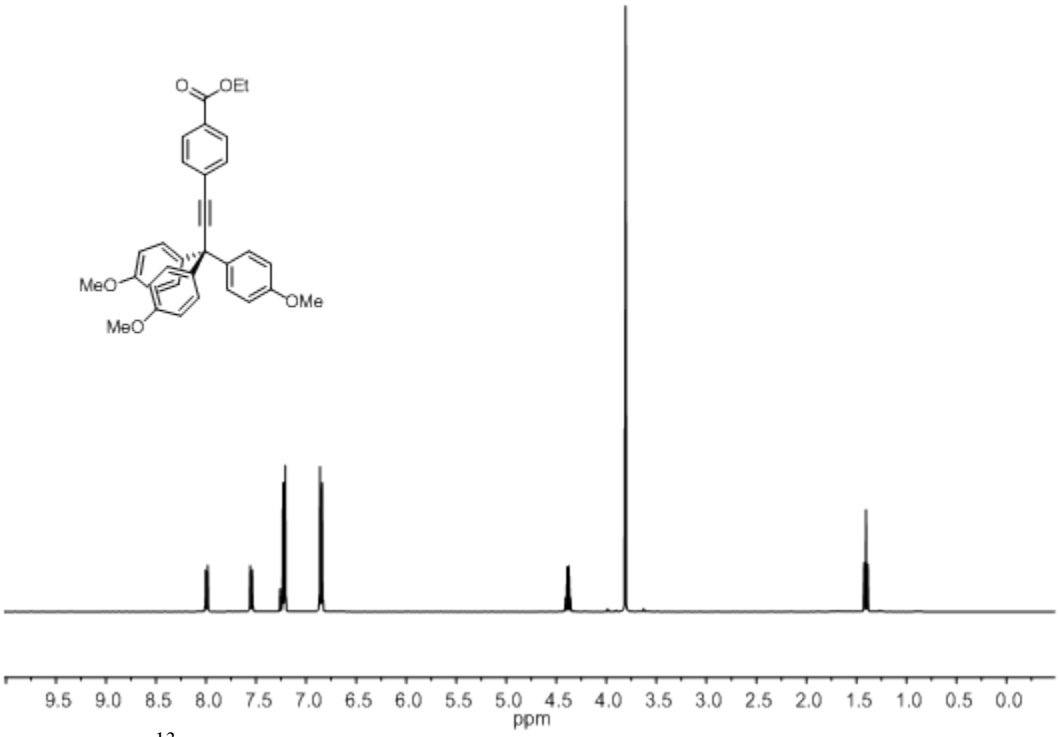

Figure A4.2. ^{13}C NMR of **S1** (101 MHz, $CDCl_3$, 298K).

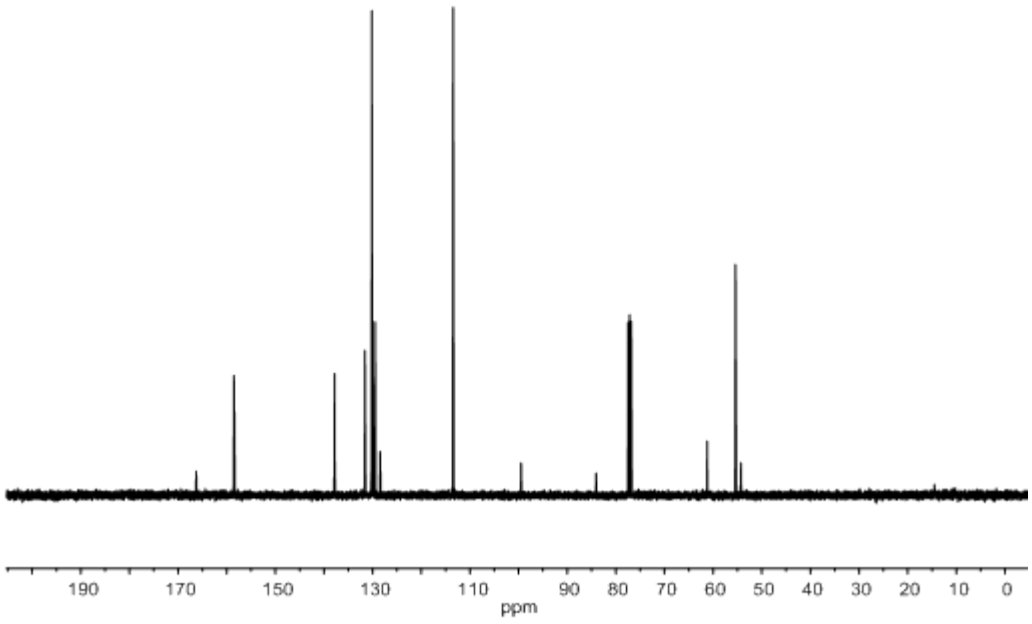

Figure A4.3. ^{1}H NMR of triol **2** (500 MHz, $(CD_3)_2CO$, 298K).

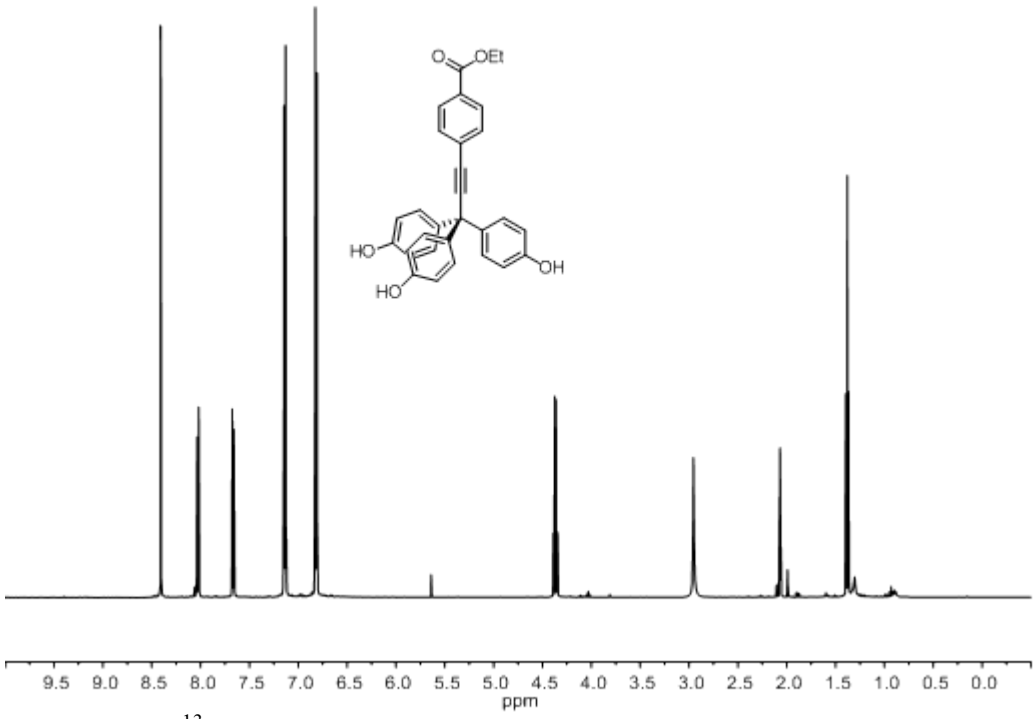

Figure A4.4. ^{13}C NMR of triol **2** (500 MHz, $(CD_3)_2CO$, 298K).

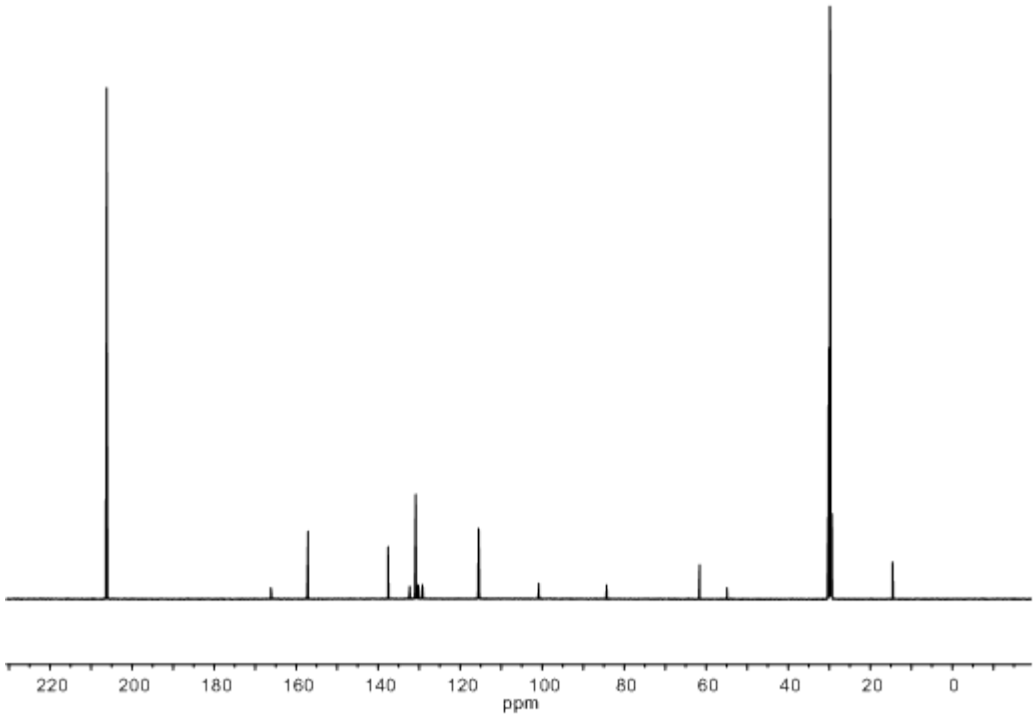

Figure A4.5. ^{1}H NMR of carboxylic acid tripod **S2** [500 MHz, $(CD_3)_2SO$), 298K].

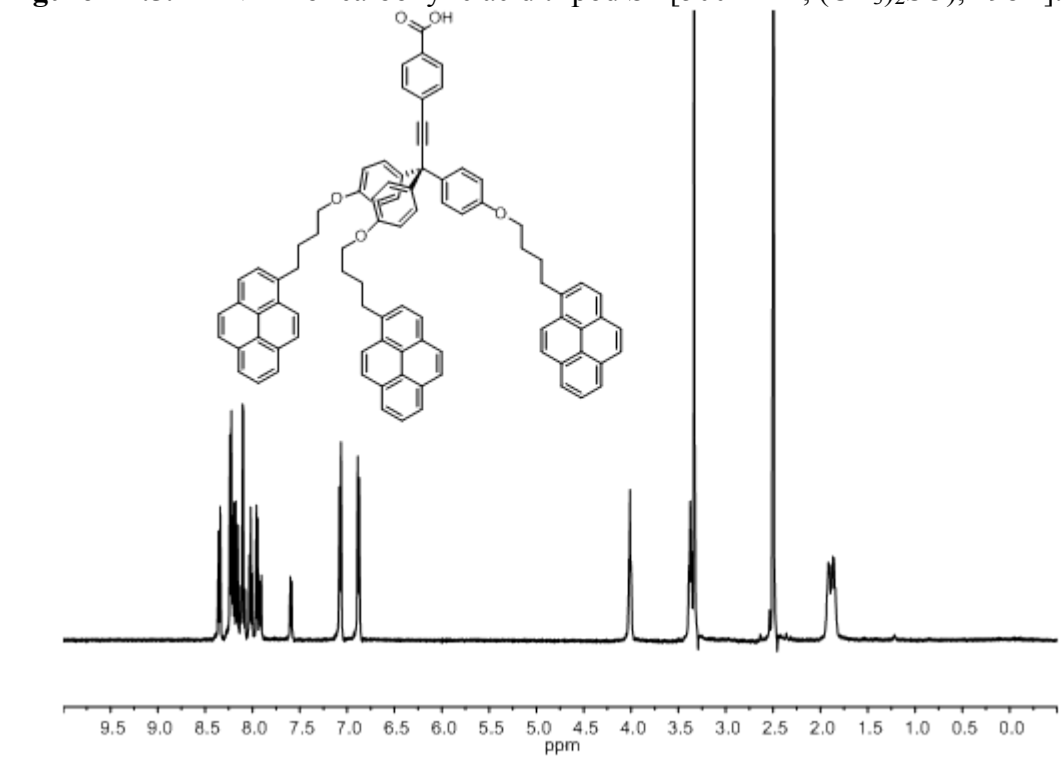

Figure A4.6. ^{13}C NMR of carboxylic acid tripod **S2** [126 MHz, $(CD_3)_2SO$), 298K].

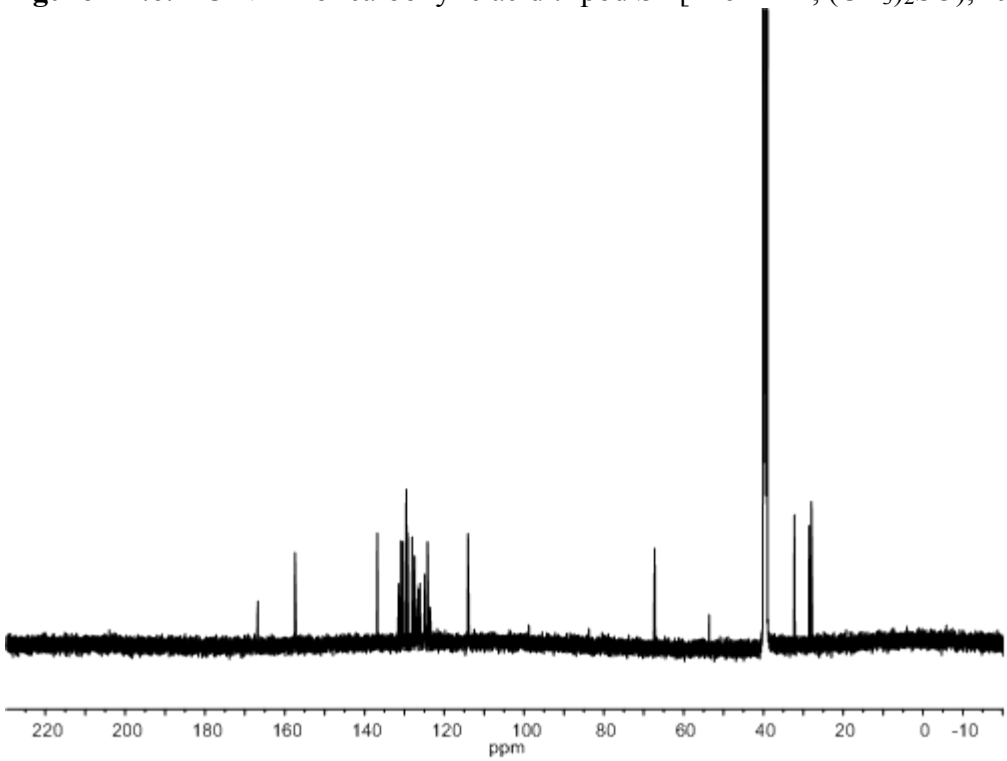

Figure A4.7. ^{1}H NMR of NHS-ester tripod **3** (500 MHz, $CDCl_3$, 298K).

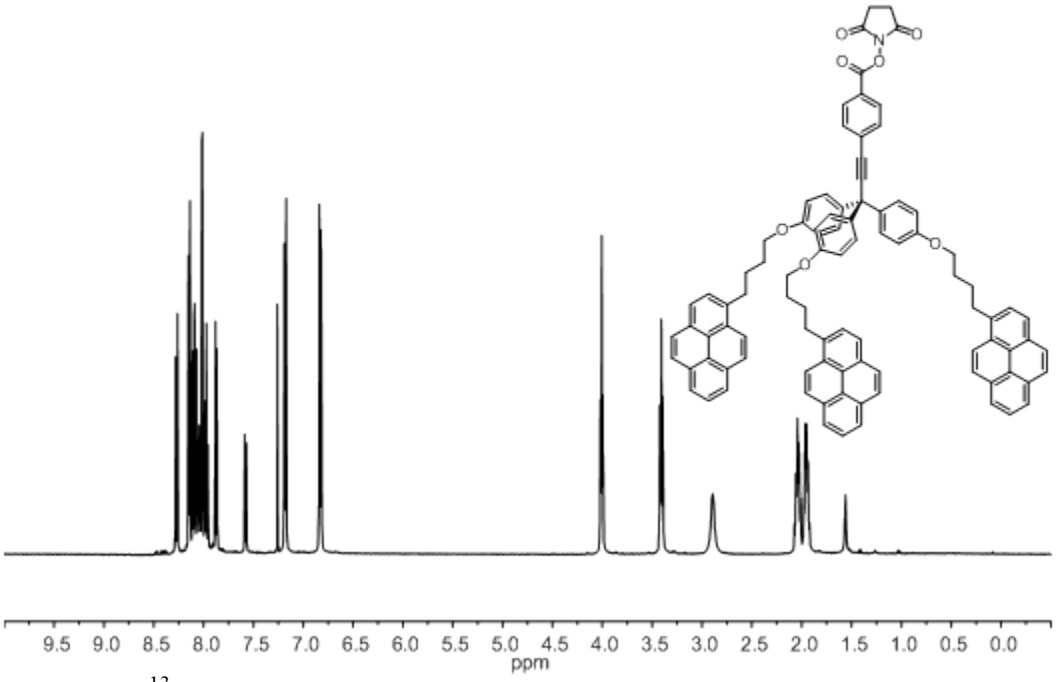

Figure A4.8. ^{13}C NMR of NHS-ester tripod **3** (126 MHz, $CDCl_3$, 298K).

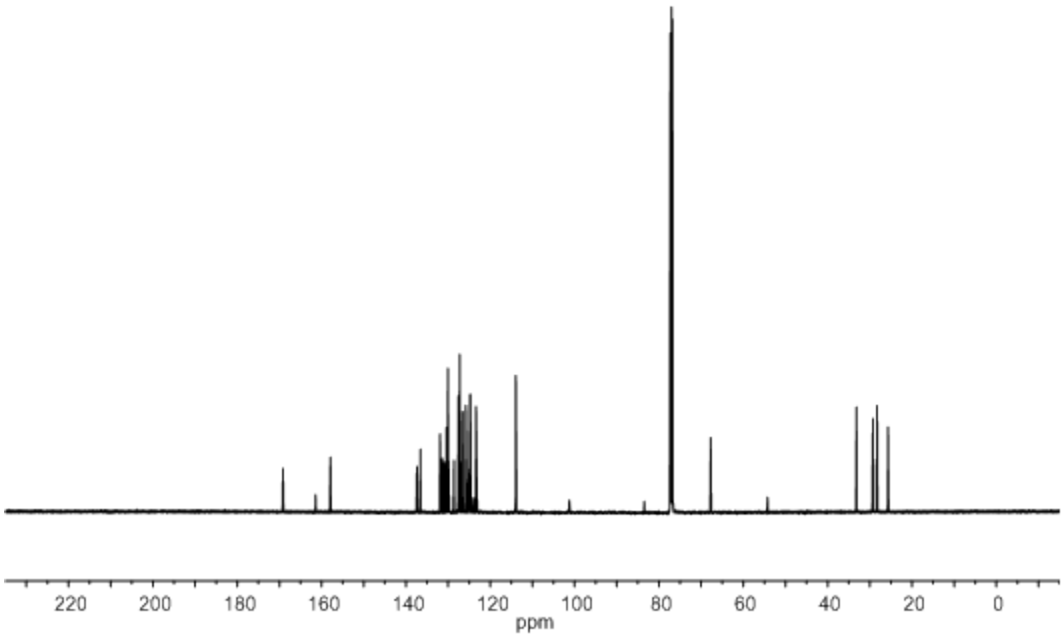

Figure A4.9. ^{1}H NMR Amide tripod **S3** (500 MHz, $CDCl_3$, 298K).

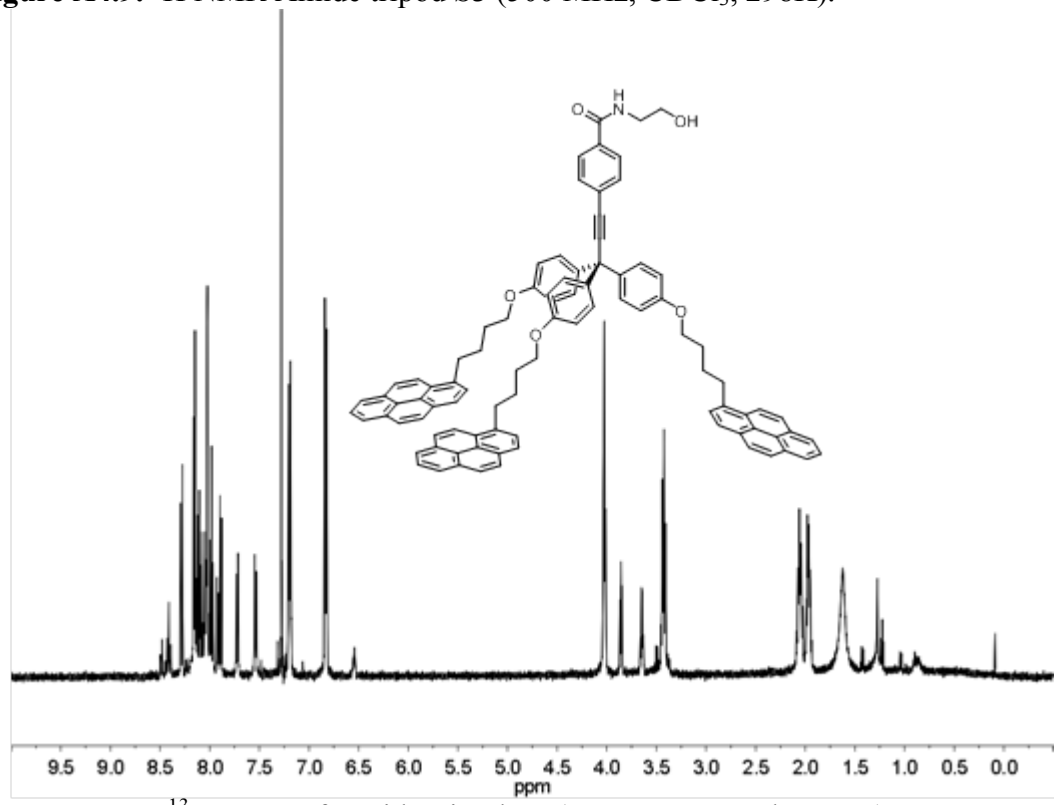

Figure A4.10. ^{13}C NMR of Amide tripod **S3** (126 MHz, $CDCl_3$, 298K).

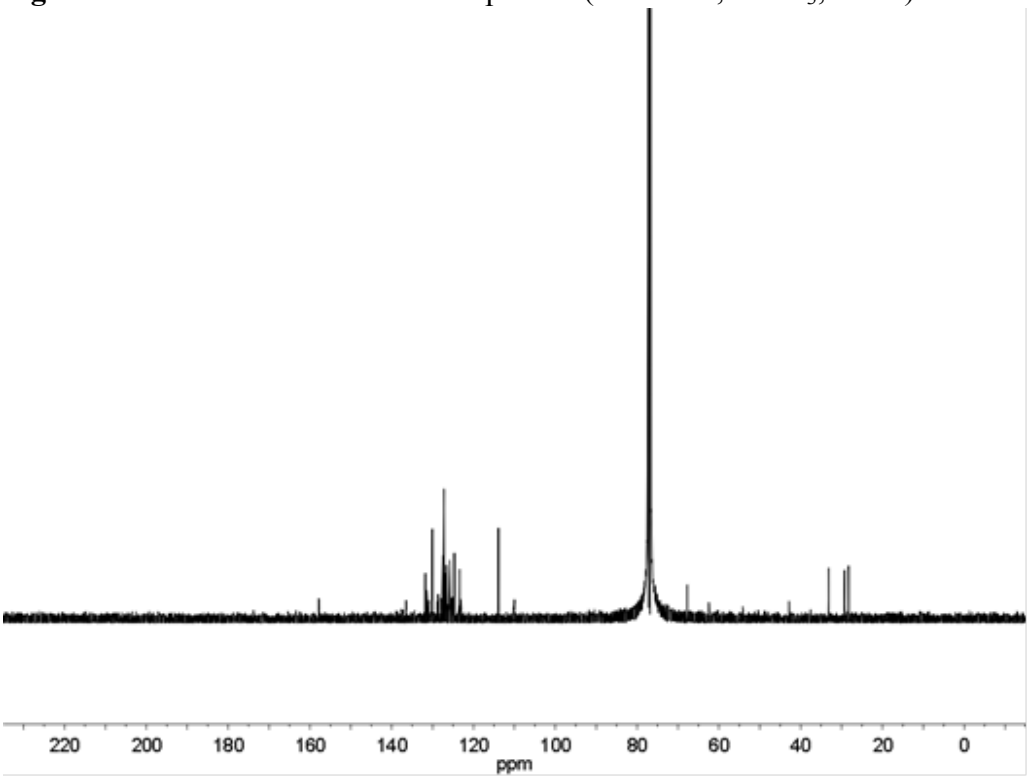

D. Cell Immobilizaion and Additional Surface Characterization.

Procedure for Cell Immobilization and Enumeration. For our cell immobilization assays we used SLG on SiO_2/Si. We prepared SAMs of both 1 and 2 by dipping as above. Subsequent bioconjugation of anti-E. coli antibody (aEAB) was accomplished by depositing 250 µL of 50µg mL^{-1} aEAB in phosphate buffered saline with 10 mM phosphate (PBS 1X) and allowing the solution to incubate on the surface for 10 min. After 10 min the solution was removed by wicking the solution away using a VWR light duty tissue wiper. The chip was then dipped in clean PBS 1X and a suspension of *E. coli* cells (10^8 cfu·mL^{-1} ·mL-1 in LB) was dropped onto the surface and allowed to incubate for 10 min. After incubation the surface was dipped in PBS 1X and sonicated for 30s to remove any weakly adsorbed bacteria. The immobilized cells were then stained using propidium iodide nucleic acid stain (0.1 mg·mL^{-1} in PBS 1X) by dropping the solution evenly over the surface and incubating for 30 min. After staining, the chip was washed by dipping in deionized water for 30s and blown dry with a gentle stream of nitrogen.

Figure A4.11. Representative image of E. coli cells on aEAB on SLG.

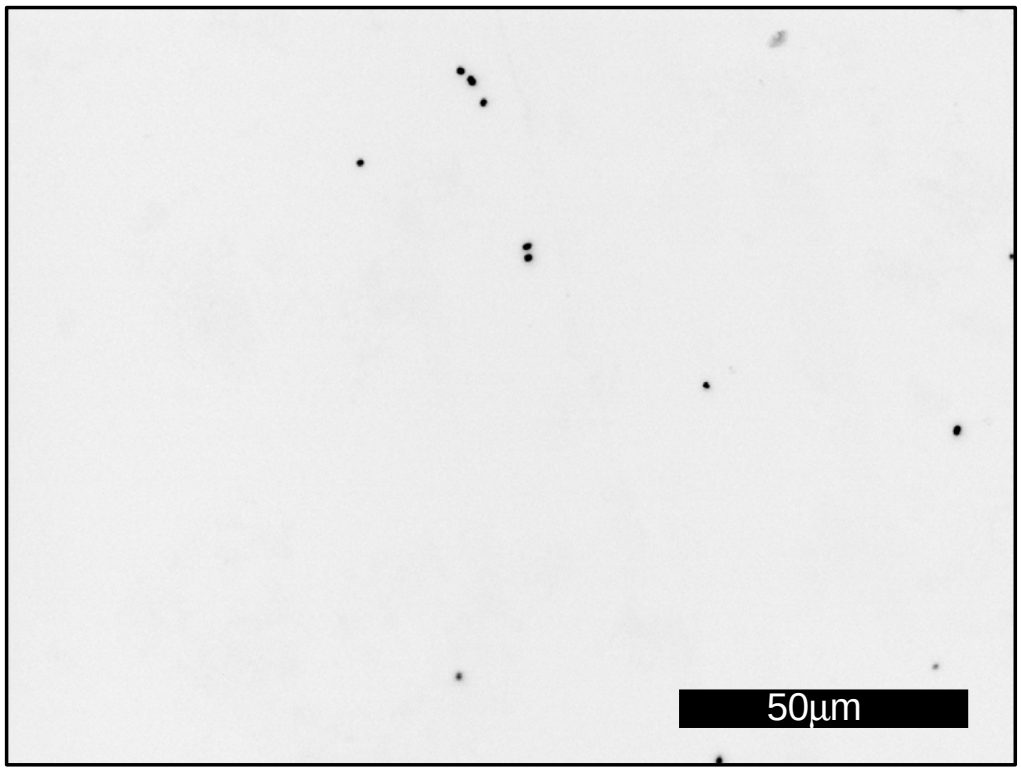

Figure A4.12. Representative image of E. coli cells on aEAB on **4** on SLG.

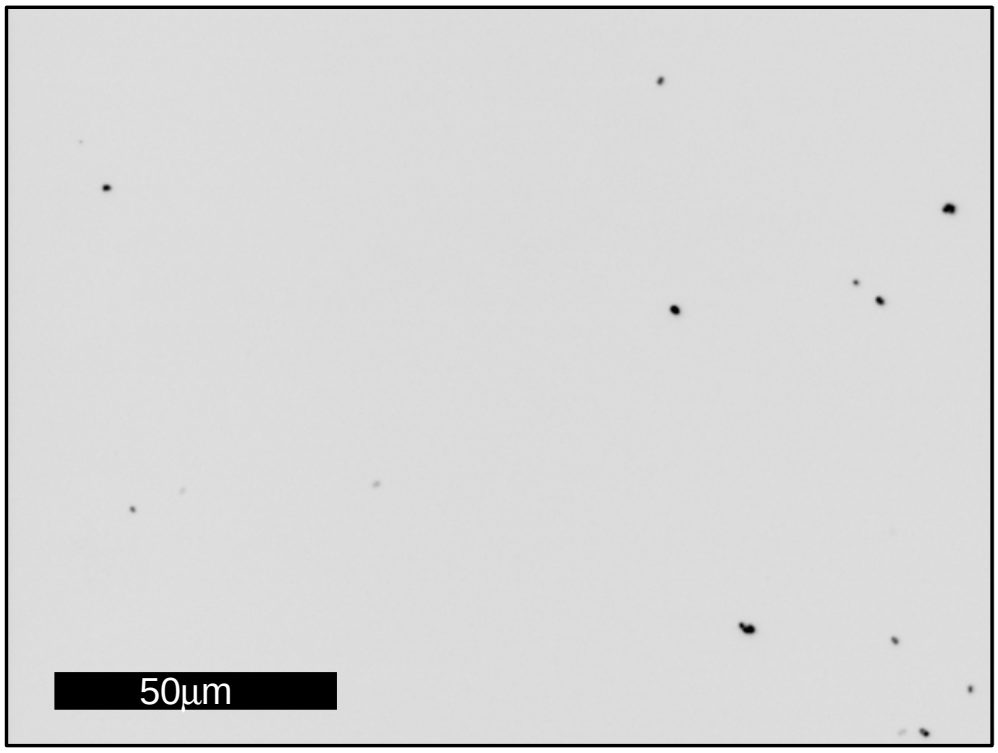

Figure A4.13. Representative image of E. coli cells on aBSA on **3** on SLG.

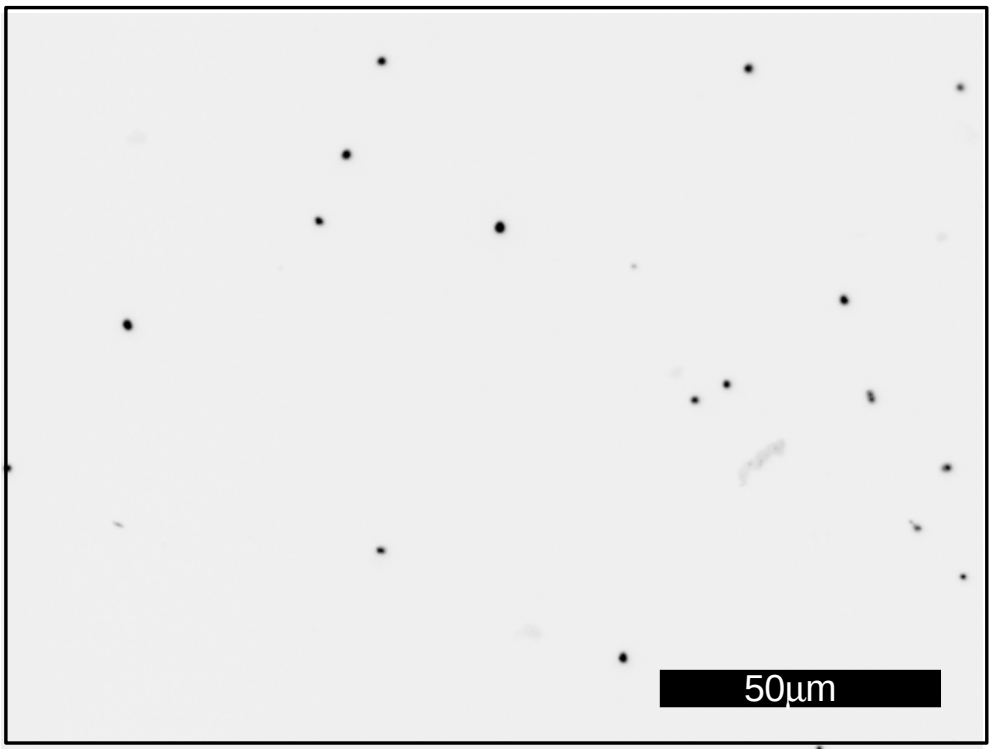

Figure A4.14. Representative image of E. coli cells on aEAB on **3** on SLG.

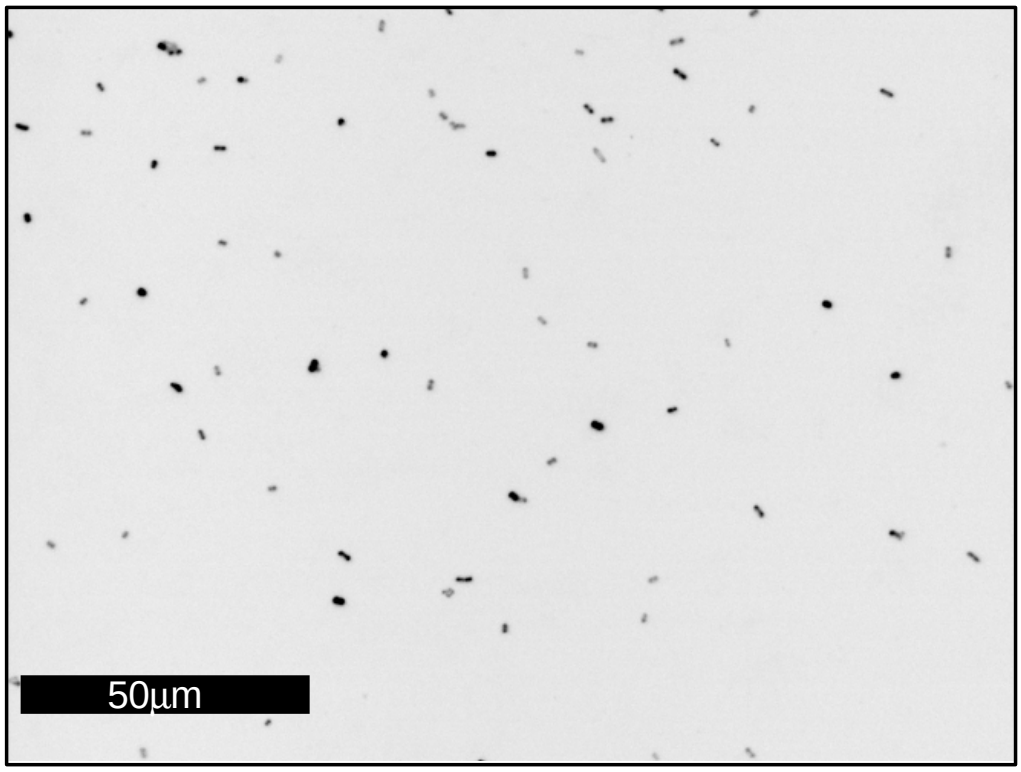

Figure A4.15. Representative AFM image of aEAB on HOPG.

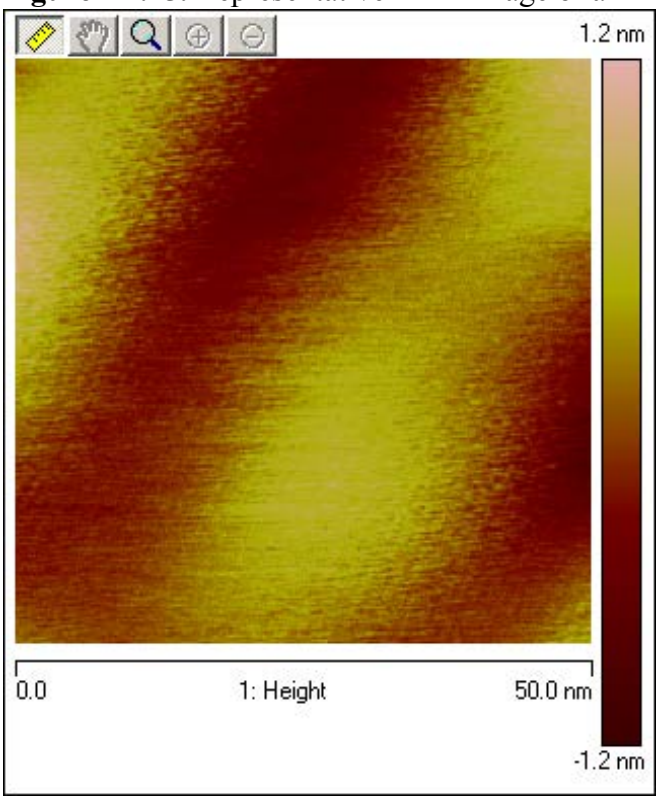

Figure A4.16. Representative AFM image of a SAM of **3** on HOPG.

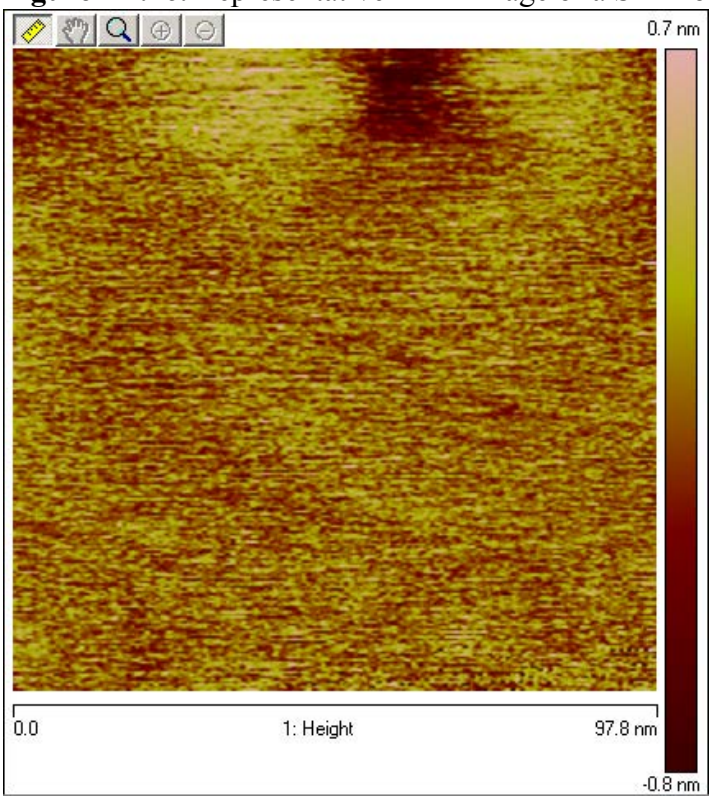

Figure A4.17. Representative AFM image of aEAB on a SAM of **3** on HOPG.

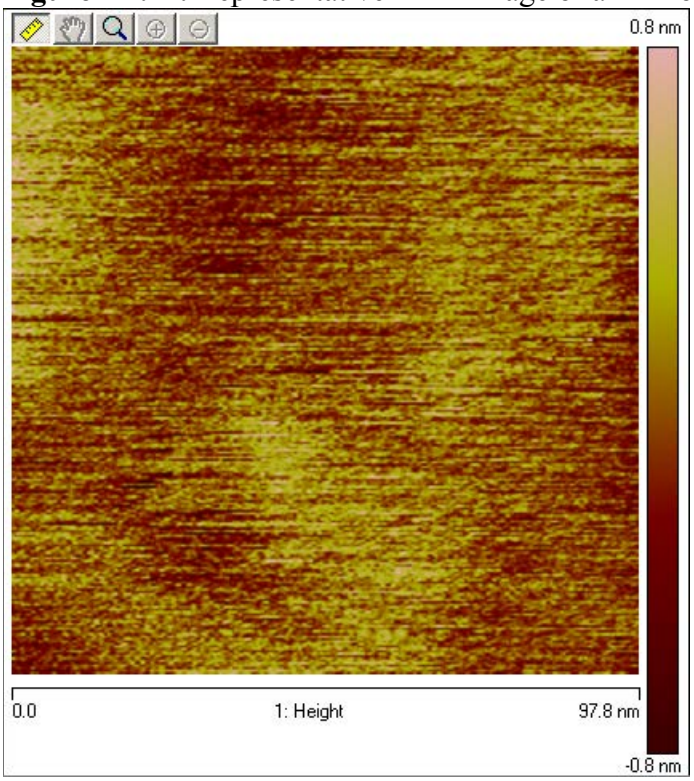

Figure A4.18. GQCM frequency (ΔMass, blue) and resistance (*ΔR*, red) responses for a surface functionalized with a SAM of **4**. A similar mass of aEAB is adsorbed compared to the bare GQCM or the GQCM functionalized with a SAM of **3**.

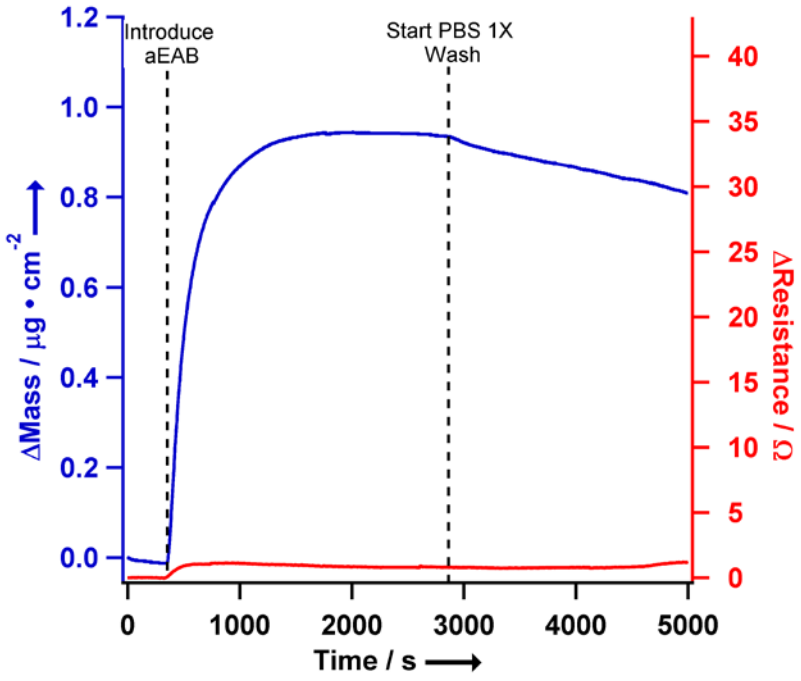

E. Evaluation of Tripods Incapable of Bioconjugation.

To evaluate the importance of the NHS-ester functionality of the tripod, we prepared derivative **S3**, which is not capable of bioconjugation (for experimental preparation and characterization of **S3**, see page S-8 and Figures S9-S10). SAMs of **S3** were subjected to the same GQCM and cell binding studies described in the manuscript for SAMs of **3**.

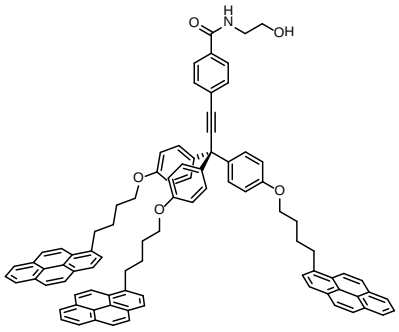

S3

Figure A4.19. GQCM frequency (ΔMass, blue) and resistance (*ΔR*, red) responses for a surface functionalized with a SAM of **S3**. A smaller mass of aEAB is adsorbed compared to either the bare GQCM or the GQCM functionalized with a SAM of **3**. There is also no detectable change in *ΔR* after *E. coli* cell introduction, consistent with the extremely low bound cell densities observed for this SAM (see below).

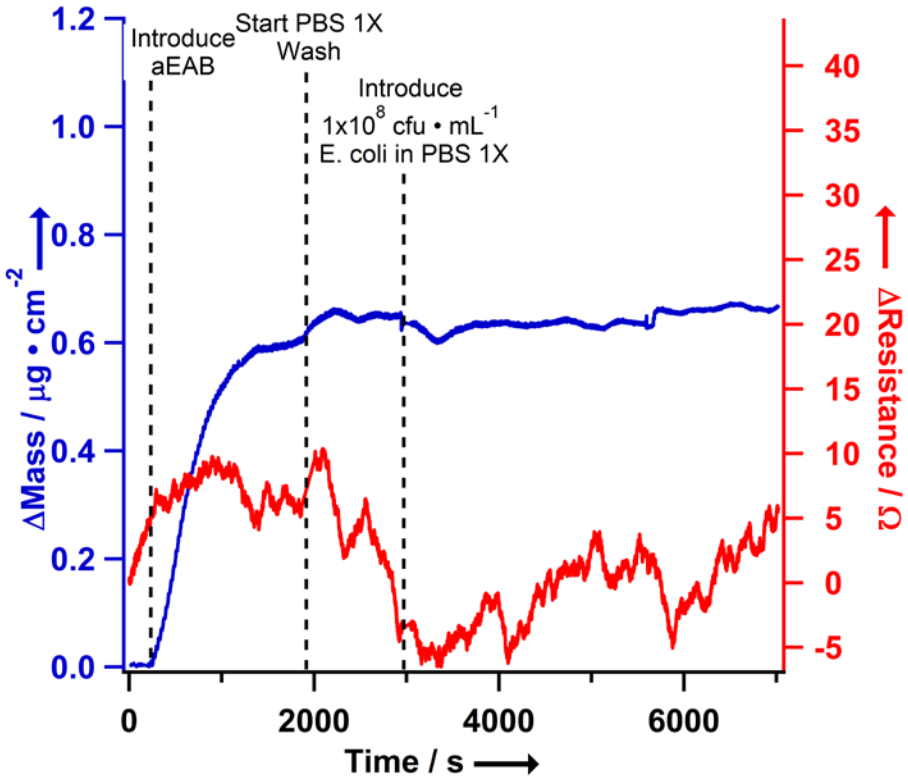

Figure A4.20. Cell count histogram for aEAB adsorbed on tripod SAMs of **S3**. The average cell density is an order of magnitude smaller than those shown in Fig. 3, indicating that **S3** decreases non-specific cell adsorption to the SLG surface relative to the other functionalization protocols.

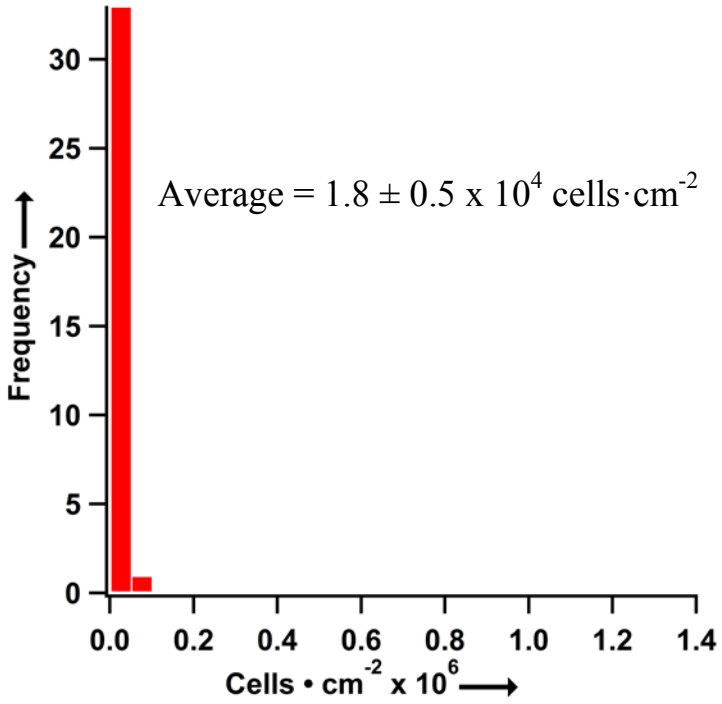

F. Additional Information on Biofilm Formation.

Single layer graphene was transferred onto quartz microscope slides (0.5 mm thick, 25.4 x 25.4 mm^2) . The quartz slides with SLG were functionalized with the NHS-tripod by immersion into a solution of NHS-Tripod (100 µM in THF) for 60 s, then rinsed in pure THF for antoher 60 s to remove excess NHS-tripod, dipped in deionized H_2O for 60 s, and finally dried under a flow of N_2.The quartz slides were then adhered SLG side up on the bottom surface of glass culture dishes with 10 mm circular aperture in the dish bottom (Ref. P35-10-C-N, MatTek, Ashland, MA)using a Loctite Superbonder 495 (Rocky Hill, CT),. The SLG was then functionalized by dropping 600 µL of •mL-1 anti-E. coli AB (50 µg·mL^{-1} in PBS 1X) onto the surface and incubating for 10 min. Rinsing with 3 streams of 1 mL PBS 1X followed this step.

Without drying the sample, the petri dish was filled with 5 mL of a solution of 1.10^8 cfu•mL-1 *E. coli* cells resuspended in PBS 1X and incubated for 10 min. Subsequently, under aseptic conditions the graphene surface was rinsed with PBS1X as described for the antibody functionalization and additionaly by filling the chamber with 5 mL PBS 1X and discarding the rinsing solution three times. Still under aseptic conditions, Petri dishes were finally filled with 5 mL LB medium, sealed hermetically and placed over the 50 X objective of an Olympus IX-70 inverted microsocpe equipped with a Retiga 2000-DC CCD camera (Q imaging).

Bacteria cells attached on the graphene surface were then observed and optical micrographs were recorded every 6 min. Care was taken that the bacteria cells observed according to this protocol were properly immobilized onto the graphene surface (i.e. in the focal plane of the coverslip) and that this immobilization was not transient. A typical series of image obtained for an individual bacterium is displayed in Figure A4.10. The bacteria immobilized start showng early signs of growth around 12 min and first signs of cellular division around 34min. The the population size of the resulting biofilm was monitored over a 230 min period. In the case of AB adsorbed on prisitine SLG, the daughter cells from the initial division failed to remain attached to the graphene surface or to the initial bacteria. De-grafting of the daughter cell and/or of the mother celloccurred consistently over time. In contrast, bacteria immobilized on AB1 conjugated to a SAM of 3 loss of cells from the surface was not observed, eventually resulting in the formation of a biofilm. Data was only collected from bacteria that exhitied signs of growth and/or cell division which represented more than 70% of the imobilized bacteria. Statistics on over fifty bacteria showing signs of

growth and/or cellular division enabled us to characterize the growth of the biofilm using the Malthusian growth model $P(t) = P_0e^{rt}$, where P_0 is the initial population, r is the growth rate, and t is time. The curve of biofilm population over time presented in the manuscript fits the Malthusian growth model with $r = 7.5 \pm 0.1 \times 10^{-3}$ min^{-1}, which represents a growth rate 50 % slower than the growth K-12 *E. coli* cells immersed in LB medium at 22 ^{o}C. This "bulk solution"growth rate ($r = 1.4 \times 10^{-2}$ min^{-1}) was characterized under the same temperature conditions and in 5 ml of LB medium (bacterial concentrations were assesed using an heamocytometer).

Figure A4.21. Series of optical micrographs showing the evolution of a K-12 *E.coli* cells biofilm attached to anti-E.coli IgG/ NHS-tripod functionalized SLG (unless otherwise mentionned the scale bar are 5 µm).

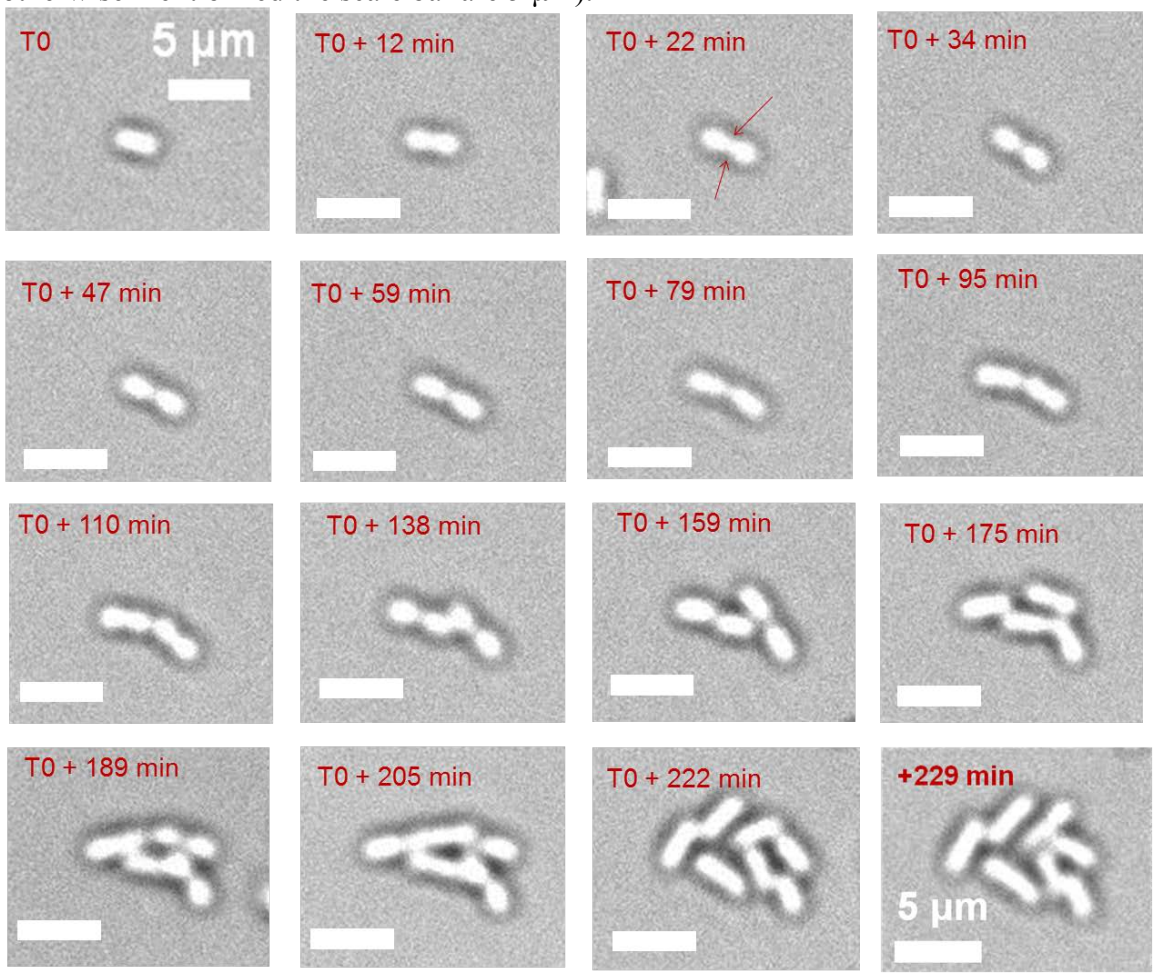

G. References

(1) (a) Wang, J.; Hanan, G. S. *Synlett* **2005**, *2005*, 1251; (b) Glass, T. E. *J. Am. Chem. Soc.* **2000**, *122*, 4522.
(2) Levendorf, M. P.; Ruiz-Vargas, C. S.; Garg, S.; Park, J. *Nano Lett.* **2009**, *9*, 4479.
(3) Schneider, C. A.; Rasband, W. S.; Eliceiri, K. W. *Nat Meth* **2012**, *9*, 671.

H. Complete References from Chapter Body

(3c) S. Bae, H. Kim, Y. Lee, X. Xu, J.-S. Park, Y. Zheng, J. Balakrishnan, T. Lei, H. Ri Kim, Y. I. Song, Y.-J. Kim, K. S. Kim, B. Ozyilmaz, J.-H. Ahn, B. H. Hong, S. Iijima, *Nature Nanotech.* **2010**, *5*, 574-578.
(3e) X. Li, W. Cai, J. An, S. Kim, J. Nah, D. Yang, R. Piner, A. Velamakanni, I. Jung, E. Tutuc, S. K. Banerjee, L. Colombo, R. S. Ruoff, *Science* **2009**, *324*, 1312-1314.

CHAPTER SIX

CONTROL OF THE GRAPHENE-PROTEIN INTERFACE IS REQUIRED TO PRESERVE ADSORBED PROTEIN FUNCTION

6.1 Abstract

Graphene's suite of useful properties makes it of interest for use in biosensors. However, graphene interacts strongly with hydrophobic components of biomolecules, potentially altering their conformation and disrupting their biological activity. We have immobilized the protein Concanavalin A onto a self-assembled monolayer of multivalent tripodal molecules on single-layer graphene. We used a quartz crystal microbalance (QCM) to show that tripod-bound Concanavalin A retains its affinity for polysaccharides containing α-D-glucopyrannose groups as well as for the α-D-mannopyranose groups located on the cell wall of *Bacillus subtilis*. QCM measurements on unfunctionalized graphene indicate that adsorption of Concanavalin A onto graphene is accompanied by near-complete loss of these functions, suggesting that interactions with the graphene surface induces deleterious structural changes to the protein. Given that Concanavalin A's tertiary structure is thought to be relatively robust, these results suggest that other proteins might also be denatured upon adsorption onto graphene, such that the graphene-biomolecule interface must be considered carefully. Multivalent tripodal binding groups address this challenge by anchoring proteins without loss of function and without disrupting graphene's desirable electronic structure. The work described in this chapter was performed in collaboration with Dr. Thomas Alava, Ms. Cécile Théodore, and Dr. Jaime Benitez under the direction of Prof. J.M. Parpia, Prof. H. G. Craighead and Prof. W. R. Dichtel and was published in the *Analytical Chemistry* (Alava, T.;

Mann, J. A.; Théodore, C.; Benitez, J. J.; Dichtel, W. R.; Parpia, J. M.; Craighead, H. G. *Anal. Chem.* **2013**, *85*, 2754.)

6.2 Introduction

Single-layer graphene (SLG) is mechanically flexible, transparent, conductive, and offers outstanding surface-to-volume ratio.[1] These properties make SLG of interest for integrated lab-on-a-chip analysis systems, particularly when it is functionalized with appropriate biosensing elements. For example, SLG has been incorporated into electrolyte-gated field effect transistors,[2] and SLG-aptamer interactions have served as active elements of a Förster resonance energy transfer-based thrombin sensor.[3] McAlpine and coworkers recently developed an implantable, wireless biosensor based on SLG functionalized with graphene-binding peptides.[4] Aromatic portions of biomolecules can interact with graphene's polarizable, hydrophobic surface. For example, the nucleobases of single-stranded DNA (ssDNA) adsorb strongly onto the graphene basal plane, and the ssDNA retains its ability to hybridize with a complementary strand. [5, 6]

In contrast, proteins, which constitute the largest and most widely employed class of biomacromolecules for surface functionalization[7-11], have also been interfaced to graphene,[2,12] but most studies do not unambiguously demonstrate that the protein remains functional.[13,14] The nature and magnitude of protein tertiary structure distortion upon adsorption onto a hydrophobic surface is dependent on many factors, including the number of non-polar amino acids and the energetics of the equilibrium between folded and denatured states.[15,16] So-called "soft" proteins, with less-stable tertiary structures, undergo larger deformations[17]. Tertiary

structure changes also depend upon the nature of the sorbent. For example, the α-helix content of cutinase and α-chymotryspin decrease when bound to hydrophobic SiO_2, yet their biological activity is mostly maintained. However, a similar decrease in α-helix content occurs upon adsorption to Teflon, but catalytic activity is lost.[18] Hydrophobic effects were also ascribed to lysozyne and α-lactoalbumin denaturation on polystyrene[19]. Furthermore, early studies have suggested changes in peptide secondary structure upon adsorption to SLG.[20] These findings suggest that many proteins might undergo conformational changes, perhaps accompanied by loss of function, when adsorbed non-specifically onto SLG.

In light of this concern, here we characterize and engineer the nature of the SLG-protein interface for a model lectin protein, Concanavalin A (Con A). We first employ a graphene-coated quartz crystal microbalance (GQCM) to characterize the immobilization of Con A on SLG. We interfaced Con A to SLG in two distinct ways: either (1) adsorbed to its pristine basal plane or (2) covalently attached to a self-assembled monolayer (SAM) of tripodal molecules bearing an activated ester for bio-conjugation. In Chapter 2, we demonstrated that these tripodal compounds bind strongly to graphene, even in organic solvents under infinite dilution conditions,[21] and diffuse in two-dimensions over the graphene surface.[22] In parallel, we have also found that antibodies attached to tripod monolayers exhibit highly specific biological recognition, while those bound to bare graphene or through a monovalent pyrene anchor lose this hallmark abitlity.[23] A complete discussion of the study using antibodies can be found in Chapter 5 of this dissertation.

After characterizing Con A adsorption onto graphene, we assessed its well-known ability to recognize α-D-glucopyrannose moieties of oligosaccharides. Con A retains activity

when attached to the tripod monolayer but shows no evidence of specific oligosaccharide recognition when adsorbed onto pristine SLG. Furthermore, Con A recognizes the α-D-mannopyranose moieties of the lipotechoic acids located on *Bacillus subtilis* cell walls. We evaluated SLG-immobilized Con A's ability to recognize *B. subtilis* by measuring the density of immobilized cells. Finally, we demonstrate that it is possible to inhibit recognition of cells by pre-saturating the Con A receptors with monomeric methyl-α-D-mannopyranose. These experiments confirm that Con A remains fully functional when attached to the tripod SAM and suggest that the tripod will provide a general strategy for interfacing biomolecules to SLG. This study also demonstrates the utility of GQCM with motional resistance monitoring to characterize the interactions of biomacromolecules with SLG.

6.3 Experimental Section

Graphene transfer. SLG was grown on Cu substrates (Alfa Aesar, Ward Hill, MA) in an atmosphere of CH_4 (36 sccm) and H_2 (60 sccm) at 980 °C for 30 min.[24] A 50 nm layer of poly(methyl methacrylate) (PMMA) was spin-coated onto the SLG, after which the Cu substrate was etched using aqueous $FeCl_3$ (1M, Transene, Danvers, MA). The SLG/PMMA was transferred into three fresh baths of deionized H_2O. Finally, the SLG/PMMA was transferred, SLG side down, onto a substrate, either a quartz crystal microbalance resonator or a silicon wafer with a thermally grown 280 nm-thick SiO_2 layer (Si/SiO_2, for cell immobilization studies). The SiO_2 layer provides sufficient optical contrast to visualize the SLG directly[25]. After deposition, the SLG was dried for 3 h, after which the PMMA was removed by soaking the substrate in anisole for 15 min and then CH_2Cl_2 for 12 h. The SLG

was found to be continuous and predominantly single layer (>95%) using Raman spectroscopy (see Appendix).

Reagents. Con A from *Canavalia ensiformis* (Jack bean, Sigma Aldrich, Saint Louis, MO) was dissolved in phosphate-buffered saline 1X solution (PBS 1X, 10 mM, pH 7.3) to a concentration of 200 $\mu g \cdot mL^{-1}$. Working solutions of Con A were prepared from aliquots of this stock solution before the beginning of each experiment by dilution with PBS 1X to a concentration of 50 $\mu g \cdot mL^{-1}$. Guanadinium hydrochloride, α-D-glucose, propidium iodide, methyl α-D-mannopyranose and Lysogeny Broth (LB) were purchased from Sigma Aldrich. Saturated solution of polysaccharides containing α-D-glucopyrannose moieties with the proper configuration to be recognized by Con A[26] were prepared according to a reported procedure,[27] and diluted by a factor 1:2 in PBS 1X, and stored at 4 °C until use (see Appendix). Propidium iodide was dissolved in deionized H_2O (500 $\mu g \cdot mL^{-1}$). Suspensions of *B. subtilis* were prepared by inoculating 5 ml of LB medium with an overnight culture of *B. subtilis* under sterile conditions. The inoculated media was incubated under an aerobic atmosphere with 6.5% CO_2 with constant shaking until the optical density at 600 nm (OD_{600}) reached 0.6, corresponding to mid-log phase growth. The *B. subtilis* cells were re-suspended in PBS1 X and diluted to a concentration of 10^8 $cfu \cdot mL^{-1}$. *B. subtilis* concentrations were estimated using a heamocytometer.

Non-covalent functionalization protocol. Monolayers of the N-hydroxysuccinimidyl ester tripod (NHS-tripod) were formed by submerging the SLG-functionalized substrate into a solution of NHS-tripod in THF (100 μM) for 1 min. The substrate was rinsed with fresh THF

and was then submerged in deionized H_2O for 1 min. The synthesis of the NHS-tripod is described elsewhere.[23]

Cell surface density counting. Graphene supported on the Si/SiO_2 wafers, with or without a tripod monolayer, were functionalized with Con A by spreading a 100 μL droplet evenly to cover the entire graphene sample (*ca.* 1 cm^2). After incubation, the sample was rinsed gently with PBS 1X (3 x 1 mL). Care was taken to ensure that the samples did not dry during the functionalization and subsequent bacterial recognition procedures. α-D-mannopyranose solution (inhibition solution) or 6 M guanadinium hydrochloride (denaturant solution) were introduced to the SLG surface using a similar procedure. Finally, graphene samples were incubated for 20 min in a solution of *B. subtilis* re-suspended in PBS 1X (5 mL, $1x10^8$ cfu·mL^{-1}), rinsed thoroughly three times with PBS 1X, and dried under a stream of N_2. The attached bacteria were counted by depositing aqueous propidium iodide (20 μL, 500 μg·mL^{-1}) over the samples and incubating under a glass slide for 45 min. An Olympus AX-70 microscope equipped with a Photometrics Cascade II EMCCD camera was used to image the resulting surfaces and determine the bound cell density.

Quartz crystal microbalance. SLG-functionalized quartz substrates were inserted into a Kynar crystal holder (Stanford Research Systems (SRS), model # O100RH) equipped with a flow cell (SRS model # O100FC) and peristaltic pump (Gilson, Middleton, WI). Stable temperatures were maintained by submerging the crystal holder in a controlled-temperature water bath at 27°C (Thermo scientific, Precision 280 series, Temperature uniformity of ±0.2°C at 27°C). Solutions were pumped over the active SLG substrate using a flow rate of 30 μL·min^{-1}. The crystal holder electrodes were connected to a controller interface (SRS, model

QCM-200) delivering the resonance frequency and the motional resistance signal. Once acquired, the data are corrected to remove baseline drift and external vibration artifacts (see Appendix). Throughout the manuscript, representative QCM resonance frequency and resistance curves are displayed, and numerical data are reported as the mean of three replicates.

6.4 Results and Discussion

Con A is a tetrameric lectin protein that binds one α-glucopyrannosyl (αGP) moiety at each subunit[26]. We selected Con A for this study because lectin proteins represent appropriate models for biosensing applications because of their ability to recognize specific carbohydrate bonding patterns. This ability has been used to engineer self-regulated insulin delivery systems,[28] demonstrating the value of Con A for future biomedical devices.[29] In addition, Con A is a relatively stable protein with respect to denaturation[30] and has been used previously to study protein adsorption on various surfaces.[31-35] Our experimental approach is depicted in Figure 6.1, in which we employed GQCM to characterize films of Con A formed by physisorption onto bare SLG and by chemisorption onto tripod SAMs bearing amine-reactive NHS esters. Changes in resonant frequency (Δf) and resistance (ΔR) of the QCM measure the mass deposition and viscoelastic behavior, respectively, of the adsorbed films. Δf can be related to mass of Con A deposited on the quartz surface (Δm) using the Sauerbrey equation , assuming that the film is both uniform and rigidly coupled to the resonator surface: $\Delta f = -C_f \, \Delta m$. Where C_f is a constant dependent on the quartz properties, 56.6 $Hz \cdot \mu g^{-1} \cdot cm^2$ for the 5 MHz AT-cut quartz used here[36].

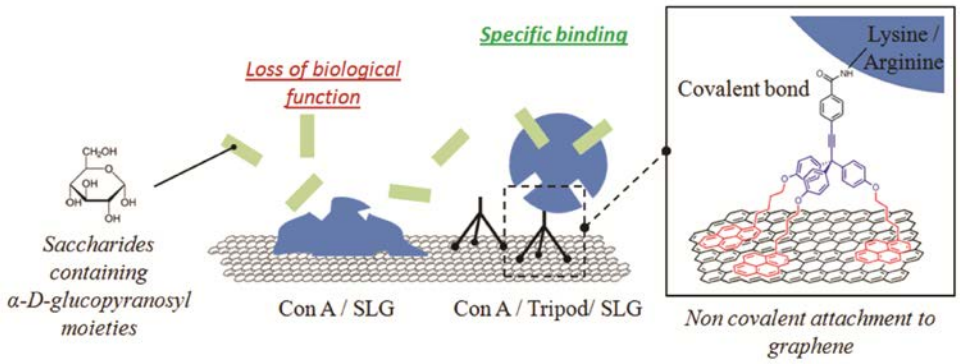

Figure 6.1. Schematic depiction of the strategies used to interface Concanavalin A to single-layer graphene and evaluate its carbohydrate-binding function.

Figure 6.2 shows the GQCM responses for the functionalized and unfunctionalized resonators upon introduction of Con A. Although Con A deposits on both substrates, the mass and the viscoelastic properties of the resulting films differ. When Con A is adsorbed on bare graphene, Δf_a stabilizes after 30 min to -38 ± 1.2 Hz, corresponding to a mass of 671 ± 21 ng/cm^2. Δf_t is slightly lower over the same period when the tripod monolayer is present, -33 ± 0.8 Hz, corresponding to an adsorbed mass of 583 ± 14 ng/cm^2. These measurements indicate that more Con A deposits onto bare SLG than onto the tripod monolayer. Surface coverage calculations indicate that the mass of adsorbed Con A corresponds to 0.75 - 1.7 monolayers in the presence of the tripod monolayer and 0.85 - 2.05 layers for Con A adsorbed to bare SLG (see Appendix). Under specific conditions satisfied in this study (see Appendix), changes in quartz resistance (ΔR) correspond to variations in the acoustic impedance of the film deposited onto the quartz resonator.[37] The acoustic impedance provides insight into the film's viscoelastic properties, which for biological thin films depends on many factors, such as their degree of hydration.[38]

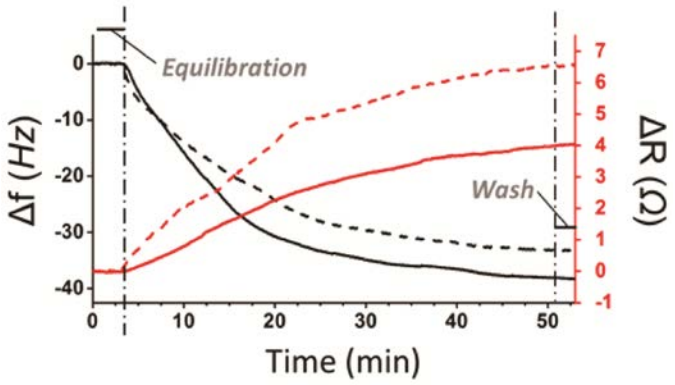

Figure 6.2. Changes in GQCM resonance frequency (Δf, left axis) and resistance (ΔR, right axis) upon introducing Con A into the flow cell. Two cases are compared: Con A immobilization onto bare SLG (Δf_a and ΔR_a, solid traces) and covalent attachment to a monolayer of tripodal binding compound (Δf_t and ΔR_t, dotted traces).

Thus, differences in ΔR between films of Con A on bare SLG (ΔR_a) and on tripod SAMs (ΔR_t) qualitatively indicate differences in their physical properties and the nature of their solvent interactions. The film deposited by adsorption of Con A on bare graphene, in addition to containing more mass, is more rigid ($\Delta R_a = 4 \pm 0.6\ \Omega$) than the film deposited on the tripod monolayer ($\Delta R_t = 6.6 \pm 0.8\ \Omega$). This difference, in combination with the activity studies described below, is consistent with Con A interacting with SLG through its non-polar amino acid residues. We associate this phenomenon with protein denaturation, which results in a denser, more rigid film compared to when it is covalently attached to the tripod SAM.[39]

We next characterized Con A's ability to recognize α-D-glucopyrannose or α-D-mannopyranose moieties of oligosaccharides to evaluate the adsorbed protein's level of function[40]. A flow of PBS 1X buffer solution was established over the Con A-functionalized GQCM flow cell until the frequency stabilized, after which a saturated solution of oligosaccharides containing α-D-glucopyrannose moieties (PαDG) was introduced. A sudden decrease in the resonant frequency of about 5 Hz is first observed, consistent with a change in

solvent viscosity (Figure 6.3). [41] The resonant frequency continued to decrease over the next 30 min, corresponding to PαDG interacting with the Con A film. Finally, the cell is washed with PBS buffer, which reverses the initial 5 Hz shift related to the change in solvent viscosity. We observed a significant dependence of PαDG binding on the Con A attachment protocol (Table 6.1). Con A films that were attached to tripod monolayers underwent a GQCM resonant frequency shift of -33.2 ± 2.3 Hz; whereas the resonant frequency shift of Con A films adsorbed on bare SLG was only -13.3 ± 0.8 Hz.

Table 6.1. The resonance frequency shift associated with the binding of PαDG to Con A-conjugated single layer graphene (error bars are ± σ). As a negative control, the resonance frequency shift associated with introducing the PαDG solution over bare SLG is displayed.

Table 6.1. Binding of PαDG on various GQCM substrates

	Pristine SLG	Con A adsorbed on SLG	Con A attached to tripod	Denatured Con A attached to tripod
Resonance frequency shift (*Hz*)	- 12.9 ± 1.3	-13.3 ± 0.8	-33.2 ± 2.3	-11.5 ± 1.1

This activity difference between Con A on SLG and Con A on a tripod SAM cannot be explained by the protein simply adopting different orientations upon immobilization on the graphene surface, as no single orientation would restrict access to all four of Con A's α-D-glucopyrannose binding sites. As such, we hypothesized that Con A retains its function when covalently attached to the tripod but denatures upon adsorption to bare SLG. To investigate this idea, we denatured the tripod-bound Con A by introducing a solution of guanadinium hydrochloride (GdmCl, 6M) into the flow cell before evaluating PαDG binding.

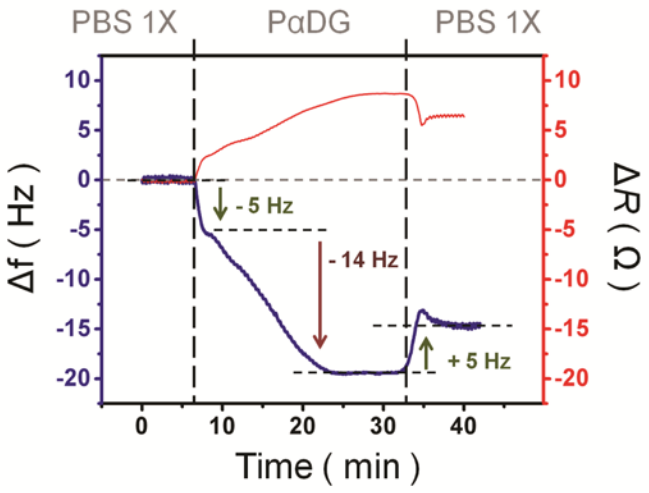

Figure 6.3. Time evolution of the GQCM resonance frequency (blue) and motional resistance (red) of an unfunctionalized GQCM during a PαDG binding experiment. The following solution sequence was introduced to the GQCM: PBS 1X equilibration (t = 0–6 min), PαDG solution (t = 6–32 min), PBS 1X washing (t = 32–42 min). The resonance frequency shifts associated with switching between PBS 1X and PαDG solutions (±5 Hz) and nonspecific adsorption of PαDG to the GQCM (−14 Hz) are indicated.

The denatured Con A/tripod film, the adsorbed Con A/SLG film, and a pristine GQCM substrate each exhibited similar GQCM resonant frequency variation in the presence of PαDG (Table 1), which we attribute to nonspecific PαDG binding. Only the intact Con A/tripod film exhibits a larger resonant frequency shift than the nonspecific PαDG response. Figure 6.4 shows the QCM frequency response to PαDG exposure for each of these films. One notable feature is the loss of mass *ca.* 12 min for Con A adsorbed on bare SLG, which we attribute to the desorption of additional Con A nonspecifically bound to the protein monolayer.[42,43] Furthermore, the frequency response of the Con A/tripod films is an order of magnitude too large to correspond simply to the mass of bound oligosaccharides (see Appendix). We attribute this non-Sauerbrey response to a change in aggregation state of Con A upon PαDG binding, which has been noted previously in the presence of polyvalent oligosaccharides.[44]

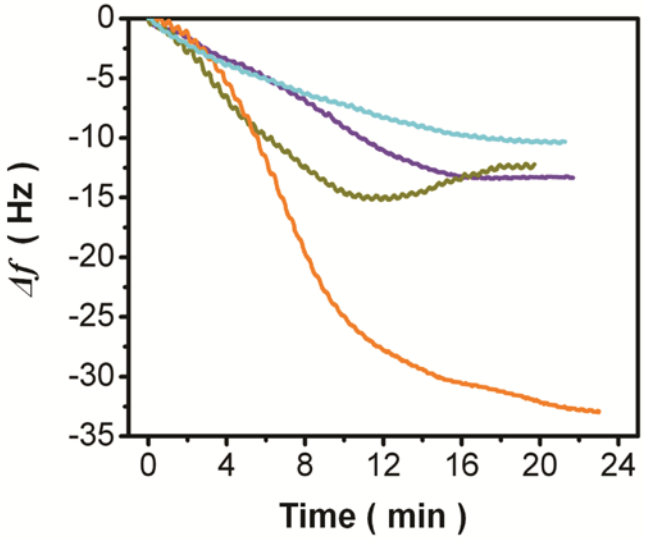

Figure 6.4. Time evolution of the GQCM resonant frequency after introducing the PαDG solution to bare SLG (purple), Con A adsorbed on bare graphene (green), Con A bound to tripod (orange), and denatured Con A bound to tripod (cyan).

We further confirmed that the PαDG binding observed for tripod-supported Con A is attributable to an intact, functioning protein using an inhibition experiment developed by Doyle and Birdsell for Con A in solution.[45] This experiment exploits Con A's ability to specifically recognize α-D-mannopyranosyl residues of lipotechoic acids, which are located on the cell walls of gram-positive *B. subtilis* bacteria. We measured the density of *B. subtilis* cells that bound to Con A films, which were either adsorbed onto bare SLG (Figure 6.5, green bars) or attached to the tripod monolayer (Figure 6.5, yellow bars). Approximately five times more *B. subtilis* cells bind to the Con A/tripod films per unit area (4826 ± 1030 mm^{-2}, orange bars) than the adsorbed Con A films (911 ± 449 mm^{-2}, green bars). This difference is consistent with the results of the PαDG binding studies using GQCM described above. Con A/tripod films that were denatured, again using 6M GdmCl, reduced the bound *B. subtilis* cell density (913 ± 401 mm^{-2}, Figure 6.5, cyan bars) to a level similar to that of the adsorbed Con A.

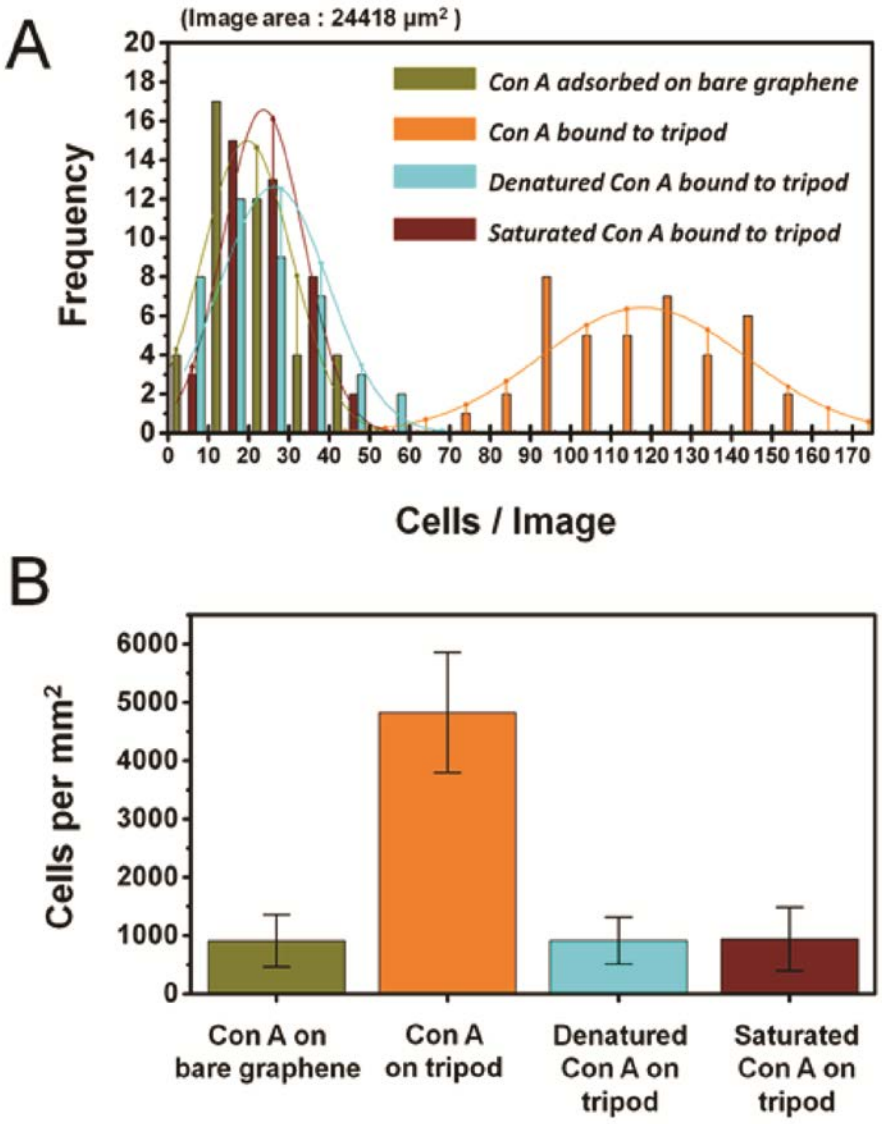

Figure 6.5. (A) Histogram of *Bacillus subtilis* cell density (image field of view = 24418 μm^2) bound to SLG functionalized as follows: Con A adsorbed onto SLG (green bars); Con A bound to the tripod monolayer (orange bars); Con A bound to the tripod monolayer and then denatured with GdmCl solution (red bars); Con A bound to the tripod monolayer and then saturated with a methyl α-D-mannopyranoside solution (Cyan bars). Normal distribution curves centered on the mean cell density values are overlaid onto each data set. (B)Surface densities of *Bacillus subtilis* cells (cells / mm^2) bound to SLG for the above surface preparation protocols. The data presented in this figure and the calculated mean cell densities were obtained from three replicate surfaces of each experiment.

Finally we inhibited Con A function by saturating the binding sites of the active Con A/tripod films with methyl α-D-mannopyranose prior to introducing the *B. subtilis* cells.

Under these conditions, the *B. subtilis* cell density was reduced by 83-100% (941 ± 543 mm^{-2}, Figure 6.5, red bars) to a similar level as the non-specific binding observed for denatured or adsorbed Con A. The results of this inhibition experiment further confirm that the Con A protein retains its function when covalently attached to the tripod SAM. Collectively, these cell recognition experiments illustrate the importance of engineering the protein/graphene interface in order for proteins to retain their higher order structure and function.

6.5 Conclusions

This study has demonstrated through complementary GQCM and cell binding studies that the lectin protein Con A readily adsorbs to graphene but loses its ability to recognize oligosaccharides. The viscoelastic properties of these adsorbed Con A films are also consistent with a physisorption mechanism driven by changes in Con A's structure. In contrast, Con A retains its function when it is covalently tethered to a monolayer of a tripodal compound, which binds to graphene through non-covalent interactions. These findings demonstrate that the QCM is a powerful tool to study protein adsorption and function on graphene as this material begins to fulfill its outstanding technological promises. Given that Con A is relatively stable with respect to denaturation, these findings are likely to be applicable to a broad range of other less-stable proteins. Our results emphasize that adsorption to bare SLG, or even to monovalent pyrene anchors, may be an ineffective biofunctionalization strategy, and that protein function should be demonstrated

unambiguously in such cases. In contrast, the tripodal NHS-ester used in this study preserves Con A function and represents a general approach to interface proteins to SLG. We are currently performing studies in which graphene's desirable electronic properties enable electronic sensing simultaneously with GQCM mass and dissipation measurements.

REFERENCES

1. Geim, A. K.; Novoselov, K. S.; *Nature Mater.*, **2007**, *6*, 183-191.

2. Ohno, Y.; Maehashi, K.; Matsumoto, K. *J. Am. Chem. Soc.* **2010**, *132*, 18012–18013.

3. Haixin Chang, H. ; Tang, L.; Wang, Y. ;Jiang, J.; Li, J. *Anal. Chem.,* **2010**, *82* , 2341–2346.

4. Mannoor, S. M.; Tao, H.; Clayton, J. D.; Sengupta, A.; Kaplan, D. L.; Naik, R. R.; Verma, N.; Omenetto, F. G.; McAlpine, M.C. *Nat. Commun*., **2012**, *3*, 763

5. Lu, C.-H. ; Yang, H.-H. ; Zhu, C.-L. ; Chen, X. ; Chen, G.-N. ; *Angew. Chem. Int. Ed.*,**2009**, *48*, 4785–4787 DNA

6. He, S.; Song, B.; Li, D.; Zhu, C.; Qi, W.; Wen, Y.; Wang, L.; Song, S; Fang, H.; Fan, C., *Adv. Funct. Mater.*, **2010**, *20*, 453-459.

7. Cameron J. Wilson, C. J.; Clegg, R. E.; Leavesley, D; I.; Pearcy, M. *J. Tissue. Eng.*, **2005,** *11*, 1-18.

8. Gray, J. J., *Curr. Opin. Struct. Biol.* ,**2004**, *14*, 110-115.

9. Yanik, A. A.; Huang, M.; Kamohara, O.; Artar, A.; Geisbert, T. W.; Connor, J. H.; Altug, H. *Nano Lett.*, **2010**, *10*, 4962–4969.

10. Lyu, Y.-K; Lim K.-R.; Lee, B. Y.; Kim, K. S.; Lee W.-Y. *Chem. Comm.,* **2008**, 4771-4773

11. Wang, J. J. of Pharm. Biomed. Anal., 1999, 19(1–2), 47–53.

12. Mohanty, N; Fahrenholtz, M.; Nagaraja, A.; Boyle; Berry, V. Nano Lett., 2011, 11 (3), 1270–1275

13. Lee, J. S., Joung, H.-A., Kim, M.-G.; Park, C. B., *ACS Nano*, **2012**, *6*, 2978-2982.

14. Kodali, V. K.; Scrimgeour, J. ; Kim, S. ; Hankinson, J. H.; Carrol, K. M.; de Heer, W. A.; Berger, C.; Curtis, J. E.; *Langmuir*, **2011**, *27*, 863-865

15. Haynes, C; A.; Norde, W.; *Coll. Surf., B.*, **1994**, *2*, 517-566.

16. Roach, P.; Farrar, D.; Perry, C. C., *J. Am. Chem. Soc.*, **2005**, *127*, 8168-8173

17. Nakanishi, K.; Sakiyama, T.; Imamura, K. *J. Biosc. Bioeng.*, **2001**, *91*, 233-244.

18. Zoungrana, T.; Findenegg, G. H.; Norde, W., *J. Colloid InterfaceSci.*, **1997**, *190*, 437-448.

19. Haynes, C. A. ; Norde, W., *J. Colloid InterfaceSci.,* **1995**, *169*, 313-328.

20. Katoch, J.; Nyon, S. N.; Kuang, Z.; Farmer, B. L.; Naik, R. R.; Tatulian, S. A.; Ishigami, M., *Nano Lett.*, **2012**, *12*, 2342-2346

21. Mann, J. A.; Rodríguez-López, J. ; Abruña, H. D. ; Dichtel, W. R. ; *J. Am. Chem. Soc.* 2011, *133, 17614-176***17.**

22. Rod*r*íguez-López, J. ; Ritzert, N. L. ; Mann, J. A.; Tan, C.; Dichtel, W. R.; Abruña, H. D.; *J. Am. Chem. Soc.*, **2012**, *134*, 6224-6236.

23. Mann, J. A.; Alava, T.; Craighead, H. G.; Dichtel, W. R. *Angew. Chem. Int. Ed.*, Accepted for publication. DOI: 10.1002/anie.201209149

24. Li, X.; Cai, W.; An, J.; Kim, S.; Nah J.; Yang D.; Piner, R.; Velamakanni, A; Jung, F.; Tutu, E.; Banerjee, S. K.; Colombo L.; Ruoff, R. S., *Science*, **2009**, *324*, 1312-1314.

25. Abergel, D. S. L.; Russel, A.; Falko, V. I., *App. Phys. Lett.*, **2007**, *91*, 063125 - 063125-3.

26. Goldstein, I. J.; Hollerman, C. E.; Merrick, J.M., *Biochim. Biophys. Acta,* **1965,** *97* , 68-76.

27. Sugisawa, H.; Edo, H., *J. Food Sci.*, **1996**, *31*, 561–565.

28. Brownlee, M.; Cerami, A.; *Science,* **1979**, *206*, 1190-1191.

29. Qiu, Y.; Park, K.; *Adv. Drug. Deliver. Rev.* , **2001**, *53*, 321-339.

30. Chatterjee, A.; Mandal, D. K.; *Biochim. Biophys. Acta*, **2003**, *1648*, 174-183.

31. Diniz, F. B.; Ueta, R. R.; *Electrochim. Acta*, **2004**, *25*, 4281-4286.

32. Mielczarski, J.A.; Dong, J.; Mielczarski, E. ; *J. Phys. Chem. B*, **2008**, *112*, 5228-5237.

33. Gallinet, J.-P.; Gauthier-Manuel, B.; *Eur. Biophys. J.* , **1993**, *22*, 195-199.

34. Archambault, J. G.; Brash, J. L.; Coll. Surf. B Biointerf. , 2004, 25 (1-2), 9-16.

35. Gümüşderelioğlu, M.; Agi, P.; *React. Funct. Polym.*, **2004**, *61*, 211-220.

36. Buttry, D., Electroanalytical Chemistry, Eds.: Allen Bard, Marcel Dekker, **1991**, 23-33.

37. Geelhood, S. J.; Frank, C. W.; Kanazawa, K., *J. Electrochem. soc.*, **2002**, *149*, H33-H38.

38. Höök, F.; Rodahl, M. ; Kasemo, B ; Brzezinski, P. , *Proc. Natl. Acad ; Sci.*, **1998**, *95*, 12271-12276.

39. Rodahl, M. ; Höök, F. ; Fredriksson, C. ; Keller, C. A. ; Krozer, A. ; Brzezinski, P. ; Voinova, M ; Kasemo, B . *Faraday Discuss.*, **1997**, *107*, 229-246.

40. Iyeri, R. N.; Goldstein, I. J. Immunochem. **1973**, 10, 313– 322

41. Auge, J.; Hauptmann, P; Hartmann, J.; Rösler, S.; Lucklum, R., *Sens. and Act. B : Chem.*, **1995**, *24-25*, 43-48.

42. Yuan, Y. J.; van der Werff, M. J.; Chen, H.; Hirst, E. R.; Xu, W. L.; Bronlund, J. E., *Anal. Chem.,* **2007**, *79*, 9039-9044.

43. Johansson, T.; Affinity *Measurements Using, Quartz Crystal Microbalance (QCM)*, Springer: Berlin Heidelberg, **2010**, 683-693.

44. Goldstein, I. J.; Hollerman, C. E.; Merrick, J.M., *Biochim. Biophys. Acta*, **1965**, *97* , 68-76

45. Doyle, R. J.; Birdsell, D. C., *J. Bacteriol.*, **1972**, 652-658.

APPENDIX FIVE

Table of Contents

A. Quartz Crystal Microbalance Data Treatment :

The QCM data for resonance frequency and motional resistance were processed to remove baseline drift and external vibrations artifacts as described below. Figure A5.1 shows the two modifications made to the raw data. Baseline drift was assessed by observing the evolution of the resonant frequency and motional resistance of the QCM under a flow of PBS 1X solution at 30 μL/min. The QCM flow cell was immersed in a controlled temperature water bath set at 27 ºC. The PBS 1X solution was flowed for at least 1 h prior to the experiment. Under these conditions, the QCM response stabilized to exhibit a constant linear drift within 30 min, before which it exponentially approaches this constant drift. Thus, allowing the GQCM to stabilize for an appropriate period of time resulted in a constant drift over the course of the experiment. This baseline drift was measured after the signal had stabilized and before introducing the reagents required by the experiment.

External vibration artifacts are perturbations that cause a sudden, limited in time, short-duration (<30 s) discontinuities in the QCM response. These artifacts appear as sharp spikes in the mean path of the resonance frequency or motional resistance signal and are caused by external mechanical perturbations to the resonating system, such as handling the tubes connected to the fluidic cell when switching from one reagent to another. These artifacts were removed from the processed QCM response, as illustrated in the upper right and lower left portions of Fig. S1, respectively.

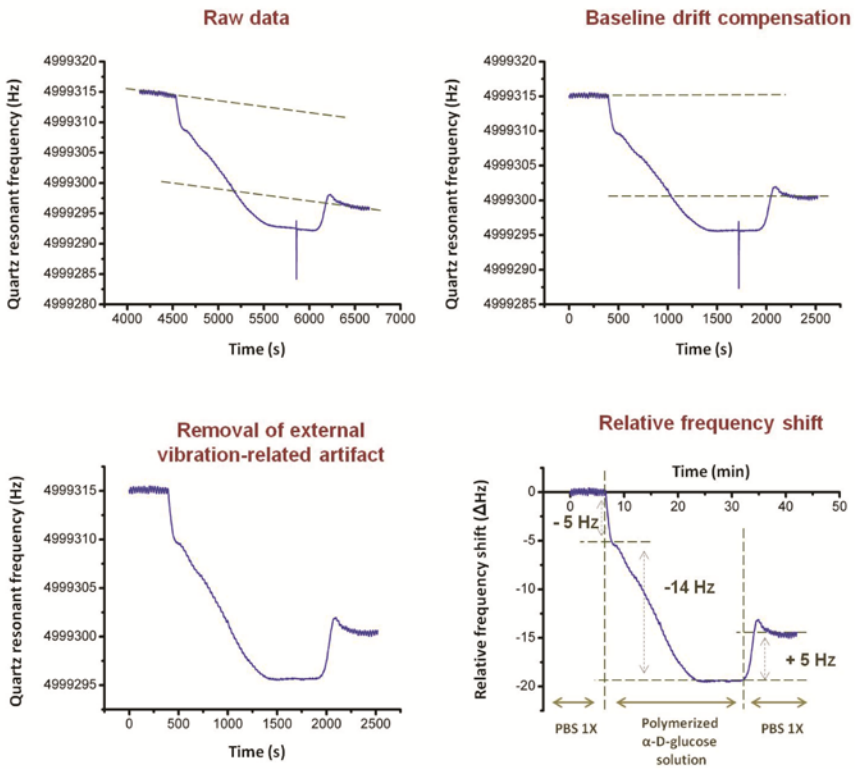

Figure A5.1. Processing of the raw QCM responses used in this study is comprised of two steps: baseline drift cancellation and external mechanical vibration caused artifacts.

B. Quartz Crystal Microbalance Motional Resistance:

Before each recording of resonance frequency changes and motional resistance change of the vibrating quartz, the parasitic capacitance C_0 (representing the sum of the static capacitances of the crystal's electrode, holder and connector capacitance) is cancelled using the manufacturer's included nulling system (SRS, QCM200). Under this condition, changes in the equivalent series resistance of the vibrating quartz provide insight into the viscoelastic properties of the adsorbed layer, similar to the dissipation technique.[1] This latter technique is based on monitoring the exponential decay of the quartz oscillation amplitude upon disconnecting the actuation circuit. This technique is a promising method to study the viscoelastic properties of biomolecular thin films deposited on the QCM[2,3]. Studies have

shown that the rigorous cancellation of the quartz static capacitance implies a good agreement between results obtained using the dissipation technique and monitoring of the quartz equivalent series electrical resistance,[4] here referred to "motional" resistance.

C. Estimation of Concanavalin A Surface Coverage on the GQCM :

Conacanavalin A adopts a tetramer configuration[5] under our experimental conditions (four monomers with one binding site each for pH>5.5) with a hydrodynamic radus of 3.57 nm.[6] To estimate the adsorbed mass of Con A that corresponds to monolayer coverage, we assume a spherical conformation of this radius. We next determine the coverage for monolayers of two different densities (Figure A5.2). These calculations are summarized in Table A6.1. These estimates are consistent with the formation of approximately 1-2 monolayers of protein during the graphene functionalization procedures.

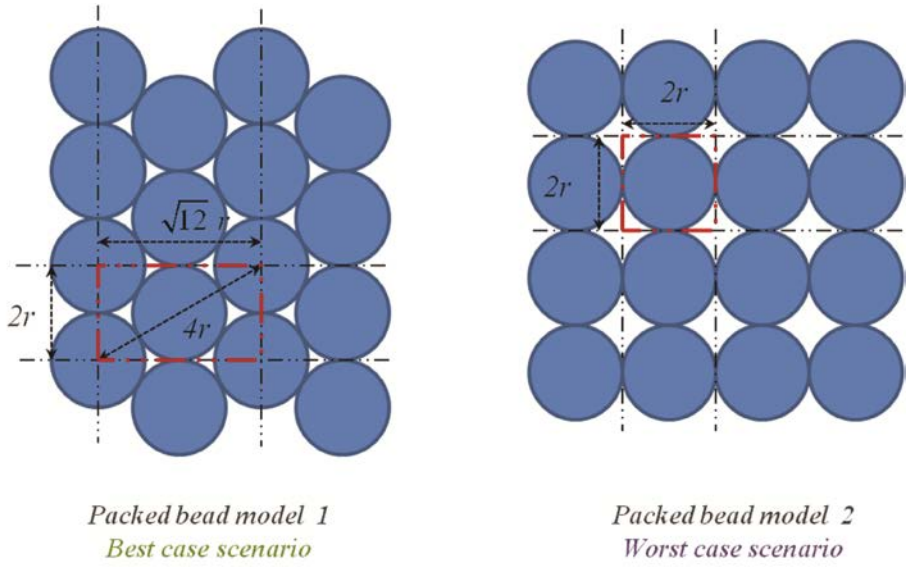

Figure A5.2. Schematic description of two models used to estimate the surface coverage of graphene-immobilized Concanavalin A. The red dotted square represents the equivalent surface occupied by respectively two protein units (left image) and one protein unit (right image)

Surface coverage estimation according different arrangement scenarios

GQCM functionalization	Arrangement model	**Monolayers**
Con A adsorbed on bare SLG	**Model 1**	0.85
	Model 2	2.05
Con A attached to NHS-tripod	**Model 1**	0.75
	Model 2	1.70
Concanavalin A tetramer hydrodynamic radius : 3.57 nm [5]		

Table A5.1. Estimation of the number of Concanavalin A layers formed on the GQCM for each functionalization method, based on the active area of the GQCM, the adsorbed mass of Con A, and its hydrodynamic radius.

D. Polymerization of α-D-glucose.

α-D-glucose (100 mg/mL) was polymerized in PBS 1X (10 mM, pH 7.3) at 150 °C for 2.5 h with intermittent stirring. The final solution was brown in color and was dissolved in PBS 1X at a 1:2 ratio and was stored at 4°C. This protocol was adapted from a similar procedure for the thermal polymerization of glucose (caramelization) described by Golon *et al.*[7] A qualitative description of byproducts from thermal polymerization of glucose can be found additionally in Sugisawa *et al.*[8] These products include several mono-, di- and oligo-saccharides containing α-D-glucopyranosyl groups, for which Concanavalin A has a strong affinity.[9] For example, polysaccharides incorporating Kojibiose, Sophorose, Nigerose, Laminaribiose or Cellobiose contain one or more α-D-glucopyranosyl groups that are recognized by Con A.

We analyzed the composition of our PαDG solution by matrix assisted laser desorption ionization time-of-flight (MALDI-TOF) mass spectrometry (Figure A5.3), which

indicated a complex mixture of oligosaccharides predominantly comprised of di-, tri-, and tetrasaccharides. This finding is consistent with that reported by Golon *et al.*[7]

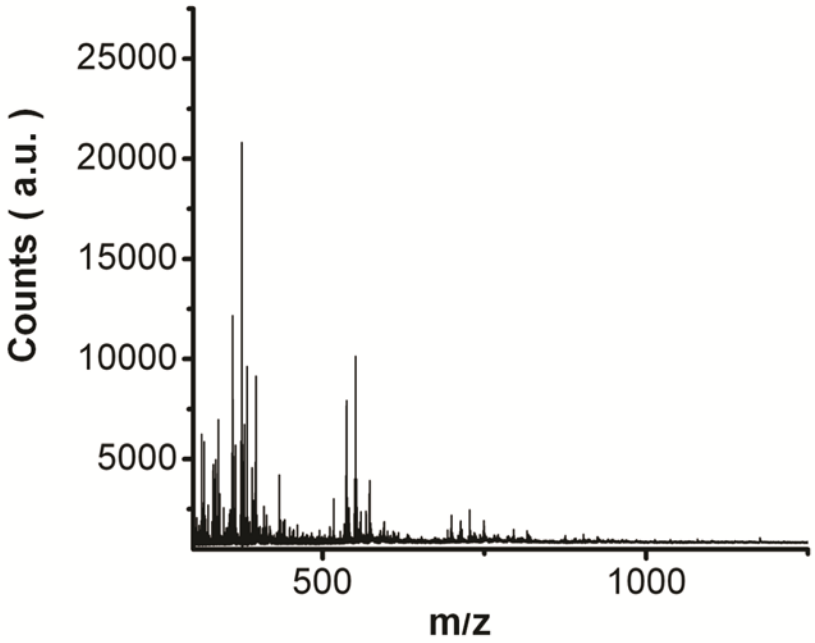

Figure A5.3. MALDI-TOF MS of the PαDG solution

E. Graphene Analysis by Raman Spectroscopy :

We characterized the uniformity of the graphene samples by Raman spectoscopy, which confirmed its single layer nature, as shown by the ratio between the G band peak (~ 1586 cm^{-1}) to the 2D peak (~ 2695 cm^{-1}), I(G)/I(2D)<0.5, and a narrow, single Lorentzian-like 2D band (FWHM ~33 cm-1). [10] Figure A5.4, S5, and S64 present Raman spectra of the graphene before and after transfer: as produced on copper foil, transferred on SiO_2/Si wafer, and tranferred on quartz crystals (thus supported by the gold top electrode of the quartz crystal). Figure A5.7 shows representative Raman spectra from various areas of the film (indicated in inset optical micrograph), demonstrating uniformity over a large area.

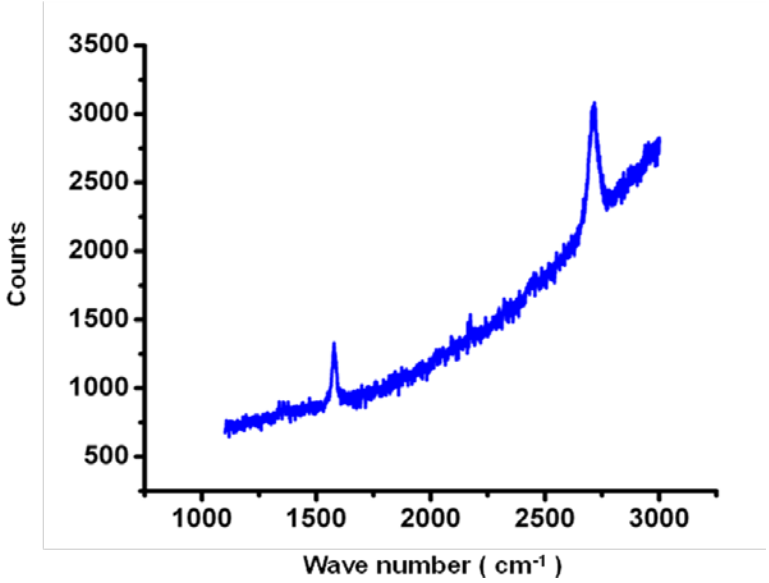

Figure A5.4. Raman spectrum of SLG as assembled on Cu foil.

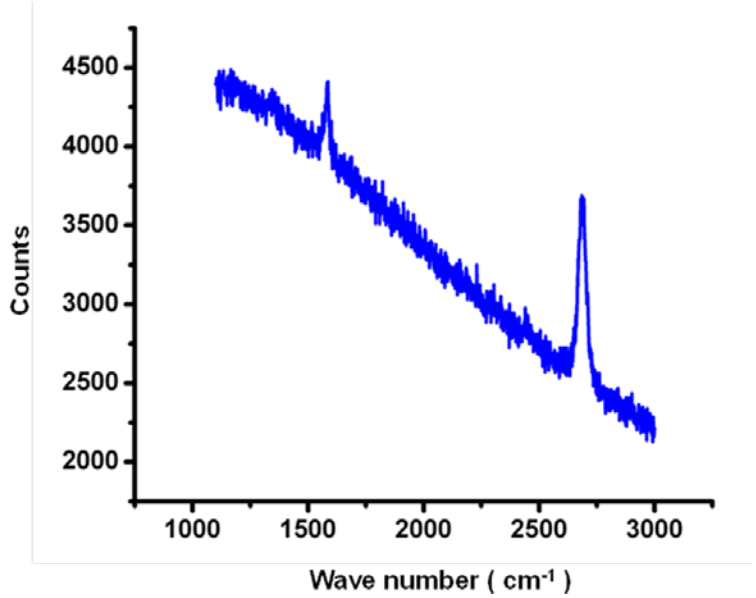

Figure A5.5. Raman spectrum of SLG as transferred on top of the QCM crystal (the background contribution is from the Au contacts on the quartz top electrode).

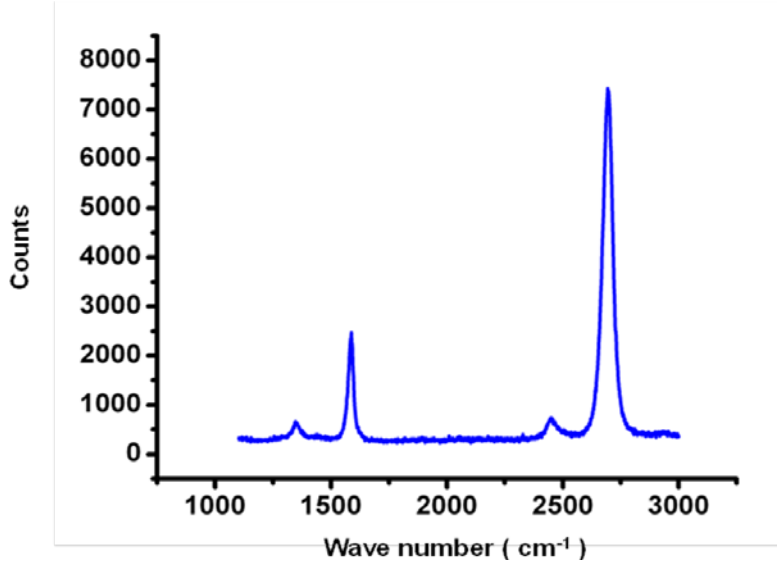

Figure A5.6. Raman spectrum of SLG as transferred onto a Si wafer coated with 280 nm SiO_2.

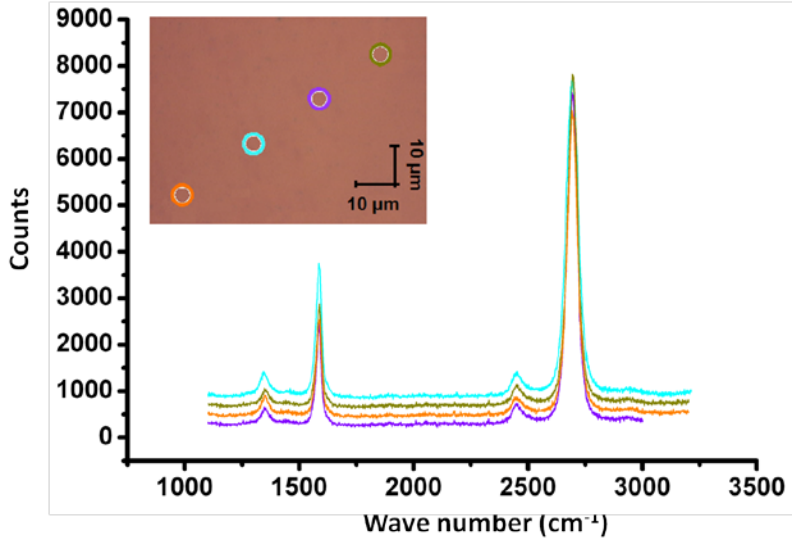

Figure A5.7. Raman spectra of SLG transferred onto SiO_2/Si substrates. The inset shows a photograph of the graphene sample with colored circles that indicate the location of the four Raman spectra.

F. Fluorescence Microscopy Images And Cell Counting Method :

A nucleic acid staining procedure was used to determine the *Bacillus subtilis* cell density on various functionalized SLG substrates. Bright field and fluorescence micrographs

were overlayed to confirm that each counted unit corresponded to a bacterial cell. As described in the mansucript, when conjugated to the tripodal monolayer, Con A shows the expected selective binding of carbohydrates, including those on the cell walls of *Bacillus subtilis* cells. For the Con A/tripod films, analysis of the *Bacillus subtilis* fluorescence micrographs revealed the formation of aggregates of up to 15 agglutinated cells (Figure A5.8b). The large number and the size of aggregates observed in this case is also consistent with normal Con A function, as Con A-mediated agglutination of other biological organisms has been reported in litterature. [11,12]

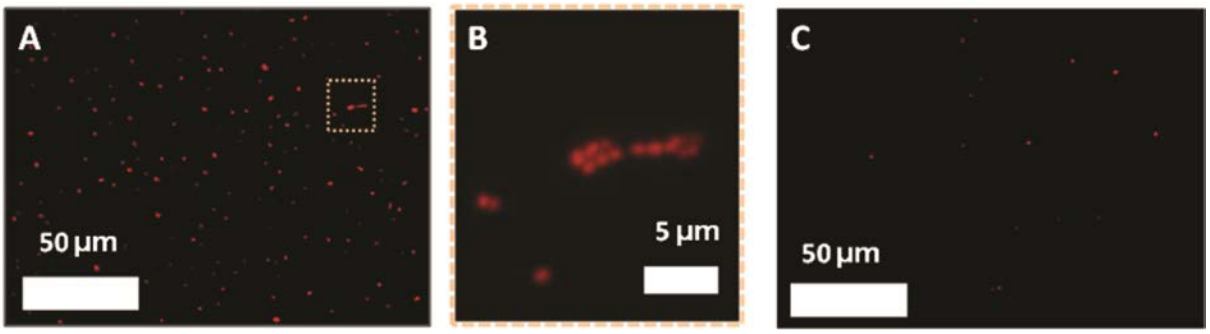

Figure A5.8. A) Representative fluorescence micrograph of *Bacillus subtilis* cells deposited onto a Con A/tripod film on SLG. The cells are stained with propidium iodine nucleic acid stain. B) Representative fluorescence micrograph at higher magnification, indicating the formation of *Bacillus subtilis* aggregates observed for Con A/tripod films. C) Representative fluorescence micrograph of *Bacillus subtilis* cells deposited onto a Con A film adsorbed to bare SLG.

G. Motional Resistance Data For PαDg Binding Experiment :

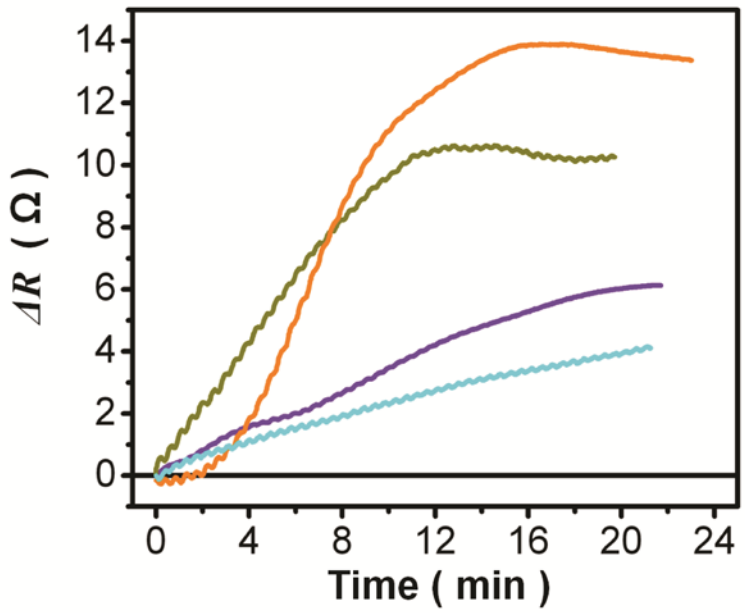

Figure A5.9. Changes in the motional resistance of the GQCM upon introducing PαDG to bare SLG (purple), Con A adsorbed on bare graphene (green), Con A bound to tripod (orange), and denatured Con A bound to tripod (cyan).

The largest changes in motional resistance upon PαDG introduction are observed for Con A bound to the NHS-tripod, which suggests greater modification of the viscoelastic properties of these films (Figure A5.10). The magnitude of the relative frequency shifts is too large to correspond to the mass of bound PαDG. We attribute this non-Sauerbrey response of the resonance frequency to changes in Con A aggregation state upon binding, a phenomenon noted before for both Con A[13] and other proteins.[14]

H. AFM Characterization of NHS-Tripod Monolayer :

Figure A5.11 shows an AFM images of a self-assembled monolyer (SAM) of NHS-tripod on single layer graphene. In order to characterize properly the monolayer uniformity, the formation of the NHS-tripod SAM has been realized here on top of a single layer of

graphene produced by mechanical exfoliation of Highly Ordered Pyrolytic Graphite (HOPG). The image show uniform topology confirming the uniformity of the NHS-tripod SAM.

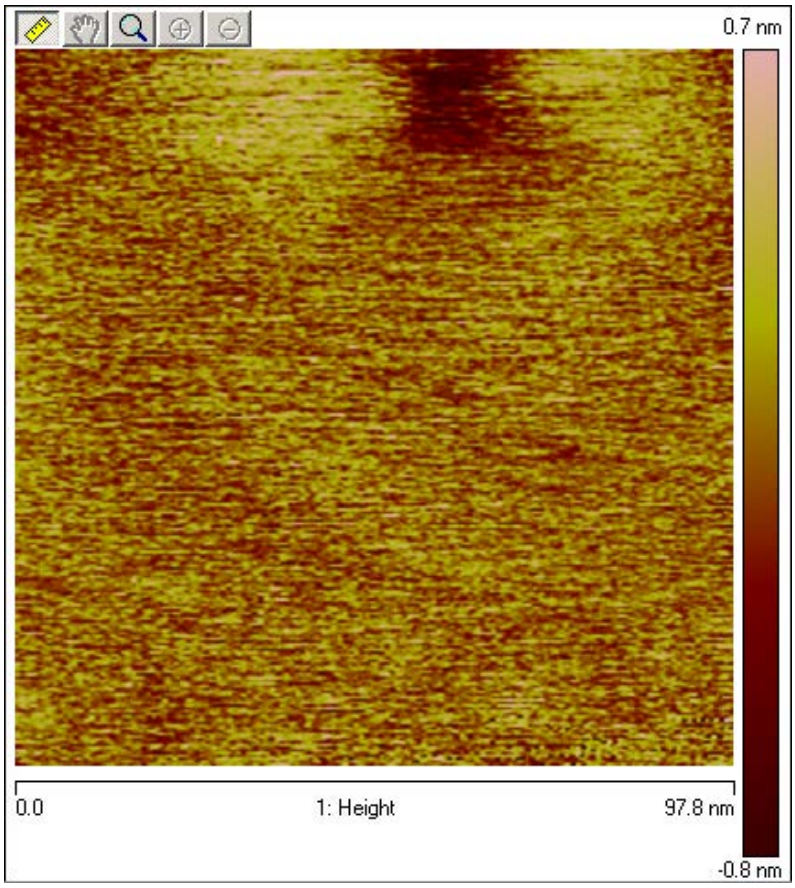

Figure A5.10. Representative AFM image of a self-assembled monolayer of **3** on freshly cleaved highly ordered pyrolytic graphite (HOPG)

I. Supplementary References .

46. Rodahl, M. ; Höök, F. ; Fredriksson, C. ; Keller, C. A. ; Krozer, A. ; Brzezinski, P. ; Voinova, M ; Kasemo, B . *Faraday Discuss.*, **1997**, *107*, 229-246

47. Höök, F.; Kasemo, B.; Nylander, T.;Fant, C.; Scott, K.; Elwing, H, *Anal. Chem.*, **2001**, *73*, 5796-5804.

48. Fredriksson, C.; Kihlman, S.; Rodahl, M.; Kasemo, B., *Langmuir* **1998**, *14*, 248-251

49. Geelhood, S. J.; Frank, C. W.; Kanazawa, K., *J. Electroch. Soc.*, **2002**, *149*, H33-H38

50. Goldstein, I. J.; Reichert, C. M.; Misaki, A. *Ann. N. Y. Acad. Sci.,* **1974**, *234*, 283-296

51. Sawyer, W. H.; Dabscheck, R.; Nott, P. R.; Selinger, B. K.; Kuntz, I. D. *J. Biochem*, **1975**, *147*, 613-615.

52. Golon, A.; Kuhnert, N. *J. Agric. Food Chem.,* **2012***, 60*, 3266-3274.

53. Sugisawa, H.; Edo, H. *J. Food Sci.*, **1996**, *31*, 561–565.

54. Goldstein, I. J.; Hollerman, C. E.; Merrick, J.M., *Biochim. Biophys. Acta*, **1965**, *97* , 68-76.

55. Casiraghi, C.; Pisana, S.; Novoselov, K. S.; Geim, A. K.; Ferrari, A. C., *Appl. Phys. Lett.* **2007**, *91*, 233108.

56. Capo, C.; Garrouste, F.; Benoliel, A. M.; Bongrand, P.; Ryter, A.; Bell, G. I.; *J. Cell. Sci.*, **1973**, *243*, 218-220.

57. Nicolson, G. L.; *Nature New Biol.*, **1973**, *243*, 218-220.

58. So, L.L.; Goldstein, I. J. J. Biol. Chem., **1967**, *242 (7)*, 1617-1622

59. Fant, C.; Elwing, H.; Höök, F. *Biomacromol.* **2002**, *3*, 732-741